Noninvasive Stroke Volume Monitoring by Electrical Impedance Tomography

THÈSE N^{O} 8343 (2018)

PRÉSENTÉE LE 19 JANVIER 2018
À LA FACULTÉ DES SCIENCES ET TECHNIQUES DE L'INGÉNIEUR
LABORATOIRE DE TRAITEMENT DES SIGNAUX 5
PROGRAMME DOCTORAL EN GÉNIE ÉLECTRIQUE

ÉCOLE POLYTECHNIQUE FÉDÉRALE DE LAUSANNE

POUR L'OBTENTION DU GRADE DE DOCTEUR ÈS SCIENCES

PAR

Fabian BRAUN

acceptée sur proposition du jury:

Dr S. Carrara, président du jury
Prof. J.-Ph. Thiran, Dr J. M. Sola i Caros, directeurs de thèse
Prof. A. Adler, rapporteur
Prof. I. Frerichs, rapporteuse
Dr J.-M. Vesin, rapporteur

ÉCOLE POLYTECHNIQUE
FÉDÉRALE DE LAUSANNE

Suisse
2018

The more I learn, the more I realize how much I don’t know.
— Albert Einstein

To *you*, the interested reader…

Acknowledgements

This thesis would simply have been impossible without different collaborations and the support of various people I owe my deep gratitude to. Therefore, I would like to *sincerely express my thanks* to:

My supervisor at CSEM, Dr Josep Solà for not only guiding me up the rocks of *Creux du Van* or down some snow-covered hills but through this entire thesis. Even in the most hopeless situations you never lost your optimism and always had a syringe of motivation ready. Without you sharing your knowledge and without your guidance I would never have stayed on the right route and probably not have found its end. Moltes gràcies Josep!

My supervisor at EPFL, Prof. Jean-Philippe Thiran for making this thesis possible at all. Also for your confidence, especially that you allowed me to carry out my research "far" away from Lausanne and with a lot of freedom. Merci beaucoup Jean-Philippe!

Dr Sandro Carrara, Dr Jean-Marc Vesin, Prof. Andy Adler and Prof. Inéz Frerichs for having accepted to be members of my doctoral thesis jury.

Prof. Andy Adler, a true expert in the field of EIT, for the uncountable hours you spent giving wise advice and fresh ideas either via one of the many Skype sessions or also during your visits here in Neuchâtel. Also for lending us your EIT device and for introducing us to other people who played crucial parts in this thesis. Thank you so much Andy!

The team at CHUV Lausanne, in particular Dr Fabrizio Gronchi, Dr Carlo Marcucci and Virgile Zimmermann, for your patience with the engineer "lost" in the hospital and for showing me what *real* clinical scenarios are. Even though our measurements did not turn out as expected, it was an unforgettable and invaluable experience for me. Grazie mille!

The team at UKSH Kiel, especially Prof. Inéz Frerichs, Dr Tobias Becher and Anna Wendler for acquiring and sharing valuable EIT data and for giving me another insight into the clinical reality. Thank you Tobi for the many interesting discussions, engineer-proof explanations and the delicious Currywürste. Vielen herzlichen Dank euch allen!

The remaining people who made real-world EIT measurements happen. Dr Thomas Riedel for lending us your two EIT machines and sharing your experience of clinical EIT. Merci vielmol Tom! Without your priceless contribution, most of the EIT data in this thesis would simply not exist. My former colleagues at Swisstom AG, notably, Andreas Waldmann, Beat Müller

and Peter Krammer, for keeping calm when answering my – often unusual – questions and demands. Dr Günter Hahn for giving technical support for the good old Goe MF II device.

The many people involved in the creation of the bioimpedance model. In particular Dr Simone Coppo and Dr Orestis Vardoulis for the MRI data acquisition. Dr Xènia Albà, Dr Karim Lekadir and Prof. Alejandro F. Frangi for performing the MRI segmentation of the 4D heart model. Dr Andrea Borsic for advising me on meshing and for providing me with a faster forward solver. Dr Markus Jehl for helping me to make your forward solver work on a non-Unix machine.

The entire team at CSEM for the incomparably friendly and pleasant (working) environment:

- Dr Martin Proença for the mutual support during these years: the uncountable hours we have spent wondering, questioning, brainstorming, etc. Thanks for having – exceptionally – been optimistic during the moments it all looked hopeless to me. Unvermutlich! Dankrkrkrkrkrkreee BOUDIN! Et voici encore pour apprendre pour de vrai: “Gang geng gredi gäge Gümlige ga güggele, gob Guggers Gödeli geng ga Garamell gänggele geit.”
- His supervisor, Dr Mathieu Lemay, for his many valuable inputs and in particular for pushing us to pursue the model-based approach.
- (Future Dr) Michaël Rapin for the various interesting discussions and challenges, often related to the next generation cardiovascular EIT device. And also for the early morning ascents to *Chasseral* followed by the unforgettable (icy) descents.
- My boss, Dr Mattia Bertschi for providing me with many distracting but also interesting projects in a great working environment and for always finding some money to pay the many invoices I brought to you.
- Martine Cadilhe Mendes for your support concerning the legal aspects of clinical trials.
- The *phad thai* bouldering crew and the yoga enthusiasts (*Namaste!*) for assuring the necessary and highly appreciated distraction around lunchtime.
- Everyone else who somehow did – at least indirectly – contribute to this thesis.

Those who were so kind to proof-read (parts of) this thesis: Dr Josep Solà, Dr Martin Proença, (future Dr) Florian Thürk, Dr Tobias Becher, (future Dr) Michaël Rapin, Dr Josias Wacker, Dr Christopher Moufawad el Achkar, and Prof. Albert Braun.

All my former colleagues and other people I have met during my professional career and education for (not) having motivated me to go until here (e.g. “Forget it, you will never get accepted at ETHZ.”). And yes, Timon and Oli, you finally win the bet!

My friends and family for their encouragement and support over all these years. And to Alice for travelling in life with me. Domo arigatou gozaimashita!

Finally, a big thank-you to all the people who cannot see their names in these lines but think they should be there.

Neuchâtel, 1 November 2017 Fabian

Abstract

In clinical practice it is of vital importance to track the health of a patient's cardiovascular system via the continuous measurement of hemodynamic parameters. Cardiac output (CO) and the related stroke volume (SV) are two such parameters of central interest as they are closely linked with oxygen delivery and the health of the heart. Many techniques exist to measure CO and SV, ranging from highly invasive to noninvasive ones. However, none of the noninvasive approaches are reliable enough in clinical settings. To overcome this limitation, we investigated the feasibility and practical applicability of noninvasively measuring SV via electrical impedance tomography (EIT), a safe and low-cost medical imaging modality.

In a first step, the unclear origins of cardiosynchronous EIT signals were investigated *in silico* on a 4D bioimpedance model of the human thorax. Our simulations revealed that the EIT heart signal is dominated by ventricular activity, giving hope for a *heart* amplitude-based SV estimation. We further showed via simulations that this approach seems feasible in controlled scenarios but also suffers from some limitations. That is, EIT-based SV estimation is impaired by electrode belt displacements and by changes in lung conductivity (e.g. by respiration or liquid redistribution). We concluded that the absolute measurement of SV by EIT is challenging, but trending – that is following relative changes – of SV is more promising.

In a second step, we investigated the practical applicability of this approach in three experimental studies. First, EIT was applied on 16 mechanically ventilated patients in the intensive care unit (ICU) receiving a fluid challenge to improve their hemodynamic situation. We showed that the resulting relative changes in SV could be tracked using the EIT *lung* amplitude, while this was not possible via the *heart* amplitude. The second study, performed on patients in the operating room (OR), had to be prematurely terminated due to too low variations in SV and technical challenges of EIT in the OR. Finally, the third experimental study aimed at testing an improved measurement setup that we designed after having identified potential limitations of available clinical EIT systems. This setup was tested in an experimental protocol on 10 healthy volunteers undergoing bicycle exercises. Despite the use of subject-specific 3D EIT, neither the heart nor the lung amplitudes could be used to assess SV via EIT. Changes in electrode contact and posture seem to be the main factors impairing the assessment of SV.

In summary, based on *in silico* and *in vivo* investigations, we revealed various challenges related to EIT-based SV estimation. While our simulations showed that trending of SV via the EIT *heart* amplitude should be possible, this could not be confirmed in any of the experimental studies. However, in the ICU, where sufficiently controlled EIT measurements were possible, the EIT *lung* amplitude showed potential to trend changes in SV. We concluded that EIT amplitude-based SV estimation can easily be impaired by various factors such as electrode contact or small changes in posture. Therefore, this approach might be limited to controlled environments with the least possible changes in ventilation and posture. Future research should scrutinize the lung amplitude-based approach in dedicated simulations and clinical trials.

Keywords: electrical impedance tomography, EIT, cardiac output, stroke volume, noninvasive, continuous, hemodynamic monitoring, cardiovascular diseases, bioimpedance model, simulations.

Zusammenfassung

Die kontinuierliche Messung von hämodynamischen Parametern zur Überwachung des Herz-Kreislauf-Systems ist von entscheidender klinischer Bedeutung. Das Herzzeitvolumen (HZV) und das verwandte Schlagvolumen (SV) sind zwei wichtige Parameter, da sie eng mit der Sauerstoffzufuhr und dem Gesundheitszustand des Herzens verbunden sind. Die gegenwärtigen Verfahren zur Messung von HZV und SV reichen vom hochinvasiven bis hin zum nichtinvasiven Ansatz, wobei sich im klinischen Umfeld keiner der nichtinvasiven Ansätze als ausreichend verlässlich erwiesen hat. Deshalb haben wir die Machbarkeit und Praxistauglichkeit der nichtinvasiven SV-Messung mittels elektrischer Impedanztomografie (EIT) – einem sicheren und kostengünstigen Bildgebungsverfahren – untersucht.

In einer ersten Phase wurde der unklare Ursprung von kardiosynchronen EIT-Signalen *in silico* an einem 4D-Bioimpedanzmodell des menschlichen Thorax untersucht. Unsere Simulationen zeigten, dass die ventrikuläre Aktivität das EIT-Herzsignal dominiert, was für eine *herz*amplitudenbasierte SV-Schätzung spricht. Zudem scheint dieser Ansatz in kontrollierten Szenarien machbar, weist aber auch einige Einschränkungen auf. Die EIT-basierte SV-Schätzung wird nämlich durch Verschiebungen des Elektrodengürtels und Veränderungen der Lungenleitfähigkeit (z. B. durch Atmung oder Flüssigkeitsumverteilung) beeinträchtigt. Wir kamen zum Schluss, dass die absolute SV-Messung via EIT schwierig ist, das Trending – d.h. relative SV-Änderungen zu verfolgen – hingegen vielversprechender.

In einer zweiten Phase haben wir unseren Ansatz in drei experimentellen Studien untersucht. Zunächst wurde EIT an 16 mechanisch beatmeten Patienten auf der Intensivstation (ICU) gemessen, bei welchen die Hämodynamik mittels Volumengabe beeinflusst wurde. Die resultierenden relativen SV-Änderungen konnten mit der EIT *Lungen*amplitude verfolgt werden, wobei dies mit der *Herz*amplitude nicht möglich war. Die zweite Studie wurde im Operationssaal (OP) durchgeführt; musste aber wegen zu geringen SV-Änderungen und technischer Einschränkungen der EIT vorzeitig beendet werden. In einer dritten Studie wurde eine neue Messanordnung erprobt, welche entworfen wurde, um Einschränkungen von klinischen EIT-Systemen zu überwinden. Diese wurde an 10 Probanden getestet, die ein Versuchsprotokoll mit Fahrradübungen ausführten. Trotz dem Einsatz von personenspezifischer 3D EIT konnten weder Herz- noch Lungenamplituden zur SV-Bestimmung verwendet werden. Veränderungen des Elektrodenkontaktes und der Körperhaltung scheinen diese Bestimmung zu sehr zu beeinträchtigen.

Zusammenfassung

In der vorliegenden Arbeit wurden mittels *in silico* und *in vivo* Untersuchungen verschiedene Herausforderungen der EIT-basierten SV-Schätzung aufgezeigt. Obwohl unsere Simulationen zeigten, dass die relative SV-Messung mittels *Herz*amplitude möglich sein sollte, konnte dies in keiner der experimentellen Studien bestätigt werden. Auf der ICU, wo kontrollierte EIT-Messungen möglich waren, zeigte jedoch die *Lungen*amplitude Potential für SV-Trending. Wir kamen zum Schluss, dass die amplitudenbasierte SV-Schätzung mittels EIT durch verschiedene Faktoren wie Elektrodenkontakt oder Körperhaltung beeinträchtigt werden kann. Deshalb ist dieser Ansatz auf Umgebungen beschränkt, wo Ventilation und Körperhaltung möglichst kontrolliert und unverändert bleiben. In Zukunft sollte der lungenamplitudenbasierte Ansatz in speziellen Simulationen und klinischen Studien genauer untersucht werden.

Stichwörter: elektrische Impedanztomografie, EIT, Herzzeitvolumen, Schlagvolumen, nichtinvasiv, kontinuierlich, hämodynamisches Monitoring, Herz-Kreislauf-Erkrankung, Bioimpedanzmodell, Simulationen.

Résumé

En milieu clinique, monitorer l'état de santé du système cardiovasculaire d'un patient par la mesure en continu de ses paramètres hémodynamiques est d'importance primordiale. En effet, le débit cardiaque (DC) et le volume d'éjection systolique (VES) sont deux paramètres capitaux liés à l'apport d'oxygène et à l'état de santé du cœur. Qu'elles soient invasives ou non, il existe de nombreuses techniques de mesure du DC et du VES. Néanmoins, aucune approche non-invasive n'est suffisamment fiable en milieu clinique. Pour pallier cette limitation, nous avons étudié la faisabilité et l'applicabilité pratique de la mesure non-invasive du VES par la tomographie d'impédance électrique (TIE), une technique d'imagerie médicale sûre et peu coûteuse.

Dans un premier temps, les origines ambiguës des signaux TIE cardiosynchrones ont été étudiées *in silico* au moyen d'un modèle de bioimpédance 4D du thorax humain. Nos simulations ont montré que le signal provenant du cœur est principalement lié à l'activité ventriculaire, ce qui laisse présumer la possibilité d'une estimation du VES basée sur l'amplitude *cardiaque*. De plus, nous avons montré par simulation que cette approche est envisageable dans des conditions contrôlées et en tenant compte de certaines limitations. En l'occurrence, l'estimation du VES basée sur la TIE est influencée par le déplacement de la ceinture d'électrodes et par les changements de conductivité pulmonaire (p. ex. dus à la respiration ou à la redistribution de liquides). Nous avons conclu que la mesure absolue du VES basée sur la TIE est difficile, mais que le monitorage de tendances est plus prometteur.

Dans un second temps, l'applicabilité pratique de la TIE a été étudiée dans le cadre de trois études expérimentales. Premièrement, la TIE a été appliquée dans une unité de soins intensifs (USI) sur 16 patients sous ventilation mécanique recevant un bolus liquidien pour l'amélioration de leur situation hémodynamique. Nous avons montré que les changements relatifs du VES pouvaient être suivies au moyen de l'amplitude *pulmonaire* de la TIE, alors que ce n'était pas possible par l'amplitude *cardiaque*. La seconde étude, effectuée en salle d'opération, a dû être arrêtée prématurément en raison de variations trop faibles du VES et de contraintes techniques liées à la TIE. Enfin, la troisième étude avait pour objectif de tester une technique de mesure améliorée que nous avons conçue après avoir identifié les limites potentielles des systèmes cliniques TIE existants. Cette technique a été testée dans le cadre d'un protocole expérimental sur 10 volontaires sains faisant des exercices physiques contrôlés. Malgré une utilisation de TIE 3D spécifique par sujet, ni les amplitudes cardiaques, ni les amplitudes pulmonaires, n'ont pu être utilisées pour évaluer le VES. Les principaux facteurs entravant l'évaluation du VES semblent être les changements de posture et le contact des électrodes.

En résumé, à partir d'études *in silico* et *in vivo*, nous avons identifié divers contraintes liées à l'estimation du VES basée sur la TIE. Bien que nos simulations aient montré la faisabilité du monitorage de tendances du VES par la TIE au moyen de l'amplitude *cardiaque*, cela n'a pas pu être confirmé lors de nos études expérimentales. Toutefois, dans l'USI, où les mesures étaient suffisamment contrôlées, l'amplitude *pulmonaire* de la TIE a montré un certain potentiel pour le monitorage des tendances du VES. Nous en avons conclu que l'estimation du VES basée sur les amplitudes de la TIE peut facilement être influencée par divers facteurs tels que le contact des électrodes ou les changements de posture. Par conséquent, cette approche pourrait être limitée aux environnements contrôlés, en minimisant les changements de ventilation et de posture. Les recherches futures devraient minutieusement étudier l'approche basée sur l'amplitude pulmonaire dans le cadre de simulations et d'essais cliniques spécifiques.

Mots-clefs : tomographie d'impédance électrique, TIE, débit cardiaque, volume d'éjection systolique, non-invasif, surveillance en continu, monitorage hémodynamique, maladies cardiovasculaires, modèle de bioimpédance, simulations.

Contents

Acknowledgements **i**

Abstract (English/Deutsch/Français) **iii**

List of Figures **xv**

List of Tables **xix**

List of Abbreviations **xxi**

I Introduction and Background **1**

1 Introduction **3**
- 1.1 Problem Statement and Motivation 3
- 1.2 Thesis Objectives 4
- 1.3 Organization of the Manuscript 5

2 Stroke Volume and Cardiac Output **7**
- 2.1 Cardiovascular Physiology in a Nutshell 7
  - 2.1.1 Cardiovascular System and Hemodynamic Parameters 7
  - 2.1.2 Factors Affecting Stroke Volume and Cardiac Output 9
- 2.2 State of the Art of Cardiac Output Monitoring 10
  - 2.2.1 Invasive Methods 10
  - 2.2.2 Minimally-Invasive Methods 13
  - 2.2.3 Noninvasive Methods 14
- 2.3 Comparison and Validation of Cardiac Output Measurements 16
- 2.4 The Quest for the Ideal Cardiac Output Monitoring Device 17

3 Electrical Impedance Tomography **19**
- 3.1 Principle of Thoracic EIT 20
  - 3.1.1 Impedance Measurements to Assess Tissue Properties 20
  - 3.1.2 Image Reconstruction 22
  - 3.1.3 Separation of Ventilation and Cardiosynchronous Activity 25
- 3.2 Previous Work on EIT-Based Stroke Volume Estimation 26
- 3.3 Controversial Origins of Cardiosynchronous EIT Signals 28

II Investigating Cardiovascular EIT via Simulations on a Bioimpedance Model 29

4 Bioimpedance Models 31
4.1 Introduction 31
4.1.1 Motivation 31
4.1.2 Related Work 31
4.2 Hemodynamic 4D Bioimpedance Model of the Human Thorax 32
4.2.1 MRI Data 32
4.2.2 Static Thorax 33
4.2.3 Dynamic Heart 34
4.2.4 Dynamic Aorta 35
4.2.5 Dynamic Lungs 36
4.2.6 Simplified Models 36
4.3 Practical Aspects of Simulations 37
4.4 Limitations and Future Work 37

5 Investigations on the Origins of Cardiac EIT Signals 39
5.1 Introduction 40
5.2 Methods 40
5.2.1 Simulations 40
5.2.2 Signal Analysis 40
5.3 Results and Discussion 41
5.4 Limitations and Future Work 42
5.5 Conclusion 42

6 Feasibility and Limitations of EIT-Based Stroke Volume Measurement 43
6.1 Introduction 44
6.1.1 Objectives 44
6.1.2 Motivation 44
6.2 Methods 45
6.2.1 Dynamic Bioimpedance Model 45
6.2.2 Simulations Performed 46
6.2.3 SV Estimation 48
6.2.4 Analysis and Performance Evaluation 48
6.3 Results and Discussion 50
6.3.1 EIT Heart Amplitude 50
6.3.2 Analysis I - Absolute SV 50
6.3.3 Analysis II - Relative SV - Trending 55
6.3.4 Limitations and Future Work 57
6.4 Conclusion 57

III Investigating EIT-Based SV Monitoring in Clinical Environments 59

7 Rationale for Clinical EIT Measurements 61

8 Measurements in the Operating Room 63
8.1 Introduction 63
8.2 Methods 63
8.2.1 Study Protocol and Data Acquisition 63
8.2.2 Data Analysis 64
8.3 Results and Discussion 69
8.3.1 General Overview 70
8.3.2 Hypothesis 1: Absolute SV with Patient-Independent Calibration 72
8.3.3 Hypothesis 2: Absolute SV with Patient-Specific Calibration 73
8.3.4 Hypothesis 3: Relative SV with Patient-Independent Calibration 75
8.3.5 Hypothesis 4: Relative SV with Patient-Specific Calibration 75
8.3.6 Analysis Restricted to Patients with High Variations in SV_{Ref} 77
8.3.7 Limitations, Challenges and Future Work 77
8.3.8 Rationale for the Premature Termination of This Study 78
8.4 Conclusion 78

9 Measurements in the Intensive Care Unit 81
9.1 Introduction 81
9.2 Methods 82
9.2.1 Study Protocol and Data Acquisition 82
9.2.2 Data Preprocessing 83
9.2.3 Signal Processing and Data Analysis 83
9.3 Results and Discussion 84
9.3.1 Hemodynamic Variations 84
9.3.2 EIT Data Analysis 86
9.3.3 SV Trending Performance of EIT 86
9.3.4 Comparison to the Clinical Study in the Operating Room 88
9.3.5 Comparison to Simulations and Previous Studies 89
9.3.6 Limitations and Future Work 89
9.4 Conclusion 90

IV Towards an Optimized Measurement Setup for EIT-Based SV Monitoring 91

10 Considerations for an Improved Measurement Setup 93
10.1 Practical Limitations of Available Clinical EIT Systems 93
10.2 Finding a Setup Better Suited for EIT-Based SV Monitoring 94
10.3 The Challenge of Comparing Different Measurement Setups 97

11 A Versatile Noise Performance Metric for EIT Algorithms 99
11.1 Introduction 100
11.1.1 State of the Art in Hyperparameter Selection 100
11.1.2 Practical Aspects and Limitations of the State of the Art 101
11.1.3 Proposed Approach 102
11.1.4 Image Reconstruction for Difference EIT 102
11.1.5 Structure of This Chapter 103
11.2 Methods 103
11.2.1 $\overline{\text{SNR}}$ Framework 103
11.2.2 Validation Experiments 106
11.3 Results 109
11.3.1 Simulation Experiments 109
11.3.2 Practical Experiments 110
11.3.3 Open Geometry Example 113
11.4 Discussion 113
11.4.1 Simulation Experiments 113
11.4.2 Practical Experiments 114
11.4.3 Open Geometry Example 115
11.4.4 Algorithm Parameter Selection 115
11.4.5 Limitations and Future Work 116
11.5 Conclusion 117

12 Experimental Evaluation of an Improved Measurement Setup 119
12.1 Introduction 120
12.2 Methods 120
12.2.1 Study Protocol and Study Population 120
12.2.2 Data Acquisition 121
12.2.3 Data Preprocessing 122
12.2.4 Subject-Specific EIT Image Reconstruction 123
12.2.5 Data Analysis 124
12.3 Results and Discussion 126
12.3.1 General Overview of EIT Data 126
12.3.2 Hypothesis 1: Absolute SV with Subject-Independent Calibration 128
12.3.3 Hypothesis 2: Absolute SV with Subject-Specific Calibration 129
12.3.4 Hypothesis 3: Relative SV with Subject-Independent Calibration 131
12.3.5 Hypothesis 4: Relative SV with Subject-Specific Calibration 131
12.3.6 Limitations and Future Work 132
12.4 Conclusion 132

V Conclusions 135

13 Synthesis 137
- 13.1 Thesis Contributions . . . 137
- 13.2 Summary of Achievements . . . 138
- 13.3 Limitations and Future Work . . . 141
- 13.4 Conclusion . . . 142

VI Appendix 145

A Investigations on Aortic Blood Pressure Measured via EIT 147
- A.1 Introduction . . . 148
- A.2 Methods . . . 149
  - A.2.1 Hemodynamic 3D Thorax Model . . . 149
  - A.2.2 Bioimpedance Simulations . . . 153
  - A.2.3 Image Reconstruction . . . 154
  - A.2.4 Hemodynamic Simulation Experiments . . . 154
- A.3 Results . . . 157
- A.4 Discussion . . . 157
- A.5 Conclusions . . . 160

B Ensemble Averaging and Signal Quality Estimation 161

C Measurements in the Operating Room: Additional Figures 163

D Measurements in the Intensive Care Unit: Additional Figures 169

E Measurements on Healthy Volunteers: Additional Figures and Tables 177

Bibliography 187

Curriculum Vitae 203

List of Figures

2.1 Cardiovascular system and the heart 8
2.2 Main factors affecting heart rate, stroke volume and cardiac output 9
2.3 Comparison of cardiac output monitoring techniques 11
2.4 Principle of right heart catheterization and thermodilution 12

3.1 Typical acquisition and processing steps used for thoracic EIT 19

4.1 4D bioimpedance model of the human thorax 33
4.2 4D models of the heart and the aorta 35
4.3 Aortic radius as a function of the distance from the aortic valve 36

5.1 Cardiosynchronous activity images of heart signal contribution 41
5.2 EIT images of heart signal contribution 41
5.3 Contributors to the heart signal 42

6.1 Block diagram of the simulation framework 45
6.2 Block diagram of the SV estimation algorithm 45
6.3 Heart ROI detection example 49
6.4 Trending analysis example by means of four-quadrant plots 50
6.5 EIT heart amplitude $\Delta\sigma_H$ vs simulated SV 51
6.6 SV_{EIT} influenced by belt displacement 52
6.7 Relative error of SV_{EIT} resulting from electrode detachment 53
6.8 SV_{EIT} influenced by changes in hematocrit and lung air volume 54
6.9 Conceptual explanation of the heart-lung conductivity contrast (HLC) 55
6.10 Trending ability of ΔSV_{EIT} influenced by belt displacement 56

8.1 Block diagram of measurement setup in the OR 64
8.2 Block diagram of the data analysis and hypotheses testing 67
8.3 Distribution of SV reference measurements for each patient 70
8.4 Examples of activity images for three patients 71
8.5 Example recording of the measurements in the OR 71
8.6 Examples of estimated SV_{EIT} vs SV_{Ref} for H1 and H2 73
8.7 Examples of estimated ΔSV_{EIT} vs ΔSV_{Ref} for H3 and H4 75
8.8 Performance of two patients with highest variations in SV_{Ref} for H2 and H4 . . 77

9.1 Block diagram of measurement setup in the ICU 82
9.2 Hemodynamic variations for each patient recorded in the ICU 85
9.3 EIT analysis example for patient V17 of the ICU study 85
9.4 Trending analysis for all measurements in the ICU 87
9.5 Trending analysis of the ICU measurements limited to reliable data 88

10.1 Electrode positions more suitable for EIT-based SV monitoring 94
10.2 Genetic algorithm used to find a better stimulation and measurement pattern 95
10.3 Forward sensitivities for three different stimulation and measurement patterns 96

11.1 Three hyperparameter selection approaches commonly used in EIT 100
11.2 Block diagram of the $\overline{\text{SNR}}$ framework 103
11.3 Overview of the $\overline{\text{SNR}}$ simulation experiments 108
11.4 Noise performance for different GN reconstructions 110
11.5 Noise performance for different GREIT reconstructions 110
11.6 Noise performance for various cases of GN reconstructions 111
11.7 Noise performance of practical experiments with fixed noise figure 112
11.8 Noise performance of practical experiments with fixed $\overline{\text{SNR}}$ 112
11.9 $\overline{\text{SNR}}$ applied to an open geometry example 113

12.1 Temporal evolution of the experimental protocol 120
12.2 Block diagram of the setup of measurements performed on healthy volunteers. 121
12.3 EIT electrode placement with 3D thorax image and 3D thorax model 122
12.4 Block diagram of the data analysis on healthy volunteers. 124
12.5 3D EIT images of respiration for the same measurement of all volunteers 126
12.6 ECG-gated 3D EIT images for the same measurement of all volunteers 127
12.7 3D EIT example images for ten measurements of the same volunteer 127
12.8 SV_{EIT} vs SV_{Ref} with subject-specific calibration 128
12.9 Temporal evolution of SV_{Ref}, heart rate and EIT-based features for subject S03 . 130
12.10 Trending ability of $\Delta\text{SV}_{\text{EIT}}$ vs $\Delta\text{SV}_{\text{Ref}}$ by means of four-quadrant plot 131

A.1 Thorax and heart model 150
A.2 Simple geometric heart model 152
A.3 Block diagram of the simulation framework 153
A.4 Block diagram of the PAT and SNR experiments 155
A.5 Example relationship between the estimated and simulated aortic PAT values . 156
A.6 Relative error and aortic contribution for different algorithm configurations . . 158
A.7 Relative error and aortic contribution as a function of GREIT weighting radius 158

C.1 Best possible fits for absolute SV with patient-independent calibration (H1) . . 164
C.2 Best possible fits for absolute SV with patient-specific calibration (H2) 165
C.3 Best possible fits for relative SV with patient-independent calibration (H3) . . . 166
C.4 Best possible fits for relative SV with patient-specific calibration (H4) 167

D.1 Ensemble averaged EIT analysis for patient V05 169
D.2 Ensemble averaged EIT analysis for patient V06 170
D.3 Ensemble averaged EIT analysis for patient V07 170
D.4 Ensemble averaged EIT analysis for patient V08 171
D.5 Ensemble averaged EIT analysis for patient V09 171
D.6 Ensemble averaged EIT analysis for patient V10 172
D.7 Ensemble averaged EIT analysis for patient V11 172
D.8 Ensemble averaged EIT analysis for patient V12 173
D.9 Ensemble averaged EIT analysis for patient V13 173
D.10 Ensemble averaged EIT analysis for patient V14 174
D.11 Ensemble averaged EIT analysis for patient V15 174
D.12 Ensemble averaged EIT analysis for patient V16 175
D.13 Ensemble averaged EIT analysis for patient V18 175
D.14 Ensemble averaged EIT analysis for patient V19 176
D.15 Ensemble averaged EIT analysis for patient V20 176

E.1 Temporal evolution of $\mathrm{SV_{Ref}}$, heart rate and EIT-based features for subject S01 . 178
E.2 Temporal evolution of $\mathrm{SV_{Ref}}$, heart rate and EIT-based features for subject S02 . 178
E.3 Temporal evolution of $\mathrm{SV_{Ref}}$, heart rate and EIT-based features for subject S04 . 179
E.4 Temporal evolution of $\mathrm{SV_{Ref}}$, heart rate and EIT-based features for subject S05 . 179
E.5 Temporal evolution of $\mathrm{SV_{Ref}}$, heart rate and EIT-based features for subject S06 . 180
E.6 Temporal evolution of $\mathrm{SV_{Ref}}$, heart rate and EIT-based features for subject S08 . 180
E.7 Temporal evolution of $\mathrm{SV_{Ref}}$, heart rate and EIT-based features for subject S09 . 181
E.8 Temporal evolution of $\mathrm{SV_{Ref}}$, heart rate and EIT-based features for subject S10 . 181

List of Tables

3.1 Overview of clinical EIT devices 21

4.1 Tissue conductivity and composition 34

6.1 Simulated physiological parameters 46
6.2 Errors of SV_{EIT} for belt displacement 51
6.3 Errors of SV_{EIT} for electrode detachment 53
6.4 Errors of SV_{EIT} for changes in hematocrit and lung air volume 53
6.5 Trending performance of ΔSV_{EIT} for belt displacement 56
6.6 Trending performance of ΔSV_{EIT} for changes in hematocrit and lung air volume 57
6.7 Synthesis of feasibility and limitations for absolute and relative SV_{EIT} 58

8.1 List of features extracted from EIT for SV estimation 66
8.2 Ranking critera and acceptance thresholds for OR analysis 69
8.3 Overview of patients enrolled for measurements in the OR 70
8.4 Hypothesis 1 - Goodness of fit for absolute SV with patient-independent calibration 72
8.5 Hypothesis 2 - Goodness of fit for absolute SV with patient-specific calibration 73
8.6 Hypothesis 3 - Goodness of fit for relative SV with patient-independent calibration 74
8.7 Hypothesis 4 - Goodness of fit for relative SV with patient-specific calibration . 76

12.1 Overall performance of EIT-based SV estimation on healthy volunteers 129

13.1 Overview of experimental EIT studies performed in this thesis 140

A.1 Tissue composition of different structures in the bioimpedance model 151

E.1 Absolute SV via subject-independent calibration on healthy volunteers 182
E.2 Absolute SV via subject-specific calibration on healthy volunteers 183
E.3 Relative SV via subject-independent calibration on healthy volunteers 184
E.4 Relative SV via subject-specific calibration on healthy volunteers 185

List of Abbreviations

CAI	cardiosynchronous activity image
CO	cardiac output
ECG	electrocardiogram
EDV	end diastolic volume
EIT	electrical impedance tomography
ESV	end systolic volume
FEM	finite element model
HLC	heart-lung (conductivity) contrast
HR	heart rate
ICU	intensive care unit
MRI	magnetic resonance imaging
NF	noise figure
NP	noise performance
OR	operating room
PAC	pulmonary artery catheter
PAP	pulmonary artery pressure
PCA	pulse contour analysis
PEEP	positive end-expiratory pressure
ROI	region of interest
SV	stroke volume
SVV	stroke volume variation
TD	thermodilution

Introduction and Background Part I

1 Introduction

1.1 Problem Statement and Motivation

The human body consists of roughly $75 \cdot 10^{12}$ cells which all require oxygen in order to survive. The heart plays a vital role in supplying this oxygen as it pumps oxygen-enriched blood from the lungs to the remaining organs in the body. One key factor influencing this oxygen delivery is the cardiac output (CO), i.e. the amount of blood ejected by one of the lower heart chambers (ventricles) in one minute [48]. By way of example, in a resting adult each ventricle pumps $4-7$ liters of blood per minute and during severe physical exertion this value can raise five-fold to $25-35$ L/min [92]. On the other hand, in a diseased cardiovascular system, CO can be compromised such that the oxygen delivery is insufficient which can pose a lethal threat.

As reported by the world health organization (WHO) cardiovascular diseases (CVDs) are the main reason for death on a world-wide scale. It was estimated that in 2015, CVDs were the cause of death for 17.7 million people, which accounts for 31 % of all deaths that year [163]. One of the research priorities in order to decrease morbidity and mortality due to CVDs is to monitor trends and risk factors of these diseases [162]. Therefore, it is of great interest to have medical devices which allow the continuous measurement of *hemodynamic parameters* such as blood pressure, heart rate and CO, to name but a few. Among these parameters CO is of particular interest as it is closely linked with the oxygen delivery and the health of the heart.

However, compared to most of the other hemodynamic parameters, CO is more difficult to measure since blood is being dispersed as it travels away from the heart [37], i.e. the local blood flows through the arms, legs or to the neck represent only a portion of the total CO which itself needs to be measured directly in the heart or at its outflow tract (i.e. ascending aorta). In contrast, heart rate or blood pressure can be measured accurately enough in the periphery (e.g. arm or finger). For these reasons the challenge of developing a reliable CO measurement technique is considered as the “Holdy Grail” of hemodynamic monitoring according to Critchley [37]. CO can be expressed as the stroke volume (SV), i.e. the blood ejected by one ventricle for each heartbeat, multiplied by the heart rate (HR): $\mathrm{CO} = \mathrm{SV} \times \mathrm{HR}$. While the HR can be assessed easily via an electrocardiogram (ECG), the challenge resides in reliably measuring SV.

A myriad of technologies exist to estimate CO. However, right heart thermodilution, the technology considered as clinical gold standard has a limited accuracy [37] and requires highly invasive catheterization. This intervention is controversial as it can cause complications and has not shown to help reducing mortality [72, 128, 35]. Even though less invasive and noninvasive techniques are available [79, 99, 34, 129], they do not fulfill the requirements of an “ideal” hemodynamic monitoring device as defined by Vincent et al. [152] and detailed in the next chapter. Furthermore, a recent meta-analysis of noninvasive CO monitoring devices by Joosten et al. [87] has found that none of these devices is reliable enough when used in clinical settings. Therefore, the quest for the “ideal” CO monitoring devices continues.

To this end, the present thesis aims at investigating the potential of electrical impedance tomography (EIT) as a tool to noninvasively estimate SV and thus CO. Being a low-cost and nonionizing medical imaging modality, EIT is an appealing candidate for the continuous monitoring of CO. In brief, it consists of a belt of electrodes applied around the thorax, which measures electrical impedances by injecting weak alternating currents [52, 2, 80]. These measurements are transformed into tomographic images which represent changes in intrathoracic impedance. EIT is commonly used to monitor lung function in order to optimize regional ventilation or to diagnose lung diseases [52]. In contrast, the EIT-based assessment of cardiovascular activity is at an earlier stage of research [9]. The few studies published, which address the estimation of SV and CO via EIT [155, 114, 113, 41] are limited in various aspects and all raise the need for further investigations, in particular for measurements on humans in clinical studies. Moreover, the exact origins of cardiac EIT signals are unclear and discussed controversially in the literature [20, 118, 11]. This is an important issue to be addressed, since an appropriate and reliable processing algorithm can only be developed and validated if the source of the underlying signals is well understood.

1.2 Thesis Objectives

The present thesis aims at investigating the potential of EIT to noninvasively estimate SV, with particular focus on its practical applicability. More specifically, this thesis aims at meeting the following objectives:

a) To investigate the origins of cardiovascular EIT signals by means of simulations on a bioimpedance model of the human thorax;

b) To show the feasibility and potential limitations of EIT-derived SV monitoring by means of simulations on the same model;

c) To perform measurements on patients in clinical environments with currently available EIT systems and test whether the model-based findings can be validated experimentally;

d) To identify potential limitations of current clinical EIT systems related to SV monitoring, suggest an improved measurement setup and evaluate it experimentally.

1.3 Organization of the Manuscript

This manuscript is structured in five parts:

- Part I provides and introduction by describing the motivation and main objectives of the present thesis (Chapter 1), the background related to the physiology and the state of the art of CO monitoring devices (Chapter 2), as well as the technical aspects of EIT (Chapter 3);
- Part II first presents the creation of a bioimpedance model of a human thorax (Chapter 4), which is used in simulations to investigate the origins of cardiac EIT signals (Chapter 5), and to study the feasibility and limitations of EIT-based SV estimation (Chapter 6);
- Part III describes two clinical studies by first giving a rationale for performing measurements on patients (Chapter 7), followed by presenting the two studies, one performed in the operating room (Chapter 8), and the other in the intensive care unit (Chapter 9);
- Part IV starts by describing the limitations of currently available clinical EIT devices and suggesting an improved setup (Chapter 10), followed by presenting a novel approach allowing to fairly compare EIT image reconstructions from different setups (Chapter 11). Finally, the testing of the improved measurement setup in an experimental study on healthy volunteers is presented (Chapter 12);
- Part V concludes this thesis by providing a synthesis and suggestions for future work (Chapter 13).

In addition, the appendices in Part VI contain: A simulation-based study to investigate the feasibility of aortic blood pressure measurement via EIT (Appendix A); The mathematical aspects of ensemble averaging and the related signal quality estimator (Appendix B); Additional figures of the clinical study in the operating room (Appendix C); Additional figures of the clinical study in the intensive care unit (Appendix D); Additional figures and tables of the experimental study on healthy volunteers (Appendix E).

2 Stroke Volume and Cardiac Output

In this chapter we first give a brief introduction into cardiovascular physiology with particular focus on stroke volume (SV) and cardiac output (CO). Then we present the different technologies currently available for the measurement of CO ranging from the highly invasive gold standard reference to noninvasive approaches. After mentioning some aspects to be considered when comparing CO measurements of different devices, we list the requirements for an ideal CO monitoring device and the reasons why EIT might be an appropriate candidate.

2.1 Cardiovascular Physiology in a Nutshell

In the following, we give a brief background to cardiovascular physiology necessary to understand the basic mechanisms related to SV and CO. The reader interested in more detail is referred to the books by Levick [92], Nichols et al. [107] or Westerhof et al. [159].

2.1.1 Cardiovascular System and Hemodynamic Parameters

The cardiovascular system comprises the heart, the blood and the blood vessels. Its main function is the transport of substances (including oxygen, water and nutrients) to the tissues and the washout of metabolic waste products (including carbon dioxide) from these tissues. Other functions are the distribution of hormones and the regulation of body temperature [92].

The central organ of the cardiovascular system is the heart. As shown in Figure 2.1a, it is a hollow organ consisting of specialized muscular tissue forming four chambers (two atria and two ventricles) and containing four valves (two inlet and two outlet valves) which enable an unidirectional blood flow. From an engineer's perspective, the heart represents two synchronized pumps (each with one atrium, one ventricle and two valves) connected in series via the blood vessels to one circulatory system, as illustrated in Figure 2.1b. The right part of the heart – the first pump – supplies the lungs with deoxygenated blood (black) returning from the systemic circulation, whereas the left part – the second pump – collects oxygenated blood (red) from the lungs and distributes it among the different organs in the systemic circulation.

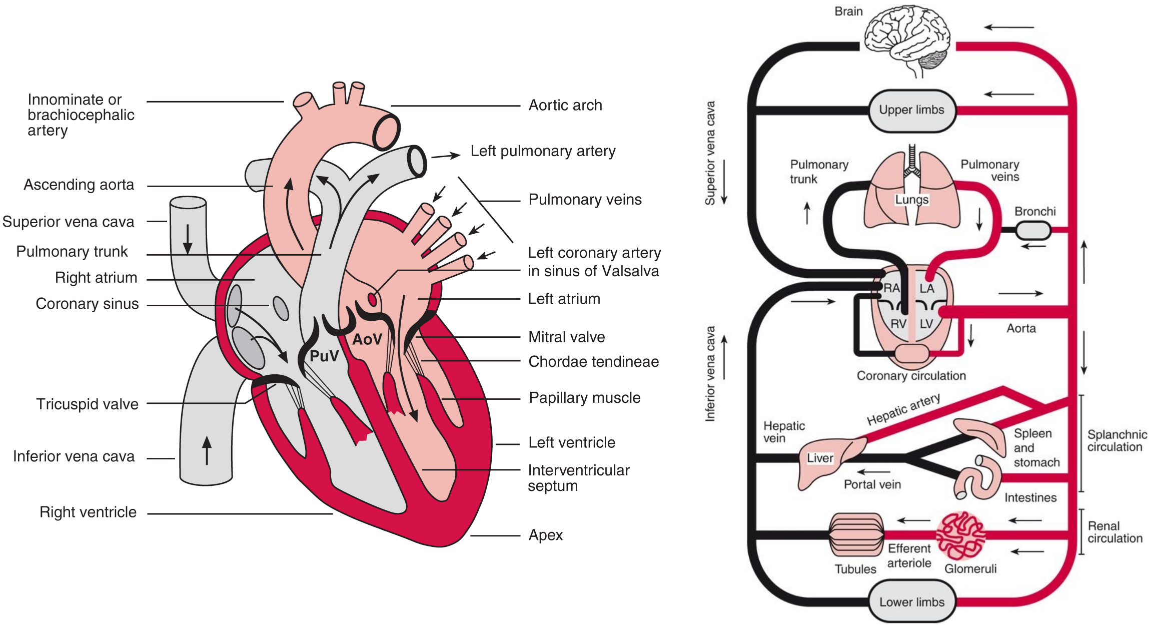
Innominate or brachiocephalic artery
Ascending aorta
Superior vena cava
Pulmonary trunk
Right atrium
Coronary sinus
Tricuspid valve
Inferior vena cava
Right ventricle
Aortic arch
Left pulmonary artery
Pulmonary veins
Left coronary artery in sinus of Valsalva
Left atrium
Mitral valve
Chordae tendineae
Papillary muscle
Left ventricle
Interventricular septum
Apex
PuV
AoV
Brain
Upper limbs
Superior vena cava
Pulmonary trunk
Lungs
Pulmonary veins
Bronchi
RA
LA
RV
LV
Aorta
Coronary circulation
Inferior vena cava
Hepatic vein
Hepatic artery
Liver
Portal vein
Spleen and stomach
Intestines
Splanchnic circulation
Renal circulation
Tubules
Efferent arteriole
Glomeruli
Lower limbs

(a) (b)

Figure 2.1 – (a) Structure of the heart: pink/gray indicating oxygenated/deoxygenated blood, respectively. AoV/PuV stands for aortic/pulmonary valve. (b) Illustration of the cardiovascular system which can be separated into pulmonary and systemic circulation. The first carries deoxygenated blood (black) from the right ventricle (RV) to the lungs and returns oxygenated blood (red) to the left atrium (LA). The latter feeds all systemic organs with oxygenated blood from the left ventricle (LV) and returns deoxygenated blood back to the right atrium (RA). The figure (a) is from Fig. 1.4 in [92] and (b) from Fig. 1.5 in [92], both © 2010 JR Levick.

The performance, and thus the health of the cardiovascular system, can be assessed via so-called hemodynamic parameters. One such parameter already introduced in the previous chapter is the CO, i.e. the amount of blood volume pumped by the heart through the circulation in one minute. CO is the product of heart rate (HR) and stroke volume (SV): $\mathrm{CO} = \mathrm{HR} \cdot \mathrm{SV}$. SV is the amount of blood ejected per contraction by one ventricle during the cardiac phase called *systole*. In contrast, during the second phase called *diastole*, the ventricles relax and are being refilled partly due to atrial contraction. As a result of this alternation between diastole and systole the blood pressure in the arteries is pulsatile, i.e. typical systemic pressure values vary from a minimum (diastolic value) of 80 mmHg to a maximum (systolic value) of 120 mmHg [92]. The gradient of mean blood pressure (ΔP) between the aorta (P_{AO}) and the vena cava (P_{VC}) is the driving force for blood flow through the systemic circulation:

$$\mathrm{CO} = \dot{Q} = \frac{\Delta P}{R_T} = \frac{P_{\mathrm{AO}} - P_{\mathrm{VC}}}{R_T}, \tag{2.1}$$

where $\dot{Q}$ denotes the blood flow (equivalent to CO) and R_T the total vascular resistance. While

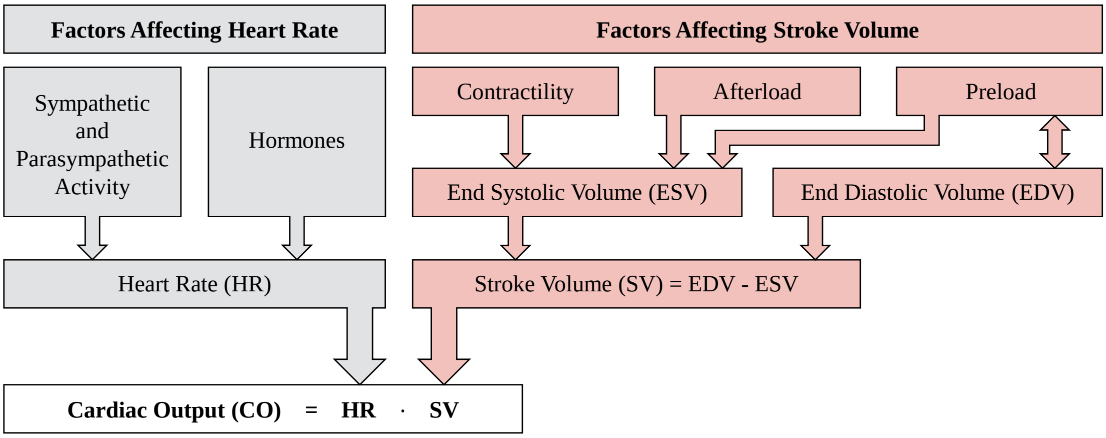
Factors Affecting Heart Rate
Factors Affecting Stroke Volume
Sympathetic and Parasympathetic Activity
Hormones
Contractility
Afterload
Preload
End Systolic Volume (ESV)
End Diastolic Volume (EDV)
Heart Rate (HR)
Stroke Volume (SV) = EDV - ESV
Cardiac Output (CO) = HR · SV

Figure 2.2 – Main factors affecting heart rate and stroke volume and thus cardiac output. Adapted and simplified from [16, Figure 19.35].

P_{AO} is in the range of 100 mmHg, P_{VC} is close to zero. Thus, the total vascular resistance of the systemic circulation is in the order of $R_T \approx 20\,\mathrm{mmHg}\cdot\mathrm{min/L}$ (= $100\,\mathrm{mmHg}/(5\,\mathrm{L/min})$) [92]. In contrast, the total vascular resistance of the pulmonary circulation is much smaller because pulmonary blood vessels are much shorter and wider. This explains why the blood pressure in the lungs is about seven-fold lower than systemic blood pressure [92]. Further particularities of the pulmonary circulation can also be found in the thesis of Proença [118].

2.1.2 Factors Affecting Stroke Volume and Cardiac Output

The main factors affecting CO are illustrated in Figure 2.2. On the one hand, CO is proportional to the HR which in turn is decreased by parasympathetic activity, increased by sympathetic activity and further influenced by various hormones [92, 16]. On the other hand, CO is proportional to the SV which is mainly influenced by the three factors listed in the following:

1. **Contractility** (or *inotropy*) is the force of contraction of the heart muscle. It is mainly controlled by activity of the sympathetic nervous system and hormones. An increase in contractility leads to a more forceful contraction, which in turn leads to a higher SV through a decrease in end systolic volume (ESV).
2. **Afterload** is defined as the load against which the ventricles have to contract to eject blood. It is closely linked to the total vascular resistance R_T and the mean arterial pressure (MAP), i.e. an increase in R_T leads to an increase in MAP which opposes ventricular ejection and thus results in a reduced SV because of a higher ESV.
3. **Preload** is an equivalent term for end diastolic volume (EDV). It determines to what extent the cardiac muscle is stretched prior to contraction. As stated by the law of *Frank-Starling*: the higher this stretch the more powerful the contraction (increased contractility) and thus the higher the SV (until an optimal point is reached). Preload is influenced by venous return (i.e. venous blood flowing back to the heart) which in turn

is influenced by various factors such as the volume of circulating blood, respiration-induced changes in pressure or gravity.

Based on these mechanisms CO is regulated primarily to meet the metabolic demand of the different tissues in the body. For example, during exercise CO can rise five-fold of the baseline level to adequately supply the muscles with oxygen and other substances [92, 16]. In contrast, in patients suffering from *heart failure*, CO is impaired which results in insufficient perfusion. This *cardiac insufficiency* is due to damage or overloading of the heart which can be caused by diverse pathological conditions, of which two examples are given hereafter. First, in *cardiac ischemia* the blood supply of the heart muscle (*myocardium*) is restricted which results in decreased contractility. This is usually caused by obstructed blood flow in the coronary arteries (*atherosclerosis*) [16]. Second, elevated blood pressure (in the systemic or pulmonary circulation) leads to an increased afterload and thus impairs ventricular ejection. To cope with this situation the heart wall thickens (*concentric hypertrophy*) and eventually the affected ventricle begins to fail [92].

While the two abovementioned examples alter the CO usually over a longer period of time, there are situations in which the CO can be deteriorated within a short period. An example are patients who undergo high-risk surgical procedures. In this type of patients, the continuous monitoring and early optimization of their hemodynamic condition (including CO) after surgery has been shown to be very important as it results in significantly reduced mortality [89, 116]. These findings encourage the development of measurement devices which enable the continuous measurement of CO and do not necessitate invasive procedures such as right-heart catheterization (presented in the next section).

2.2 State of the Art of Cardiac Output Monitoring

In the following, we list and briefly describe different techniques used to measure cardiac output (CO) and stroke volume (SV). The techniques are grouped into (highly) invasive (Section 2.2.1), minimally-invasive (Section 2.2.2) and noninvasive methods (Section 2.2.3), as also shown in Figure 2.3. The more interested reader is referred to the book chapters by Critchley [37] and Levick [92], or to different review articles on this subject [79, 99, 34, 129, 87, 124].

2.2.1 Invasive Methods

Fick's Principle

The first method to measure CO was proposed by Adolf Fick in 1870 [92]. It is based on the principle that in steady state, the oxygen removed from the alveoli in the lungs is equal to the oxygen uptake by the pulmonary bloodstream. From this it follows that one can assess pulmonary blood flow $\dot{Q}$ and thus CO (in L/min) by dividing the rate of alveolar oxygen uptake

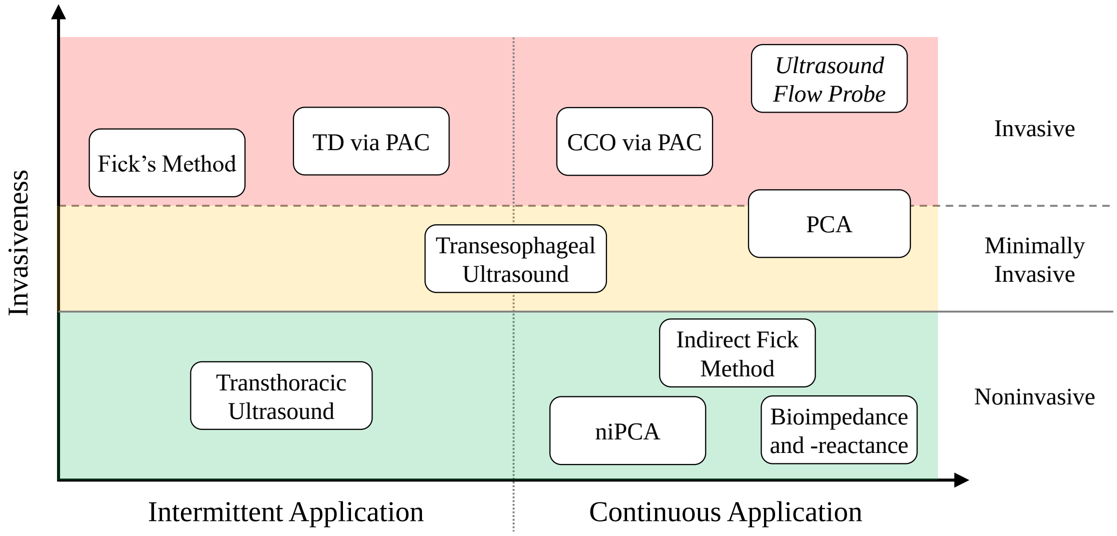
Invasiveness
Ultrasound Flow Probe
Fick's Method
TD via PAC
CCO via PAC
Invasive
PCA
Transesophageal Ultrasound
Minimally Invasive
Indirect Fick Method
Transthoracic Ultrasound
niPCA
Bioimpedance and -reactance
Noninvasive
Intermittent Application
Continuous Application

Figure 2.3 – Comparison of different techniques available for CO monitoring by means of their invasiveness and their applicability for continuous measurements. TD: thermodilution; PAC: pulmonary artery catheter; CCO: continuous cardiac output; PCA: pulse contour analysis; niPCA: noninvasive pulse contour analysis. Note that ultrasound flow probes are applicable in animal experiments only.

($\dot{V}_{O_2}$, in mL/min) by the arteriovenous oxygen difference ($C_{A_{O_2}} - C_{V_{O_2}}$, in mL/L):

$$\mathrm{CO} = \dot{Q} = \frac{\dot{V}_{O_2}}{\left(C_{A_{O_2}} - C_{V_{O_2}}\right)}. \tag{2.2}$$

While $\dot{V}_{O_2}$ can be measured noninvasively via spirometry, the measurement of arterial $C_{A_{O_2}}$ and venous oxygen concentration $C_{V_{O_2}}$ require catheterization. In particular, $C_{V_{O_2}}$ needs to be measured in the right ventricle or main pulmonary artery and thus requires highly invasive right heart catheterization. Besides, this technique is further limited in that it cannot measure rapid changes in hemodynamics as performing one single measurement takes between 5 to 10 minutes [92]. The indirect Fick method, described later on in Section 2.2.3, represents a noninvasive alternative as it estimates CO via rebreathed gases (i.e. CO_2).

Thermodilution via Pulmonary Artery Catheter (PAC)

With the invention of the Swan-Ganz catheter in the year 1971 [56], the technique of PAC thermodilution has become widely used and is still today considered as the clinical gold-standard method for CO measurements [87, 37, 124]. This specific catheter is inserted via a vein through the right heart into the pulmonary artery, as also illustrated in Figure 2.4a. A CO measurement is initiated by injecting an injectate of known temperature and volume – usually cold saline or dextrose [124] – in the right ventricle (via the proximal port of the catheter, ① in Figure 2.4a). Then, the CO is determined via the resulting temperature changes in the

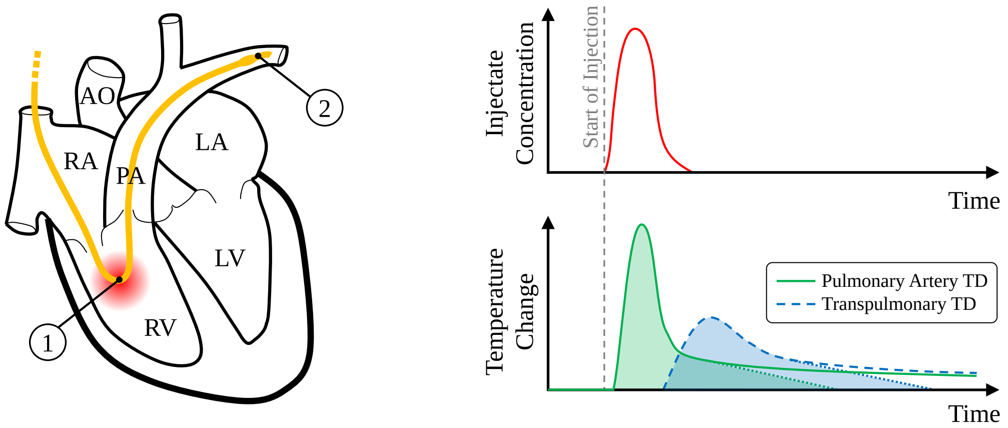

(a)

(b)

Figure 2.4 – (a) Schematic example of a Swan-Ganz catheter (with ① the proximal port for injection and ② the thermistor at the tip) inserted into the heart (RA: right atrium, LA: left atrium, RV: right ventricle, LV: left ventricle, PA: pulmonary artery, AO: aorta). Adapted from [118]. (b) Thermodilution (TD) exemplified by means of the temporal evolution of (Top) the injectate concentration and (Bottom) the resulting change in temperature measured either directly in the PA (——green) or in the systemic circulation (- - -blue). The CO is inversely proportional to the shaded area under the curves which represent the duration of transit of cooled blood times the mean temperature change [124].

pulmonary artery (measured with a thermistor at the tip of the catheter, ② in Figure 2.4a), i.e. CO is inversely proportional to the area under the curve of the temperature change as illustrated in Figure 2.4b. This is known as the Stewart-Hamilton principle and is extensively described in the work by Reuter et al. [124] and Levick [92].

In contrast to the Fick's principle, CO can be measured via PAC thermodilution within 30 seconds and successive measurements can be performed rapidly. Nonetheless, these measurements are not continuous and their number is limited by a maximally allowed volume of injectate [124].

Continuous Cardiac Output (CCO) via PAC

To overcome the limitation of intermittent measurements, a modified version of the Swan-Ganz catheter has been developed. It includes a second thermistor and a heating filament in the proximal port of the catheter (① in Figure 2.4a). This heating is switched on and off in a pseudorandom binary sequence and the resulting temperature gradients (① vs ② in Figure 2.4a) are analyzed [79]. Even though the CO measurements via the CCO method are continuous, they are limited by a non-negligible time lag of up to 12 minutes and are therefore not applicable to assess fast hemodynamic changes [124].

Ultrasound Flow Probe – The True Gold Standard

As also mentioned above, PAC thermodilution is considered as the clinical gold-standard method [34]. However, strictly speaking this is not true as it is rather the most accepted reference method which can have high errors of up to ±30 % [37]. Lower errors of less than ±5 % could be achieved by placing an ultrasound flow probe around the aorta (or pulmonary artery), which can be considered as a true gold standard [37, 124]. Yet, under no circumstances this highly invasive procedure is possible in humans and its use is limited to animal studies. Therefore, to this day, there exists no true gold standard for CO measurements in human studies [87, 37, 79].

2.2.2 Minimally-Invasive Methods

The clinical usefulness of the PAC has been questioned and it has been shown in multicenter clinical trials that its use can lead to complications and that it is not reducing mortality [72, 128, 35]. Therefore, alternative and less invasive methods, have been developed which are described hereafter. These are usually referred to as *minimally-invasive*, and are defined as those methods which do not require central venous catheterization [34].

Pulse Contour Analysis (PCA)

In pulse contour analysis (PCA), arterial pressure is measured and CO is derived from the area under the systolic part of the pressure curve (which is related to SV via the systemic vascular resistance) or a comparable approach. Currently available systems can be grouped into those with and without the need for calibration via transpulmonary indicator dilution [99].

One system of the first group, the PiCCO (Pulsion, Munich, Germany) needs to be calibrated using transpulmonary thermodilution [124], which involves the administration of the injectate via central venous access[1]. The injectate then travels through the right heart, pulmonary circulation, left heart, aorta and is finally measured in the femoral artery (see Figure 2.4b). Another system, the LiDCO (LiDCO Ltd., Cambridge, UK) uses transpulmonary lithium indicator dilution for calibration, which is less sensitive to temperature but influenced by electrolyte and hematocrit concentrations [79]. Moreover the LiDCO system only requires access to a peripheral artery and vein, making it less invasive [124].

Two systems of the second group, FloTrac-Vigileo (Edwards Lifesciences, Irvine, USA) and MostCare-PRAM (Vytech Health, Padua, Italy), do not rely on an external calibration and thus solely require central or peripheral arterial access. While the FloTrac requires patient data for internal calibration [79, 99], the MostCare system does not require any external data [99].

Once in place (and calibrated), all systems provide estimations of SV, CO and other hemodynamic parameters including SV variations (SVV), a valuable estimate to assess fluid-responsiveness of ventilated patients [100]. The PiCCO and LiDCO systems can further provide estimates for extravascular lung water (a measure of pulmonary edema) and global end-diastolic volume (a measure of cardiac preload), which cannot be obtained from PAC-based thermodilution [124]. Nonetheless, all of the PCA systems rely on an arterial pressure signal of good quality which is not always available, e.g. the signal has shown to be distorted in up to 30 % of patients in the intensive care unit (ICU). Moreover, there the measurements can be severely impaired by arrhythmias and aortic valve disease [34].

---

[1] Note that because of the need for central venous access, the PiCCO system is the only PCA system which is strictly-speaking *not* minimally-invasive, according to the definition of Clement et al. [34].

Transesophageal Ultrasound

CO can also be determined from an ultrasound device placed in the esophagus in two different ways. First, in transesophageal echocardiography, CO is assessed from blood flow in the heart measured via Doppler ultrasound (across a cardiac valve or in a ventricular outflow tract) and the cross-sectional area of the measurement site. This approach is limited to intermittent measurements which are – in addition – time consuming and operator dependent as they require a high level of skills and knowledge. Although unsuitable for routine CO monitoring, this technique allows for a fast diagnosis of heart function in critical hemodynamic situations [79]. Second, in transesophageal aortic Doppler ultrasound, the blood flow through the descending aorta is measured and combined with the aortic cross-sectional area. CO values further need to be scaled with a constant factor to correct for the not-measurable portion of flow from the arteries branching of more proximal to the heart (e.g. coronary and brachiocephalic arteries). While this technique provides continuous CO measurements, its correct operation also requires a lot of experience and training [37]. Both of the aforementioned ultrasound-based techniques are limited by their operator dependency [79] and mainly restricted to the use in intra-operative and intensive care scenarios [37].

2.2.3 Noninvasive Methods

Indirect Fick Method

Analogously to the Fick's principle using oxygen measurements as stated in Equation (2.2), CO can also be estimated via carbon dioxide concentrations, i.e. $\mathrm{CO} = \dot{V}_{\mathrm{CO}_2} \Big/ \left(C_{\mathrm{A}_{\mathrm{CO}_2}} - C_{\mathrm{V}_{\mathrm{CO}_2}} \right)$. This is known as the indirect Fick or partial CO_2 rebreathing method and is implemented in the NICO system (Novametrix Medical Systems, Wallingford, USA). While this measurement can be performed noninvasively, it is limited to intubated and ventilated patients as it requires a rebreathing extension loop to be attached to the ventilator [86]. Due to these limitations and insufficient accuracy NICO is rarely used in the ICU [34].

Another noninvasive alternative is the estimation of CO solely via the oxygen uptake $\dot{V}_{\mathrm{O}_2}$ as suggested by Stringer et al. [143]. They observed that Equation (2.2) can be simplified since, during physical exercise, the arteriovenous oxygen difference $(C_{\mathrm{A}_{\mathrm{O}_2}} - C_{\mathrm{V}_{\mathrm{O}_2}})$ increases linearly with $\dot{V}_{\mathrm{O}_2}$

normalized by the maximal oxygen uptake $\dot{V}_{O_2\text{-max}}$. $\dot{V}_{O_2}$ and $\dot{V}_{O_2\text{-max}}$ are thus sufficient to estimate CO with an experimentally-derived equation[2], CO = $\dot{V}_{O_2} \Big/ \left(57.21 + 104.7 \frac{\dot{V}_{O_2}}{\dot{V}_{O_2\text{-max}}}\right)$ [143]. This approach is for example implemented in the MetaMax 3B device (CORTEX Biophysik GmbH, Leipzig, Germany) which was used in this thesis (see Chapter 12).

Noninvasive Pulse Contour Analysis (niPCA)

With the niPCA technique the arterial pressure waveform is estimated fully noninvasively. The subsequent calculation of CO and other hemodynamic parameters is similar to its invasive equivalent, the aforementioned PCA approach. The two systems CNAP (CNSystems Medizintechnik AG, Graz, Austria) and ClearSight/NexFin (Edwards Lifesciences, Irvine, USA) estimate the pressure waveform via a finger cuff and the volume clamp method [34, 129], i.e. the distension of the digital artery is measured via photoplethysmography and is controlled to be kept constant by applying an external counter-pressure which in turn is proportional to the arterial pressure. A third system, the T-Line TL-200 (Tensys Medical Inc., San Diego, USA) uses a tonometer placed on the wrist to assess radial artery pressure, similar to manual pulse palpation [34, 129]. For calibration, all three systems use patient data and the CNAP further requires a brachial cuff. As their invasive counterparts, niPCA systems also rely on a pressure signal of high quality. This can be highly impaired in the case of peripheral hypoperfusion or finger oedema [129]. Moreover, these approaches are sensitive to sensor displacement caused by movement of the patient's arm or fingers [129, 34].

Transthoracic Doppler Ultrasound

In transthoracic Doppler ultrasound a probe is placed on the chest and blood flow is measured in the ventricular outflow tracts, ascending aorta or pulmonary artery. As for the transesophageal techniques, this is also operator dependent and necessitates a lot of experience and training. Additionally, it cannot be used for continuous monitoring. Yet, it is considered as the most accurate technique available for the use in the ICU according to the recent review by Clement et al. [34]. Moreover, it is popular in pediatrics due to its non-invasiveness and for the reason that in small children a signal of higher quality can be obtained [37].

Thoracic Electrical Bioimpedance

In impedance cardiography (ICG) the electrical bioimpedance of the human thorax is measured via four electrodes placed around the neck and the upper abdomen. CO is then derived from cardiosynchronous pulsatile changes in bioimpedance [40]. Since its discovery in 1966 by Kubicek et al. [90] various advancements have been made regarding the equations for CO estimation [15, 40]. Nonetheless, the origins of the ICG signal remain controversial and unclear

---

[2] Note that the coefficients differ from the original equation in [143] because of differences in units. Here $\dot{V}_{O_2\text{-max}}$, $\dot{V}_{O_2}$ and CO are all expressed in L/min.

[42, 40] and the initial hypothesis that aortic blood volume changes are the main contributor to the ICG signal has been questioned by Patterson [111]. Moreover, this technique is prone to electrical interferences of other devices and is influenced by changes in lung water. As clearly stated by Critchley [37] and Clement et al. [34] the use of ICG in clinical scenarios is highly unreliable and has even been abandoned.

Bioreactance represents an alternative approach to ICG which is considered to be less sensitive to lung water and electrical interferences [34, 129]. This is because – unlike ICG – it does not estimate CO from the amplitude but from the phase shift of the bioimpedance signal [140]. As with ICG, bioreactance suffers from the unclear signal origins and is still sensitive to electrical interferences [129]. In contrast to ICG, more promising results were obtained in clinical environments but still require further evaluation [34, 37].

2.3 Comparison and Validation of Cardiac Output Measurements

As mentioned in Section 2.2.1, the clinically accepted reference method (PAC thermodilution) has a high measurement error of up to ±30 % [37]. Therefore, the question arises as to what extent CO values measured via different approaches are comparable. In a recent study Lamia et al. [91] compared five CO measurement techniques (PAC thermodilution, bioreactance via NICOM, PCA via LiDCOplus, FloTrac, and PiCCOplus) during post-surgery in 21 cardiac patients. They found that even though the devices measured similar mean CO values, they significantly differed in terms of bias and precision values when compared relative to each other. Yet, all five devices investigated showed a good ability in trending, i.e. to follow changes in CO values. In a similar manner, Pironet et al. [115] compared four CO measurement techniques (including aortic flow probe and transpulmonary thermodilution) in seven pigs. While all CO measurements were highly repeatable with an error below 7 %, the different techniques showed a poor agreement.

These findings highlight the challenging nature of obtaining reliable CO measurements and emphasize the need for assessing the ability of a device to follow relative changes (trending). Another reason for trending is that in most of the clinical situations an absolute CO value is not of primary interest. However, the ability to track changes is very important, i.e. after an intervention (e.g. fluid challenge or drug administration) knowing the relative CO change with respect to before is essential [99, 34, 152]. By way of example, when the CO changes from 5 L/min to 6 L/min in response to an intervention, it is more important – and often sufficient – to know the relative change of 20 % rather than the absolute values in L/min. Trending ability can be assessed via four-quadrant or polar plot analysis as extensively discussed by Critchley [37] and Saugel et al. [130]. For the different reasons stated by Saugel et al. [130], four-quadrant plot analysis was used in this thesis and is described in more detail later on in Section 6.2.4 at the time of first use.

2.4 The Quest for the Ideal Cardiac Output Monitoring Device

In the previous sections we presented the most common techniques available to measure CO along with their assets and drawbacks. However, as already alluded to in the previous chapter, none of the currently available techniques fulfills the ten requirements for an "ideal" hemodynamic monitoring device which were specified by a consensus of sixteen renowned physicians. According to Vincent et al. [152] the "ideal" device:

(1) Provides measurement of relevant variables;
(2) Provides accurate and reproducible measurements;
(3) Provides interpretable data;
(4) Is easy to use;
(5) Is readily available;
(6) Is operator-independent;
(7) Has a rapid response-time;
(8) Causes no harm;
(9) Is cost-effective;
(10) Should provide information that is able to guide therapy.

All of the techniques presented in Sections 2.2.1 and 2.2.2 are limited in that they "cause harm", i.e. they are at least minimally-invasive. Even though, the noninvasive techniques in Section 2.2.3 would overcome this limitation, none of these devices has been found to be reliable enough in clinical settings according to the meta-analysis by Joosten et al. [87]. Therefore, on the quest for the ideal CO monitoring device, we investigate to what extent thoracic EIT can be used to fulfill as many of the abovementioned requirements as possible. As low-cost and noninvasive medical imaging modality, EIT does already meet requirements (8) and (9). Yet, how many of the other requirements can it fulfill? Does it prove to be a reliable technique for continuous and unsupervised CO monitoring?

Before addressing these questions, we first introduce the basic principle and technical aspects of EIT in the following chapter.

3 Electrical Impedance Tomography

In this chapter we introduce electrical impedance tomography (EIT), the medical imaging modality investigated in this thesis. While we provide only a brief overview, the more interested reader is referred to the book by Holder [80] or the review articles by Adler et al. [2, 9] and Frerichs et al. [52] (including its extensive supplementary material).

After giving a brief historical and clinical background, we describe the typical acquisition and processing steps used in thoracic EIT. These steps are illustrated in Figure 3.1 and comprise the impedance measurements performed by the EIT device (Step 1, Section 3.1.1), the reconstruction algorithms transforming these measurements into a sequence of tomographic images (Step 2, Section 3.1.2), and the separation of these into cardiosynchronous and ventilation-related changes (Step 3, Section 3.1.3). In Section 3.2 we discuss previous approaches by other research groups to estimate SV from cardiosynchronous EIT images (Step 4). The chapter is concluded in Section 3.3 by addressing the issue of the unclear origins of cardiosynchronous EIT signals.

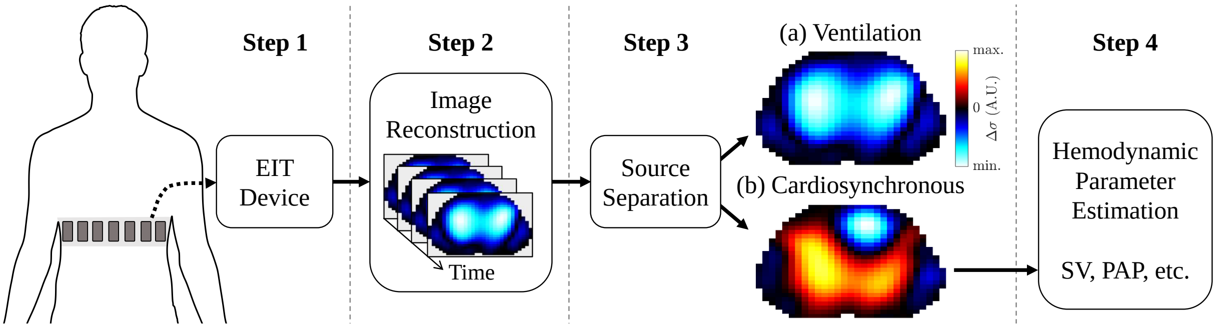

Figure 3.1 – Typical acquisition and processing steps used for thoracic EIT. Filtering in step 3 is applied to separate (a) ventilation-related and (b) cardiosynchronous activity. The images in (a) and (b) show the conductivity change $\Delta\sigma$ of (a) one breath (inspiration vs full expiration) and (b) one heartbeat (end systole vs end diastole). Note that (a) and (b) share the same colorbar but are scaled individually to their corresponding minimum and maximum because cardiosynchronous activity in (b) is about factor 10 weaker than ventilation shown in (a).

3.1 Principle of Thoracic EIT

EIT is not only used for medical applications but also in geophysics [127] or industrial applications [168, 80]. However, this chapter only covers the clinical application of EIT, in particular the measurement of time-difference EIT on the chest [52, 9]. As also illustrated in Figure 3.1, in thoracic EIT, electrodes are applied around the thorax to measure the impedance of the underlying biological tissues. These impedances measured on the body surface are then fed into an advanced mathematical reconstruction algorithm, which results in an image sequence showing the temporal change in thoracic electrical impedance. The observed change is due to the difference in impedance of the underlying tissues which is caused by different phenomena such as variations in lung (i.e. air) and blood volume or organ movement. Even though the resulting spatial resolution is low [132, 160], EIT enables a fast acquisition at typically up to 50 frames[1] per second. Additional characteristics such as portability, low-cost and the use of nonionizing radiation make EIT an appealing candidate for bedside patient monitoring.

Since the introduction of the first thoracic *impedance camera* in 1978 by Henderson and Webster [75], a lot of research has been going on to investigate and further improve EIT [80, 9]. Most of the clinical research focuses on monitoring regional ventilation in view of optimizing ventilator settings in mechanically ventilated patients or diagnosing chronic lung diseases [52, 9]. Nevertheless, EIT has not yet fully found its way into clinical practice and still requires large multicenter trials for its validation [52]. The release of two commercial EIT devices in this decade (Dräger Medical in 2011, Swisstom in 2013) are a cause for hope that EIT will have its breakthrough into daily practice in the near future, provided that it proves clinically useful.

3.1.1 Impedance Measurements to Assess Tissue Properties

Thoracic time-difference EIT is based on the fact that the electrical impedance of tissues differ, e.g. the lungs filled with air at end of inspiration are much less conductive than the lungs at end of expiration. To measure these differences in impedance, n_s electrodes are placed on the body surface (usually on one single transversal plane) and small alternating currents in the kHz range are injected between different pairs of electrodes. For these measurements a compromise between frequency and amplitude of the injected current and the complexity of the electronic design has to be made by keeping in mind the safety regulations [82]. On the one hand, higher frequencies are preferable due to a lower skin-electrode impedance and a higher maximal permitted current [82, 2]. On the other hand, the complexity of the analog circuitry and the effects of parasitic capacitances are lower at smaller frequencies. Numerous EIT devices exist but most of them are mainly used for research purposes (see [53, page 19] for an extensive list). The devices of primary interest for this thesis are those five with certification for clinical monitoring as listed in Table 3.1.

Another important aspect of EIT systems is the so-called stimulation and measurement

---

[1] Note that the terms EIT frame and EIT image are used interchangeably.

Table 3.1 – Overview of EIT devices available for clinical measurements. With n_s as the number of electrodes, f_{FM} as the maximal possible frame rate, f_I as the stimulation frequency and Skip as the number of inactive electrodes in between the two ones actively measuring voltage/injecting current. For more details see [118, page 45], [52, Table E1.1] or [53, page 19].

Device Name	n_s	Type of Electrodes	f_{FM} (Hz)	f_I (kHz)	Skip
Swisstom BB[2]	32	Textile belt, active	50	195[a]	Skip 4[a]
Dräger PulmoVista™ 500	16	Elastic belt, passive	50	80 – 130	Adjacent[b]
Timpel ENLIGHT™ 800	32	Individual, passive	50	125	Skip 3
CareFusion Goe MF II	16	Individual, passive	48	5 – 500	Adjacent[b]
Maltron Sheffield MK 3.5	8	Individual, passive	25	2 – 1600	Adjacent[b]

Note: [a] Even though the hardware would allow the configuration of different settings these cannot be modified in the current version of the software; [b] Adjacent is a synonym for skip 0.

pattern, i.e. the selection of one or more pairs of electrodes used to inject a current and those electrode pairs used to measure the resulting voltages. With n_s electrodes placed around the thorax, various ways of measuring the thoracic impedance exists. These patterns range from rather complex but optimal patterns [80, 94] to simpler patterns with pair drive [2, 80] as explained hereafter. While the former require more complex hardware with multiple and well-calibrated current sources, the latter can be build with one single current source and one voltage measurement channel via the use of time-multiplexing. Since the second approach is used in all the clinical EIT devices listed in Table 3.1 it is described in more detail in the following by the example of the so-called adjacent stimulation pattern (pair drive with skip 0).

This particular stimulation pattern (adjacent or skip 0) is illustrated and explained in Figure 3.2. For this pattern, the total number of impedance measurements n_d required to generate one EIT image is equal to the number of electrodes n_s (i.e. the number of current injections) times the number of pairwise differential voltage measurements ($n_s - 3$, when excluding those in contact with the current source). Consequently, $n_d = n_s(n_s - 3) = 208$ impedance measurements need to be acquired and this procedure is repeated to record up to $f_F = 50$ frames per second. In most of the clinical devices this is done via time-multiplexing, i.e. each of the n_d measurements is performed one after the other[2]. While this approach simplifies the hardware and reduces the cost of the device it also has its disadvantages. Assuming a system with $n_s = 32$ electrodes, injecting currents at $f_I = 100\,\text{kHz}$ and imaging at $f_F = 50$ frames per second which sequentially acquires $n_d = 928$ measurements. The time remaining for a single measurement is not more than roughly two periods ($\frac{1}{f_F n_d} \approx 2\frac{1}{f_I}$) of which one is lost due to switching transients [2]. Besides, sequential data acquisition is known to introduce artefacts when the EIT frame rate is not substantially higher than the frequency of the physiological phenomena observed [165, 166]. Another issue is that 3 out of 5 of the clinical EIT systems

---

[2] With the exception of the Timpel device which performs all voltage measurements in parallel but still uses time-multiplexing for current injections as stated in [52, Table E1.1].

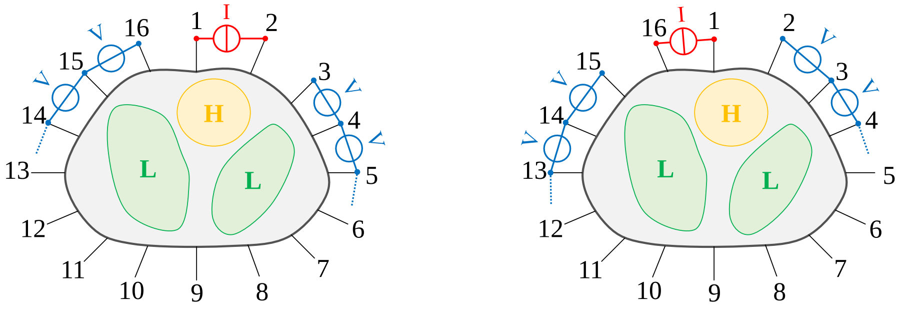

(a) (b)

Figure 3.2 – Schematic illustration of $n_s = 16$ electrodes applied to a human thorax (with heart H and lungs L) shown in transversal view. The two illustrations exemplify the adjacent stimulation pattern (pair drive with skip 0) with the (a) first and (b) last 13 impedance measurements acquired for one EIT frame. In (a) the current is injected between electrodes $\{1,2\}$ and the resulting 13 voltages are measured between the remaining electrode pairs. This is repeated 14 times for current injections between $\{2,3\},\{3,4\},\ldots,\{15,16\}$, until finally, (b) the current is injected between electrodes $\{16,1\}$ and the resulting 13 voltages are measured between the remaining electrode pairs. All the 13 voltage measurements of each of the 16 current injections result in a set of $n_d = 13 \cdot 16 = 208$ measurements acquired for one single EIT image.

listed in Table 3.1 use the adjacent stimulation pattern, known for its low performance in terms of sensitivity and signal-to-noise ratio (in the center) [134, 8]. Better performance in this regard can be expected from the two devices with 32 electrodes, which have a certain number – known as skip – of inactive electrodes in between the active pairs, i.e. Timpel with skip 3 or Swisstom with skip 4. These are still not the optimal patterns [80, 8] but improve the performance of the device while keeping its complexity low.

3.1.2 Image Reconstruction

The current section covers the mathematical aspects on how the aforementioned n_d impedance measurements obtained for each EIT frame are transformed into tomographic images. To this end, the n_d measurements of one EIT frame are stored in the vector $\boldsymbol{v} \in \mathbb{R}^{n_d}$.

We have Ω as the body under measurement (i.e. the thorax in 3D) with boundary $\partial\Omega$ and internal conductivity distribution $\sigma(\boldsymbol{x})$ as a function of the spatial variable $\boldsymbol{x}$. The scalar potential $\phi(\boldsymbol{x})$ inside the body is related to $\sigma(\boldsymbol{x})$ via the continuum version of Kirchhoff's law[3] [80, 7]:

$$\nabla \cdot \big(\sigma(\boldsymbol{x})\nabla\phi(\boldsymbol{x})\big) = 0 \quad \text{for } \boldsymbol{x} \in \Omega \setminus \partial\Omega. \tag{3.1}$$

---

[3] This is by using the quasi-static approximation assuming that the magnetic field can be neglected due to the use of low current frequencies [80]. Furthermore, it is only valid for isotropic media. More general definitions can be found in [7] or [80].

The boundary conditions are given by the current density $J(\boldsymbol{x})$, the outward unit normal to $\partial\Omega$ denoted as $\boldsymbol{n}$ and $\boldsymbol{x}_e \in \partial\Omega$ as the set including all positions of current injecting electrodes:

$$\sigma(\boldsymbol{x})\frac{\partial\phi(\boldsymbol{x})}{\partial\boldsymbol{n}} = \begin{cases} J(\boldsymbol{x}) \neq 0 & \text{for } \boldsymbol{x} \in \boldsymbol{x}_e, \\ J(\boldsymbol{x}) = 0 & \text{for } \boldsymbol{x} \in \partial\Omega \setminus \boldsymbol{x}_e. \end{cases} \tag{3.2}$$

Using Equations (3.1) and (3.2) to calculate the scalar potential $\phi(\boldsymbol{x})$ inside a body Ω with conductivity distribution $\sigma(\boldsymbol{x})$ is known as the *forward problem* described hereafter.

Forward Problem

The aforementioned equations can only be solved analytically for very simple geometries and conductivity distributions [80]. However, for more practical cases numerical methods are used which requires both the geometry and the conductivity to be discretized. To this end, the body is typically represented as a finite element model (FEM) of a mesh with n_e tetrahedral elements and the element-wise conductivity vector $\boldsymbol{\sigma} \in \mathbb{R}^{n_e}$ [7, 80]. The forward model can be expressed by the operator $F(\cdot)$ which provides the vector $\boldsymbol{v}$ containing n_d surface voltage[4] measurements for a given conductivity distribution $\boldsymbol{\sigma}$.

However, in EIT the problem is the opposite: it is an *inverse problem* where we seek the internal conductivity distribution $\boldsymbol{\sigma}$ for a given set of surface measurements $\boldsymbol{v}$. As the number of surface measurements n_d is (much) lower than the number of internal conductivities n_e it is an *ill-posed* problem. In addition, in EIT the physics of the probing energy is diffusive which results in wide variations of sensitivity across the body, i.e. EIT is much more sensitive to conductivity changes near its electrodes (e.g. variations in skin-electrode impedance) than to changes deeper in the body (e.g. variations in heart or aorta volume). Solving this inverse problem requires regularization which is addressed in the next section.

In the following, we first consider an important principle typically applied for the reconstruction of clinical data: *difference* EIT. In time *difference* EIT difference data is used to provide more robust images. That is, both the conductivity and the surface measurements are expressed as changes with respect to a working point (called reference or baseline), i.e. $\Delta\boldsymbol{\sigma} = \boldsymbol{\sigma} - \boldsymbol{\sigma}_r$ and $\boldsymbol{d} = \Delta\boldsymbol{v} = \boldsymbol{v} - \boldsymbol{v}_r$. In doing so the reconstructed images are less affected by imperfections which remain stable during the measurement, such as electrode errors, differences in channel gains or mismatch between model and real body shape [1, 29, 2]. The reference measurement $\boldsymbol{v}_r$ is usually defined as the temporal mean over a section of the recording and is implicitly related to $\boldsymbol{\sigma}_r$, i.e. $\boldsymbol{v}_r = F(\boldsymbol{\sigma}_r)$.

As we only seek to reconstruct changes $\Delta\boldsymbol{\sigma}$ with respect to $\boldsymbol{\sigma}_r$, we can further simplify the problem by linearizing the function $F(\boldsymbol{\sigma})$ in its current operating point $\boldsymbol{\sigma}_r$ [80, 93, 7]:

---

[4] Note that the EIT raw data $\boldsymbol{v}$ are usually available as voltages and not necessarily as impedances. As they are related by a simple scaling factor – the amplitude of the injected current – we use the following three terms interchangeably: voltage measurements, impedance measurements or raw measurements.

$$F(\boldsymbol{\sigma}) \approx F(\boldsymbol{\sigma}_r) + \boldsymbol{J}\Delta\boldsymbol{\sigma}, \text{ with } [\boldsymbol{J}]_{i,j} = \left.\frac{\partial[\boldsymbol{d}]_i}{\partial[\Delta\boldsymbol{\sigma}]_j}\right|_{\boldsymbol{\sigma}_r}, \tag{3.3}$$

where $\boldsymbol{J} \in \mathbb{R}^{n_d \times n_e}$ is the Jacobian or sensitivity matrix, with its elements $[\boldsymbol{J}]_{i,j}$ representing the sensitivity of the i^{th} surface voltage measurement to a conductivity change in the j^{th} model element. We can now attempt to estimate the change in intra-thoracic conductivity $\Delta\hat{\boldsymbol{\sigma}}$:

$$\Delta\hat{\boldsymbol{\sigma}} = \underset{\boldsymbol{\sigma}}{\arg\min}\, ||(\boldsymbol{v} - \boldsymbol{v}_r) - (F(\boldsymbol{\sigma}) - F(\boldsymbol{\sigma}_r))||^2 - \boldsymbol{\sigma}_r \approx \underset{\Delta\boldsymbol{\sigma}}{\arg\min}\, ||\boldsymbol{d} - \boldsymbol{J}\Delta\boldsymbol{\sigma}||^2. \tag{3.4}$$

However, this will not lead to a satisfying solution as we are dealing with an ill-posed and ill-conditioned problem which requires regularization.

Regularized Inverse Problem

The reconstruction is regularized by introducing additional constraints which allow for numerically stable results and make them more robust to interference and noise [80, 93]. A usual approach is Tikhonov regularization which seeks the estimate $\Delta\hat{\boldsymbol{\sigma}}$ by using the matrix $\boldsymbol{P}$ which penalizes noisy images:

$$\Delta\hat{\boldsymbol{\sigma}} = \underset{\Delta\boldsymbol{\sigma}}{\arg\min} \left\{||\boldsymbol{d} - \boldsymbol{J}\Delta\boldsymbol{\sigma}||^2_{\boldsymbol{W}} + \lambda^2\, ||\Delta\boldsymbol{\sigma}||^2_{\boldsymbol{P}}\right\}, \tag{3.5}$$

where:

- $\boldsymbol{W} \in \mathbb{R}^{n_d \times n_d}$ is the **weighting matrix** used to attenuate measurements which are classified as unreliable, e.g. too noisy. $\boldsymbol{W}$ can be adapted to either completely remove failing electrodes [97] or attenuate measurements classified as noisy [71, 98].
- The **hyperparameter** $\lambda \in \mathbb{R}$ controls the amount of regularization, and can be seen as a trade-off parameter between image robustness and accuracy [2]. In many cases, this choice can be described as a "resolution-noise performance trade-off".
- The **regularization matrix** $\boldsymbol{P} \in \mathbb{R}^{n_e \times n_e}$ can be chosen in various ways [80, 2], such as:
    i) When set equal to the identity matrix ($\boldsymbol{P} = \boldsymbol{I}$), zeroth-order Tikhonov regularization is used. This simply penalizes for too high amplitudes of $\Delta\hat{\boldsymbol{\sigma}}$ [5];
    ii) By setting $\boldsymbol{P}$ based on edge-sensitive spatial filters (e.g. Laplacian) the reconstructed image is penalized for sharp edges and thus forced to smoothness [5];
    iii) The NOSER prior [33] calculated from $\boldsymbol{J}$ penalizes elements with higher sensitivity.

Equation (3.5) can be further simplified to matrix form:

$$\Delta\hat{\boldsymbol{\sigma}} = \left(\boldsymbol{J}^T\boldsymbol{W}\boldsymbol{J} + \lambda^2\boldsymbol{P}\right)^{-1}\boldsymbol{J}^T\boldsymbol{W}\boldsymbol{d} = \boldsymbol{R}\boldsymbol{d}, \tag{3.6}$$

where the reconstruction matrix $\boldsymbol{R} \in \mathbb{R}^{n_e \times n_d}$ now allows to obtain an EIT image $\Delta\hat{\boldsymbol{\sigma}}$ via a one single matrix multiplication with the difference data $\boldsymbol{d}$. This is known as one-step Gauss-Newton (GN) reconstruction, a typical algorithm used for reconstructing clinical EIT in real-time. Another typical approach is the GREIT algorithm which is extensively described in [6, 66]. Various other algorithms (non-linear, recursive, etc.) exist, which would exceed the scope of this work. The interested reader is referred to [10, 80, 7].

Issues Concerning Hyperparamter Selection

When creating and configuring an EIT reconstruction algorithm, a key decision is the selection of an appropriate value for the hyperparameter λ. This value is often chosen empirically, which is, however, not the solution of choice when one wants to compare two different types of algorithms. To do this more systematically, different approaches exist which automatically choose λ. Yet, none of these work well when one wants to compare measurement configurations which differ in electrode position, electrode number or skip pattern.

This particular issue has been investigated in more detail in the present thesis and is presented later on in Chapter 11. There, we also review the existing methods to select λ along with the related problems and then present our novel approach able to overcome some of these problems.

3.1.3 Separation of Ventilation and Cardiosynchronous Activity

Before analyzing EIT images for hemodynamic parameters, there is a third processing step required. This is the extraction of cardiosynchronous changes, which need to be separated from ventilation-induced impedance variations (see Step 3 in Figure 3.1). This is challenging, since the former are about one order of magnitude lower than the latter and are thus also more sensitive to measurement errors [52]. To perform this step, various approaches have been proposed in literature as listed in the following:

- The simplest method is to perform a temporary breath-hold (apnea) [47]. While this approach is often used in animal experiments it is not necessarily applicable in clinical scenarios. Moreover, the hemodynamic changes resulting from apnea (e.g. hypoxic vasoconstriction, absence of ventilation-induced SV variations) are not always desirable.
- Another method is the use of frequency domain filtering (e.g. high-pass or comb filters) [106]. Even though adaptive filters can be used, their ability to track variations in heart rate may not be sufficient enough.
- A third approach known as ECG-gated ensemble averaging consists in aligning the data to a trigger reoccurring at cardiac frequency (e.g. the ECG's R-peak) and averaging the aligned data to one representative cardiac cycle (see Appendix B). Ensemble averaging can be interpreted as a comb filter at cardiac frequency and its harmonics [139]. Averaging N heartbeats attenuates noise by a factor of $\sqrt{N}$ [122, 139]. In previous studies usually 100 to 200 heartbeats were averaged leading to an attenuation of 10 to 14 [106].

While ensemble averaging is efficient and easy to implement, it can neither be used in cases of cardiac arrhythmia nor to assess ventilation-induced variations of SV.

- A more advanced approach based on the decomposition via principal component analysis has been proposed by Deibele et al. [43] and was further developed by Pikkemaat [112, 113]. While these methods provide continuous (i.e. beat-to-beat) cardiosynchronous EIT image sequences they could not be successfully applied in clinical measurements.

In the current thesis, ECG-gated ensemble averaging was the method of choice because of its simplicity and effectiveness when used on clinical data.

3.2 Previous Work on EIT-Based Stroke Volume Estimation

After having isolated the cardiosynchronous changes, the resulting EIT image sequences can be processed in view of hemodynamic parameter estimation (see Step 4 in Figure 3.1). In the current section we review previous work with particular focus on EIT-based SV estimation.

Compared to lung-related EIT, only little work has been published on the topic of cardiovascular EIT. Most of the studies targeted regional pulmonary perfusion which can be assessed using injections of hypertonic saline as contrast agent [18, 50] or other – more indirect – approaches listed in [52]. Besides this, Solà et al. [137] reported on the feasibility of estimating central blood pressure via EIT using the pulse wave velocity principle in the descending aorta. Two older studies address the signal interpretation [46] or suggest a better belt placement [154] for cardiac imaging. Very recently, Proença et al. [120] have successfully shown the measurement of pulmonary artery pressure via the pulse wave velocity assessed in the lung region. Apart from that, most of the remaining literature in cardiovascular EIT concentrated on the estimation of SV or CO via EIT which is presented hereafter in more detail.

(a) In 2000 Vonk Noordegraaf et al. [155] were the first to report on the estimation of SV via EIT. Using pulmonary artery catheter thermodilution as a reference they trained their algorithm on 23 patients. The calculations are based on the impedance change from a region hypothesized to stem solely from ventricular activity. However, they could not find a direct correlation between SV and this impedance change. Without further reasoning they included a timing parameter as a second variable into their model to achieve a better fit. The algorithm was then successfully validated on 11 healthy volunteers showing an error of 0.7 ± 5.4 mL, when compared to cardiac MRI as SV reference. In contrast to the traditional transversal EIT belt placement, they placed the electrodes in an oblique plane, which is expected to improve the separation of atrial and ventricular activity in the EIT images [154]. Data was measured using the Sheffield mark I system [27] and processed after ECG-gating of 200 cardiac cycles.

(b) Some years later, in 2006, Zlochiver et al. [173] suggested to avoid the generation of images by using a parametric reconstruction approach. Hence, an ellipsis representing the left ventricle was optimized to best fit the impedance values measured. The SV was then simply estimated as the changes in volume of this ellipsis. A major drawback of this study is the use of the controversial ICG technique (see Section 2.2.3) as reference measure for SV. Furthermore, the approach is highly dependent on anatomical a priori knowledge. In a later publication the same group presented a theoretical study – again by using parametric EIT – showing the feasibility of SV estimation via six internal electrodes of an implanted pacemaker device [102].

(c) In 2014 Pikkemaat et al. [114] demonstrated the feasibility of estimating SV in 14 pigs via the heart-related impedance change by using a subject-specific one-point calibration. In certain animals they observed an unclear scaling of the heart amplitude and hypothesized that it might be related to lung volume and also to the relative position of the heart with respect to the EIT electrode plane. Due to these unresolved issues they underlined the need for further investigations. Moreover, they questioned the accuracy of thermodilution PCA as their SV reference and suggested using a second measurement technique for validation purposes. Data was measured using the Dräger EIT Evaluation Kit 2 and processed after PCA-based decomposition [112, 113].

While not available in the corresponding publication [114], in his thesis [113], Pikkemaat also reports on the analysis of the lung-related impedance change $z^{\mathrm{SV_p}}$. In experiments where SV was modulated by changing the ventilation settings (the positive end-expiratory pressure – PEEP), $z^{\mathrm{SV_p}}$ showed a higher correlation with SV ($r = 0.69$) when compared to the heart amplitude $z^{\mathrm{SV_c}}$ ($r = 0.64$). On the other hand, when SV was modified using Dobutamine – a positive inotropic agent – $z^{\mathrm{SV_p}}$ correlated less with SV ($r = 0.61$) than $z^{\mathrm{SV_c}}$ ($r = 0.64$).

(d) Very recently da Silva Ramos et al. [41] performed investigations in twelve pigs where EIT-based SV was estimated from the systolic amplitude in the lung region (ΔZ_{sys}). Large variations in SV were induced via hemorrhagic shock and subsequent fluid challenges. ΔZ_{sys} was compared to SV reference measurements from transpulmonary thermodilution and showed an acceptable trending ability (91.2 % concordance rate). In contrast, absolute SV measurements were only accurate when taking into account body dimensions. Data was measured using the Timpel ENLIGHT™ device and processed after ECG-gating with a fixed time window of unknown length.

(e) Maisch et al. [96] were not estimating SV itself but its variations induced by ventilation (known as SVV) and showed the feasibility of measuring this quantity in eight pigs by means of EIT. Measuring SVV is of interest since it can be used to assess fluid responsiveness and therefore help to improve the intravascular volume of mechanically ventilated patients [99]. Similar to the aforementioned method of central blood pressure estimation [137], this approach exploits signal information from the descending aorta. In 2017 Trepte et al. [148] reported on further investigations on 30 other animals where EIT-based SVV estimation showed to be feasible in healthy lungs but comprised in acute lung injury. In both studies data was measured using the Timpel ENLIGHT™ device.

All the studies presented above show the necessity for further investigations and validations, in particular for measurements on humans in real clinical environments – the main goal of this thesis.

3.3 Controversial Origins of Cardiosynchronous EIT Signals

An important aspect to consider when aiming for EIT-derived hemodynamic parameter estimation is the origins of cardiovascular EIT signals. As previously mentioned for ICG (see Section 2.2.3), the issue is similar for cardiovascular EIT, namely that the exact origins of the signals are unclear [106] and different interpretations exist [20].

For example, it is still widely assumed that the cardiosynchronous signals in the lung region mainly reflect pulmonary perfusion which is not entirely correct as discussed by Hellige and Hahn [74] and Adler et al. [11]. Moreover, the EIT heart signal is not solely caused by changes in ventricular blood volume but mainly affected by cardioballistic effects of the heart as shown in a recent simulation-based study by Proença et al. [119].

Therefore, before immediately starting to develop algorithms for hemodynamic parameter estimation, it is of advantage to better understand the genesis of those signals. One approach to this is by performing simulations on bioimpedance models – as it is already done for ICG [149, 40, 42]. Afterwards, appropriate algorithms shall be created and verified with the aid of the knowledge gained from these simulations.

To this end, we investigated cardiovascular EIT based on simulations on a bioimpedance model of the human thorax which is presented in the subsequent chapters.

Part II

Investigating Cardiovascular EIT via Simulations on a Bioimpedance Model

4 Bioimpedance Models

4.1 Introduction

4.1.1 Motivation

In the previous chapter, we have mentioned the lack of understanding and the controversial interpretations existing regarding the origins of cardiovascular EIT signals. To partly overcome this issue we have created bioimpedance models of the human thorax which are presented in the current chapter. Simulations on these models allow for the virtual measurement of EIT data of which some would simply be impossible to obtain from real EIT recordings.

In contrast to the *in vivo* approach, the virtual – *in silico* – EIT measurements can be performed with a quasi unlimited number of different configurations (electrode placements, EIT device settings, etc.) simultaneously. Moreover, in view of gaining more understanding about the EIT signal origins, the simulation-based approach allows to individually deactivate certain structures (e.g. heart, aorta, etc.) and thus simulate the individual influence of each structure. Finally, having the bioimpedance model linked to a hemodynamic model, further allows to study the feasibility and limitations of EIT-based hemodynamic monitoring.

In the next section we review existing work on bioimpedance models and then present the models created and used throughout this thesis.

4.1.2 Related Work

Upon initiation of the present research, only a few studies were available which reported on bioimpedance simulations for EIT [76, 164]. However, these studies did not investigate conductivity changes resulting from cardiovascular but from respiratory activity.

While in the work by Proença et al. [119] a dynamic 2.5D bioimpedance model was presented and used to investigate the genesis of cardiac EIT signals, this model is limited by its lack of dimensionality, i.e. a fully 3D model is necessary to simulate scenarios like belt displacements, or to assess effects resulting from out-of-EIT-plane sensitivity, etc.

During the course of the present thesis, other groups have developed 4D ($3D + t$) bioimpedance models specifically targeted to simulate EIT measurements of cardiovascular changes:

- Dinkelbach and Stender [44] have created a 4D model of a porcine thorax from dynamic CT scans with high resolution. They placed EIT belts of 16 electrodes at five different transversal planes located around the center of mass of the left ventricle. In view of EIT-based CO monitoring, they correlated each EIT pixel with left ventricular blood volume changes and concluded the following. First, electrode belts located at the level of the ventricular center of mass or lower – towards the apex of the heart – are most suited for CO estimation via EIT. Second, belt level variations of ±4 cm along the craniocaudal axis, “only slightly impaired” their results in terms of correlation index.
- Murphy et al. [105] and Arshad et al. [13] have made use of the 4D XCAT model [133] – a 4D phantom of the human thorax for multimodality imaging research – to investigate the feasibility of EIT-based CO monitoring. They both use the reconstructed heart area (of the difference EIT signal between end diastole and end systole) as surrogate measure for SV. While they observe a strong correlation between this feature an the simulated SV, they also reveal a non-negligible influence of respiration, which they suggest to overcome by using breath-gating.

Besides, in the field of impedance cardiography (ICG) various bioimpedance models have been created and simulations have been performed to investigate the unclear origins of the ICG signal [40]. An overview of such studies is given in the review by de Sitter et al. [42].

The objective of the present work was the development of a 4D bioimpedance model for EIT which allows to (a) gain more understanding about the cardiovascular EIT signals, and (b) to investigate the feasibility and limitations of EIT-based SV monitoring.

4.2 Hemodynamic 4D Bioimpedance Model of the Human Thorax

In the following sections we describe the creation of the hemodynamic 4D ($3D + t$) bioimpedance model as also shown in Figure 4.1. First, we present the MRI data this model is based on (Section 4.2.1), and then, each of the structures the model contains: the heart (Section 4.2.3), the aorta (Section 4.2.4) and the lungs (Section 4.2.5).

4.2.1 MRI Data

The models presented hereafter are based on the following three magnetic resonance imaging (MRI) recordings which were performed on a human volunteer (62 kg, 178 cm, 28 years old) in supine position during expiratory breath-hold:

- (*M1*) A batch of 2D transverse plane scans covering the thorax outline from the diaphragm up to the apices of the lungs;
- (*M2*) Two 2D batches of dynamic cardiac cine scans showing the whole heart in short axis or in four chamber long axis view, covering 25 frames of the cardiac cycle;
- (*M3*) Dynamic 2D scans located at four different placements along the aorta revealing the distension of the aortic cross section with at least 60 frames / heart cycle.

4.2.2 Static Thorax

The thorax outline was segmented from the MRI scan *M1* by a region-growing algorithm using OsiriX [125] and then meshed to a smoothed 3D volume with Netgen [131]. Using the open-source EIT software toolbox EIDORS [5], five EIT belts – each comprised of 64 electrodes – were applied at different levels along the craniocaudal axis as follows (see also Figure 4.1a): (1) the TM (*transversal middle*) belt was placed at the average level of the heart, which is in between the 9-th and 10-th thoracic vertebra; The belts (2) TH (*transversal high*) and (3) TL (*transversal low*) were placed 3.5 cm higher and lower than TM, which is at the level of the 8-th (for TH) or in between the 10-th and 11-th (for TL) thoracic vertebra; The remaining two belts, (4) TMH (*transversal middle-high*) and (5) TLM (*transversal low-middle*), were placed 1.75 cm higher and lower than TM, corresponding to the 9-th (for TMH) or 10-th (for TLM) thoracic vertebra level. To ensure accurate calculations, the FEM was refined in the vicinity of the electrodes with the approach described by Grychtol and Adler [65].

Additionally, a sixth belt, OM (*oblique middle*) is available (see Figure 4.1b). This electrode placement was obtained by tilting the TM belt by 30° from transverse to coronal, as suggested for improved cardiac EIT by Vonk Noordegraaf et al. [154]. In the current thorax model, the

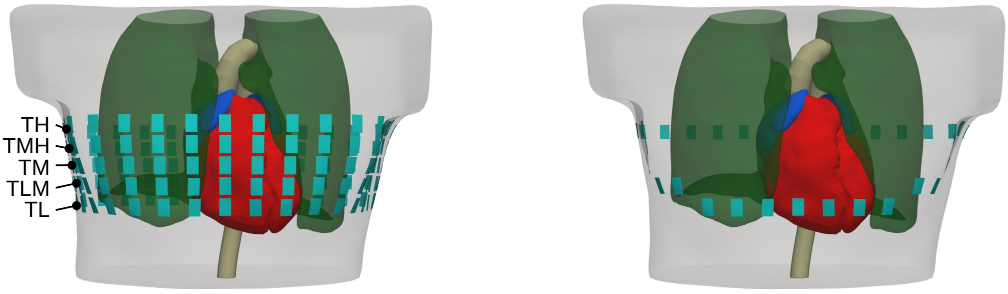

(a) Transversal Belts

(b) Oblique Belt

Figure 4.1 – 4D bioimpedance model of the human thorax with (a) transversal and (b) oblique electrode belt placements (see text Section 4.2.2). The EIT electrodes are shown in light blue. The static thorax model contains the following dynamic structures: heart with atria (dark blue) and ventricles (red), aorta (gray) and both lungs (green). Please note that for the sake of clarity only 32 (instead of 64) electrodes are shown per belt.

OM belt placement is approximated in that it was created by combining electrodes already available from the transversal belts. Even though this approximative approach might lead to slight positioning errors, it was preferred since it significantly reduces computation time.

Based on observations from the MRI scans, the intra-thoracic background conductivity is composed of a mixture of 48 % muscle, 47 % fat and 5 % bone (Table 4.1), which is in line with observations from thoracic CT scans [117].

Table 4.1 – Tissue conductivities and composition of the different structures present in the bioimpedance model.

Structure	Tissue Composition	Tissue Conductivity: σ_{Tissue} (S/m)
Background	Muscle, Fat, Bone	$f(0.384, 0.0435, 0.0211) = 0.206$
Heart (Endocardium)	Blood	0.710
Heart (Epicardium)	Myocardium	0.238
Aorta	Blood	0.710
Lungs	Blood, Lung Alveolar Tissue	$f(0.710, 0.100)$ [118, p. 89]

Note: All values are at 200 kHz and based on the public database provided by Hasgall et al. [73].

4.2.3 Dynamic Heart

The heart is represented by a 4D surface model of its four chambers: left/right atria/ventricles, as also shown in Figure 4.2a. For each of these structures a dynamic representation of its inner and outer boundaries (i.e. the endo- and epicardium) were segmented from the dynamic MRI scans *M2* with the approach by Hoogendoorn et al. [81] as described in [21].

This model was further improved in view of altering the ventricular volumes, i.e. to obtain different SVs. To this end, the volumes of the left (LV) and right ventricle (RV) were artificially modified over the entire cardiac cycle as follows. For both ventricular structures a median line was defined ranging from its apex to the center of its semilunar valve at end diastole. Then, to alternate the ventricular volume, all vertices of the corresponding model were displaced radially to the aforementioned median line. This leads to either shrinking or dilating of the corresponding ventricle. To obtain a specific ventricular volume the abovementioned procedure is applied in an iterative manner until the volume of the scaled ventricles matches the desired volume. Besides, for each iterative step, the endocardial structure is scaled first and then the epicardial structure is adapted keeping a constant volume difference between the two structures and thus ensuring the quasi incompressibility of myocardial tissue [156, 17].

With this approach, end systolic (ESV) and end diastolic volumes (EDV) of both, left and right ventricles, can be adjusted artificially. Moreover, the SV of the left and right heart were defined to be identical: $\text{SV}_\text{R} = \text{EDV}_\text{R} - \text{ESV}_\text{R} = \text{SV}_\text{L} = \text{EDV}_\text{L} - \text{ESV}_\text{L}$. Besides, a constant difference of $\text{EDV}_\text{R} - \text{EDV}_\text{L} = 28\,\text{mL}$ was set to account for the physiological difference between left and

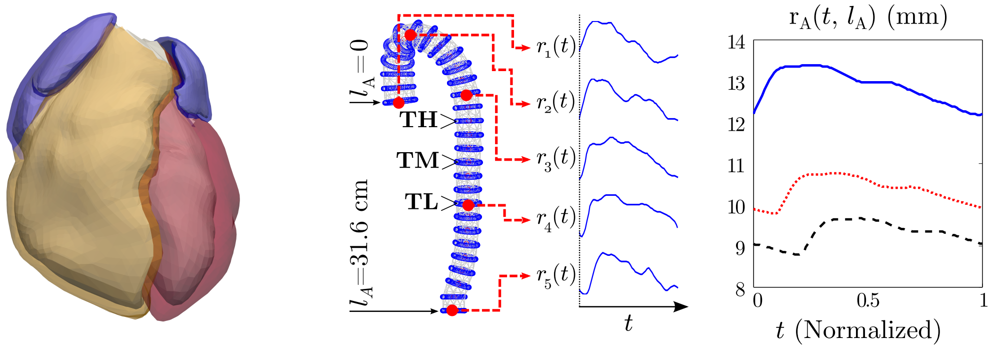

(a) (b) (c)

Figure 4.2 – (a) The 4D heart model in end diastole with the epicardia of the atria (blue), the right (yellow) and left (red) ventricle. The epicardia are slightly transparent such that the underlying endocardia are visible. (b) Circular model of the aorta (> indicate three belt levels) with the distension dynamics $r_1(t)$ to $r_5(t)$ at five locations (red arrows) which were combined to obtain (c) the time- and position-dependent aortic radius modulation curve $r_A(t, l_A)$, shown at three different positions (——blue, ······red, - - -black: $l_A = 0$, 15.8 or 31.6 cm) along the aorta.

right ventricular volume observed in the MRI scans.

Epicardia and endocardia are assigned with myocardial and blood conductivity as listed in Table 4.1.

4.2.4 Dynamic Aorta

The volume of the aorta was extracted from MRI scan *M1* by applying a volumetric snake segmentation [169]. Then, the centreline of the aorta was obtained by skeletonization of this volume. Finally, the aortic model was constructed by interconnecting 29 circles equidistantly spaced on this centreline (Figure 4.2b), which all allow individual modulation of their radii.

To determine the temporal development of the aortic radius, an aorta-specific 2D + t snake segmentation [77] was applied to the MRI scans *M3*, leading to a measure of aortic radius at five different locations along the aorta ($r_1(t)$ to $r_5(t)$ in Figure 4.2b). These were averaged to one single normalized aortic waveform $P_A(t)$, and combined with the radius of the aorta in relaxed state $R_A(l_A)$ (at a position l_A from the aortic valve, see Figure 4.3), resulting in the aortic radius modulation function $r_A(t, l_A)$ depicted in Figure 4.2c and defined as follows:

$$r_A(t, l_A) = R_A(l_A)\left[1 + \mathrm{DIST}_A \cdot P_A\left(t - \frac{l_A}{\mathrm{PWV}_A}\right)\right], \tag{4.1}$$

where PWV_A denotes the aortic pulse wave velocity at which the pressure wave travels along the aorta, and DIST_A the maximal relative radial distension of every single aorta circle. DIST_A was simplified as constant value of 10 %, which is more conservative than the 12 % observed

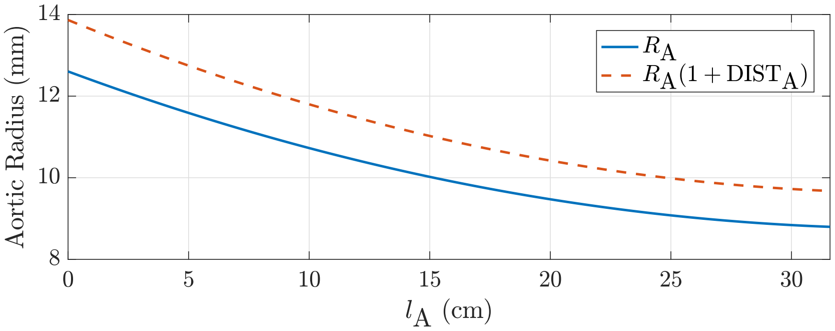

Figure 4.3 – Aortic radius as a function of the distance l_A from the aortic valve in two states: minimal (—–blue) and maximal distension (- - -red).

in the MRIs and in the range of normotensive subjects [83].

The individual modulation of the 29 aortic radii based on Equation (4.1), in combination with different $\mathrm{PWV_A}$ settings, thus allows the simulation of different systemic blood pressure values.

The aorta model is assigned uniformly with the conductivity of blood (Table 4.1).

4.2.5 Dynamic Lungs

The spatio-temporal representation of the electrical conductivity in the lungs is based on a detailed model of the pulmonary circulation proposed by Proença et al. and further explained in [118, 121].

This model allows the simulation of different levels of pulmonary artery pressure (PAP) and various types of pulmonary hypertensive conditions: PAH (pulmonary arterial hypertension), PHLHD (pulmonary hypertension due to left heart disease), HAPE (high altitude pulmonary edema), CTEPH (chronic thromboembolic pulmonary hypertension).

4.2.6 Simplified Models

At an earlier stage of the present thesis, a simplified version of the current model was available. This includes a heart model mainly consisting of two cropped ellipsoids (Section A.2.1), a static lung model (Section A.2.1) and the aorta model already described above (Section 4.2.4).

This first version of the model was used in a study, in which different EIT measurement settings were investigated in view of measuring systemic blood pressure via the aortic pulse arrival time. This study is available in Appendix A.

4.3 Practical Aspects of Simulations

In order to perform virtual EIT measurements with the dynamic bioimpedance model presented above, for each moment in the cardiac cycle simulated, the static thorax model (Section 4.2.2) is assigned a different conductivity, thus incorporating the dynamics of the model. Each of the structures (aorta, heart, etc.) is processed in a prioritized order, and all FEM elements having their center of mass within the 3D surface of the corresponding structure [95] are assigned its conductivity.

The approach of using a static thorax model was chosen for the reason that forward solving can be much faster when performed always on the same model. Besides, time consuming and complex mesh deformations can be avoided and there is no risk of potential artefacts arising from mesh variability [4].

To minimize quantization errors arising from this approach, the static thorax mesh was refined in the vicinity of moving structures and the refinement level adapted to the magnitude of displacement of the corresponding structure. In our particular case, the default maximal edge length of the finite elements of 5 mm was reduced to 2 mm and 1 mm close to the border of the heart and the aorta, respectively. The local mesh refinement of the volume mesh was performed using the gmsh software [59].

Finally, to allow for faster computation times, a parallel forward solver – similar to [19] – was used. One cardiac cycle could thus be simulated within less than 30 min, instead of the initial 2 h.

4.4 Limitations and Future Work

One could criticize different aspects of the current model. In the following, we attempt to list such limitations which could be improved in future work:

- General Aspects
  - The entire model is based on data from only one single healthy subject in supine position.
  - The current model is based on MRI scans in expiratory breath-hold and no changes related to respiration (except for changes in alveolar lung conductivity) can be simulated. Even though thorax excursions due to respiration have shown to be small [170], organ deformation and displacement resulting from respiration have shown to be more important [170] and should be taken into account.
  - As thoroughly studied by Gaw [57] and other researchers, the conductivity of blood is anisotropic and depends on the orientation of the red blood cells. The changes in blood conductivity resulting from blood flow should thus be considered in future

  models. This is also stated as a requirement in the review by de Sitter et al. [42] (for the application of ICG).
  - Additionally, skeletal muscles have shown to be a big contributor to the impedance signal [111] and are suggested to be included in models according to de Sitter et al. [42]. Even though this is for the application of ICG, with an electrode placement different to that of EIT, it might be worth considering this aspect.
  - Further cardiosynchronous conductivity changes which should be considered in a more extensive model are listed in [11].

- Dynamic Heart
  - Even though the current dynamic heart model enables the simulation of different SVs, these changes were generated fully artificially with a manual initialization of the median line (see Section 4.2.3). The use of a statistical heart model (e.g. a publicly available one [151]) covering realistic variations of a larger population, would be more representative.
  - The abovementioned displacement and deformation of the heart resulting from its interaction with the breathing lungs would be worth considering. Using an existing model would be a good starting point: e.g. the XCAT model [133].

- Dynamic Aorta
  - Currently, the distension of the aortic radii is only modulated in time but not in amplitude. A more advanced circulatory model (similar to the one of the lungs [118]) could be combined with the existing geometric model to a more realistic representation of the aorta.
  - The aorta is represented by blood conductivity only. For being more precise, a different conductivity should be assigned to the aortic wall.

- Dynamic Lungs
  - Limitations concerning the lung model are discussed by Proença [118, page 103].

- Model Validation
  - The present model is further limited in that it could only be partially validated. That is, the findings from simulations on the pulmonary model regarding EIT-derived PAP estimation performed by Proença et al. [121] have been confirmed by practical measurements [120]. However – although directly derived from real MRI scans – neither the heart nor the aorta model were validated against real EIT measurements which is recommended for future work.

Despite these limitations, the bioimpedance model was successfully applied to investigate the origins of cardiac EIT signals, as well as the feasibility and challenges of EIT-based SV estimation, which is described in the two subsequent chapters.

5 Investigations on the Origins of Cardiac EIT Signals

Adapted from the post-print version of [21]:

4D Heart Model Helps Unveiling Contributors to Cardiac EIT Signal

Fabian Braun[1,2], Martin Proença[1,2], Michael Rapin[1], Xenia Alba[3], Karim Lekadir[3], Mathieu Lemay[1], Josep Solà[1], Alejandro F. Frangi[4], and Jean-Philippe Thiran[2,5]

[1]Systems Division, Centre Suisse d'Electronique et de Microtechnique (CSEM), Neuchâtel, Switzerland

[2]Signal Processing Laboratory (LTS5), Ecole Polytechnique Fédérale de Lausanne (EPFL), Lausanne, Switzerland

[3]Center for Computational Imaging and Simulation Technologies in Biomedicine, Universitat Pompeu Fabra, Barcelona, Spain

[4]Center for Computational Imaging and Simulation Technologies in Biomedicine, University of Sheffield, Sheffield, UK

[5]Department of Radiology, University Hospital Center (CHUV) and University of Lausanne (UNIL), Lausanne, Switzerland

Published in the proceedings of the 16th International Conference on Biomedical Applications of Electrical Impedance Tomography (EIT 2015), Neuchâtel, Switzerland

DOI:10.5281/zenodo.17752

5.1 Introduction

As alluded to in the previous chapters, one remaining issue regarding cardiovascular EIT is the poor understanding of the signal origins. A better understanding of the cardiac EIT signal genesis is crucial for the development of reliable algorithms in view of advancing EIT towards daily clinical use.

To do so, we performed simulations on the 4D hemodynamic bioimpedance model presented in the previous chapter. In particular, we investigated the origins of EIT signals in the heart region for two different electrode belt placements commonly used in cardiac EIT.

5.2 Methods

5.2.1 Simulations

The current simulations were performed on the bioimpedance model consisting of the static thorax model (Section 4.2.2) in combination with the dynamic models of the heart (Section 4.2.3), aorta (Section 4.2.4) and lungs (Section 4.2.5). Using this model, EIT impedance measurements were simulated for two electrode belts placed either in a transversal plane at the level of the heart (TM belt, see Figure 4.1a) or in an oblique plane by tilting the TM belt by 30° from transverse to coronal (OM belt, see Figure 4.1b) – initially suggested by Vonk Noordegraaf et al. [154] for a better separation of atrial and ventricular activity in cardiac EIT.

Simulations were performed on 32 equidistantly spaced electrodes with a skip 4 measurement pattern [53]. EIT images were reconstructed using the GREIT algorithm with the recommended settings [6] and a noise figure (NF) of 0.5 [62].

First, for each belt, one heart cycle was simulated with all structures (ventricles, atria, lungs and aorta) contributing to the intra-thoracic impedance change. Then, to investigate the individual signal contribution, each structure was simulated independently. This lead to the simulation of five different heart cycles per belt placement: (a) all structures active, or only the (b) ventricles, (c) atria, (d) lungs or (e) aorta. This assumes that the superposition of all individual simulations (b) to (e) is equal to the simultaneous simulation of all structures (a).

5.2.2 Signal Analysis

For each of the cardiac cycles simulated, a *cardiosynchronous activity image* (CAI) was calculated. These images were computed via the pixel-wise standard-deviation in the time domain and thus represent the signal strength – i.e. the cardiosynchronous EIT activity – at each single pixel.

Then, the heart region was determined from the CAI of simulation (a), where all structures

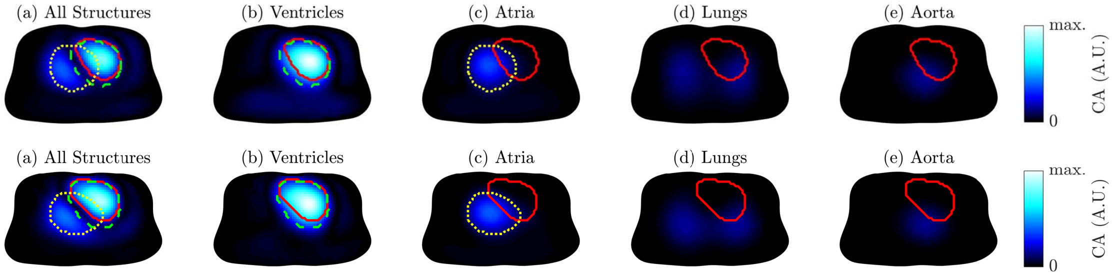
(a) All Structures
(b) Ventricles
(c) Atria
(d) Lungs
(e) Aorta
max.
0
CA (A.U.)
(a) All Structures
(b) Ventricles
(c) Atria
(d) Lungs
(e) Aorta
max.
0
CA (A.U.)

Figure 5.1 – Images of cardiosynchronous activity (CA) for (a) all structures together and (b) to (e) all structures separately: (Top) transversal and (Bottom) oblique belt placement. The delineated regions represent the heart (——red), the ventricles (- - -green), and the atria (······yellow).

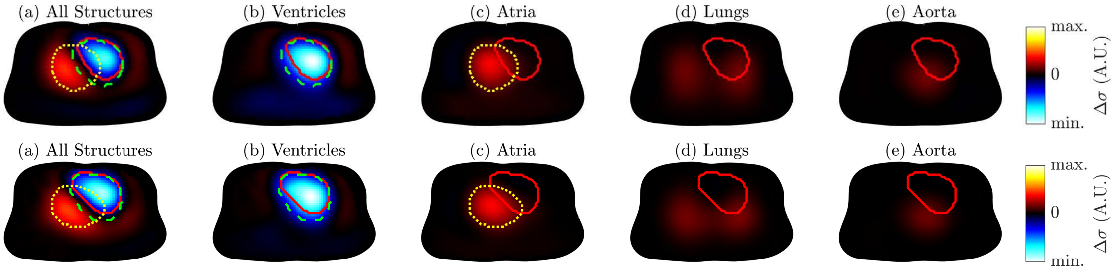
(a) All Structures
(b) Ventricles
(c) Atria
(d) Lungs
(e) Aorta
max.
0
min.
$\Delta\sigma$ (A.U.)
(a) All Structures
(b) Ventricles
(c) Atria
(d) Lungs
(e) Aorta
max.
0
min.
$\Delta\sigma$ (A.U.)

Figure 5.2 – EIT images showing the conductivity difference (end systole relative to end diastole) for (a) all structures together and (b) to (e) all structures separately: (Top) transversal and (Bottom) oblique belt placement. The delineated regions represent the heart (——red), the ventricles (- - -green), and the atria (······yellow).

were active. To this end, one pixel of the heart region was manually selected and the region automatically extended to all pixels of the CAI image above a certain threshold (25 % of the maximal amplitude).

Finally, the contribution of each individual structure to the global impedance change in the heart region was determined by summing up all pixels of the corresponding CAI in that region.

5.3 Results and Discussion

Figure 5.1 shows the cardiosynchronous activity for both belt placements and all different simulations. The corresponding EIT difference images are shown in Figure 5.2. It can be observed that the heart region (——red) obtained from (a) coincides more with ventricular (- - -green) and less with atrial activity (······yellow).

The contribution of each structure (b) to (e) to the overall cardiac EIT signal (a) is illustrated in Figure 5.3. For the transversal belt the cardiac signal originates for: 77.4 %, 9.7 %, 7.4 %, 5.5 %, and for the oblique belt for: 82.6 %, 9.7 %, 4.5 %, 3.3 % from ventricular, atrial, pulmonary or aortic activity, respectively. The ratios between ventricular and atrial contribution do not vary

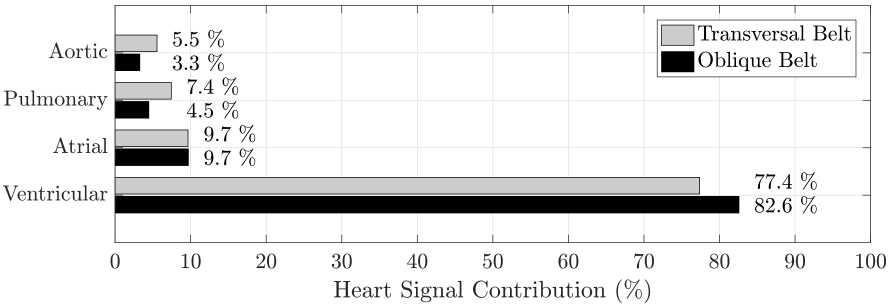

Figure 5.3 – Bar chart showing the percentage to which each structure is contributing to the EIT heart signal for transversal and oblique belt placements.

considerably between transversal (77.4 %/9.7 % = 8.0) and oblique belts (82.6 %/9.7 % = 8.5). This is not in line with the findings by Vonk Noordegraaf et al. [154] since an oblique belt placement did not lead to a significantly improved separation between atrial and ventricular activity in the EIT heart region. Nevertheless, the use of an oblique belt slightly reduces the pulmonary and aortic activity and thus also marginally increases ventricular contribution in the heart region.

5.4 Limitations and Future Work

The current findings are limited in that only one specific scenario with fixed EIT device settings and hemodynamic parameters was simulated. If this research question gains higher importance, different hemodynamic parameters and belt placements should be investigated.

Besides, the current analysis relies on the assumption that the superposition of individual simulations of each structure (simulations (b) to (e)) is equal to simulating all structures at the same time (simulation (a)). This is strictly speaking wrong, but can be valid to a certain extent. To verify the validity of this approach, the CAI of simulation (a) was compared to the CAI of the superposition of simulations (b) to (e). The mean relative error in the heart region was found to be less than 2.2 %, which justifies the use of this assumption for this particular analysis.

5.5 Conclusion

In view of gaining more understanding about the signal origins of EIT signals in the heart region we performed simulations on the 4D bioimpedance model.

Our findings reveal that – for two commonly used belt placements – the EIT heart signal is dominated by ventricular activity (≥77 % contribution). In contrast to previous studies [154], we could not observe a substantially better separation between ventricular and atrial activity when using an oblique instead of a transversal belt placement, but to a small extent less contribution from pulmonary and aortic activity.

6 Feasibility and Limitations of EIT-Based Stroke Volume Measurement

Adapted from the pre-print version of [24] and the post-print version of [23]:

Limitations and Challenges of EIT-Based Monitoring of Stroke Volume and Pulmonary Artery Pressure

Fabian Braun[1,2], Martin Proença[1,2], Mathieu Lemay[1], Mattia Bertschi[1], Andy Adler[3], Jean-Philippe Thiran[2,4] and Josep Solà[1]

[1]Systems Division, Centre Suisse d'Electronique et de Microtechnique (CSEM), Neuchâtel, Switzerland

[2]Signal Processing Laboratory (LTS5), Ecole Polytechnique Fédérale de Lausanne (EPFL), Lausanne, Switzerland

[3]Systems and Computer Engineering, Carleton University, Ottawa, Canada

[4]Department of Radiology, University Hospital Center (CHUV) and University of Lausanne (UNIL), Lausanne, Switzerland

Accepted for publication in **Physiological Measurement**

DOI:10.1088/1361-6579/aa9828

EIT-Derived Stroke Volume is Impaired by Belt Displacement

Fabian Braun[1,2], Martin Proença[1,2], Josep Solà[1], Mathieu Lemay[1], and Jean-Philippe Thiran[2,3]

[1]Systems Division, Centre Suisse d'Electronique et de Microtechnique (CSEM), Neuchâtel, Switzerland

[2]Signal Processing Laboratory (LTS5), Ecole Polytechnique Fédérale de Lausanne (EPFL), Lausanne, Switzerland

[3]Department of Radiology, University Hospital Center (CHUV) and University of Lausanne (UNIL), Lausanne, Switzerland

Published in the proceedings of the 16th International Conference on Electrical Bio-Impedance and 17th International Conference on Biomedical Applications of Electrical Impedance Tomography (ICEBI & EIT 2016), Stockholm, Sweden

DOI:10.5281/zenodo.55753

6.1 Introduction

6.1.1 Objectives

As shown in the previous chapter, the EIT heart signal is strongly dominated by ventricular activity. This gives hope for the feasibility of an EIT-based SV monitor, which is investigated in detail in the present chapter by means of simulations on the bioimpedance model.

The goal of these investigations is two-fold. First, we study the feasibility of EIT-based SV monitoring. Then, we investigate and quantify potential limitations and challenges one could face in experimental and clinical scenarios when assessing SV by means of EIT.

6.1.2 Motivation

In the past, several studies have investigated the feasibility of EIT-based SV either via simulations [173, 119, 44, 105, 13] or real measurements [155, 114, 113, 41]. However, only a few studies describe limitations and challenges related to cardiovascular EIT monitoring, in particular concerning the monitoring of SV. Patterson et al. [110] concluded that, in healthy volunteers, the cardiac EIT signal depends strongly on electrode position, lung volume and posture. In pig experiments, Pikkemaat et al. [114] observed variations in the subject-specific scaling of the cardiac EIT signal, which were interpreted to stem from lung volume or heart and belt position. In a simulation study, Arshad et al. [13] showed a strong respiration-related dependence in the EIT heart signal.

As accurate monitoring results are of importance for reliable diagnostics, we investigate to what extent SV monitoring via EIT can be impaired. Specifically we seek to estimate the amount of uncertainty introduced into this EIT-based hemodynamic parameter due to the variability in realistic clinical and ambulatory scenarios. To do so, we first list potential confounding factors and then study how seriously some of these factors affect the estimation of SV. The four confounding factors selected are: (1) electrode belt displacement, (2) electrode detachment, (3) changes in hematocrit, and (4) changes in lung air volume.

In the current study we perform simulations on the 4D thoracic bioimpedance model presented in Chapter 4. This allows a systematic and individual investigation of potential confounding factors, which is practically impossible in real measurements. As mentioned above, the few limitations reported for SV monitoring via EIT are mainly based on observations from real measurements. This is thus – to the best of our knowledge – the first work systematically identifying and quantifying potential challenges for EIT-based SV monitoring, based on simulations on a bioimpedance model.

6.2 Methods

In the following, we first refer to the dynamic bioimpedance model used to perform EIT simulations. Next, we list potential confounding factors and describe the four potentially harmful ones investigated, together with other simulation parameters. Then we explain the signal processing steps used to estimate SV from EIT image sequences. Finally, we describe the analysis applied to evaluate and quantify the decrease in performance resulting from each of the confounding factors.

6.2.1 Dynamic Bioimpedance Model

The current simulations were performed on the bioimpedance model consisting of the static thorax model (Section 4.2.2) in combination with the dynamic models of the heart (Section 4.2.3), aorta (Section 4.2.4) and lungs (Section 4.2.5). These models and the simulation framework are also illustrated in Figure 6.1.

All simulations were performed on each of the five transversal belts with 32 electrodes using a bipolar stimulation pattern with four inactive electrodes between the two ones actively measuring voltage/injecting current, also known as skip 4 [55] and employed by the Swisstom BB^2 device.

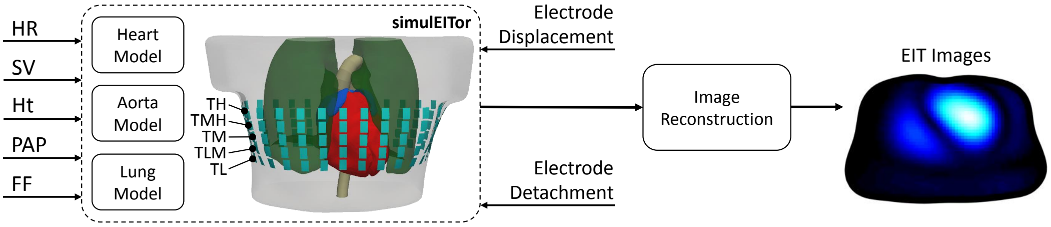
HR
SV
Ht
PAP
FF
Heart Model
Aorta Model
Lung Model
simulEITor
TH
TMH
TM
TLM
TL
Electrode Displacement
Electrode Detachment
Image Reconstruction
EIT Images

Figure 6.1 – Block diagram of the simulation framework and the possible parameters to be adjusted in the bioimpedance model: heart rate (HR), stroke volume (SV), hematocrit (Ht), pulmonary artery pressure (PAP), lung filling factor (FF). This framework further allows the simulation of electrode displacement and detachment. EIT image sequences of a full cardiac cycle are reconstructed for each simulation.

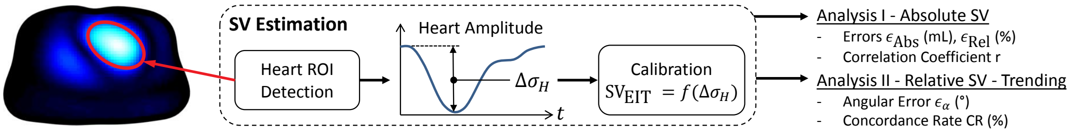
SV Estimation
Heart ROI Detection
Heart Amplitude
$\Delta\sigma_H$
t
Calibration
$SV_{EIT} = f(\Delta\sigma_H)$
Analysis I - Absolute SV
- Errors ϵ_{Abs} (mL), ϵ_{Rel} (%)
- Correlation Coefficient r
Analysis II - Relative SV - Trending
- Angular Error ϵ_α (°)
- Concordance Rate CR (%)

Figure 6.2 – Block diagram of the analysis used to estimate SV from EIT image sequences.

6.2.2 Simulations Performed

Physiological Parameters

In view of mimicking physiological meaningful SV variations, different cases of changes in preload, afterload and inotropy were simulated. Initially proposed in [119, 118] and adapted to the current model, this lead to eleven values of SV_{Ref} as listed in Table 6.1.

Table 6.1 – Simulated physiological parameters adapted from [119, 118]: end diastolic (EDV) and end systolic volume (ESV), stroke volume (SV_{Ref}) and pulmonary artery pressure (PAP).

Description	EDV (mL)	ESV (mL)	SV_{Ref} (mL)	PAP (mmHg)
Preload (large decrease)	85.9	39.9	46.0	12.06
Preload (moderate decrease)	99.0	45.6	53.4	12.71
Preload (small decrease)	112.0	51.3	60.7	13.35
Inotropy (decrease)	140.6	79.8	60.8	13.37
Afterload (increase)	135.4	74.1	61.3	13.41
Baseline	125.0	57.0	68.0	14.00
Afterload (decrease)	119.8	45.6	74.2	14.55
Inotropy (increase)	114.6	39.9	74.7	14.59
Preload (small increase)	140.6	59.9	80.8	15.13
Preload (moderate increase)	156.3	62.7	93.6	16.25
Preload (large increase)	171.9	65.6	106.3	17.38

Note: All simulations assumed a constant heart rate (HR = 80 bpm) and PAP was calculated assuming a constant pulmonary vascular resistance ($R_t = 0.0662\,\text{mmHg}\cdot\text{s/mL}$): $\text{PAP} = R_t \cdot SV_{Ref} \cdot \text{HR}/60 + 8\,\text{mmHg}$

Investigations on Potential Confounding Factors

When measuring EIT in realistic clinical or ambulatory scenarios, various factors – external (i.e. affecting the EIT system) or internal (i.e. affecting the human body under measurement) – can alter the EIT data measured and thus also the SV estimates derived thereof.

In the following, we first attempt to elucidate possible factors affecting cardiovascular EIT measurements. These are: (1) electrode displacement: shifting during a measurement or misplacement between different measurements; (2) issues with electrode contact, e.g. detachment or drying out of contact gel; (3) changes in blood conductivity due to changes in hematocrit; (4) changes in lung conductivity due to respiration, liquid redistribution, extra-vascular lung water, etc.; (5) respiration-induced thorax excursion, displacement and deformation of heart, lungs and other tissues; (6) posture- and gravity-induced changes such as organ and liquid redistribution; (7) electronic noise and disturbances; (8) impedance changes due to the pulsatile reorientation of red blood cells [57] or other anisotropic structures, e.g. the myocardium [11].

While (5) and (7) can – at least partly – be reduced and averaged with the proper filtering technique (i.e. ECG-gated ensemble averaging), (6) might be less important when targeting bedside EIT. Due to its complexity and the assumed equally importance of the other remaining factors, (8) was not investigated in the present work.

The remaining four potential confounding factors (1), (2), (3), and (4) were studied and are described in more detail hereafter:

1. **Electrode belt displacement**: When using an EIT system where all electrodes are included in a belt, the whole of electrodes can be displaced in longitudinal (up/down) direction or rotated (left/right). This problem can occur during the same measurement or between different measurements where the belt needs to be reapplied – without necessarily having the knowledge of the exact belt position of the preceding measurement. For an EIT system based on self-adhesive electrodes only the latter can apply.

   The TM belt (located at the height of the ventricles, see Figure 6.1) is considered as the "baseline" belt placement to which all the other displacements are being compared to. By using the other four belts (TL, TLM, TMH, TH) a up- and downward displacements of 1.75 and 3.5 cm were simulated.

   For rotational belt displacements, two levels of magnitude were simulated by shifting the belt by 0.5 or 1.0 electrode spacing to the left/right, respectively. At the present thorax circumference of about 90 cm these shifts correspond to rotational displacements of 1.4 and 2.8 cm, respectively.

2. **Electrode detachment**: The contact of certain EIT electrodes with the human body can be or become bad for various reasons (movement of the patient via internal or external influence, drying of electrode gel, *pectus excavatum*, etc.). To ensure reliable EIT images, the measurements related to these electrodes need to be removed prior to reconstruction. To this end, we simulated the detachment of each single electrode and all possible pairs of electrodes, leading to $\binom{32}{1} + \binom{32}{2} = 528$ combinations. Failing electrodes are compensated during EIT image reconstruction with the algorithm described in [97].

3. **Lung air volume changes**: Due to respiration, intra-thoracic conductivity distribution changes significantly between in- and expiration. To this end, we simulated four different lung air volume levels: (1) forced expiration, (2) expiration, (3) between in- and expiration, and (4) inspiration. These four levels, corresponding to filling factors of $\text{FF} = [1.3, 2.0, 3.0, 4.8]$, were simulated using lung alveolar tissue conductivities of $\sigma_\text{L} = [0.12, 0.10, 0.08, 0.06]$ S/m according to [126]. Even though respiratory activity normally involves other changes (i.e. deformation and/or displacement of lungs, heart and thorax [170]) the current model simulates breath-hold and does therefore only support changes in σ_L.

4. **Hematocrit changes**: The percentage of red blood cells in the blood – known as hemato-

crit – does significantly influence the electrical conductivity of blood σ_{B}. To investigate the influence of hematocrit-related changes, we simulated five physiological hematocrit levels (Ht = [35, 40, 45, 50, 55] %), which were transformed to the corresponding blood conductivity levels ($\sigma_{\mathrm{B}} = [0.87, 0.78, 0.70, 0.63, 0.56]$ S/m) according to [58].

EIT Image Reconstruction

Following the pipeline illustrated in Figure 6.1: the raw data resulting from simulations were reconstructed into EIT images using the GREIT algorithm [6] with the recommended parameters and a noise figure (NF) of 0.5 [62]. The reconstruction is based on a coarse version of the forward model with uniform conductivity and uses the TM belt placement.

6.2.3 SV Estimation

The present approach to estimate SV from EIT image sequences is based on hypothesis that the amplitude of the EIT heart signal is proportional to the SV, as also reported by other groups [114, 155]. The algorithm used is fully automatic and consists of the following three steps also illustrated in Figure 6.2: (1) determination of the heart ROI, (2) estimation of the heart sum signal amplitude $\Delta\sigma_{\mathrm{H}}$ as SV surrogate measure, and (3) the calibration function.

The heart ROI detection is exemplified in Figure 6.3 and performed as follows. First, each pixel is assigned to the heart or non-heart region according to its phase at cardiac frequency (similar to the lung ROI detection in [120, 118]). Second, the potential timing of end systole is identified as the minimum of the sum signal of all potential heart pixels. Thirdly, a difference image (end diastole minus end systole) is calculated. Finally, the heart region is identified as the biggest region with positive amplitude in this difference image where all pixels with an amplitude below an automatically determined threshold [109] got removed. The heart amplitude $\Delta\sigma_{\mathrm{H}}$ is then computed from the sum signal in the aforementioned heart ROI as the amplitude between end diastole and end systole. The calibration transforming $\Delta\sigma_{\mathrm{H}}$ from arbitrary units into $\mathrm{SV}_{\mathrm{EIT}}$ expressed in mL is described in the next section.

6.2.4 Analysis and Performance Evaluation

To investigate the performance of the EIT-based SV estimates, different figures of merit were defined to quantitatively assess the errors caused by the aforementioned confounding factors. The influence of each of the confounding factors is assessed by comparing to the baseline configuration: TM belt, no belt displacement, no detached electrode, $\sigma_{\mathrm{L}} = 0.10$ S/m (FF = 2.0) and $\sigma_{\mathrm{B}} = 0.70$ S/m (Ht = 45 %).

The conductivity amplitude in the heart region $\Delta\sigma_{\mathrm{H}}$ (computed as described in Section 6.2.3), is transformed into SV values expressed in mL as follows. We first compute the linear fit ($f_H(x) = a \cdot x + b$) between the simulated SV values $\mathrm{SV}_{\mathrm{Ref}}$ and the EIT-derived heart-amplitude

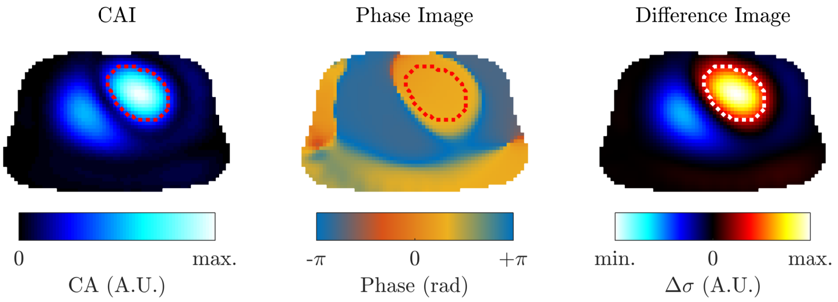

Figure 6.3 – Example output of the algorithm used for detecting the heart ROI (dotted lines in images) as described in Section 6.2.3. CAI stands for cardiosynchronous activity image (i.e. the pixel-wise standard deviation in the temporal domain). The phase image depicts the phase shift φ of the first harmonic at cardiac frequency f_c proportional to $\cos\left(2\pi f_c t + \varphi\right)$, where $t = 0$ is defined as end diastole.

$\Delta\sigma_{\mathrm{H}}$ of the baseline configuration. All $\Delta\sigma_{\mathrm{H}}$ are then transformed into SV values with exactly the same calibration function, i.e. $\mathrm{SV}_{\mathrm{EIT}} = f_H(\Delta\sigma_{\mathrm{H}})$. This allows to investigate the influence of the different confounding factors while assuming an initial calibration of the EIT vs a SV reference.

In a first analysis (Analysis I), based on Bland-Altman analysis [12], we quantify the absolute ϵ_{Abs} and relative error ϵ_{Rel} between the estimate $\mathrm{SV}_{\mathrm{EIT}}$ of the current vs the baseline configuration. Besides, the correlation coefficient r between $\mathrm{SV}_{\mathrm{EIT}}$ and $\mathrm{SV}_{\mathrm{Ref}}$ is computed. Measurements are considered as reliable if the 95 % confidence interval of ϵ_{Rel} does not exceed ±10 %, which is one third of the ±30 % error reported for invasive thermodilution and thus assumes averaging of at least three reference measurements as typically done in practice [37].

In a second analysis (Analysis II), we analyze the trending ability of the EIT-based SV values, that is the ability of $\mathrm{SV}_{\mathrm{EIT}}$ to track changes in SV, but not absolute values of SV. To this end, we first compute the changes of SV from an initial starting measurement and obtain the SV changes $\Delta\mathrm{SV}_{\mathrm{EIT}}$ and $\Delta\mathrm{SV}_{\mathrm{Ref}}$, respectively. Then we plot $\Delta\mathrm{SV}_{\mathrm{EIT}}$ vs $\Delta\mathrm{SV}_{\mathrm{Ref}}$ in a four-quadrant plot, a common methodology to assess trending ability [37, 130] (see examples in Figure 6.4). The four-quadrant plot was chosen over the polar plot because of its more intuitive interpretability and the fact that only noisy but not the most discordant measurements are excluded [130]. We further quantify the trending ability by means of (1) the angular error ϵ_α and (2) the angular concordance rate CR. (1) ϵ_α is defined as the angle between the identity line ($\Delta\mathrm{SV}_{\mathrm{EIT}} = \Delta\mathrm{SV}_{\mathrm{Ref}}$) and the line from the origin to the point ($\Delta\mathrm{SV}_{\mathrm{Ref}}$, $\Delta\mathrm{SV}_{\mathrm{EIT}}$); (2) CR represents the percentage of measurements with an angular error within a given threshold of $\epsilon_\alpha \leq \pm 30\,\%$, which is more restrictive than the traditional concordance rate (including all measurements lying in the 1st and 3rd quadrant). According to Critchley et al. [38] the following criteria are required to ensure acceptable trending ability: CR > 92 %, mean angular error < ±5°, confidence interval of angular error < ±30°.

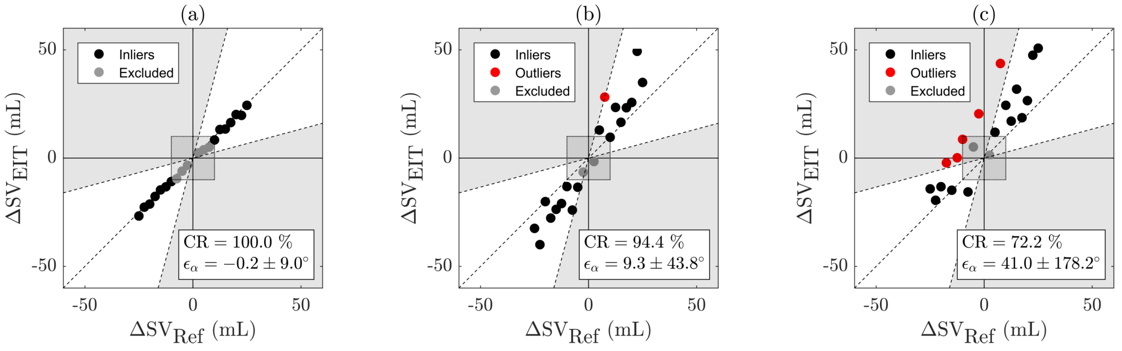

Figure 6.4 – Illustrative examples of trending analysis by means of four-quadrant plots [37, 130]. Three cases were artificially generated: (a) the best case with no single outlier (CR = 100 %) and an angular error within the accepted limits defined in Section 6.2.4; (b) mediocre case with CR within the accepted limits but with a too high deviation and bias of ϵ_α; (c) worst case where both CR and the ϵ_α are unacceptable. In all plots the exclusion zone (gray shaded square area) was set to ±10 mL.

6.3 Results and Discussion

6.3.1 EIT Heart Amplitude

Before analyzing $\mathrm{SV}_{\mathrm{EIT}}$ values, we first examine the relationship between the uncalibrated heart amplitude $\Delta\sigma_{\mathrm{H}}$ and the reference $\mathrm{SV}_{\mathrm{Ref}}$. This is because the analysis of $\Delta\sigma_{\mathrm{H}}$ can reveal more information which might not be apparent in $\mathrm{SV}_{\mathrm{EIT}}$, as certain information might get lost during the calibration from $\Delta\sigma_{\mathrm{H}}$ to $\mathrm{SV}_{\mathrm{EIT}}$.

Figure 6.5 shows the heart amplitude $\Delta\sigma_{\mathrm{H}}$ for the eleven $\mathrm{SV}_{\mathrm{Ref}}$ and five belt placements simulated. For all placements, a high correlation ($r \geq 0.998$) was observed between $\Delta\sigma_{\mathrm{H}}$ and $\mathrm{SV}_{\mathrm{Ref}}$, which is in line with other simulation-based studies [44, 105]. However, one can also observe that there is an inferior limit of detection where $\Delta\sigma_{\mathrm{H}}$ crosses the $\mathrm{SV}_{\mathrm{Ref}}$ axis. This limit ($\mathrm{SV}_{\mathrm{Min}}$) varies from 20 mL (for the lowermost belt) to 40 mL (for the uppermost belt). It is hypothesized that $\mathrm{SV}_{\mathrm{Min}}$ is given by the ratio of signal strength between ventricular versus other signal sources (e.g. lungs, atria, aorta), which are attenuating the former. The lower the belt is placed the lower $\mathrm{SV}_{\mathrm{Min}}$ due to the stronger ventricular and lower pulmonary signal contribution and vice versa. The apparent high variations of $\Delta\sigma_{\mathrm{H}}$ arising from changes in belt placement, in particular the resulting error on $\mathrm{SV}_{\mathrm{EIT}}$, are analyzed hereafter.

6.3.2 Analysis I - Absolute SV

Belt Displacement

The influence of up/down and left/right electrode belt displacement are shown in Figure 6.6 and the resulting errors are listed in Table 6.2. It can be observed that after all types of belt displacement $\mathrm{SV}_{\mathrm{EIT}}$ still remains highly correlated with $\mathrm{SV}_{\mathrm{Ref}}$ ($r \geq 0.99$ in Table 6.2, which is in

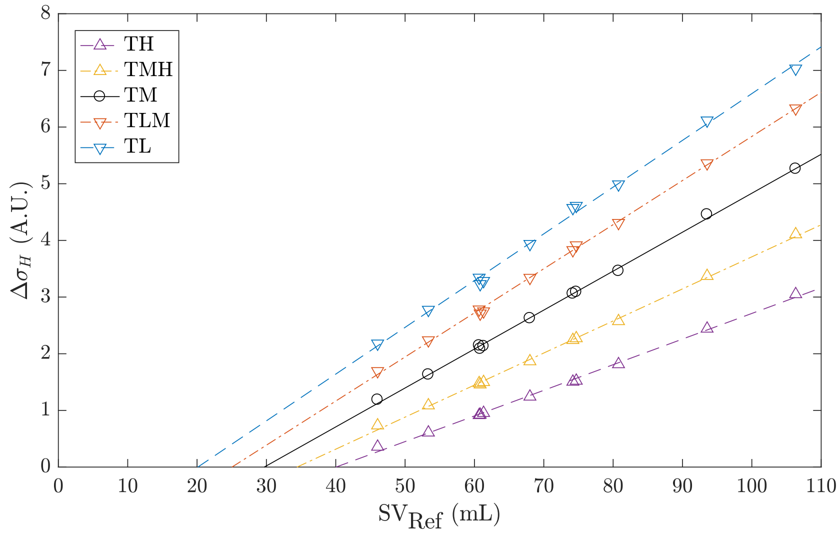

Figure 6.5 – EIT-derived heart amplitude $\Delta\sigma_{\mathrm{H}}$ as a function of simulated stroke volume $\mathrm{SV_{Ref}}$ for five different transversal belt placements: TH, TMH, TM, TLM, TL (see Figure 6.1).

line with other simulation-based studies [44, 105].

However, the up- and downwards belt shifts introduce a significant bias in $\mathrm{SV_{EIT}}$, i.e. a downwards shift leads to an increase and a upwards shift to a decrease of $\mathrm{SV_{EIT}}$, respectively. This can be explained by the increase of ventricular and decrease of the pulmonary signal contribution when shifting the belt downwards, whereas the opposite applies for an upwards shift. This bias can get as high as 28.2 % and as low as −29.2 % when shifting the belt downwards or upwards by 3.5 cm, respectively.

In contrast, the errors caused by the rotational belt shifts are smaller: i.e. a leftwards shift of 2.8 cm results in a bias of 13.4 % whereas the bias for rightwards shifts is highest at 1.4 cm with only −5.3 %. The asymmetry of errors observed between left and right shifts is assumed to be due to the non-central position of the heart and the uneven distribution of lung volume between left and right.

Table 6.2 – Absolute error (ϵ_{Abs}), relative error (ϵ_{Rel}) and correlation coefficient (r) of $\mathrm{SV_{EIT}}$ for different electrode belt displacements when compared to the baseline configuration. Cell shadings indicate whether the acceptance criteria (see Section 6.2.4) are met (green) or not (red).

	Up/Down Displacement				**Left/Right Displacement**			
	↑ 3.5 cm	↑ 1.8 cm	↓ 1.8 cm	↓ 3.5 cm	← 2.8 cm	← 1.4 cm	→ 1.4 cm	→ 2.8 cm
ϵ_{Abs} (mL)	−20.9 ± 6.1	−11.2 ± 3.1	10.7 ± 2.4	19.7 ± 3.7	9.6 ± 2.7	5.0 ± 1.4	−3.8 ± 1.2	−2.2 ± 0.5
ϵ_{Rel} (%)	−29.2 ± 1.6	−15.6 ± 0.8	15.2 ± 0.7	28.2 ± 2.1	13.4 ± 1.0	7.1 ± 0.7	−5.3 ± 0.8	−3.4 ± 1.3
r	0.9987	0.9993	0.9995	0.9984	0.9995	0.9998	0.9993	0.9990

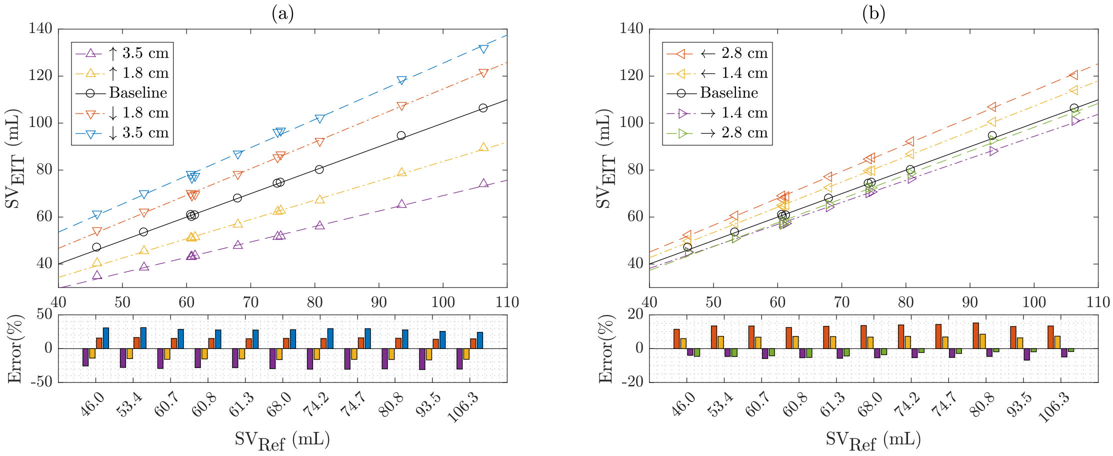

Figure 6.6 – Influence on SV_{EIT} by (a) up/down and (b) left/right electrode belt displacements. The relationship of reference SV (SV_{Ref}) and EIT-based SV estimates (SV_{EIT}) is shown in the upper plots. The lower plots depict the relative error between SV_{EIT} and the baseline configuration.

Electrode Detachment

The relative errors in SV_{Ref} resulting from the detachment of one or two electrodes are shown in Figure 6.7. The errors were calculated over the eleven SV_{Ref} simulated and are visualized per electrode to show the influence for each of the electrodes individually. Table 6.3 further lists the error statistics for a selection of eight electrodes when involved in the removal of two electrodes.

The overall error is -1.08 ± 1.23 % (-0.78 ± 0.95 mL) when removing one electrode (Figure 6.7a) and -2.28 ± 1.79 % (-1.66 ± 1.44 mL) when removing two electrodes (Figure 6.7c), respectively. However, it has to be noted that detaching electrodes (1 to 4, 31 and 32) located in the ventral left region – close to the heart – results in higher errors (see also Figure 6.7b). These findings highlight the importance of a good electrode contact in the ventral region. In practice this can be quite challenging, especially for EIT systems having the electrodes included in a belt, where electrode contact is often impaired in the sternum region (e.g. *pectus excavatum*). This issue might be party circumvented by using more sophisticated simulation and measurement patterns or even by adapting them in real-time.

Changes in Hematocrit and Lung Air Volume

Figure 6.8a shows how changes in hematocrit influence SV_{EIT}. The corresponding errors are listed in Table 6.4. An increase in blood conductivity σ_B – resulting from a decrease in hematocrit – leads to a higher SV_{EIT} and in return, a decrease in σ_B to a lower SV_{EIT}. Nevertheless, the errors remain rather low, i.e. over the entire physiological range of Ht from 35 % to 55 %, the relative bias changes only from 2.3 % to −3.4 %.

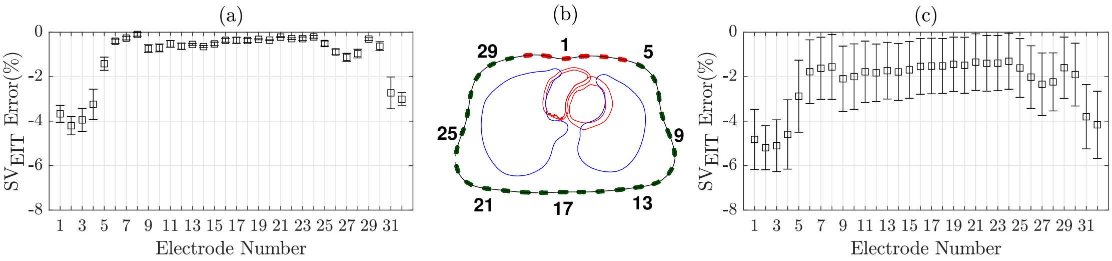

Figure 6.7 – Relative error of SV_{EIT} resulting from the detachment of (a) a single electrode or (c) all possible pairs of electrodes. The error statistics shown are calculated over the 11 SV states simulated. The transversal EIT plane in (b) shows the position of the 32 electrodes (in green) and highlights the ones with higher errors (in red).

Table 6.3 – Absolute error (ϵ_{Abs}), relative error (ϵ_{Rel}) and correlation coefficient (r) of SV_{EIT} resulting from the detachment of 2 electrodes when compared to the baseline configuration. Cell shadings indicate whether the acceptance criteria (see Section 6.2.4) are met (green) or not (red).

	Elec. 1	**Elec. 5**	**Elec. 9**	**Elec. 13**	**Elec. 17**	**Elec. 21**	**Elec. 25**	**Elec. 29**
ϵ_{Abs} (mL)	-3.4 ± 1.4	-2.1 ± 1.4	-1.5 ± 1.2	-1.3 ± 1.0	-1.1 ± 1.0	-1.0 ± 1.0	-1.2 ± 1.1	-1.1 ± 1.1
ϵ_{Rel} (%)	-4.8 ± 1.4	-2.9 ± 1.6	-2.1 ± 1.5	-1.7 ± 1.3	-1.5 ± 1.3	-1.3 ± 1.3	-1.6 ± 1.3	-1.6 ± 1.4
r	0.9975	0.9968	0.9973	0.9978	0.9979	0.9978	0.9977	0.9976

In contrast, changes in lung alveolar tissue conductivity σ_{L} – resulting from changes in lung air volume between normal inspiration and forced expiration – have a higher influence on SV_{EIT}. This is depicted in Figure 6.8b and also listed in Table 6.4. Normal inspiration ($\sigma_{\text{L}} = 0.06$ S/m) compared to normal expiration (baseline state) introduces a relative bias of 8.0 %. On the other hand, full expiration ($\sigma_{\text{L}} = 0.12$ S/m) lowers the bias to −3.2 %.

Table 6.4 – Absolute error (ϵ_{Abs}), relative error (ϵ_{Rel}) and correlation coefficient (r) of SV_{EIT} for changes in hematocrit and lung air volume when compared to the baseline configuration. Cell shadings indicate whether the acceptance criteria (see Section 6.2.4) are met (green) or not (red).

	Hematocrit Changes				**Lung Air Volume Changes**		
	$\sigma_B = 0.56$ (Ht = 55 %)	$\sigma_B = 0.63$ (Ht = 50 %)	$\sigma_B = 0.78$ (Ht = 40 %)	$\sigma_B = 0.87$ (Ht = 35 %)	$\sigma_L = 0.06$ (FF = 4.8)	$\sigma_L = 0.08$ (FF = 3.0)	$\sigma_L = 0.12$ (FF = 1.3)
ϵ_{Abs} (mL)	-2.6 ± 1.4	-1.2 ± 0.7	1.0 ± 0.6	1.8 ± 1.1	6.1 ± 3.9	2.9 ± 1.7	-2.4 ± 1.4
ϵ_{Rel} (%)	-3.4 ± 1.0	-1.5 ± 0.5	1.4 ± 0.5	2.3 ± 1.0	8.0 ± 3.3	3.9 ± 1.4	-3.2 ± 1.2
r	0.9997	0.9996	0.9995	0.9995	0.9996	0.9997	0.9993

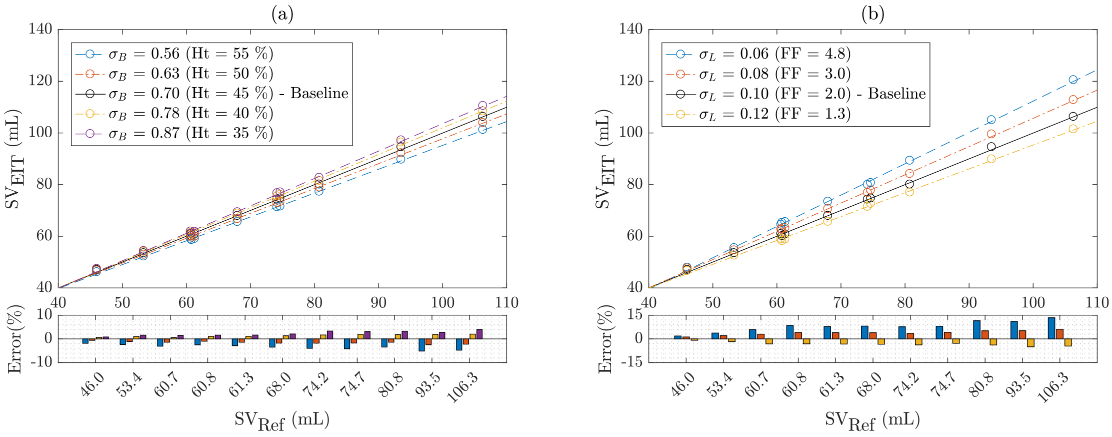

Figure 6.8 – Influence on SV_{EIT} by changes in (a) hematocrit and (b) lung air volume. The relationship of reference SV (SV_{Ref}) and EIT-based SV estimates (SV_{EIT}) is shown in the upper plots. The lower plots depict the relative error between SV_{EIT} and the baseline configuration.

Summary

Among the potential confounding factors investigated for absolute SV measurement, we could show that up- and downwards electrode displacements have the highest influence in terms of relative error, i.e. a shift of 1.8 or 3.5 cm can already introduce a relative error bias of about 15 or 30 %, respectively. These findings call into question the feasibility of absolute SV measurements by means of single plane (2D) EIT without recalibrating upon each displacement or reattachment of the EIT belt. The use of two EIT planes (3D) [66] might help to reduce the sensitivity on belt displacements in the craiocaudal direction, and thus reduce the error on SV estimation in case of belt shifts. However, a subject-specific calibration is still necessary, as the absolute heart impedance signal remains influenced by various other factors (thorax morphology, lung conductivity, etc.), as also shown in experimental findings on pigs [114, 41].

Rotational belt shifts of one electrode spacing (i.e. 2.8 cm) can introduce relative errors with a bias of up to 13 %. This highlights the importance of a correct belt placement and the necessity to have an accurate enough reconstruction model with possibly updating it (in real-time) according to the thorax morphology [147].

Furthermore, changes in lung alveolar tissue conductivity σ_L resulting simply from a respiratory cycle have shown to introduce a high bias in relative error ranging from 8 % to −3 % (from normal inspiration to full expiration). The higher the SV the higher the influence of this effect. This is because – unlike suggested by other researchers [114, 155] – changes in EIT heart impedance are *not* solely related to changes in cardiac blood volume but scaled by a heart-lung-conductivity contrast and other factors (see Figure 6.9 for illustration and detailed explanation). Other factors such as heart displacement due to respiration or postural changes and changes of σ_L due to edema, pneumothorax or posture-induced liquid redistribution were not taken into account but might even worsen the current results.

These findings reveal further challenges of EIT-based SV monitoring and call for more detailed and targeted studies to assess the influences of these different confounding factors to show the extent and the conditions under which EIT-based SV is feasible in clinical scenarios at all.

The current outcomes are in line with the findings in [45, 41]. That is, absolute SV is hard, but trending should be possible. Therefore, we performed a second analysis presented in the next section assessing the trending ability of EIT-based SV.

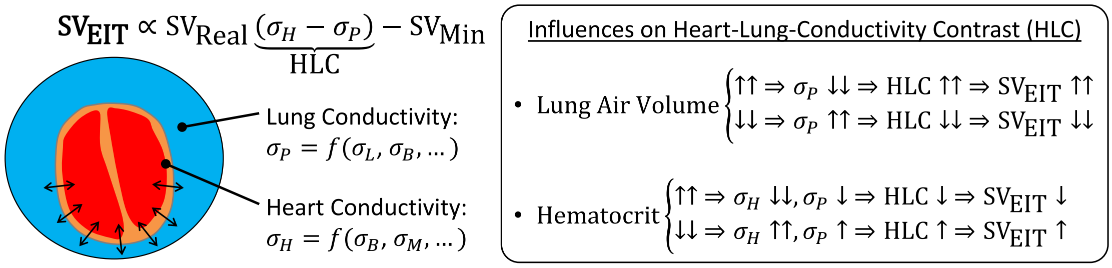
$\mathrm{SV_{EIT}} \propto \mathrm{SV_{Real}} \underbrace{(\sigma_H - \sigma_P)}_{\mathrm{HLC}} - \mathrm{SV_{Min}}$
Lung Conductivity:
$\sigma_P = f(\sigma_L, \sigma_B, \dots)$
Heart Conductivity:
$\sigma_H = f(\sigma_B, \sigma_M, \dots)$
Influences on Heart-Lung-Conductivity Contrast (HLC)
Lung Air Volume
$\uparrow\uparrow \Rightarrow \sigma_P \downarrow\downarrow \Rightarrow \mathrm{HLC} \uparrow\uparrow \Rightarrow \mathrm{SV_{EIT}} \uparrow\uparrow$
$\downarrow\downarrow \Rightarrow \sigma_P \uparrow\uparrow \Rightarrow \mathrm{HLC} \downarrow\downarrow \Rightarrow \mathrm{SV_{EIT}} \downarrow\downarrow$
Hematocrit
$\uparrow\uparrow \Rightarrow \sigma_H \downarrow\downarrow, \sigma_P \downarrow \Rightarrow \mathrm{HLC} \downarrow \Rightarrow \mathrm{SV_{EIT}} \downarrow$
$\downarrow\downarrow \Rightarrow \sigma_H \uparrow\uparrow, \sigma_P \uparrow \Rightarrow \mathrm{HLC} \uparrow \Rightarrow \mathrm{SV_{EIT}} \uparrow$

Figure 6.9 – Conceptual explanation of the heart-lung conductivity contrast (HLC) influencing the EIT-based heart impedance signal used for estimating $\mathrm{SV_{EIT}}$. During a cardiac cycle heart tissue is spatially replaced by lung tissue and vice versa (black arrows). These changes in conductivity are assumed to be the main contributor to the EIT-based heart signal. Unlike sometimes assumed, this signal and thus $\mathrm{SV_{EIT}}$ cannot be directly proportional to the real blood volume change $\mathrm{SV_{Real}}$ as it is (1) scaled with the HLC and (2) limited to an inferior level of detection $\mathrm{SV_{Min}}$ (due to ringing and overlapping of other signal sources like the lungs or atria). HLC is defined as the difference of heart conductivity σ_H (depending on blood conductivity σ_B and myocardial conductivity σ_M) and lung conductivity σ_P (depending on lung alveolar tissue conductivity σ_L and blood conductivity σ_B). An increase in lung air volume leads to an increase in HLC and thus to an augmented $\mathrm{SV_{EIT}}$, and vice versa. On the other hand, increasing hematocrit levels (Ht $\uparrow \Rightarrow \sigma_\mathrm{B} \downarrow$) lead to a decrease in σ_H and a less strong decrease of σ_P. The result is a slight decrease in HLC and a reduced $\mathrm{SV_{EIT}}$. It needs to be stressed out that this remains a simplified explanation as the heart impedance signal can be influenced by further factors such as heart motion [119], out-of-(EIT-)plane motion of the heart, σ_B dependence on blood flow [57], anisotropy of the myocardium, etc. [11].

6.3.3 Analysis II - Relative SV - Trending

In this section we address the question whether trending of SV via EIT is feasible, i.e. can we follow the changes in SV over time after an initial calibration with $\mathrm{SV_0}$. For the subsequent analysis the baseline ($\mathrm{SV_{Ref}} = 68.0\,\mathrm{mL}$) was chosen as calibration value.

Belt Displacement

The trending ability after up/down and left/right belt displacement are shown in Figure 6.10a and Figure 6.10b, respectively, by means of four-quadrant plots with the corresponding errors listed in Table 6.5. All concordance rates CR are at 100 % and thus fulfill the first requirement for trending according to Critchley et al. [38]. The second requirement of an angular error bias of less than 5° is only fulfilled for the 1.8 cm downwards shift and all left/right shifts. However, the angular bias resulting from a 3.5 cm downwards or 1.8 cm upwards shifts are only close above the threshold and might lead to a sufficient enough trending performance, given that the CR and the confidence interval of ϵ_α are well within the acceptable limits.

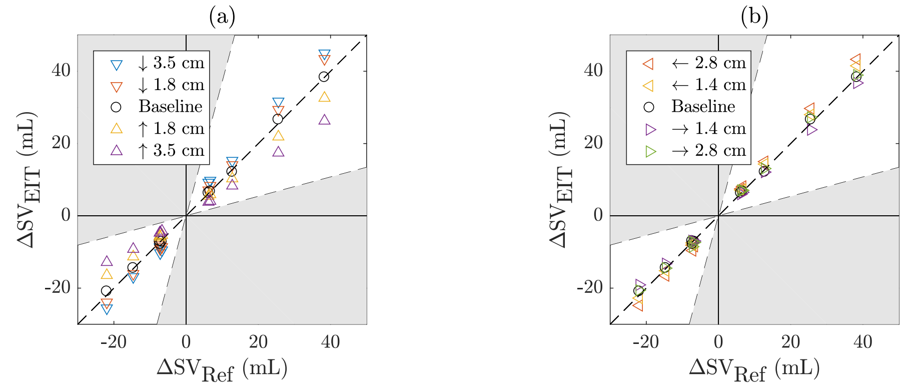

Figure 6.10 – Trending ability of $\Delta\mathrm{SV}_{\mathrm{EIT}}$ vs $\Delta\mathrm{SV}_{\mathrm{Ref}}$ as influenced by (a) up/down and (b) left/-right electrode belt displacements. The gray shaded area depicts the zone in which measurements are considered as unsuitable for trending analysis.

Table 6.5 – Trending performance by means of angular error (ϵ_α) and concordance rate (CR) of $\mathrm{SV}_{\mathrm{EIT}}$ as influenced by electrode belt displacements. Cell shadings indicate whether the acceptance criteria (see Section 6.2.4) are met (green) or not (red).

	Up/Down Displacement				**Left/Right Displacement**			
	↓ 3.5 cm	↓ 1.8 cm	↑ 1.8 cm	↑ 3.5 cm	← 2.8 cm	← 1.4 cm	→ 1.4 cm	→ 2.8 cm
ϵ_α (°)	7.1 ± 3.0	4.3 ± 1.8	−5.7 ± 1.7	−12.5 ± 1.3	4.8 ± 1.7	2.4 ± 1.1	−1.3 ± 1.6	1.3 ± 2.1
CR (%)	100.0	100.0	100.0	100.0	100.0	100.0	100.0	100.0

Changes in Hematocrit and Lung Air Volume

The ϵ_α and CR resulting from changes in hematocrit and lung air volume are shown in Table 6.6 and do all fulfill the requirements for trending as specified in Section 6.2.4.

Summary

These outcomes give hope for EIT-based trending of SV but at the same time reveal the strong influence of up/down belt displacements – especially on the angular bias. Besides, multiple confounding factors could simultaneously deteriorate $\mathrm{SV}_{\mathrm{EIT}}$ (e.g. up and left belt displacement together with lung air volume changes) and thus worsen the current results. To reduce these influences we suggest the use of 3D EIT and an adaptation of the reconstruction model to the

Table 6.6 – Trending performance by means of angular error (ϵ_α) and concordance rate (CR) of SV_{EIT} as influenced by hematocrit and lung air volume changes. Cell shadings indicate whether the acceptance criteria (see Section 6.2.4) are met (green) or not (red).

	Hematocrit Changes				**Lung Air Volume Changes**		
	$\sigma_B = 0.56$ (Ht = 55 %)	$\sigma_B = 0.63$ (Ht = 50 %)	$\sigma_B = 0.78$ (Ht = 40 %)	$\sigma_B = 0.87$ (Ht = 35 %)	$\sigma_L = 0.06$ (FF = 4.8)	$\sigma_L = 0.08$ (FF = 3.0)	$\sigma_L = 0.12$ (FF = 1.3)
ϵ_α (°)	-2.2 ± 1.0	-0.9 ± 1.2	1.4 ± 1.4	2.4 ± 1.7	4.6 ± 1.6	2.2 ± 1.0	-1.6 ± 1.9
CR (%)	100.0	100.0	100.0	100.0	100.0	100.0	100.0

thorax geometry, as alluded to in the previous section.

6.3.4 Limitations and Future Work

The present work is restricted by different limitations of the bioimpedance model (as listed in Section 4.4) such as the lack of respiration-related displacements and deformations. Incorporating those into the model might allow to obtain more detailed insights. Besides, posture-induced heart displacement, lung liquid distribution, pneumothorax or edema should be studied as they could be additional confounding factors for EIT based SV monitoring.

Moreover, it needs to be stressed out that the exact origins of the EIT heart signal remain unclear and that ventricular SV is not the only signal contributor. There are other effects such as heart motion [119], flow-induced reorientation of red blood cells [57], myocardial anisotropy, etc. [11]. If the magnitudes of the other contributors are strong and they do not change proportional to SV, the heart signal will not be a reliable source to estimate SV from.

Even though we have only investigated a part of all possible confounding factors on a model with certain limitations, we believe to have revealed some important challenges for SV via EIT mostly due to belt displacements and the heart-lung-conductivity contrast.

Future clinical studies aiming for SV_{EIT} should concentrate on the use of 3D EIT, constant posture and ventilator settings – if applicable – to avoid most of the confounding factors observed here from occurring, and then – in a next step – investigate the influence of each of the factors individually.

6.4 Conclusion

In this chapter, we focus on the feasibility of EIT-based SV monitoring and the uncertainty introduced into this measurement due to variability in configuration and physiology which occur in experimental and clinical use.

To this end, we investigated the four confounding factors potentially deteriorating SV_{EIT}: (1) electrode belt displacement, (2) electrode detachment, changes in (3) hematocrit and (4) lung air volume. Based on simulations on a 4D bioimpedance model, we could show how seriously each of these factors affect the estimation of relative or absolute SV, as also summarized in Table 6.7.

Although SV_{EIT} has shown to correlate well with the simulated reference SV_{Ref}, the amplitude-based feature to assess SV is highly sensitive to – mostly up/down – belt displacements and to variations in lung air volume. Although these limitations might be partly overcome by using 3D EIT, our results indicate that the absolute measurement of SV via EIT remains extremely challenging. Nonetheless, we can conclude that the trending ability of SV_{EIT} – that is following changes in SV after an initial calibration – remains promising.

Table 6.7 – Findings of the SV analyses performed for the four confounding factors investigated. The results are classified according to the percentage falling within the acceptance criteria: ✓ 100 % (good); ✗ ≥ 75 % (mediocre); ✗✗ < 75 % (bad).

		Absolute SV	**Relative SV - Trending**
		Analysis I	*Analysis II*
1. Belt displacement	up/down	✗✗	✗✗ or ✗[a]
	left/right	✗	✓
2. Electrode detachment		✓	(*not applicable*)
3. Hematocrit changes		✓	✓
4. Lung air volume changes		✗✗	✓

[a] If the acceptance limit for the angular bias is relaxed from < ± 5 % to < ± 10 %.

Part III

Investigating EIT-Based SV Monitoring in Clinical Environments

7 Rationale for Clinical EIT Measurements

In the previous chapters we presented simulations on a bioimpedance model performed to investigate the feasibility and potential limitations of EIT-based SV monitoring. The conclusions are that even under these very controlled conditions, the absolute measurement of SV without a patient-specific calibration is hardly possible. However, using a patient-specific calibration or simply tracking changes of relative SV (i.e. trending) is more promising. Yet, electrode (belt) displacement or lung conductivity changes can impair the EIT-derived SV measurements.

Even though we made an attempt to include clinically-relevant limitations in our simulations, our bioimpedance model does by far not include all of the possible physiological and practical limitations. As the practical applicability is of main interest in the present thesis, in the following chapters, we investigate to what extent the abovementioned findings can be translated into real-world measurements. While other research groups have investigated similar approaches in pig experiments [114, 113, 41], we are primarily interested in the applicability in humans. Therefore, we made use of clinically available EIT devices and performed two clinical trials which are presented in the following two chapters.

In particular, the study in Chapter 8 compares EIT-based SV to thermodilution measurements before and after the induction of anesthesia of patients in the operating room (OR), where large per-patient variations in SV were expected. In Chapter 9 transpulmonary thermodilution is used as reference and SV is measured before and after fluid challenge (i.e. the injection of fluid into the circulation to improve the hemodynamic situation) of patients in the intensive care unit (ICU), where a very controlled measurement environment was expected.

8 Measurements in the Operating Room

8.1 Introduction

In the present study we investigate the feasibility of noninvasively measuring SV in the operating room (OR). Some patients undergoing major operational procedures in the OR are equipped with a right heart catheter to monitor their central hemodynamics. The presence of this catheter allows the measurement of CO – and thus SV – via pulmonary-artery thermodilution [56], the clinical reference method for CO determination (see Section 2.2.1).

In the following, we present a clinical study, where changes in SV before and after the induction of general anesthesia are assessed by means of EIT and compared to pulmonary-artery thermodilution. Based on this data, we test four hypotheses H1 to H4, namely whether EIT can be used to measure (H1) absolute SV with a patient-independent calibration, (H2) absolute SV with a patient-specific calibration, (H3) relative SV with a patient-independent calibration, or (H4) relative SV with a patient-specific calibration.

8.2 Methods

8.2.1 Study Protocol and Data Acquisition

The current study was performed on eleven patients (8 male/3 female, weight: 79.8 ± 18.4 kg, height: 172.0 ± 9.4 cm, BMI: 26.8 ± 5.1 kg/m^2). It was approved by the local ethics committee of the canton of Vaud, Switzerland (CER-VD, 2015-00203) and registered at clinicaltrials.gov (NCT02639468). All participants provided written informed consent. It is worth noting that initially measurements on a total of 30 patients were planned but the study had to be prematurely terminated because of technical issues and too low intra-patient SV variations as further detailed in the discussion in Section 8.3.8.

All measurements were performed in the OR facilities of the University Hospital Lausanne (CHUV, Lausanne, Switzerland). Upon arrival in the OR, the patients were equipped with the

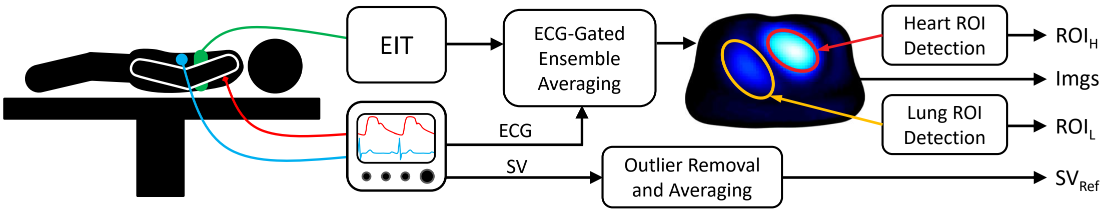

Figure 8.1 – Block diagram of the measurement setup in the OR. For each measurement the EIT images are averaged to one representative cardiac cycle (Imgs) from which heart (ROI$_H$) and lung regions (ROI$_L$) are extracted. These are further used to extract various features for SV estimation. The outlier-free reference measurements are averaged to SV$_{Ref}$.

EIT SensorBelt (Swisstom AG, Landquart, Switzerland) – a textile belt integrating 32 active EIT electrodes [157] – and connected to the BB^2 EIT device (Swisstom AG, Landquart, Switzerland). Hemodynamic data (including ECG, CO, systemic and pulmonary blood pressure) were measured using a MP50/X2 monitor (Philips, Eindhoven, the Netherlands) and recorded via the ixTrend software (ixellence GmbH, Wildau, Germany). This is also illustrated in Figure 8.1.

In total, twelve measurements of CO were performed per patient: six prior and six after induction of general anesthesia. For each of these measurements, three CO reference measurements via thermodilution were acquired and averaged.

8.2.2 Data Analysis

Preprocessing

First, EIT and hemodynamic data were manually aligned in the time domain with the help of deliberate spikes induced via synchronous tapping on EIT and ECG electrodes at the beginning and at the end of each recording. Then, EIT samples were interpolated in the time domain to correct for the sporadic loss of certain EIT frames. Furthermore, a clock drift between the EIT and the hemodynamic signals of around 0.1 s/h was observed and corrected for.

For each of the twelve CO measurements, three thermodilution injections were performed. Each CO reference value CO$_{Ref}$ was then obtained from the average of these three injections. If at least one of the three injections deviated more than 10 % [37] from the average it was excluded and CO$_{Ref}$ recomputed as the average from the remaining injections. If there were two remaining injections, again not deviating more than 10 %, the reference measurement was considered as valid, otherwise it was excluded from analysis. The corresponding SV reference measurements SV$_{Ref}$ were obtained by dividing CO$_{Ref}$ by the instantaneous heart rate obtained from ECG.

As also illustrated in Figure 8.1, EIT data was averaged via ECG-gated ensemble averaging (see Section 3.1.3) to one representative cardiac cycle per measurement. To do so, all data were first high-pass filtered (4th-order Butterworth with $f_c = 0.75 \cdot \mathrm{HR}/60$, with HR as the current heart rate) and aligned to the ECG's R-peaks located in the range from the start of thermodilution injections until 25 s later. EIT raw voltages were reconstructed into sequences of images with 32 × 32 pixels using the GREIT algorithm [6] with the recommended parameters in combination with the 2.5D model of an adult human thorax available in the EIDORS toolbox [5]. Then, for each resulting EIT image sequence, heart and lung regions were determined using the following algorithms: the heart was detected as described in Section 6.2.3 and the lungs via the algorithm proposed by Proença et al. [120, 121].

Feature Extraction

To extensively investigate EIT-based SV monitoring, and not solely testing the initial hypothesis (that the EIT heart amplitude is proportional to SV), a variety of features were extracted from the EIT images (representing one averaged cardiac cycle per measurement). Among others, these include features known from the literature such as the heart amplitude [114, 155], lung amplitude [41, 113], and heart region size [105, 13]. As shown in Table 8.1 the features are categorized in six groups (I) to (VI), which are based on: (I) raw voltage data; (II) the temporal average of absolute EIT images; (III) the temporal signal within the heart, lung or entire image; (IV) the temporal derivative of the signal in the heart or lung; (V) the cardiosynchronous activity image (CAI, see example in Figure 8.1); (VI) geometrical information of the heart or lung. In the following, we list some particular considerations for certain (groups of) features:

- Features 2, 3, and 4 (group II) are based on the temporal average of absolute EIT images. These images were very roughly approximated by reconstructing the EIT raw data against a zero reference (null vector).
- The features of the temporal signals in the lung, heart or entire image region (5 to 10, group III) estimate the amplitude during cardiac systole in different ways. Additionally, features 11 to 14 (group IV) estimate the amplitudes of the corresponding temporal derivatives.
- Features 15 to 24 make use of the cardiosynchronous activity image, that is the pixel-wise standard deviation in the time domain, representing cardiosynchronous activity during one cardiac cycle (see EIT image in Figure 8.1 for an example). Using this image, the heart or lung amplitude (15 to 17 and 18 to 20, group V) or the corresponding centers of gravity (21 to 24) are being calculated.
- All features which limit their analysis to the heart or lung ROI made use of an averaged ROI per subject. To do so, the individual ROIs resulting from the twelve measurements were merged to one single averaged ROI (including all pixels ≥50 % (educated guess) of maximal amplitude in the average). This was used to reduce possible variations in the corresponding features, induced by undesirable changes of the ROIs. Obviously, this does not apply to features 25 and 26, as they represent changes in the size of these ROIs.

Even though some of these features might not have a direct – physiological – relation with changes in SV, they were investigated for the sake of completeness. In a next step, for a more detailed analysis, the number of features was reduced to a set of basic features which are either likely to be linked to SV or assumed to be necessary for normalization of changes in heart-related amplitude. Finally, this basic set was extended by creating various combinations of the features, which lead to the following three sets of features:

(1) *All features* include features 1 to 26.

(2) *Basic features* include only features 1 to 6, 8, 10, 11, 13, 15, 18, 25, and 26.

(3) *Extended features* include the *basic* features and: (a) The reciprocal ($1/x$) of each feature; (b) All previous features (including the reciprocals) multiplied with three "main" features either known from the literature to represent changes in SV (tAmp_H and tStd_H) [114, 155] or expected to be helpful for normalizing non-SV-related changes (AvgC_G); (c) The ratio of all identical heart vs lung features (i.e. $\text{tStd}_\text{H}/\text{tStd}_\text{L}$, $\text{CaiSm}_\text{H}/\text{CaiSm}_\text{L}$, etc.), also expected to be useful for normalization of non-SV-related changes of amplitudes.

The features are stored in a matrix per patient p: $\boldsymbol{F}^p \in \mathbb{R}^{n_f \times n_m}$, with $n_m = 12$ measurements and a total of n_f features depending on the feature set: (1) $n_f = 26$, (2) $n_f = 14$, or (3) $n_f = 102$.

Table 8.1 – List of features extracted from EIT image sequences and used for SV estimation.

Group	ID	Name	Description
I	1	Vtg_G	Sum over temporal average of raw voltages used for image reconstruction
II	2	AvgC_G	Sum over temporal average of absolute EIT images
II	3	AvgC_H	Sum over temporal average of absolute EIT images in heart ROI
II	4	AvgC_L	Sum over temporal average of absolute EIT images in lung ROI
III	5	tAmp_H	Amplitude (max-min) of temporal signal in heart ROI (similar to [114, 155])
III	6	tStd_H	Standard deviation of temporal signal in heart ROI
III	7	tIqr_H	Inter quartile range of temporal signal in heart ROI
III	8	tStd_L	Standard deviation of temporal signal in lung ROI (similar to [41, 113])
III	9	tIqr_L	Inter quartile range of temporal signal in lung ROI
III	10	tStd_G	Standard deviation of overall temporal signal
IV	11	ddtS_H	Standard deviation of temporal derivative of signal in heart ROI
IV	12	ddtI_H	Inter quartile range temporal derivative of signal in heart ROI
IV	13	ddtS_L	Standard deviation of temporal derivative of signal in lung ROI
IV	14	ddtI_L	Inter quartile range temporal derivative of signal in lung ROI
V	15	CaiSm_H	Sum of cardiosynchronous activity image in heart ROI
V	16	CaiMx_H	Maximum of cardiosynchronous activity image in heart ROI
V	17	CaiMd_H	Median of cardiosynchronous activity image in heart ROI
V	18	CaiSm_L	Sum of cardiosynchronous activity image in lung ROI
V	19	CaiMx_L	Maximum of cardiosynchronous activity image in lung ROI
V	20	CaiMd_L	Median of cardiosynchronous activity image in lung ROI
VI	21	CogX_H	Center of gravity (X-coordinate) of cardiosynchronous activity in heart ROI
VI	22	CogY_H	Center of gravity (Y-coordinate) of cardiosynchronous activity in heart ROI
VI	23	CogX_L	Center of gravity (X-coordinate) of cardiosynchronous activity in lung ROI
VI	24	CogY_L	Center of gravity (Y-coordinate) of cardiosynchronous activity in lung ROI
VI	25	szRoi_H	Size (number of pixels) of heart ROI (similar to [105, 13])
VI	26	szRoi_L	Size (number of pixels) of lung ROI

Hypotheses and Hypotheses Testing

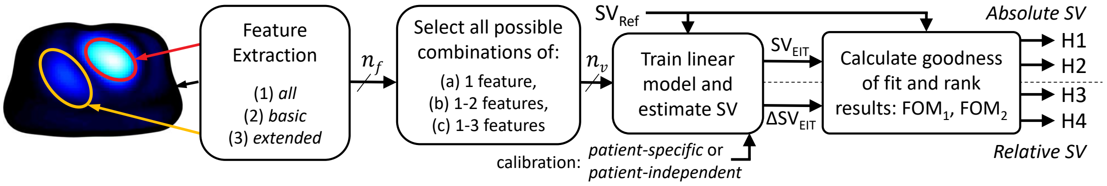

Figure 8.2 – Block diagram of the data analysis and hypotheses testing.

To study the feasibility of SV estimation via EIT, four different hypotheses H1 to H4 were defined and tested as described in this section and also illustrated in Figure 8.2. In particular, we tested whether it is possible to measure absolute SV or relative changes in SV with either a patient-independent calibration (identical for all subjects) or an individual (patient-specific) calibration. Such calibrations are necessary to transform the features (available in arbitrary units) into physiological meaningful SV values expressed in mL.

We hypothesize that the measured changes in SV can be estimated from linear combinations of the extracted features. Based on this hypothesis, the EIT-based SV estimates SV$_{\mathrm{EIT}}$ were obtained from a linear regression model: $f_{\boldsymbol{\kappa}}(\boldsymbol{X}) = \boldsymbol{\kappa}_0 + \sum_{i=1}^{n_v} \boldsymbol{\kappa}_i \boldsymbol{X}_i$, with the vector $\boldsymbol{\kappa}$ containing $n_v + 1$ model coefficients and the matrix $\boldsymbol{X} \in \mathbb{R}^{n_v \times n_n}$ with n_v selected features for n_n measurements. $\boldsymbol{X}$ was assigned with all possible combinations of n_v features available in the aforementioned matrix $\boldsymbol{F}^p \in \mathbb{R}^{n_f \times n_m}$, containing a total of n_f features for n_m measurements per patient p. The model was trained and evaluated against the reference measurements in vector $\boldsymbol{r}^p \in \mathbb{R}^{1 \times n_m}$, containing n_m reference measurements (SV$_{\mathrm{Ref}}$) for each patient p. The training and evaluation of the linear model depends on the hypothesis as described hereafter:

(H1) **Hypothesis 1 – Absolute SV with Patient-Independent Calibration**

We hypothesize that EIT can be used to assess absolute SV (in mL) with one single – patient-independent – calibration.

For this case a leave one out (LOO) calibration was performed. That is, for each patient c an individual model was trained: $\hat{\boldsymbol{\kappa}}^c = \arg\min_{\boldsymbol{\kappa}} \left(\left| \boldsymbol{y} - f_{\boldsymbol{\kappa}}(\boldsymbol{X}) \right|^2 \right)$ (with $\boldsymbol{y}$ and $\boldsymbol{X}$ containing reference values from $\boldsymbol{r}^p$ and n_v selected features from $\boldsymbol{F}^p$, for all patients p except for the current one c). Then, this model was used to obtain SV estimates for the current patient c: $\hat{\boldsymbol{y}}^c = f_{\hat{\boldsymbol{\kappa}}^c}(\boldsymbol{X})$, where $\boldsymbol{X}$ now contains n_v features from the current patient c.

The estimates $\hat{\boldsymbol{y}}^c$ and the corresponding reference measurements $\boldsymbol{r}^c$ of all patients were assigned to SV$_{\mathrm{EIT}}$ and SV$_{\mathrm{Ref}}$, respectively. Then, the goodness of fit between SV$_{\mathrm{EIT}}$ and SV$_{\mathrm{Ref}}$ was evaluated by means of Bland-Altman analysis [12]. The first figure of merit FOM$_1$ is defined as the absolute maximum of the limits of agreement LOA$_{\mathrm{max}}$, and the second FOM$_2$ as the standard deviation of the absolute error ϵ_{Abs} resulting from Bland-Altman analysis. The results were then ranked first by the lowest FOM$_1$ and then by the lowest FOM$_2$, i.e. the fit with lowest FOM$_2$ among all fits having the lowest FOM$_1$ was considered as best.

(H2) **Hypothesis 2 – Absolute SV with Patient-Specific Calibration**
We hypothesize that EIT can be used to assess absolute SV (in mL) with a patient-specific calibration.

This case is very similar to H1, except for the model training. That is, in the first step, the model was trained with $\boldsymbol{X}$ and $\boldsymbol{y}$ from the current patient c and not – as for H1 – from all other patients. The figures of merit are identical to those in H1.

(H3) **Hypothesis 3 – Relative SV (Trending) with Patient-Independent Calibration**
We hypothesize that EIT can be used to assess changes of SV (in %) relative to an initial state and with one single – patient-independent – calibration.

When aiming for trending of SV, we are not interested in the absolute value (in mL) but in the change (in %) relative to an initial baseline value SV_0. To this end, both, the reference vector $\boldsymbol{r}^p$ and feature matrix $\boldsymbol{F}^p$ were expressed relative to their corresponding baseline values as follows. The relative reference vector was defined as $\tilde{\boldsymbol{r}}^p = (\boldsymbol{r}^p - r_0^p)/r_0^p$, where r_0^p is the patient-specific baseline value SV_0[1]. Similarly, each feature in each row of the relative feature matrix $\tilde{\boldsymbol{F}}^p$ was individually set relative to its corresponding baseline value. Then, the model was trained analogously to H1, except that $\boldsymbol{y}$ was assigned with values from $\tilde{\boldsymbol{r}}^p$ and $\boldsymbol{X}$ with values from $\tilde{\boldsymbol{F}}^p$.

The estimates $\hat{\boldsymbol{y}}^c$ and the corresponding reference measurements $\tilde{\boldsymbol{r}}^c$ of all patients were denoted as $\Delta\mathrm{SV}_{\mathrm{EIT}}$ and $\Delta\mathrm{SV}_{\mathrm{Ref}}$, respectively. Then, the goodness of fit between $\Delta\mathrm{SV}_{\mathrm{EIT}}$ and $\Delta\mathrm{SV}_{\mathrm{Ref}}$ was evaluated via trending analysis by means of four-quadrant plots [37, 130], also explained in Section 6.2.4. FOM_1 is defined as the angular concordance rate CR and FOM_2 as the absolute maximum of the limits of agreement $\mathrm{LOA}_{\mathrm{max}}$ of the angular error ϵ_α. The results are then ranked first by the highest FOM_1 and then by the lowest FOM_2, i.e. the fit with lowest FOM_2 among all fits with *highest* FOM_1 is considered as best. Besides, all CR values above the acceptable threshold [38], i.e. between 92 and 100 %, were considered as equal for this ranking. Moreover, the exclusion zone was set to ±10 %.

(H4) **Hypothesis 4 – Relative SV (Trending) with Patient-Specific Calibration**
We hypothesize that EIT can be used to assess changes of SV (in %) relative to an initial state and with a patient-specific calibration.

For H4, the model was trained analogously to H2, except that $\boldsymbol{y}$ assigned with relative reference values from $\tilde{\boldsymbol{r}}^p$ and $\boldsymbol{X}$ with relative features from $\tilde{\boldsymbol{F}}^p$ (as described for H3). The figures of merit are identical to those in H3, with $\mathrm{FOM}_1 = \mathrm{CR}$ and $\mathrm{FOM}_2 = \mathrm{LOA}_{\mathrm{max}}$.

Besides the ranking based on FOM_1 and FOM_2 as described above for each hypothesis individually, a third criterion was introduced. This criterion checks whether all coefficients of the linear model $\boldsymbol{\kappa}^c$ (except for the offset $\boldsymbol{\kappa}_0^c$) have an identical sign, i.e. that $\boldsymbol{\kappa}_1^c$ of all patients c are either all positive or all negative, and so on for $\boldsymbol{\kappa}_2^c, \ldots, \boldsymbol{\kappa}_{n_v}^c$. This assures that the information

---

[1] In the current implementation SV_0 was defined as the average of the three lowest values of $\mathrm{SV}_{\mathrm{Ref}}$.

Table 8.2 – Ranking criteria and acceptance thresholds for the four hypotheses analyzed.

	Hypothesis 1 and 2	**Hypothesis 3 and 4**
1st ranking	All prefer solutions with coefficient $\boldsymbol{\kappa}$ having identical signs	
2nd ranking ($\mathbf{FOM}_1$)	Lowest $\max\left\|\mathrm{LOA}_{\epsilon_{\mathrm{Abs}}}\right\|$	Highest $\min\{\mathrm{CR}, 92\,\%\}$
3rd ranking ($\mathbf{FOM}_2$)	Lowest $\mathrm{std}(\epsilon_{\mathrm{Abs}})$	Lowest $\max\left\|\mathrm{LOA}_{\epsilon_\alpha}\right\|$
Acceptance thresholds	ϵ_{Abs} with LOA $\leq \pm 10\,\mathrm{mL}$	$\mathrm{CR} \geq 92\,\%$ ϵ_α with bias $\leq \pm 5\,\%$ ϵ_α with LOA $\leq \pm 30\,\%$

Note: LOA stands for 95 % limits of agreement and std(·) denotes the standard-deviation operator. The LOA_x are defined as $[\mathrm{mean}(x) - 1.96 \cdot \mathrm{std}(x), \mathrm{mean}(x) + 1.96 \cdot \mathrm{std}(x)]$.

of each feature is considered coherently for all patients, e.g. an increase in heart amplitude tAmp_H leads to an increase in SV_EIT for all patients (coefficients have identical sign) and not to a decrease in some and an increase in the other patients (coefficients have not identical sign). This criterion is stronger than FOM_1 and FOM_2 in that, independently of FOM_1 and FOM_2, solutions with model coefficients having an identical sign for all patients are higher ranked (see also Table 8.2). In doing so more realistic and practical solution are favored over solutions with a – most probably – coincidentally high FOM.

Moreover, in the current analysis, absolute errors ϵ_{Abs} of SV_EIT vs SV_Ref are considered acceptable if their 95 % limits of agreement do not exceed a threshold of ±10 mL (= 15 %[2] of the average SV_Ref). On the other hand, trending via four-quadrant plot analysis of $\Delta\mathrm{SV}_\mathrm{EIT}$ vs $\Delta\mathrm{SV}_\mathrm{Ref}$ is considered acceptable according to the limits defined by Critchley et al. [38], which are CR≥92 % and ϵ_α with a bias ≤ ± 5° and the 95 % limits of agreement not exceeding ±30°. These acceptance thresholds are summarized in Table 8.2. Finally, to test different orders of complexity, a varying number n_v of model coefficients $\boldsymbol{\kappa}$ was used, either: (a) only 1 (b) 1 and 2, and (c) 1, 2 and 3.

In summary, as also illustrated in Figure 8.2, we test the four hypotheses H1 to H4 each for three different orders of model complexity (a) to (c) and three features sets (1) to (3), resulting in nine tests for each hypothesis.

8.3 Results and Discussion

In the following sections we first give a general overview concerning data quality, outliers, dropout rate and show some examples of EIT images. Then, we specifically address the investigations of each of the four hypotheses H1 to H4.

---

[2] This is by assuming that averaging of a PAC thermodilution doublet leads to an error of 15 %, which might be optimistic as it is only slightly above the ±13 % error reported for an averaged triplet [124, 142].

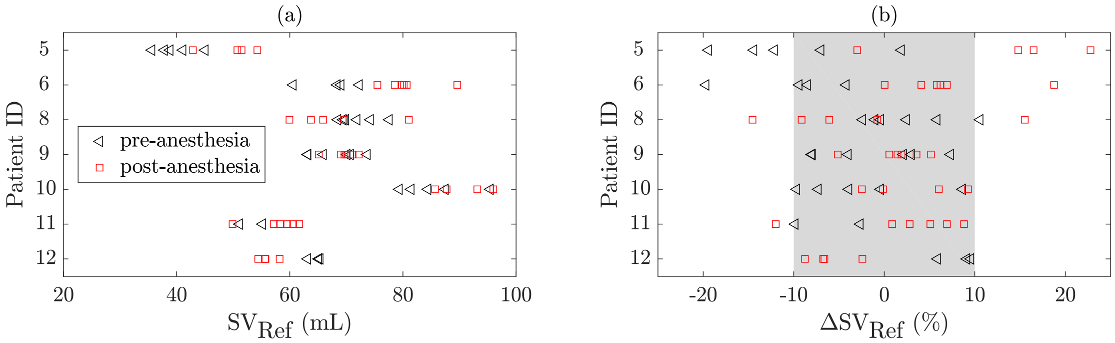

Figure 8.3 – Distribution of SV reference measurements for each patient shown as (a) absolute values SV_{Ref} or (b) variations ΔSV_{Ref} relative to the mean value. The gray shaded area depicts the measurement error to be expected when optimistically assuming that the ±30 % error reported for thermodilution [37] reduces to ±10 % after averaging of three measurements.

Table 8.3 – Overview of patients and the reasons for which some got excluded from the analysis.

Description	Number of Patients	Percentage
Technical issues with SV_{Ref} catheter	1	9 %
Cardiac arythmia	1	9 %
Low cardiac signal	2	18 %
Remaining patients for analysis	7	64 %
Total	11	100 %

8.3.1 General Overview

From the eleven patients enrolled in the study, four had to be excluded from analysis for different reasons; For one, the SV_{Ref} measurements from the right heart catheter were missing; Another had cardiac arrhythmia impairing ECG-gated averaging; Finally, two more patients were excluded as they had very low cardiac signals in the EIT images (see Figure 8.4) most likely due to the EIT belt placed too low/high with respect to the heart. This corresponds to a dropout rate of 4/11 = 36 %, as also listed in Table 8.3.

From the remaining seven patients, all SV reference measurements SV_{Ref} are shown in Figure 8.3. One can observe, in particular in Figure 8.3b, that for most patients the variations in SV_{Ref} are rather low and they barely exceed the ±10 % error expected from thermodilution. Therefore, a limited analysis can be expected due to these low variations in SV_{Ref}.

In Figure 8.5, an example of analysis from one patient is given by means of cardiosynchronous activity images (including heart ROI), the temporal heart signal as well as the overall EIT signal, the heart rate and the reference measurements SV_{Ref}.

In the following sections we analyze each of the four hypotheses in more detail.

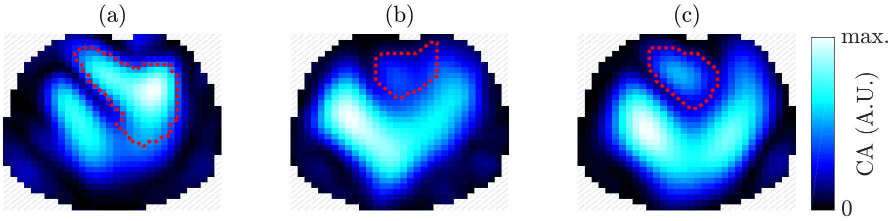

Figure 8.4 – Images of cardiosynchronous activity (CA) for three different patients showing (a) one example with high activity in the heart region (······red), and (b) and (c), two examples with too low activity in the heart region (······red) which had to be excluded from analysis. The ratio of cardiac vs total activity is less than 10 % for (b) and (c) and more than 40 % for (a).

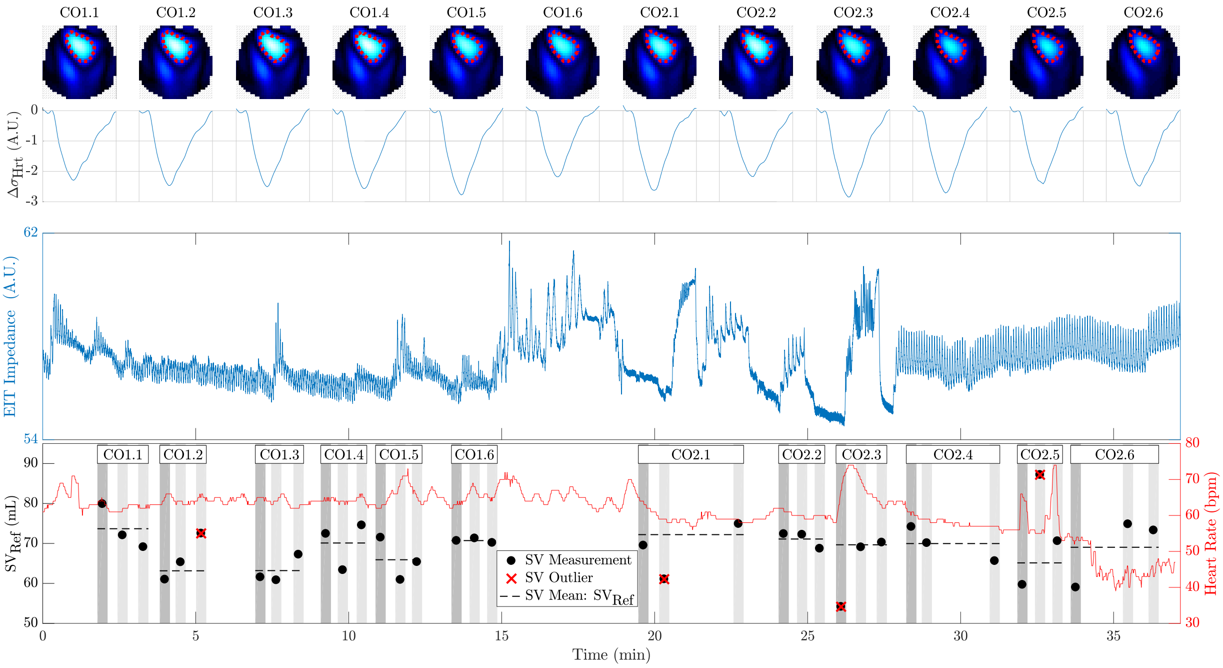

Figure 8.5 – Typical recording example of one patient (P09) showing (Top) cardiosynchronous activity images (see Figure 8.4) with the heart ROI (······red) for all twelve measurements with the corresponding heart signals $\Delta\sigma_{\mathrm{Hrt}}$ below (temporal axis normalized to one cardiac cycle). CO1.1 to CO1.6 denote CO/SV measurements prior to anesthesia and CO2.1 to CO2.6 those after induction of anesthesia. (Middle) The total EIT impedance signal mainly showing respiratory activity starting with spontaneous respiration, followed by some apnea sequences with manual ventilation and ending with mechanical ventilation. (Bottom). Time course of the heart rate (red) and the CO/SV reference measurements. The gray shaded areas indicate the duration of each thermodilution measurement during which the EIT data were averaged and analyzed.

Table 8.4 – Absolute error ϵ_{Abs} between $\mathrm{SV}_{\mathrm{EIT}}$ and $\mathrm{SV}_{\mathrm{Ref}}$ for the best possible fits for H1 (absolute SV with patient-independent calibration) for each feature set (basic, all, extended) and number of features studied.

	Model Complexity – Number of Features		
	1 Feature	1–2 Features	1–3 Features
basic	$\epsilon_{\mathrm{Abs}} = -0.16 \pm 11.12\,\mathrm{mL}$ $(\mathrm{AvgC_G})$	$\epsilon_{\mathrm{Abs}} = -0.16 \pm 11.12\,\mathrm{mL}$ $(\mathrm{AvgC_G})$	$\epsilon_{\mathrm{Abs}} = -0.16 \pm 11.12\,\mathrm{mL}$ $(\mathrm{AvgC_G})$
all	$\epsilon_{\mathrm{Abs}} = -0.16 \pm 11.12\,\mathrm{mL}$ $(\mathrm{AvgC_G})$	$\epsilon_{\mathrm{Abs}} = -0.16 \pm 11.12\,\mathrm{mL}$ $(\mathrm{AvgC_G})$	$\epsilon_{\mathrm{Abs}} = -0.16 \pm 11.12\,\mathrm{mL}$ $(\mathrm{AvgC_G})$
extended	$\epsilon_{\mathrm{Abs}} = -0.16 \pm 11.12\,\mathrm{mL}$ $(\mathrm{AvgC_G})$	$\epsilon_{\mathrm{Abs}} = 0.79 \pm 9.57\,\mathrm{mL}$ $(\mathrm{AvgC_G}/\mathrm{ddtS_H}, 1/\mathrm{ddtS_H})$	$\epsilon_{\mathrm{Abs}} = -0.42 \pm 7.79\,\mathrm{mL}$ $(\mathrm{CaiSm_H} \cdot \mathrm{tAmp_H},$ $\mathrm{tAmp_H}/\mathrm{Vtg_G}, \mathrm{Vtg_G} \cdot \mathrm{AvgC_G})$

Note: The features used to obtain the best possible performance shown, are given in the parentheses below the error. The corresponding figures are available in Figure C.1 in the appendix. All errors with their 95 % limits of agreement exceeding ±10 mL (= 15 % of the average $\mathrm{SV}_{\mathrm{Ref}}$) are shaded in red. The errors ϵ_{Abs} are given as Mean ± Std and the 95 % limits of agreement correspond to $[\mathrm{Mean} - 1.96 \cdot \mathrm{Std}, \mathrm{Mean} + 1.96 \cdot \mathrm{Std}]$.

8.3.2 Hypothesis 1: Absolute SV with Patient-Independent Calibration

Table 8.4 shows the best possible fits (in terms of absolute error ϵ_{Abs}) for the different model complexities and feature sets tested for H1. When using either *all* or the *basic* features, despite the possibility of using up to three features, one single feature remains enough. $\mathrm{AvgC_G}$ turns out to be the most appropriate feature to represent absolute values of $\mathrm{SV}_{\mathrm{Ref}}$. As for the *extended* case, with more complex feature combinations (always including $\mathrm{AvgC_G}$) the error can be further reduced. However, this feature – the global conductivity $\mathrm{AvgC_G}$ – is not likely to represent changes in SV but rather – if at all – an approximative baseline level around which the SV of each particular patient will vary. Thus, using this feature simply “lifts” the estimates $\mathrm{SV}_{\mathrm{EIT}}$ of most patients close to the mean level of $\mathrm{SV}_{\mathrm{Ref}}$ but does not really follow the variations in SV (see also example in Figure 8.6a). Besides, all of the errors exceed the defined limit of acceptance of ±10 mL.

Our analysis suggests that the most appropriate feature would be the global conductivity ($\mathrm{AvgC_G}$), which is highly unlikely to be reliable for SV estimation, since $\mathrm{AvgC_G}$ is known to be influenced by other factors such as the end-expiratory lung volume [78]. Therefore, based on the current data and analysis, we reject hypothesis H1. As also discussed in Chapter 6, it is known that numerous factors such as thorax morphology [41], belt placement or heart position [114] are influencing the estimated features, and do require a patient-specific calibration. Therefore, we investigate in the next section, whether such a calibration can lead to better results.

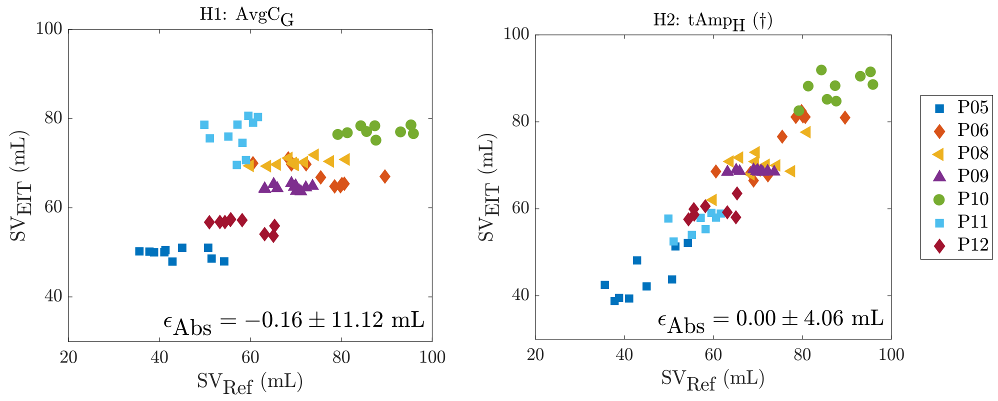

(a) (b)

Figure 8.6 – Examples of estimated SV$_{EIT}$ vs SV$_{Ref}$ showing the best possible goodness of fit for one single feature and the *basic* feature set for (a) H1 or (b) H2. The (†) indicates solutions with model coefficients $\boldsymbol{\kappa}$ *not* having identical sign for all patients.

8.3.3 Hypothesis 2: Absolute SV with Patient-Specific Calibration

Table 8.5 shows the best possible fits (in terms of absolute error ϵ_{Abs}) for the different model complexities and feature sets tested for H2. One can observe that the heart amplitude related feature tAmp$_H$ is present in most of the cases. This is in line with the literature [155, 114]

Table 8.5 – Absolute error ϵ_{Abs} between SV$_{EIT}$ and SV$_{Ref}$ for the best possible fits for H2 (absolute SV with patient-specific calibration) for each feature set (basic, all, extended) and number of features studied.

	Model Complexity – Number of Features		
	1 Feature	1–2 Features	1–3 Features
basic	$\epsilon_{Abs} = 0.00 \pm 4.06$ mL (†) (tAmp$_H$)	$\epsilon_{Abs} = 0.00 \pm 3.38$ mL (†) (tAmp$_H$, AvgC$_H$)	$\epsilon_{Abs} = 0.00 \pm 2.85$ mL (†) (tStd$_G$, tStd$_L$, szRoi$_H$)
all	$\epsilon_{Abs} = 0.00 \pm 4.06$ mL (†) (tAmp$_H$)	$\epsilon_{Abs} = 0.00 \pm 3.37$ mL (†) (tAmp$_H$, CogX$_H$)	$\epsilon_{Abs} = 0.00 \pm 2.71$ mL (†) (tStd$_G$, CaiSm$_L$, CaiMd$_L$)
extended	$\epsilon_{Abs} = 0.00 \pm 4.01$ mL (†) (tAmp$_H \cdot$ CaiSm$_H$)	$\epsilon_{Abs} = 0.00 \pm 3.05$ mL (†) (tAmp$_H \cdot$ szRoi$_L$, ddtS$_H$/ddtS$_L$)	$\epsilon_{Abs} = 0.00 \pm 3.28$ mL (tStd$_H$, tStd$_G$, tStd$_G \cdot$ tStd$_H$)

Note: The features used to obtain the best possible performance shown, are given in the parentheses below the error. The corresponding figures are available in Figure C.2 in the appendix. The (†) indicates solutions with model coefficients $\boldsymbol{\kappa}$ *not* having identical sign for all patients, a criterion defined in Section 8.2.2. None of the errors exceed the defined threshold of ±10 mL (= 15 % of the average SV$_{Ref}$). Solutions are shaded in yellow if the coefficients $\boldsymbol{\kappa}$ do *not* have identical sign (†) and in green if they do. The errors ϵ_{Abs} are given as Mean ± Std and the 95 % limits of agreement correspond to [Mean – 1.96 · Std, Mean + 1.96 · Std].

Table 8.6 – Concordance rate CR and angular error ϵ_α resulting from four-quadrant plot analysis between ΔSV_{EIT} and ΔSV_{Ref} for the best possible fits for H3 (relative SV with patient-independent calibration) for each feature set (basic, all, extended) and number of features studied.

	Model Complexity – Number of Features		
	1 Feature	1–2 Features	1–3 Features
basic	$CR = 90.5\,\%$ $\epsilon_\alpha = -0.1 \pm 23.4°$ $(tStd_H)$	$CR = 92.3\,\%$ $\epsilon_\alpha = -4.7 \pm 21.8°$ $(tStd_H, CaiSm_H)$	$CR = 92.3\,\%$ $\epsilon_\alpha = -4.7 \pm 21.8°$ $(tStd_H, CaiSm_H)$
all	$CR = 90.5\,\%$ $\epsilon_\alpha = -0.1 \pm 23.4°$ $(tStd_H)$	$CR = 97.4\,\%$ $\epsilon_\alpha = -5.2 \pm 18.4°$ $(tStd_H, CaiMd_H)$	$CR = 100.0\,\%$ $\epsilon_\alpha = -6.8 \pm 14.2°$ $(tStd_H, tStd_L, CaiMd_H)$
extended	$CR = 93.0\,\%$ $\epsilon_\alpha = 0.0 \pm 22.6°$ $\left(tAmp_H / ddtS_H\right)$	$CR = 100.0\,\%$ $\epsilon_\alpha = -7.5 \pm 15.6°$ $(tStd_H \cdot CaiSm_H, 1/ddtS_H)$	$CR = 100.0\,\%$ $\epsilon_\alpha = -7.5 \pm 15.6°$ $(tStd_H \cdot CaiSm_H, 1/ddtS_H)$

Note: The features used to obtain the best possible performance shown, are given in the parentheses below the error. The corresponding figures are available in Figure C.3 in the appendix. Performances falling outside the thresholds ($CR \geq 92\,\%$, ϵ_α with bias $< \pm 5°$ and 95 % limits of agreement $< \pm 30°$) are shaded in red. The errors ϵ_α are given as Mean ± Std and the 95 % limits of agreement correspond to $[\text{Mean} - 1.96 \cdot \text{Std}, \text{Mean} + 1.96 \cdot \text{Std}]$.

and our initial hypothesis that the EIT heart amplitude is – among others – modulated by SV. Nevertheless, except for one case shown in Table 8.5, no solution could be found where the model coefficients $\boldsymbol{\kappa}$ have the same sign for all patients. Yet, for the most simple solution shown in Figure 8.6b, except for one patient (P09), all model coefficients have identical sign (results not shown). This particular patient has the lowest variations in SV_{Ref}, which makes it difficult to correctly train the linear model and could explain this outlier. Furthermore, P12 shows lower variations in SV_{EIT} than in SV_{Ref}. But the variations in SV_{Ref} are low and close to the measurement error of the reference device. Therefore, it is not clear whether the low variations in SV_{EIT} are normal (i.e. the physiological SV does not change but SV_{Ref} does due to measurement errors) or whether, for this patient, $tAmp_H$ is not sensitive to changes in SV.

The heart amplitude $tAmp_H$ alone might be a reliable feature for EIT-based SV estimation – given an individual (patient-specific) calibration. However, based on the current data with low variations in SV_{Ref}, it is not possible to show this. Nonetheless, based on the current analysis, hypothesis H2 is confirmed, as a complex combination of three features ($tStd_H$, $tStd_G$, and $tStd_G \cdot tStd_H$) leads to an acceptable performance with calibration coefficients of same sign.

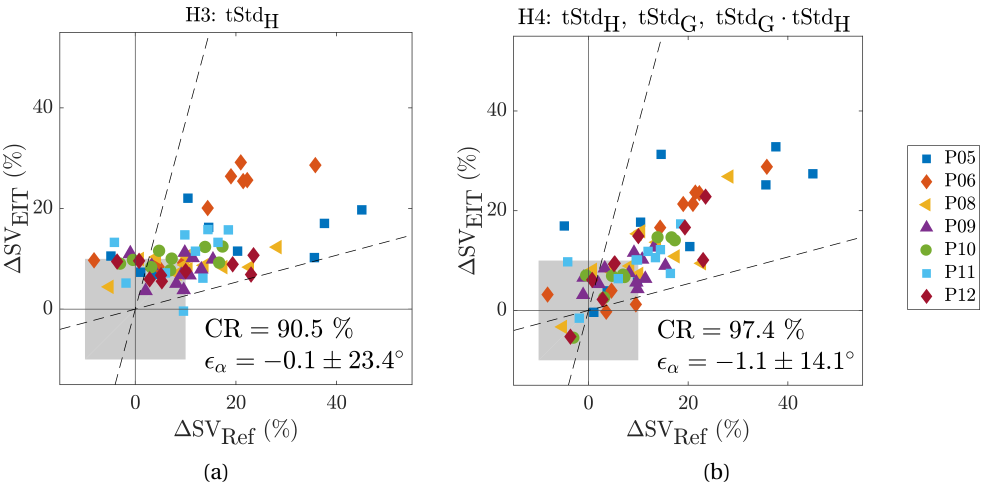

(a)

(b)

Figure 8.7 – Examples of estimated ΔSV_{EIT} vs ΔSV_{Ref} by means of four-quadrant plots showing the best possible goodness of fit for (a) one single feature of the *basic* feature set for H3 and (b) for three features of the *extended* feature set for H4.

8.3.4 Hypothesis 3: Relative SV with Patient-Independent Calibration

Table 8.6 shows the best possible fits (in terms of concordance rate CR and angular error ϵ_α) for the different model complexities and feature sets tested for H3. Similar to the previous hypothesis (H2), also for H3, features related to the heart amplitude, $tAmp_H$ or $tStd_H$, lead to the best possible results. None of the solutions have an angular error ϵ_α within the limits of acceptance. When only considering the concordance rate (as also done in recent pig experiments [41]), already the most basic solution using solely $tStd_H$ (also shown in Figure 8.7a) leads to an angular concordance rate CR close to the threshold of acceptance (CR ≥ 92 %). However, it needs to be highlighted that for certain patients (e.g. P09 or P10), the variations in ΔSV_{Ref} are much stronger than the corresponding variations in ΔSV_{EIT}. But again, due to the low variations in SV_{Ref}, it is difficult to conclude whether the lack of variation in ΔSV_{EIT} for these particular patients is because of measurement errors in ΔSV_{Ref} or ΔSV_{EIT} (but hypothesis H3 still holds) or the heart amplitude $tStd_H$ not being sensitive to changes in SV for these patients (hypothesis H3 does not hold).

When only considering the concordance rate CR, already the feature $tStd_H$ alone might be sufficient for the relative measurement of SV via EIT with a patient-independent calibration. But again, the variations in SV_{Ref} are too low to confirm this. However, as all errors ϵ_α are above the threshold of acceptance, we reject hypothesis H3 for the current data and analysis.

8.3.5 Hypothesis 4: Relative SV with Patient-Specific Calibration

Table 8.7 shows the best possible fits (in terms of concordance rate CR and angular error ϵ_α) for the different model complexities and feature sets tested for H4. While five out of the nine

Table 8.7 – Concordance rate CR and angular error ϵ_α resulting from four-quadrant plot analysis between $\Delta\text{SV}_\text{EIT}$ and $\Delta\text{SV}_\text{Ref}$ for the best possible fits for H4 (relative SV with patient-specific calibration) for each feature set (basic, all, extended) and number of features studied.

	Model Complexity – Number of Features		
	1 Feature	1–2 Features	1–3 Features
basic	CR = 93.0 % (†) $\epsilon_\alpha = -2.7 \pm 22.1°$ (CaiSm_L)	CR = 100.0 % (†) $\epsilon_\alpha = -6.8 \pm 12.3°$ $\left(\text{CaiSm}_\text{L}, \text{Vtg}_\text{G}\right)$	CR = 100.0 % (†) $\epsilon_\alpha = -2.5 \pm 9.0°$ $\left(\text{tAmp}_\text{H}, \text{tStd}_\text{L}, \text{tStd}_\text{G}\right)$
all	CR = 93.0 % (†) $\epsilon_\alpha = -2.7 \pm 22.1°$ (CaiSm_L)	CR = 100.0 % (†) $\epsilon_\alpha = -2.8 \pm 12.2°$ $(\text{CaiMx}_\text{L}, \text{CaiMd}_\text{L})$	CR = 100.0 % (†) $\epsilon_\alpha = -2.0 \pm 7.8°$ $\left(\text{tAmp}_\text{H}, \text{AvgC}_\text{H}, \text{CogX}_\text{H}\right)$
extended	CR = 97.3 % (†) $\epsilon_\alpha = -5.2 \pm 13.9°$ $\left(\text{tAmp}_\text{H}/\text{ddtS}_\text{H}\right)$	CR = 100.0 % (†) $\epsilon_\alpha = -2.9 \pm 9.8°$ $\big(\text{tAmp}_\text{H} \cdot \text{CaiSm}_\text{H},$ $\text{tAmp}_\text{H} \cdot \text{CaiSm}_\text{L}\big)$	CR = 97.4 % $\epsilon_\alpha = -1.1 \pm 14.1°$ $(\text{tStd}_\text{H}, \text{tStd}_\text{G},$ $\text{tStd}_\text{G} \cdot \text{tStd}_\text{H})$

Note: The features used to obtain the best possible performance shown, are given in the parentheses below the error. The corresponding figures are available in Figure C.4 in the appendix. Performances falling outside the thresholds (CR ≥ 92 %, ϵ_α with bias < ±5° and 95 % limits of agreement < ±30°) are shaded in red. The (†) indicates solutions with model coefficients $\boldsymbol{\kappa}$ *not* having identical sign for all patients, a criterion defined in Section 8.2.2. Solutions with errors within the acceptable thresholds are shaded in yellow if the model coefficients $\boldsymbol{\kappa}$ do *not* have identical sign (†) and in green if they do. The errors ϵ_α are given as Mean ± Std and the 95 % limits of agreement correspond to $[\text{Mean} - 1.96 \cdot \text{Std}, \text{Mean} + 1.96 \cdot \text{Std}]$.

solutions show a trending performance within the acceptance criteria, only one solution has model coefficients $\boldsymbol{\kappa}$ with the same sign for all patients. Yet, it is questionable whether this particular case (shown in Figure 8.7b) and making use of a complex combination of three features (tStd_H, tStd_G, and $\text{tStd}_\text{G} \cdot \text{tStd}_\text{H}$), is not simply coincidentally leading to reasonable results on the current data (overfitting). Besides, when investigating the single feature tStd_H (among the best features for H3 but not for H4), its performance (CR = 88.4 %, $\epsilon_\alpha = 1.4 \pm 23.7°$) is lower when compared to H3 shown in Figure 8.7a, i.e. lower CR and higher ϵ_α. This slight decrease in performance when going from (H3) subject-independent to (H4) subject-specific calibration, shows the difficulty to obtain a reasonable individual calibration for patients with low variations in SV_Ref.

The observations on H4 are also impaired by the issue of too low variations in SV_Ref and only one complex combination of three features (tStd_H, tStd_G, and $\text{tStd}_\text{G} \cdot \text{tStd}_\text{H}$) leads to acceptable performances but remains questionable due to possible overfitting. Therefore, based on the current data and analysis hypothesis H4 is confirmed.

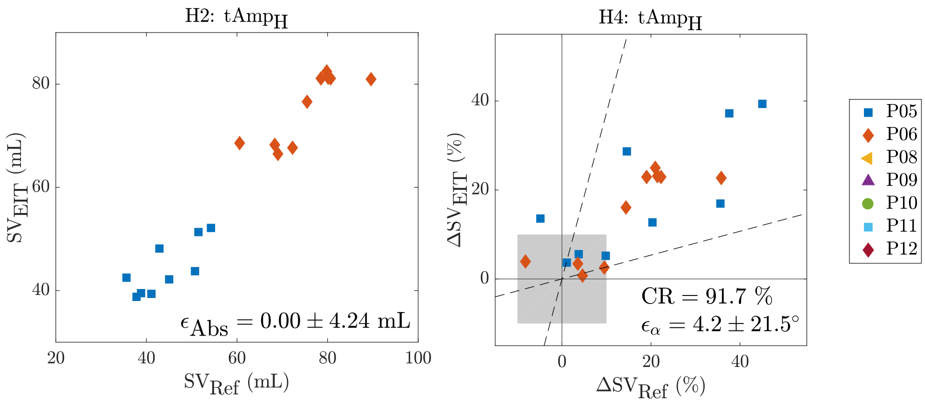

(a)

(b)

Figure 8.8 – Performance from analysis limited to the two patients with highest variations in SV_{Ref} using the systolic heart amplitude $tAmp_H$ for (a) of SV_{EIT} vs SV_{Ref} for H2 (absolute SV with patient-specific calibration), and (b) of ΔSV_{EIT} vs ΔSV_{Ref} for H4 (relative SV with patient-specific calibration).

8.3.6 Analysis Restricted to Patients with High Variations in SV_{Ref}

It has been observed that for most patients the variations in SV_{Ref} are low which can impair the model fitting and lead to the unrealistic calibration coefficients. When restricting the analysis to solely the two patients with highest variations in SV_{Ref} (P05 and P06) and using the heart amplitude $tAmp_H$ as a feature, it can be shown that H2 is feasible (Figure 8.8a) but the performance of H4 still falls narrowly[3] outside the acceptance criteria (Figure 8.8b). Nevertheless, these results are based on a fraction of all measurements (19 out of more than 100) and are too few to draw any conclusions.

8.3.7 Limitations, Challenges and Future Work

The biggest limitation of the present study is that the SV reference measurements SV_{Ref} of each patient are varying too little in between different measurements. The induction of anesthesia does have a less strong effect on the SV than expected during the planning of the study.

The current analysis is further limited in that the EIT images were reconstructed using a single – patient-unspecific – reconstruction model. Nonetheless, using the image data directly reconstructed by the EIT device (which uses proprietary patient models adapted to height, weight and gender of the patient) did not lead to any improvements (results not shown).

To avoid a too low cardiac signal, the EIT belt should be placed at the height where most ventricular activity is present. Given that sufficient time is available for preparation, this could be determined in advance via echocardiography or by means of EIT in an iterative procedure.

---

[3] This is mainly caused by one outlier measurement from P05 located in the 2nd quadrant. When calculating ϵ_α via the median and the inter-quartile range (IQR) we obtain an acceptable error of $\epsilon_\alpha = 1.5 \pm 13.4°$ (median ± IQR).

Another issue resides in performing EIT measurements in the OR which has shown to be challenging due to: high electromagnetic noise from a variety of other devices, undesired touching or moving of the patient during a measurement, time pressure, etc. At least the latter two could probably be avoided when performing measurements in a different environment such as the intensive care unit for example.

8.3.8 Rationale for the Premature Termination of This Study

As mentioned in Section 8.2.1, 30 patients were initially planned to be enrolled in the present study. However, after a total of 11 patients[4] the study was prematurely terminated for the following reasons. As mentioned before, for most of the patients the variations in SV_{Ref} are too low, i.e. only three patients have at least one measurement above and one below the 10 % error specified for SV_{Ref} (see Figure 8.3). Extrapolating this ratio (only data of 3 out of 11 patients, i.e. 27 %, is exploitable) to the initially planned requirement of at least 13 patients with high enough variations in SV_{Ref} meant that at least 48 patients would have needed to be measured. However, this was not feasible for various reasons (including limitations in time and other resources) which lead to the decision of prematurely terminating the present study.

8.4 Conclusion

In view of noninvasively measuring SV via EIT, we performed a study on patients in the OR. For each patient, up to twelve SV estimates obtained from ECG-gated EIT images were compared to SV reference measurements from right heart thermodilution. With the aim of achieving high variations in SV, measurements were performed before and after induction of anesthesia. A variety of SV-related features were extracted from the EIT images and all possible combinations of up to three features were used to train a linear model in an exploratory fashion.

From the eleven patients enrolled in this study four had to be excluded from analysis due to: (a) technical issues with the SV catheter; (b) cardiac arrhythmia which impair the averaging method (ECG-gating) used for EIT; (c) too low cardiac signals caused by a too high/low placement of the EIT belt. This corresponds to a dropout rate of 36 %.

In the remaining seven patients we tested the four different hypotheses H1 to H4, i.e. whether EIT can be used to measure (H1) absolute SV with a patient-independent calibration, (H2) absolute SV with a patient-specific calibration, (H3) relative SV with a patient-independent calibration, or (H4) relative SV with a patient-specific calibration. The current findings disprove H1 and H3, and corroborate H2 and H4. That is, both absolute and relative SV are only possible via a patient-specific calibration. However, these results (of H2 and H4) are either based on complex combinations of features likely to be coincidentally leading to reasonable results (model overfitting) or have unrealistic calibration coefficients (not having the same sign for all patients and thus not coherently exploiting the information of each feature). Moreover, it has been observed that for most patients the variations in SV_{Ref} are low which can impair the model fitting and lead to the aforementioned unrealistic calibration coefficients. In the literature, neither patient-independent nor patient-specific calibration functions are available. Therefore, a high number of measurements and large variations in SV are required for every single patient in order to properly validate these hypotheses.

---

[4] Strictly speaking thirteen patients were measured in total. The eleven patients mentioned in Section 8.2.1 already exclude the first two patients with unusable data which were measured with an old EIT device being very sensitive to electromagnetic noise in the OR.

In future studies, a different protocol leading to higher SV variations – for every single patient – should be designed. Besides, in view of reducing the high dropout rate, performing measurements in a less challenging environment than the OR would be of advantage. And, to improve the signal strength in the heart region, the EIT belt should be placed based on echocardiography measurements or 3D EIT should be applied.

9 Measurements in the Intensive Care Unit

9.1 Introduction

In this chapter we present a clinical study aiming at the noninvasive assessment of changes in SV via EIT in intensive care unit (ICU) patients. It is common practice in ICUs to administer a certain amount of fluid, to improve the hemodynamic situation of those patients which are expected to be *fluid responsive*. This is because an increase in blood volume will lead to an increased venous return and thus right heart preload, which in turn results in an increased SV via the Frank-Starling mechanism (see Section 2.1.2).

In the present study, EIT measurements were performed before and after this so-called fluid challenge. These are compared to SV measurements obtained via transpulmonary thermodilution which were performed in parallel to EIT. We then test whether EIT can be used to track relative SV changes induced by this fluid challenge or – in other words – whether EIT can assess if a particular patient is responsive to an administration of fluid. In contrast to the previous study, solely the feasibility of tracking SV via a subject-independent calibration is tested since only three measurements are available per patient.

In particular we test the two hypotheses that the amplitude of the temporal signal in either (a) the heart or (b) the lung region can be used to assess changes in SV by means of EIT. As detailed in Section 3.2, the first hypothesis has initially been proposed by Vonk Noordegraaf et al. [155] and was also tested in pig experiments by Pikkemaat et al. [114, 113] with mixed outcomes. He further tested the second hypothesis which – depending on the type of experiment – led to either a superior or inferior performance [113], when compared to the first hypothesis[1]. On the contrary, in a recent publication, da Silva Ramos et al. [41] successfully showed the ability of EIT to trend relative changes in SV via the EIT-derived lung amplitude when measured in pigs. Given these partly contradictory findings from animal experiments, we test both (a) the heart and (b) lung amplitude for their applicability to assess SV changes in ICU patients.

---

[1] This has not been reported in the corresponding publication [114] but in his thesis [113] which is only available in German. As summarized in Section 3.2, the lung amplitude correlates better with SV than the heart amplitude for PEEP experiments but the opposite applies for Dobutamine experiments.

9.2 Methods

9.2.1 Study Protocol and Data Acquisition

The current study was performed on twenty patients. However, as for the first four patients no ECG signal was recorded, only the last sixteen patients (12 male/4 female, weight: 80 ± 11 kg, height: 176 ± 7 cm, BMI: 26 ± 3 kg/m^2) were considered for analysis. The study was approved by the local ethics committee of Christan-Albrechts University Kiel, Germany (EC-Study-ID D486/16) and registered at clinicaltrials.gov (NCT02992002). Due to the purely observational nature of the study, a waiver of informed consent was granted by the ethics committee. The study included ventilated patients in the ICU with the need of fluid administration and both EIT and extended hemodynamic monitoring. In return, the following criteria lead to the exclusion of patients: an age below 18 years, BMI >35 kg/m^2, open lung injuries, instable injuries of spine or skull, metallic implants in the thorax region (e.g. pacemaker).

All measurements were performed in the ICU facilities of the University Medical Center Schleswig-Holstein (UKSH, Kiel, Germany). The patients were equipped with a 16 electrode EIT belt placed around their chest at the level of the 4th to 5th intercostal space and connected to the PulmoVista™ 500 EIT device (Dräger Medical, Lübeck, Germany). Hemodynamic data (including ECG and systemic blood pressure) were measured using a Datex-Ohmeda hemodynamic monitor (S/5, Datex-Ohmeda, Helsinki, Finland) and recorded via the S/5 Collect software (Datex-Ohmeda, Helsinki, Finland). SV reference measurements were obtained by averaging three transpulmonary thermodilutions performed with the PiCCO plus device (Pulsion, Munich, Germany). This measurement setup is also illustrated in Figure 9.1.

For each patient three SV reference measurements (M1 to M3) were performed during the following protocol: (M1) 30 minutes after application of the EIT belt and prior to the fluid challenge via the injection of 500 mL of balanced electrolyte solution (Sterofundin ISO, B. Braun, Melsungen, Germany); (M2) right after the fluid challenge; (M3) 30 minutes after (M2). For those patients being *fluid responsive*, an increase in SV is expected from (M1) to (M2). Moreover, if all of the injected liquid remains in the circulation, SVs of (M3) and (M2) are expected to be comparable.

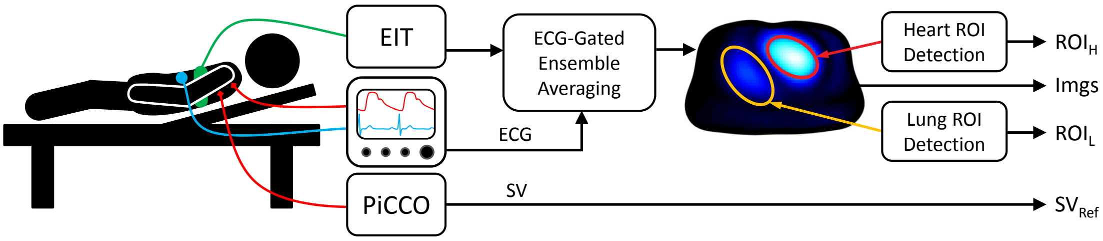

Figure 9.1 – Block diagram of the measurement setup in the ICU. For each SV measurement the EIT images are averaged to one representative cardiac cycle (Imgs) from which heart (ROI_H) and lung regions (ROI_L) are extracted. The amplitudes of the temporal signals in these two regions are further compared to the SV reference measurement SV_{Ref}.

9.2.2 Data Preprocessing

First, EIT and hemodynamic data were manually aligned in the time domain with the help of deliberate spikes induced via synchronous tapping on EIT and ECG electrodes at the beginning and at the end of each recording. Then, EIT samples were interpolated in the time domain to correct for the sporadic loss of certain EIT frames. Furthermore, a clock drift between EIT and hemodynamic signals was corrected for.

As also illustrated in Figure 9.1, EIT data was averaged via ECG-gated ensemble averaging (see Section 3.1.3) to one representative cardiac cycle per measurement (M1 to M3). To do so, all data were first high-pass filtered (4^{th}-order Butterworth with $f_c = 0.75 \cdot \text{HR}/60$, with HR as the current heart rate) and aligned to all ECG's R-peaks located in the 2 minute window centered around the mean time of injection of the PiCCO thermodilution triplets. EIT raw voltages were reconstructed into sequences of images with 32×32 pixels using the GREIT algorithm [6] with the recommended parameters in combination with the 2.5D model of an adult human thorax available in the EIDORS toolbox [5]. Then, for each resulting EIT image sequence, heart and lung regions were determined using the following algorithms: the heart was detected as described in Section 6.2.3 and the lungs via the algorithm proposed by Proença et al. [120, 121].

9.2.3 Signal Processing and Data Analysis

In contrast to the previous study presented in Chapter 8, here only three measurements are available per patient. Moreover, absolute SV via a single calibration has shown to be difficult (see Sections 6.3.2 and 8.3.2). Therefore, the analysis was restricted to solely investigate the trending of relative SV changes via a subject-independent calibration.

As mentioned in the introduction, we tested the two hypotheses: whether SV can be assessed by means of EIT via the signal amplitude in either (a) the heart [155, 114, 113] or (b) the lung region [113, 41]. To do so, in each region, the amplitude was estimated in two different ways for each of the averaged EIT image sequences (Imgs) and four features ($\Delta\sigma_{\text{H}}$, $\Delta\sigma_{\text{L}}$, tStd_{H} and tStd_{L}) were computed as defined hereafter. First, the systolic heart ($\Delta\sigma_{\text{H}}$) or lung amplitude ($\Delta\sigma_{\text{L}}$) were determined via the minimum and maximum of the temporal signal in the corresponding region. Second, the temporal standard deviation of the heart (tStd_{H}) or lung signal (tStd_{L}) were calculated over the entire cardiac cycle (systole and diastole) and are expected to be more robust amplitude estimates. To allow for a fair comparison between the three measurements of each patient (M1 to M3), the abovementioned amplitudes were calculated from the same averaged heart and lung regions, denoted as $\overline{\text{ROI}}_{\text{H}}$ and $\overline{\text{ROI}}_{\text{L}}$, respectively. The averaged ROIs contain all pixels which are present in at least two out of the three individual ROIs, e.g. $\overline{\text{ROI}}_{\text{H}} = (\text{ROI}_{\text{H}}^{\text{M1}} + \text{ROI}_{\text{H}}^{\text{M2}} + \text{ROI}_{\text{H}}^{\text{M3}}) \geq 2$.

In a first step, the trending ability was tested for the total of 48 measurements (16 patients with 3 measurements each). To this end, each of the four amplitude features was transformed into relative changes between the current measurement c and a baseline b: $\Delta\text{SV}_{\text{EIT}}^{b \to c} = (x^c - x^b)/x^b$, where x represents the feature under test ($\Delta\sigma_\mathrm{H}$, $\Delta\sigma_\mathrm{L}$, tStd_H, or tStd_L). The reference measurements SV_Ref were transformed similarly and denoted as $\Delta\mathrm{SV}_\mathrm{Ref}$. As further justified in the results and discussion section, for each patient, the relative changes of the two transitions M1 to M2 and M2 to M3 were tested, i.e. $\Delta\mathrm{SV}_\mathrm{Ref}^{\mathrm{M1}\to\mathrm{M2}}$ vs $\Delta\mathrm{SV}_\mathrm{EIT}^{\mathrm{M1}\to\mathrm{M2}}$ and $\Delta\mathrm{SV}_\mathrm{Ref}^{\mathrm{M2}\to\mathrm{M3}}$ vs $\Delta\mathrm{SV}_\mathrm{EIT}^{\mathrm{M2}\to\mathrm{M3}}$ were compared by means of four-quadrant plot analysis [37, 130], also explained in Section 6.2.4. For the various reasons detailed by Saugel et al. [130], the four-quadrant plot was preferred over the polar plot. The resulting trending performance was evaluated by means of the angular error ϵ_α (angular deviation of each data point ($\Delta\mathrm{SV}_\mathrm{Ref}$,$\Delta\mathrm{SV}_\mathrm{EIT}$) with respect to the identity line) and the angular concordance rate CR (percentage of measurements with ϵ_α not exceeding ±30°). According to the criteria defined by Critchley [37, 38], trending performance is considered as acceptable if ϵ_α has a bias $< \pm 5°$, its 95 % limits of agreement do not exceed ±30° and CR is ≥92 %[2].

In a second step, the analysis was restricted to solely those measurements with consistent heart and lung ROI and with low noise in the corresponding region. To do so, two types of quality indices were introduced and used to reject outliers. First, the similarity measures J_H and J_L compare the agreement of the current heart or lung ROI with the averaged ROI via the so-called *Jaccard index* [84], e.g. $J_H = |\mathrm{ROI_H} \cap \overline{\mathrm{ROI}}_\mathrm{H}| / |\mathrm{ROI_H} \cup \overline{\mathrm{ROI}}_\mathrm{H}|$. Second, the signal quality indicators N_H and N_L estimate the average relative noise level in the heart and lung regions from the relative deviation of each pulse used for ensemble averaging as explained in Appendix B. Finally, all heart amplitude measurements ($\Delta\sigma_\mathrm{H}$ and tStd_H) were excluded as outliers if the corresponding $J_H < 75\%$ or $N_H > 0.484$. Lung amplitudes measurements ($\Delta\sigma_\mathrm{L}$ and tStd_L) were considered as outliers if the corresponding $J_L < 75\%$ or $N_L > 0.750$. The thresholds of N_H and N_L were set such that at least 25 % of the "worst" measurements, i.e. those with highest noise level, got excluded from analysis.

9.3 Results and Discussion

9.3.1 Hemodynamic Variations

The average changes in reference SV between the three measurements (M1, M2 and M3) are as follows: the fluid challenge generally leads to an increase of SV (M2 vs M1: $\Delta\mathrm{SV}_\mathrm{Ref}^{\mathrm{M1}\to\mathrm{M2}} = 9.2\,\%$) while 30 minutes after SV returns to its baseline level (M3 vs M1: $\Delta\mathrm{SV}_\mathrm{Ref}^{\mathrm{M1}\to\mathrm{M3}} = -0.3\,\%$). These changes are shown in Figure 9.2 for each patient individually. As mentioned in the introduction, a fluid challenge is leading to an increased SV in patients which are fluid responsive. The subsequent return of SV to baseline can be explained by the type of fluid used for injection. It is known that a few minutes after fluid challenge with crystalloids, only roughly 25 % of the injected volume remain in the circulation [63], explaining the return of SV to its baseline level. Moreover, the changes in $\Delta\mathrm{SV}_\mathrm{Ref}$ are generally low and rarely exceed the ±13 % error marked

---

[2] It needs to be mentioned that the angular concordance rate used in the present analysis is more conservative than the "traditional" concordance rate (assessing the ratio of "good" vs "bad" measurements located in the 1st and 3rd vs 2nd and 4th quadrant) and based on which the ≥92 % acceptance limit was defined [37, 38].

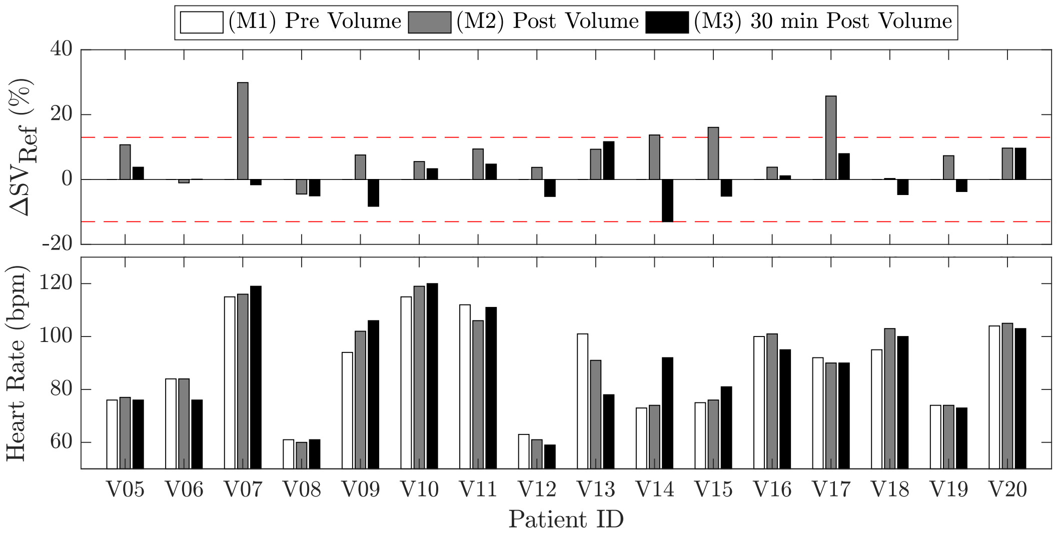

Figure 9.2 – Hemodynamic variations for the three measurements (M1 to M3) of each patient showing (Top) the changes of SV reference measurements $\mathrm{SV}_{\mathrm{Ref}}$ relative to M1 and (Bottom) the corresponding heart rates. The dashed red lines in the upper graph show the ±13 % error to be expected from averaging a triplet of thermodilution measurements [124, 142].

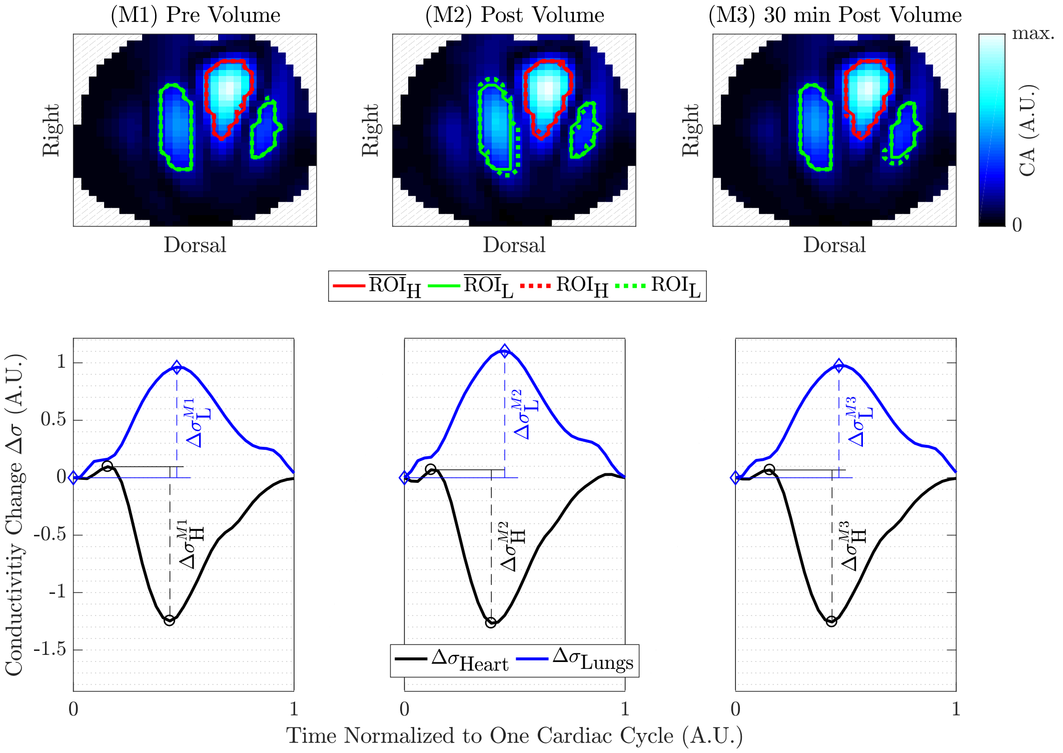
(M1) Pre Volume
(M2) Post Volume
(M3) 30 min Post Volume
Right
Dorsal
max.
CA (A.U.)
0
ROI_H
ROI_L
ROI_H
ROI_L
Conductivitiy Change Δσ (A.U.)
1
0.5
0
-0.5
-1
-1.5
Δσ_L^M1
Δσ_H^M1
Δσ_L^M2
Δσ_H^M2
Δσ_L^M3
Δσ_H^M3
Δσ_Heart
Δσ_Lungs
0
1
Time Normalized to One Cardiac Cycle (A.U.)

Figure 9.3 – EIT analysis example for patient V17. (Top) images of cardiosynchronous activity (CA) for the three measurements M1 to M3 with the averaged (——) and individual (······) ROIs. (Bottom) the corresponding temporal signals of conductivity change in the heart (black) and lung (blue) regions with the minima and maxima used to estimate the amplitudes $\Delta\sigma_{\mathrm{H}}$ and $\Delta\sigma_{\mathrm{L}}$.

by the dashed red lines in Figure 9.2 and expected from averaged thermodilution triplets according to [124, 142]. On average, the changes are highest from M1 to M2 ($\Delta\mathrm{SV}_{\mathrm{Ref}}^{\mathrm{M1}\rightarrow\mathrm{M2}} = 9.2\,\%$) and lowest from M2 to M3 ($\Delta\mathrm{SV}_{\mathrm{Ref}}^{\mathrm{M2}\rightarrow\mathrm{M3}} = -9.5\,\%$). This justifies the choice of analyzing the trending ability from M1 to M2 and from M2 to M3, in order to get the most possible measurements not falling within the error range of the reference device.

9.3.2 EIT Data Analysis

Figure 9.3 shows an example of analysis by means of cardiosynchronous EIT images with delineated heart and lung regions together with the corresponding temporal signals and the estimated amplitudes ($\Delta\sigma_{\mathrm{H}}$ and $\Delta\sigma_{\mathrm{L}}$). Equivalent figures for the remaining patients are available in Appendix D in Figures D.1 to D.15. Based on these figures the ROI detection and amplitude estimation was verified visually.

9.3.3 SV Trending Performance of EIT

The trending performance for all measurements and the four EIT-based amplitude features is shown in Figure 9.4 by means of four-quadrant plot analysis. One can observe that for the heart-related amplitudes shown in Figures 9.4a and 9.4b at least three measurements fall within the 2nd or 4th quadrant, indicating a bad trending performance as also shown by the low CR and high angular error ϵ_{α}. In contrast, using the lung-related amplitudes leads to a better performance as shown in Figures 9.4c and 9.4d. In both cases all measurements fall within the 1st and 3rd quadrant. Nevertheless, the 95 % limits of agreement of ϵ_{α} remain above the ±30° threshold and do thus not indicate successful trending for all of the four cases.

When applying the outlier removal approach presented in Section 9.2.3, the following measurements got excluded: 13 measurements of heart-derived amplitudes ($\Delta\sigma_{\mathrm{H}}$ and $\mathrm{tStd}_{\mathrm{H}}$ of patients P09, P11, P12, P14, P16, P18 and P19) got removed due to too high noise in the heart region ($N_H > 0.484$) but none showed too high variations of the heart ROI. On the other hand, 9 measurements of lung-derived amplitudes ($\Delta\sigma_{\mathrm{L}}$ and $\mathrm{tStd}_{\mathrm{L}}$ of patients P09, P14, P16, P18 and P19) got removed mainly due to too high noise ($N_L > 0.750$) among which one also showed too high variations of the lung ROI (with $J_L < 75\,\%$).

Figure 9.5 shows the restricted analysis on the remaining measurements. One can observe that the performance of the heart-related features shown in Figures 9.5a and 9.5b still falls outside the defined thresholds of acceptance. In contrast, using the reduced set of measurements of the lung-derived amplitudes leads to an acceptable trending performance, in particular for $\mathrm{tStd}_{\mathrm{L}}$ as shown in Figure 9.5d. Yet, when using $\Delta\sigma_{\mathrm{L}}$ (Figure 9.5c), the performance falls closely outside the limits of acceptance, both in terms of CR and ϵ_{α}.

Moreover, as in the previous chapter, a more extensive set of features (see Section 8.2.2) was extracted from the EIT images and tested for their ability to trend changes in SV. However, no noteworthy improvement in performance could be achieved (results not shown) when

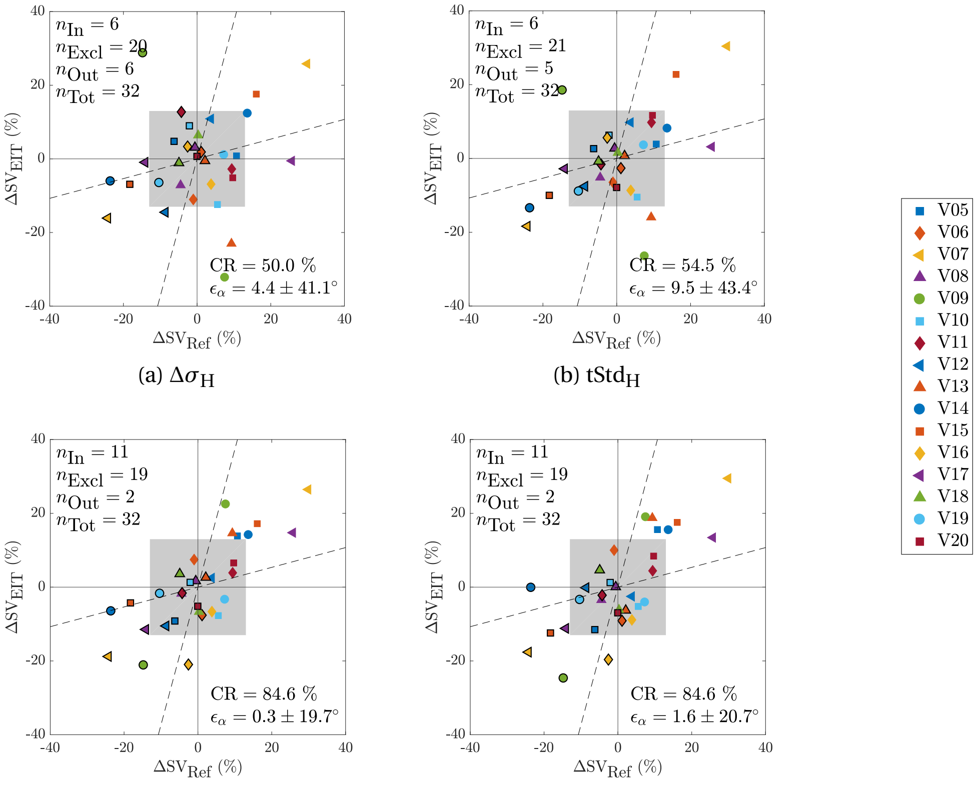

(a) $\Delta\sigma_{\mathrm{H}}$ (b) $\mathrm{tStd}_{\mathrm{H}}$

(c) $\Delta\sigma_{\mathrm{L}}$ (d) $\mathrm{tStd}_{\mathrm{L}}$

Figure 9.4 – Trending analysis between ΔSV_{EIT} vs ΔSV_{Ref} by means of four-quadrant plot analysis for two heart amplitude features ((a) and (b)) and two lung amplitude features ((c) and (d)). The performance is assessed using the angular concordance rate CR and the angular error ϵ_α. This analysis includes the total of 32 measurement points (from all 16 patients) representing relative changes from M2 to M3 (with black border) and changes from M1 to M2 (no border). The exclusion zone was set to ±13 %, the error to be expected from averaging a triplet of thermodilution measurements [124, 142]. The errors ϵ_α are given as Mean ± Std and the 95 % limits of agreement correspond to $[\mathrm{Mean} - 1.96 \cdot \mathrm{Std}, \mathrm{Mean} + 1.96 \cdot \mathrm{Std}]$.

compared to the simple use of the lung-related feature $\mathrm{tStd}_{\mathrm{L}}$.

Based on the present analysis we must reject the hypothesis that the EIT heart amplitude ($\Delta\sigma_{\mathrm{H}}$ and $\mathrm{tStd}_{\mathrm{H}}$) can be used for trending of SV. This is also the case when reducing the measurements by excluding 41 % (13 out of 32) potential outliers. In contrast, our analysis confirms that the EIT lung amplitude ($\mathrm{tStd}_{\mathrm{L}}$) can be successfully used for noninvasive trending of SV. However, this only applies to the analysis where 28 % (9 out of 32) of measurements with high noise level were excluded and shows the sensitivity to noise-induced variability of this approach. It needs to be highlighted that the reduced performance evaluation is based on solely 7 measurements of 4 patients (for $\Delta\sigma_{\mathrm{H}}$ and $\mathrm{tStd}_{\mathrm{H}}$) and 8 measurements of 5 patients (for $\Delta\sigma_{\mathrm{L}}$ and $\mathrm{tStd}_{\mathrm{L}}$).

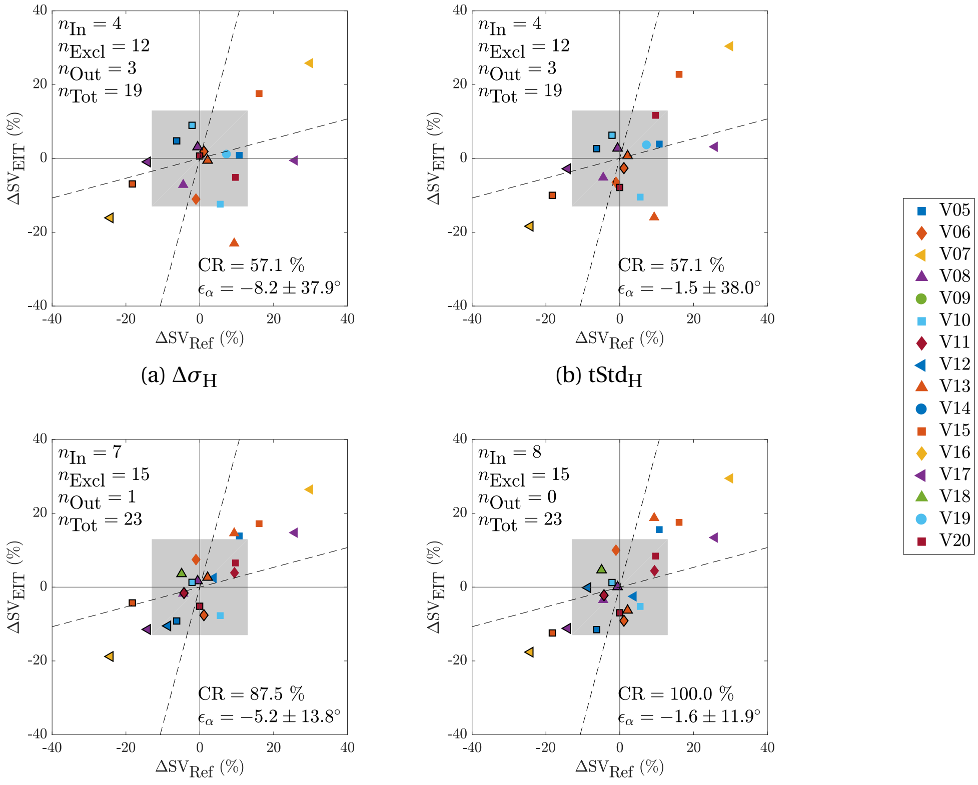

(a) $\Delta\sigma_{\text{H}}$

(b) tStd_{H}

(c) $\Delta\sigma_{\text{L}}$

(d) tStd_{L}

Figure 9.5 – Trending analysis between $\Delta\text{SV}_{\text{EIT}}$ vs $\Delta\text{SV}_{\text{Ref}}$ by means of four-quadrant plot analysis for two heart amplitude features ((a) and (b)) and two lung amplitude features ((c) and (d)). The performance is assessed using the angular concordance rate CR and the angular error ϵ_α. This analysis excludes outliers with high noise and an instable ROI. It includes a total of 19 (for (a) and (b)) and 23 (for (c) and (d)) measurement points representing relative changes from M2 to M3 (with black border) and changes from M1 to M2 (no border). The exclusion zone was set to ±13 %, the error to be expected from averaging a triplet of thermodilution measurements [124, 142]. The errors ϵ_α are given as Mean ± Std and the 95 % limits of agreement correspond to $[\text{Mean} - 1.96 \cdot \text{Std}, \text{Mean} + 1.96 \cdot \text{Std}]$.

9.3.4 Comparison to the Clinical Study in the Operating Room

In comparison to the study in the OR presented in Chapter 8, the current study in the ICU leads to a more promising outcome (i.e. the lung amplitude allows for the trending of relative SV changes). The main difference for these diverging results is hypothesized to stem from the fact that the measurements in the ICU are much more stable in terms of ventilation settings and less distorted by external influences such as touching or moving of the patient by medical staff. For example, it has been shown by Vogt et al. [153] that changes in arm or torso position in sitting subjects can have a significant effect on EIT images. In view of these findings, it is also likely that EIT-derived amplitude estimates of the OR study are impaired by changes in arm and torso position.

9.3.5 Comparison to Simulations and Previous Studies

Our findings indicate that the trending of SV by means of EIT is not possible based on the heart amplitude. This is not only in contradiction with the simulation-based findings presented in Chapter 6 but also partly with the previous studies by Vonk Noordegraaf et al. [155] and Pikkemaat et al. [114]. We hypothesize that in our case the heart-based SV estimation is impaired by ventilation-induced out-of-EIT-plane movement of the heart and/or changes in the heart-lung conductivity contrast (see Figure 6.9) caused by the injection of fluid or other influences. None of these effects was considered in simulations which might explain the contradictory results. While in the pig experiments by Pikkemaat et al. more accurate belt placements might have lead to a less pronounced influence of the first effect in certain pigs, it was mentioned as a main limitation for other pigs [114].

In contrast, SV trending via the lung amplitude is more promising, which would confirm the recent work by da Silva Ramos et al. [41] but is at the same time partly in contradiction with the mixed results obtained by Pikkemaat [113]. Besides, these two studies [113, 41] were performed on pigs under laboratory conditions while our study is based on clinical data of ICU patients under real-life conditions.

9.3.6 Limitations and Future Work

Although we performed measurements on 16 patients, most of them did not show large SV variations in response to the fluid challenge, i.e. not many SV changes exceed the ±13 % error expected from thermodilution. Therefore, in a future study more patients and in particular those with higher SV variations should be included.

While our results suggest that the EIT lung amplitude is able to track changes in SV and thus global perfusion, it is of utmost importance to underline the following. There is still the widespread assumption that cardiosynchronous EIT signals in the lung region mainly reflect pulmonary perfusion which is not entirely correct as discussed by Hellige and Hahn [74] and Adler et al. [11], i.e. two pulmonary arteries with equal perfusion but different compliance result in different pulsatile EIT signal amplitudes – despite equal perfusion! Even though the present approach shows promise on the current data, further research – including long-term measurements and various pathophysiological conditions – is required to reveal likely limitations of this approach.

The current EIT images are based on one single – patient-independent – reconstruction model. It is known that a mismatch between actual thorax shape and reconstruction model can impact the measurements [64]. Therefore, it would be interesting to investigate to which extent the measurements are improved when considering a patient-specific morphology for EIT reconstruction.

9.4 Conclusion

In view of noninvasive SV monitoring at the bedside we performed EIT measurements on sixteen patients in the ICU. These measurements were performed before and after fluid challenge which is known to increase the SV in those patients which are fluid responsive. Resulting changes in EIT-derived heart and lung amplitudes were then compared to SV changes obtained via transpulmonary thermodilution.

Our analysis suggests that the trending of SV – i.e. following relative changes – by means of EIT is not possible based on the heart amplitude, which is in contradiction with previous studies by Vonk Noordegraaf et al. [155] and Pikkemaat et al. [114]. In contrast, SV trending via the EIT-derived lung amplitude is more promising, but only after excluding 9 out of 32 (28 %) measurements considered as potential outliers with too high noise level. In this case an acceptable trending performance with CR = 100 % and $\epsilon_\alpha = -1.6 \pm 11.9°$ is obtained. When compared to pig experiments, our findings would confirm the recent work by da Silva Ramos et al. [41] but are partly in contradiction with the mixed results obtained by Pikkemaat [113].

As these promising results are based on solely 8 measurements of 5 patients, further research is required to validate this approach on more patients and in particular with higher variations in SV. Moreover, it is known that the EIT lung amplitude is not merely related to pulmonary perfusion [74, 11]. Therefore, this potential limitation needs to be further investigated in dedicated clinical trials including long term measurements and addressing relevant pathophysiological conditions. Nonetheless, continuous and noninvasive SV estimation might be feasible in environments such as the ICU where controlled EIT measurements can be performed. Moreover, absolute SV estimates could be obtained by scaling the relative changes with an initial calibration value (e.g. obtained via transthoracic echocardiography).

Part IV

Towards an Optimized Measurement Setup for EIT-Based SV Monitoring

10 Considerations for an Improved Measurement Setup

In this chapter we briefly review existing limitations of available EIT systems and discuss potential approaches for finding a measurement setup better suited for EIT-based SV monitoring.

10.1 Practical Limitations of Available Clinical EIT Systems

The EIT systems currently available and certified for monitoring in clinical scenarios (see Table 3.1) have certain limitations when aiming for SV monitoring via the heart amplitude.

First, most of these systems have the EIT electrodes embedded in a belt which restricts the image reconstruction onto one single plane (2D). Yet, as shown in Chapter 6, the EIT-based SV estimates are considerably influenced by the level at which the EIT belt is placed. This is also indicated by the experimental measurements in the OR (see Chapter 8) where the data from two patients had to be excluded from analysis due to a too low heart signal (presumably caused by a too low/high EIT belt placement). Besides, even if the EIT belt was systematically placed at the same level, the EIT heart signal can be altered by respiration- or posture-induced (out-of-EIT-plane) heart displacement [170]. It is therefore assumed that the use of 3D EIT would be of great benefit to minimize these undesired influences.

Second, all of the available clinical EIT systems are limited to a bipolar stimulation and measurement pattern with one specific skip (i.e. number of inactive electrodes in between the two ones actively measuring voltage/injecting current). Moreover, certain systems (e.g. Göttingen Goe-MF II and Dräger PulmoVista™ 500) make use of the adjacent (skip = 0) pattern, which is known to have the lowest performance in terms of sensitivity and signal-to-noise ratio (in the center) [134, 8]. While the other systems use a skip > 0, to the best of our knowledge, they do not provide a possibility to change it. Even though different skips can theoretically be achieved by connecting the electrodes (of a skip 0 system) in a different order [8], this is not always practicable as the resulting increase in raw voltage amplitudes leads to saturation of the analog acquisition chain.

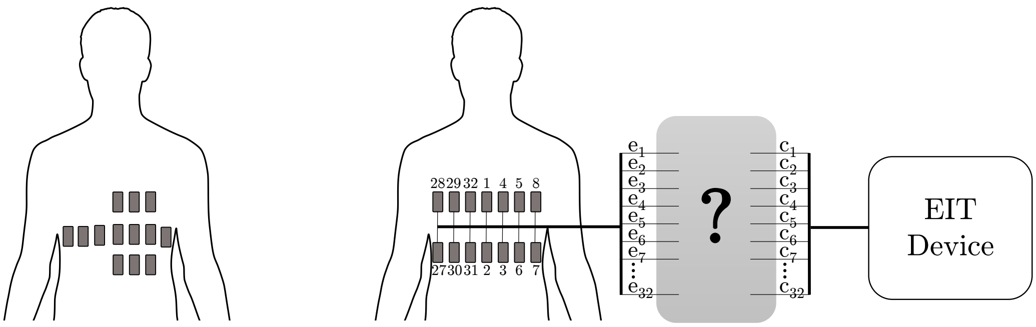

(a) (b)

Figure 10.1 – Two electrode placements assumed to be more suitable for EIT-based SV monitoring: (a) a patch of electrodes close to the heart, and (b) two transversal planes of 2 × 16 electrodes. See text in Section 10.2.

Thirdly, it is known from measurements on healthy subjects that the strength of cardiosynchronous EIT signals decreases with increasing stimulation frequency [30]. On the other hand, due to electrical safety considerations, the injected current and thus the signal-to-noise ratio is lower at frequencies below 100 kHz [2]. However, only some devices allow changing this frequency (e.g. Göttingen Goe MF II and Dräger PulmoVista™ 500) while others are fixed to a given frequency (e.g. at present Swisstom BB^2 is fixed to 195 kHz).

10.2 Finding a Setup Better Suited for EIT-Based SV Monitoring

Compared to the currently available EIT systems (primarily targeted for ventilation monitoring in the lungs), we hypothesize that there is a measurement setup better suited for EIT-based SV monitoring. In the following, besides addressing the abovementioned limitations, we also justify the *improved* measurement setup used in the experimental study presented later on in Chapter 12.

First, concerning the electrode positions, one can imagine that having a higher density of electrodes in the left ventral region (i.e. a patch of electrodes on the chest close to the heart as illustrated in Figure 10.1a) could lead to an improved sensitivity in the heart region. However, given the same total amount of electrodes, this also results in less electrodes on the sides and the back which in turn could be very sensitive to errors of this specific electrodes (detachment, contact impedance issues). In addition, if one further wants to analyze pulsatile information in the lungs, it is of advantage to have a setup not only targeted for measuring the heart. Therefore, for the *improved* measurement setup (see Chapter 12) the electrodes were placed on two transversal planes of 2 × 16 electrodes. This placement enables 3D EIT and is assumed to at least partly overcome the abovementioned undesired influences such as out-of-EIT-plane heart displacement.

Second, given a specific electrode placement has been found, there remains the challenge of

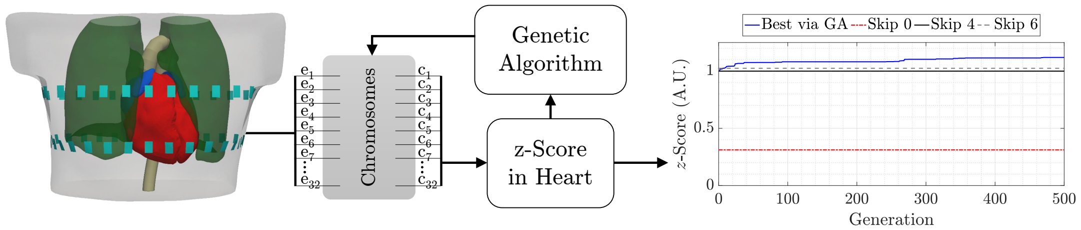

Figure 10.2 – (Left) Block diagram of the genetic algorithm (GA) [158] used to find a better stimulation and measurement pattern. The human thorax model (presented in Chapter 4) with belts TL and TH and the 2 × 16 electrode placement shown in Figure 10.1b, was used to evaluate the sensitivity in the heart region by means of the z-score (distinguishability [8]). For each of the $n_i = 500$ iterations of the GA, a population of $n_p = 256$ chromosomes was evaluated. These are n_p vectors (with a fixed length of 32 each) representing possible connections between the electrode e_i and the EIT device cable c_i (with $i \in \{1,32\}$). At the end of each iteration, the chromosome were ranked (i.e. highest z first, lowest z last), the highest ranked one was kept and the rest of the population was evolved in four steps: (1) 64 new chromosomes were generated by exchanging two randomly chosen alleles in the 25 % highest ranked chromosomes; (2) 64 new chromosomes were generated by randomly swapping all alleles in the 25 % highest ranked chromosomes; (3) 64 new chromosomes were generated by crossing over of two randomly chosen chromosomes; (4) The remaining 63 chromosomes were generated randomly. (Right) The temporal evolution of the best solution found via the GA (——blue) compared to skip 0 (-⋯-red), skip 4 (——black), and skip 6 (- - -gray).

finding the most suitable stimulation and measurement pattern, i.e. finding the particular sequence and combination of the electrodes injecting currents and those measuring the resulting voltages. Even worse, if one wanted to find the optimal solution, one would need to simultaneously optimize the electrode positions and the stimulation and measurement pattern while preferably considering real-live constraints from the EIT device used. Although this is a fascinating subject, it is out of the scope of the present thesis.

Nonetheless, if one is limited to one of the commercially available EIT systems with bipolar measurements and a fixed skip, this challenge gets simplified. When further considering the aforementioned two-plane (2 × 16) electrode placement shown in Figure 10.1b, there is one sole remaining degree of freedom influencing the stimulation and measurement pattern. This is the way on how the 32 electrodes (e_1 to e_{32}) are connected to the 32 cables of the EIT device (c_1 to c_{32}), also illustrated in Figure 10.1b. This issue is similar to the well-known *traveling salesman problem*[1]. Therefore, in an attempt to solve it, a genetic algorithm (GA) was applied which is very briefly presented and described in Figure 10.2. For more information regarding GA one is referred to the book by Weise [158]. Even though this approach does not lead to *the* optimal solution, it finds the best possible one within a reasonable amount of time. As shown in Figure 10.2, the performance of the GA-based solution does not outperform a skip

---

[1] In the *traveling salesman problem* one is given a list of cities which the salesman has to visit. The goal is then to find the shortest possible route that visits each city only once and returns back to the city of departure. Analogously we have to find the best possible order (e.g. in terms of sensitivity in the heart region) on how to connect the 32 cables of our EIT device (c_1 to c_{32}) to the 32 available electrodes (e_1 to e_{32}).

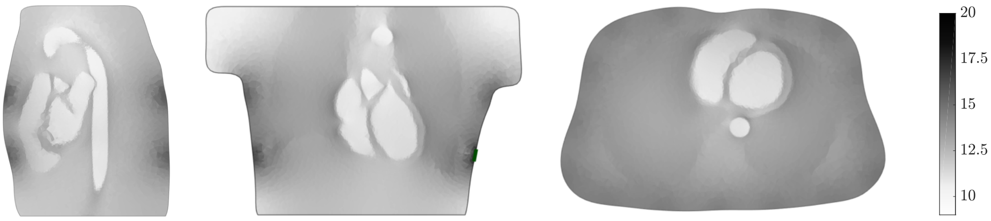

(a) Best stimulation and measurement pattern obtained via the GA

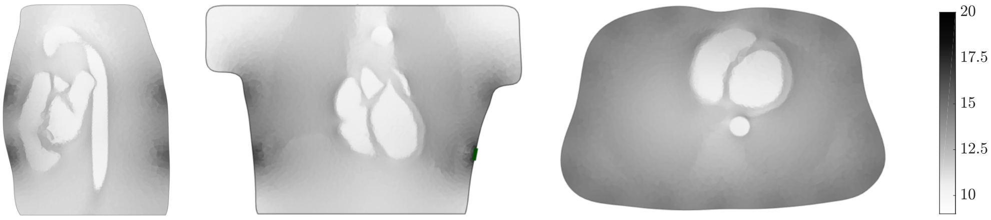

(b) Skip 4 pattern

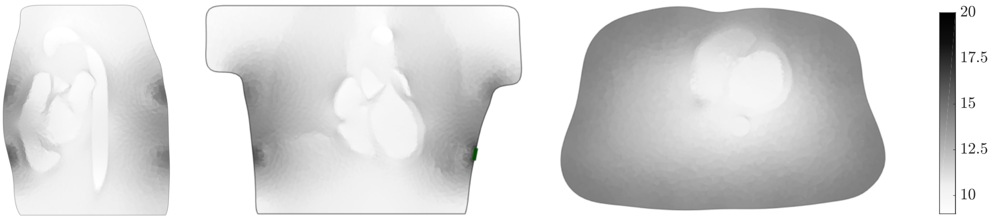

(c) Skip 0 pattern

Figure 10.3 – Forward sensitivities [66] for the human thorax model (presented in Chapter 4) with belts TL and TH and the 2×16 electrode placement shown in Figure 10.1b for three different stimulation and measurement patterns: (a) the best possible obtained via the genetic algorithm approach, (c) skip 4, (b) skip 0. Columns from left to right show: sagittal plane ($x = 30\,\mathrm{cm}$), coronal plane ($y = 10\,\mathrm{cm}$), transverse plane ($z = 40\,\mathrm{cm}$, i.e. in between the two electrode planes). All images use the same color scale.

4 pattern by more than 15 % (in terms of z-score). This is further shown in Figure 10.3 by means of forward sensitivities [66]. The best solution found via the GA (Figure 10.3a) does not significantly outperform a skip 4 pattern (Figure 10.3b). However, the latter two are clearly more sensitive than a skip 0 pattern (Figure 10.3c). For the above reasons, and for the fact that in practice complex cabling could decrease the performance of the *best* solution, the skip 4 pattern was chosen for the *improved* measurement setup and applied in the experimental study (see Chapter 12).

Finally, a remark concerning the frequency of the injected EIT current. It would be of advantage to use a stimulation frequency in the range of 100 kHz as this represents a trade-off between the signal-to-noise ratio [2] and cardiosynchronous signal strength [30]. Yet, being restricted to a specific EIT device (Swisstom BB^2) a fixed stimulation frequency of 195 kHz was used for the *improved* measurement setup.

In summary, we decided for the following *improved* measurement setup to be used in the experimental study presented later on in Chapter 12: 2 × 16 electrodes placed on two transversal planes (Figure 10.1b) with a skip 4 pattern and a stimulation frequency of 195 kHz with the Swisstom BB^2 device.

10.3 The Challenge of Comparing Different Measurement Setups

When one is aiming for an improved EIT measurement setup for a particular application (e.g. SV monitoring), at a certain point it is essential to compare EIT images. These images can be reconstructed with different algorithms or acquired with different measurement configurations (e.g. measured with different skip patterns, electrode positions or even different EIT devices). The aim is then to determine which of these setups has the best performance for a particular application. However, to compare EIT images resulting from different setups, the regularization parameter λ of the reconstruction algorithm must be set such that the comparison is fair, e.g. comparing algorithms with identical signal-to-noise ratios. As alluded to in Section 3.1.2, this was not possible with the existing state of the art. Therefore, we developed a novel approach which is presented hereafter in Chapter 11. It permits the comparison of EIT reconstruction performance across different measurement setups. In the future this approach should help to compare and thus find improved measurement setups for various applications.

While the next chapter in question mainly covers aspects of EIT image reconstruction, the reader more interested in the evaluation of the *improved* measurement setup is directly referred to the subsequent chapter (Chapter 12).

11 A Versatile Noise Performance Metric for EIT Algorithms

Adapted from the post-print version of [25]:

A Versatile Noise Performance Metric for Electrical Impedance Tomography Algorithms

Fabian Braun[1,2], Martin Proença[1,2], Josep Solà[1], Jean-Philippe Thiran[2,3], and Andy Adler[4]

[1]Systems Division, Centre Suisse d'Electronique et de Microtechnique (CSEM), Neuchâtel, Switzerland

[2]Signal Processing Laboratory (LTS5), Ecole Polytechnique Fédérale de Lausanne (EPFL), Lausanne, Switzerland

[3]Department of Radiology, University Hospital Center (CHUV) and University of Lausanne (UNIL), Lausanne, Switzerland

[4]Systems and Computer Engineering, Carleton University, Ottawa, Canada

Published in **IEEE Transactions on Biomedical Engineering**
IEEE Trans. Biomed. Eng., vol. 64, no. 10, pp. 2321–2330, 2017

DOI:10.1109/TBME.2017.2659540

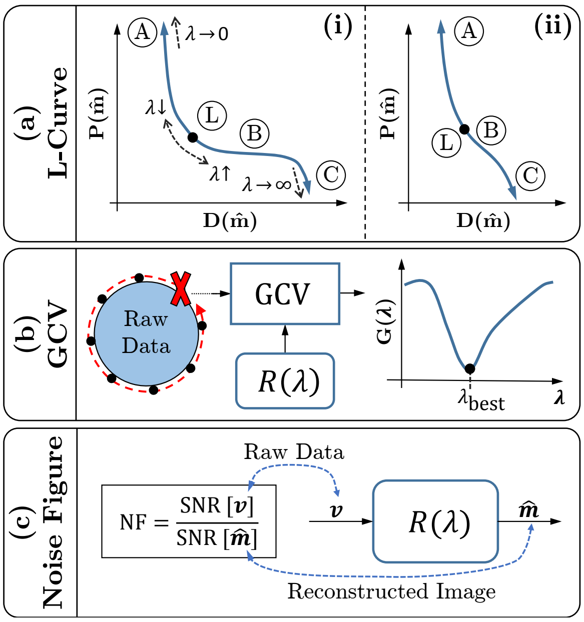

Figure 11.1 – Three hyperparameter selection approaches commonly used in EIT: (a) L-curve with (i) a classical form and (ii) a form often observed for higher data noise; (b) generalized cross-validation (GCV); (c) noise figure (NF).

11.1 Introduction

As presented in Section 3.1.2, the reconstruction of EIT images uses inverse problem techniques, which introduce additional constraints to stabilize the estimated images, and to make them more robust to interference and noise [93, 80]. Most reconstruction schemes define a hyperparameter (here λ) which controls the amount of regularization, and can be seen as a trade-off parameter between image robustness and accuracy. In many cases, this choice can be described as a “resolution-noise performance trade-off”.

In using regularization techniques, a key decision is the selection of an appropriate (or “best”) value of the hyperparameter λ. From the various λ selection approaches which have been proposed [62, 36], we review three commonly used in EIT. A key challenge with all these approaches is that they work within a given measurement configuration (electrode number and position, and stimulation and measurement pattern). They thus offer little guidance in scenarios in which measurement configurations need to be compared, for example when optimizing an EIT configuration for a specific experimental or clinical application. To address this requirement, this chapter proposes and evaluates a novel noise performance metric.

11.1.1 State of the Art in Hyperparameter Selection

We review three state-of-the-art techniques to select regularization hyperparameters. The most widely cited is the L-curve technique, proposed by Hansen [70]. It is based on finding a best compromise between the data mismatch, $D(\hat{\boldsymbol{m}}) = \|\boldsymbol{v} - F(\hat{\boldsymbol{m}})\|$ and the regularization penalty $P(\hat{\boldsymbol{m}})$. The classical form of the L-curve is shown in Figure 11.1a(i); values are obtained by calculating the solution over the full range of λ values and plotting each point. Point L is the L-curve point, which represents the "best" compromise between $D(\cdot)$ and $P(\cdot)$, in the sense that changes in λ from L increase one penalty without improving the other (L can be precisely defined in terms of the curvature). In region A, as $\lambda \to 0$, the image becomes increasingly noisy, and $P(\cdot)$ increases without significant improvement in $D(\cdot)$. Conversely, in region B, as λ increases, $D(\cdot)$ increases without significant improvement in $P(\cdot)$. Finally, for large λ, the best choice is simply to choose the values which minimizes $P(\cdot)$ without considering the data at all (region C). Thus, the L-curve can be thought of as having a "chair" shape. While the L region is well defined when the noise levels are low, in many applications with higher data noise the curve appears more like Figure 11.1a(ii), and point L can be difficult to calculate robustly [62].

Another approach is to use a cross-validation scheme, such as generalized cross validation (GCV) [61]. These are motivated by searching for a solution which is best able to predict measured values. The concept of GCV is illustrated in Figure 11.1b. A solution is calculated without each data value in turn, and the prediction error due to each missing data value is then evaluated. The best λ predicts data with the lowest cross-validation error, represented by the minimum of the GCV-function $G(\lambda)$. GCV estimates have not seen much use in EIT; a common claim has been that the GCV tends to underestimate λ, i.e. to provide under-regularized solutions [62].

The third approach, the noise figure (NF), is illustrated in Figure 11.1c. It is defined as the ratio of signal-to-noise ratio (SNR) of the input (raw data $\boldsymbol{v}$) to that of the output (reconstructed image $\hat{\boldsymbol{m}}$) [3]; $\text{NF} = \text{SNR}[\boldsymbol{v}]/\text{SNR}[\hat{\boldsymbol{m}}]$. Here, SNR is defined in terms of image amplitude rather than energy, as $\text{SNR}[\boldsymbol{x}] = \text{mean}[\boldsymbol{x}]/\text{std}[\boldsymbol{x}]$. NF is a useful parameter to compare algorithms using the same measurement configuration (for example, to compare to the original Sheffield backprojection algorithm, an EIT algorithm is recommended to have $\text{NF} = 0.5$ [6]). Limitations of the NF are mentioned at the end of the next section.

11.1.2 Practical Aspects and Limitations of the State of the Art

A common limitation associated with the L-curve, GCV and other approaches from the mathematical inverse problem literature is that the optimal λ is defined for each data measurement. From an engineering point of view this is not practical. Instead, the value would be set either when an algorithm or system is designed or manufactured, or perhaps when a system is tuned for a specific application. Thus λ should be best for an expected range of data, rather than for one specific set of measurements. Another consideration is that in practice, a "best" algorithm is defined in terms of user-level performance parameters, such as SNR, resolution, position accuracy (e.g. [6]). It is not clear how, for example, the L-curve optimal point relates to the user-level performance. One further application requirement is the need to compare the performance of different measurement system configurations. If we wish to compare different hardware settings, electrode placements, or stimulation and measurement patterns, then the measured data will necessarily differ. It is not possible to simply use the same numeric value of λ between the different configurations. In order for the comparison between the configurations to be meaningful, the setting of a given performance parameter must be the same, so that other figures of merit can be compared fairly. Most commonly, this means setting approaches to have equal noise performance (NP), i.e. the amount of measurement noise (present at the input) reflected in the images (the output of reconstruction).

One common parameter of this type has been the NF. Unfortunately, as shown later in the present chapter, NF does not work well for the comparison of different measurement configurations, such as for example a larger skip (separation between stimulation and measurement electrodes).

11.1.3 Proposed Approach

We are faced with the challenge of defining a hyperparameter selection strategy which is appropriate for: 1) choosing a suitable λ for a measurement system and a given application, and 2) fairly comparing different systems or different configurations of the same system. In the present chapter we primarily focus on 2) driven by the motivation of possible scenarios encountered in practice: having a 32 electrode EIT system with the capability to use different stimulation and measurement patterns, we would like to know which one is the best pattern e.g. to image the lungs or the heart. In a next step, we might want to compare the performance of the first device to a second device with only 16 electrodes. Once an equal NP is established for all algorithms of these diverse configurations, the image quality can be compared in terms of resolution, position errors, or other figures of merit.

To this end we develop a NP metric called $\overline{\mathrm{SNR}}$ which describes the expected image noise. This noise parameter is calculated for a given measurement system configuration which is defined to include: the stimulation and measurement patterns and the electrode positions.

11.1.4 Image Reconstruction for Difference EIT

In this chapter we focus on difference EIT, as typically used in clinical applications for stability reasons. In difference EIT a reference voltage $\boldsymbol{v}_r$ is subtracted from the voltage measurement $\boldsymbol{v}$ yielding the difference data $\boldsymbol{d}$. The result of reconstruction $\hat{\boldsymbol{m}}$ thus represents the change in conductivity relative to a reference state. For small changes in conductivity the problem may be linearised as follows:

$$\hat{\boldsymbol{m}} = \boldsymbol{R}(\lambda)\boldsymbol{d} = \boldsymbol{R}(\lambda)(\boldsymbol{v} - \boldsymbol{v}_r), \tag{11.1}$$

where $\boldsymbol{R}(\lambda)$ represents the reconstruction matrix which depends on the hyperparameter λ. Such linearised one-step difference algorithms are commonly used in clinical EIT and many

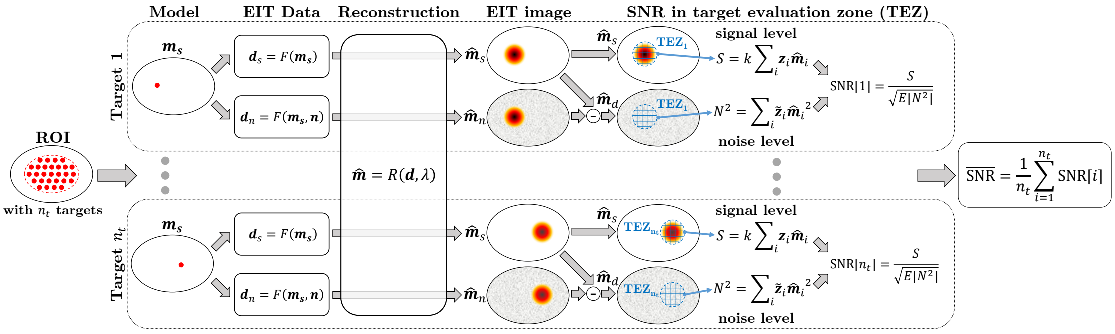
Model
EIT Data
Reconstruction
EIT image
SNR in target evaluation zone (TEZ)
Target 1
Target n_t
ROI
with n_t targets
$\boldsymbol{m}_s$
$\boldsymbol{d}_s = F(\boldsymbol{m}_s)$
$\boldsymbol{d}_n = F(\boldsymbol{m}_s, \boldsymbol{n})$
$\hat{\boldsymbol{m}} = R(\boldsymbol{d}, \lambda)$
$\hat{\boldsymbol{m}}_s$
$\hat{\boldsymbol{m}}_n$
$\hat{\boldsymbol{m}}_d$
TEZ$_1$
TEZ$_{n_t}$
signal level
$S = k\sum_i \boldsymbol{z}_i \hat{\boldsymbol{m}}_i$
$N^2 = \sum_i \tilde{\boldsymbol{z}}_i \hat{\boldsymbol{m}}_i{}^2$
noise level
$\mathrm{SNR}[1] = \frac{S}{\sqrt{E[N^2]}}$
$\mathrm{SNR}[n_t] = \frac{S}{\sqrt{E[N^2]}}$
$\overline{\mathrm{SNR}} = \frac{1}{n_t}\sum_{i=1}^{n_t} \mathrm{SNR}[i]$

Figure 11.2 – Block diagram of the proposed framework evaluating the signal-to-noise ratio (SNR) of n_t likely conductivity targets leading to the averaged $\overline{\mathrm{SNR}}$.

approaches exist to derive $\boldsymbol{R}(\lambda)$.

11.1.5 Structure of This Chapter

This chapter is structured as follows: In the methods section we first present the $\overline{\mathrm{SNR}}$ approach from the theory to its implementation. Then, we describe the simulation and practical experiments performed to validate our approach. In the results, we compare the state of the art (L-curve, GCV, NF) to the proposed method. In the discussion we consider some additional observations of this work, followed by a conclusion.

11.2 Methods

11.2.1 $\overline{\mathrm{SNR}}$ Framework

We first explain the general concept of the proposed $\overline{\mathrm{SNR}}$ approach in the next section. Then we present its specific solution for linearised one-step reconstruction, followed by its algorithmic implementation.

General Concept

The suggested $\overline{\mathrm{SNR}}$ measures the average signal-to-noise ratio in the image domain for several objects of interest – hereafter referred to as *targets*. To do so the signal strength of each target is compared to the amount of noise present in the images within the vicinity of each target. Algorithms with equal $\overline{\mathrm{SNR}}$ are thus defined to have equal noise performance (NP).

As illustrated in Figure 11.2 we evaluate the individual SNRs from n_t likely targets distributed inside a given region of interest (ROI) of our model. The approach requires a model of likely noise $\boldsymbol{n}$, which is incorporated into the difference EIT data ($\boldsymbol{d} = F(\boldsymbol{m}, \boldsymbol{n})$) prior to reconstruction ($\hat{\boldsymbol{m}} = R(\boldsymbol{d}, \lambda)$). $F(\cdot,\cdot)$ represents the forward model transforming the conductivity change $\boldsymbol{m}$ into the (noisy) difference voltage $\boldsymbol{d}$, and $R(\cdot,\cdot)$ the reconstruction of $\boldsymbol{d}$ into the

EIT image $\hat{\boldsymbol{m}}$ (i.e. the estimated conductivity change) while being controlled by the hyperparameter λ. For each of the n_t targets, we estimate the expected signal and noise level in a target-specific evaluation zone (TEZ). To this end, within the TEZ of a given target, we compute the signal level S as the average of a noise-free image $\hat{\boldsymbol{m}}_s$ and the noise level N as the expected root mean square (RMS) amplitude of a pure noise image $\hat{\boldsymbol{m}}_d$. By design, the signal level estimation should be independent of both the spatial resolution (i.e. amount of blurring), and the possible position errors of the reconstruction. Thus, the TEZ is adapted to each target, and is defined as the pixels which exceed one-fourth of the maximum amplitude of $\hat{\boldsymbol{m}}_s$, as suggested by [6]; the TEZ thus includes most of the visually significant image contributions. In this way, the estimate S always captures a comparable portion of the target response in $\hat{\boldsymbol{m}}_s$, independent of the spatial resolution of the reconstruction. The signal estimate S is further scaled with a factor $k = V_{\text{TEZ}}/V_t$ which corrects for the ratio of blurring, i.e. the size of the target response in the image domain V_{TEZ} versus the effective target size V_t. This correction factor k makes the signal estimate independent of the spatial resolution of reconstruction (i.e. size of the TEZ) and the size of the target and thus allows a fair comparison between estimates of different targets and/or algorithms.

The final NP metric $\overline{\text{SNR}}$ is expressed as the average SNR of all n_t targets which leads to the generalized equation:

$$\overline{\text{SNR}} = \text{E}_t \left[\frac{k \sum_{i=1}^{n_p} [\boldsymbol{z}]_i [\hat{\boldsymbol{m}}_s]_i}{\sqrt{\text{E}_n \left[\sum_{i=1}^{n_p} [\boldsymbol{z}]_i [\hat{\boldsymbol{m}}_d]_i^2 \right]}} \right], \tag{11.2}$$

where $\text{E}_n[\cdot]$ denotes the expected value of the noise model (stochastic domain) and $\text{E}_t[\cdot]$ the expected value calculated over the finite set of n_t targets. The target-specific vector $\boldsymbol{z}$ weighing each of the n_p image elements by its area times its contribution to the TEZ (i.e. $z_i = 0$ if image element i is outside the TEZ) is further defined in the next section.

As mentioned before, most clinical EIT applications use one-step linearised reconstruction. We therefore focus on this type of reconstruction and present a particular solution for Equation (11.2) hereafter.

Solution for Linearised Reconstruction

When using a linear model and assuming $\boldsymbol{n}$ as additive noise (characterized by a covariance $\boldsymbol{\Sigma}_n$), we have $\boldsymbol{d}_s = \boldsymbol{J}\boldsymbol{m}_s$, and $\boldsymbol{d}_n = \boldsymbol{J}\boldsymbol{m}_s + \boldsymbol{n}$, where $\boldsymbol{d}_s, \boldsymbol{d}_n \in \mathbb{R}^{n_d}$ are the difference EIT measurements and $\boldsymbol{J} \in \mathbb{R}^{n_d \times n_e}$ is the Jacobian matrix (with n_d as the number of EIT voltage measurements and n_e the number of finite elements in the forward model). The two images of interest, $\hat{\boldsymbol{m}}_s, \hat{\boldsymbol{m}}_d$ are thus calculated using Equation (11.1):

$$\hat{\boldsymbol{m}}_s = \boldsymbol{R}\boldsymbol{d}_s = \boldsymbol{R}\boldsymbol{J}\boldsymbol{m}_s \tag{11.3}$$

$$\hat{\boldsymbol{m}}_d = \boldsymbol{R}(\boldsymbol{d}_s - \boldsymbol{d}_n) = \boldsymbol{R}\boldsymbol{n}. \tag{11.4}$$

From these images we estimate the signal level S from $\hat{\boldsymbol{m}}_s$ and noise level N from $\hat{\boldsymbol{m}}_d$, with the analysis being restricted to the TEZ. To this end, we make use of the normalized weighting vector $\boldsymbol{z} \in \mathbb{R}^{n_p}$ which contains, for each image element i (e.g. pixel), its area a_i multiplied by a binary number c_i (equals 0/1 if outside/inside the TEZ), yielding $z_i \propto a_i c_i$, with $\sum z_i = 1$. For the sake of simplicity, the following equations are limited to one single target but extended to multiple targets at the end of this section. The signal level S is defined as the average of $\hat{\boldsymbol{m}}_s$ within the TEZ:

$$\mathrm{S} = k \sum_{i=1}^{n_p} [\boldsymbol{z}]_i [\hat{\boldsymbol{m}}_s]_i = k\boldsymbol{z}^t \hat{\boldsymbol{m}}_s = \tilde{\boldsymbol{z}}^t \boldsymbol{R}\boldsymbol{J}\boldsymbol{m}_s, \tag{11.5}$$

where $\tilde{\boldsymbol{z}} = k\boldsymbol{z} = (V_{\mathrm{TEZ}}/V_t)\boldsymbol{z}$ with $V_{\mathrm{TEZ}} = \sum a_i c_i$, i.e. the total area of all image elements within the TEZ, and V_t the volume of the conductivity target. The squared noise level N^2 is defined as the weighted mean square amplitude of $\hat{\boldsymbol{m}}_d$:

$$\mathrm{E}\left[\mathrm{N}^2\right] = \mathrm{E}\left[\sum_{i=1}^{n_p} [\boldsymbol{z}]_i [\hat{\boldsymbol{m}}_d]_i^2\right] = \mathrm{E}\left[||\boldsymbol{D}\hat{\boldsymbol{m}}_d||^2\right], \tag{11.6}$$

where $\boldsymbol{D}$ is a diagonal matrix with $[\boldsymbol{D}]_{ii} = \sqrt{z_i}$ yielding:

$$\begin{aligned}
\mathrm{E}\left[\mathrm{N}^2\right] &= \mathrm{E}\left[\mathrm{tr}\left[\boldsymbol{D}\hat{\boldsymbol{m}}_d\hat{\boldsymbol{m}}_d^T\boldsymbol{D}^T\right]\right] = \mathrm{E}\left[\mathrm{tr}\left[\boldsymbol{D}^T\boldsymbol{D}\hat{\boldsymbol{m}}_d\hat{\boldsymbol{m}}_d^T\right]\right] \\
&= \mathrm{E}\left[\sum_{i=1}^{n_p} [\boldsymbol{D}]_{ii}^2 [\hat{\boldsymbol{m}}_d\hat{\boldsymbol{m}}_d^T]_{ii}\right] = \mathrm{E}\left[\sum_{i=1}^{n_p} [\boldsymbol{z}]_i [\hat{\boldsymbol{m}}_d\hat{\boldsymbol{m}}_d^T]_{ii}\right] \\
&= \mathrm{E}\left[\boldsymbol{z}^t \,\mathrm{diag}(\hat{\boldsymbol{m}}_d\hat{\boldsymbol{m}}_d^T)\right] = \mathrm{E}\left[\boldsymbol{z}^t \,\mathrm{diag}(\boldsymbol{R}\boldsymbol{n}\boldsymbol{n}^t\boldsymbol{R}^t)\right] \\
&= \boldsymbol{z}^t \,\mathrm{diag}(\boldsymbol{R}\boldsymbol{\Sigma}_n\boldsymbol{R}^t).
\end{aligned} \tag{11.7}$$

The choice of calculating the noise from the diagonal entries of $\boldsymbol{R}\boldsymbol{\Sigma}_n\boldsymbol{R}^t$ rather than from the full covariance matrix stems from the fact that we are estimating N as the RMS amplitude along the spatial dimension (i.e. for each image element). If the full covariance matrix were used, noise would be estimated as the RMS amplitude (along the stochastic dimension) of a conductivity change spatially averaged over the TEZ ($\mathrm{E}\left[(\boldsymbol{z}^t\hat{\boldsymbol{m}}_d)^2\right] = \boldsymbol{z}^t\boldsymbol{R}\boldsymbol{\Sigma}_n\boldsymbol{R}^t\boldsymbol{z}$), and would sum over the off-diagonal entries in the covariance matrix. In this case, off-diagonal entries with opposite sign would reduce the estimated noise within the TEZ. This would lead to an overestimated SNR, especially in reconstruction algorithms with high spatial resolution when compared to lower resolution algorithms.

Combining Equation (11.5) and (11.7) leads to the SNR of one single target:

$$\mathrm{SNR} = \frac{\mathrm{S}}{\sqrt{\mathrm{N}^2}} = \frac{\tilde{\boldsymbol{z}}^t \boldsymbol{R}\boldsymbol{J}\boldsymbol{m}_s}{\sqrt{\boldsymbol{z}^t \operatorname{diag}\left(\boldsymbol{R}\boldsymbol{\Sigma}_n\boldsymbol{R}^t\right)}}. \tag{11.8}$$

We further extend this to multiple targets with their changes in conductivity $\boldsymbol{M} \in \mathbb{R}^{n_e \times n_t}$ and the corresponding evaluation zones $\boldsymbol{Z}, \tilde{\boldsymbol{Z}} \in \mathbb{R}^{n_p \times n_t}$, where each column in $\boldsymbol{M}$ contains the conductivity change of one target (e.g. $\boldsymbol{m}_s$), $\boldsymbol{Z}$ the TEZ of this target (e.g. $\boldsymbol{z}$) and $\tilde{\boldsymbol{Z}}$ its scaled version (e.g. $\tilde{\boldsymbol{z}}$). This leads a vector of n_t SNRs:

$$\mathbf{SNR} = \operatorname{diag}\left(\tilde{\boldsymbol{Z}}^t \boldsymbol{R}\boldsymbol{J}\boldsymbol{M}\right) \oslash \sqrt{\boldsymbol{Z}^t \operatorname{diag}\left(\boldsymbol{R}\boldsymbol{\Sigma}_n\boldsymbol{R}^t\right)}, \tag{11.9}$$

where $\oslash$ denotes the Hadamard division (element-wise division). For uncorrelated and uniform noise, where $\boldsymbol{\Sigma}_n$ is a diagonal matrix with $\boldsymbol{\Sigma}_n = \sigma_n^2 \boldsymbol{I}$, this can be simplified to:

$$\mathbf{SNR} = \operatorname{diag}\left(\tilde{\boldsymbol{Z}}^t \boldsymbol{R}\boldsymbol{J}\boldsymbol{M}\right) \oslash \left(\sigma_n \sqrt{\boldsymbol{Z}^t \operatorname{diag}\left(\boldsymbol{R}\boldsymbol{R}^t\right)}\right). \tag{11.10}$$

The final SNR is then calculated as the mean of all targets $\overline{\mathrm{SNR}} = \frac{1}{n_t}\sum_{i=1}^{n_t} [\mathrm{SNR}]_i$, in order to obtain the average NP inside the ROI. The expressions in Equation (11.9) and (11.10) are comparable to the $\mathrm{SNR}_{\mathrm{out}}$ defined by Adler et al. [3] but evaluated in a restricted region of the image – the TEZ – and averaged over multiple targets.

Algorithm Implementation

For a given application including a model of the likely body shape, the Jacobian $\boldsymbol{J}$ and – provided a given λ – the reconstruction matrix $\boldsymbol{R}(\lambda)$ are known. With Equation (11.9) and (11.10) the $\overline{\mathrm{SNR}}$ is then calculated by the following steps.

1. In the region where the conductivity changes of interest are to be observed (ROI) we distribute n_t targets of desired size and amplitude in our model, leading to $\boldsymbol{M}$.
2. For each target, we reconstruct an image $\hat{\boldsymbol{m}}_s$ of which we determine the one-fourth amplitude pixels. These pixels define the evaluation zone (TEZ) in the image domain, leading to n_t TEZs contained in $\boldsymbol{Z}$ and $\tilde{\boldsymbol{Z}}$.
3. Depending on the desired noise characteristics we compute **SNR** using Equation (11.9) or (11.10) and average to obtain $\overline{\mathrm{SNR}}$.

11.2.2 Validation Experiments

To validate the approach proposed, a number of simulation experiments were performed on a human thorax model. To this end, the aforementioned algorithm was implemented in Matlab using the open-source EIT toolbox EIDORS [5] and is freely available since release version

3.9 [10]. To illustrate the approach on measured data, a commercial EIT system was used to perform measurements on a resistor phantom. Finally, a simulation on an open geometry model was carried out to evaluate the potential of the $\overline{\text{SNR}}$ approach for other fields of EIT such as geophysics.

Algorithm Parameters

For the implementation of the proposed method in thoracic EIT applications, we recommend an ROI extending to 50% of the distance from the center of mass to the boundary as illustrated in Figure 11.3b. The therein contained $n_t = 200$ uniformly distributed spherical targets are positioned at the level of the electrodes and have a relative radius r_t of 5% of the medium radius R_m. Moreover, $\overline{\text{SNR}}$ was calculated using Equation (11.10) with $\sigma_n = 1$. The choice of these parameters is justified in the discussion section.

In order to tune an EIT reconstruction algorithm to a desired $\overline{\text{SNR}}$ i.e. selecting the hyperparameter λ of $\boldsymbol{R}(\lambda)$, a bisection search technique was applied [62].

Image Reconstruction

In the present chapter we use two reconstruction algorithms widely used for thoracic EIT: GREIT with the recommended settings [6] and one-step Gauss-Newton (GN) with a Laplace-prior [93, 80].

Simulation Experiments

The simulation experiments are illustrated in Figure 11.3 and described hereafter. A 3D extruded model of a human thorax (shown in Figure 11.3a) was used with realistic conductivities ($\sigma_{\text{Background}} = 0.20\ \text{S/m}, \sigma_{\text{Lungs}} = 0.13\ \text{S/m}, \sigma_{\text{Heart}} = 0.55\ \text{S/m}$) [73]. A set of representative difference EIT voltages $\boldsymbol{d}_r$ was generated by changing the conductivity of the left lung and the heart by 10% and -5%, respectively. The right lung was left unchanged. An example of a reconstructed EIT image is shown in Figure 11.3c. To mimic a realistic scenario, additive white Gaussian noise $\mathcal{N}(0, 1\text{E-}5)$ was added to the difference data simulated, with which $n_f = 10000$ realizations of a noisy EIT voltages $\boldsymbol{d}_n$ were generated. These EIT data were reconstructed with various algorithms $\boldsymbol{R}(\lambda)$ whose hyperparameter λ was selected based on different strategies: (a) a given $\overline{\text{SNR}}$, (b) a given noise figure (NF) [3, 62], (c) the L-curve criterion (LCC) [70, 68], or (d) the generalized cross-validation (GCV) [68]. The latter two were implemented in EIDORS using Hansen's Regularization Tools [69] and λ was selected as the median value of n_f hyperparameters resulting from applying the LCC or GCV to each of the noisy EIT voltages individually.

Additionally, the reliability of the different hyperparameter selection approaches was investigated for various scenarios by changing (a) the number and (b) position of electrodes, (c)

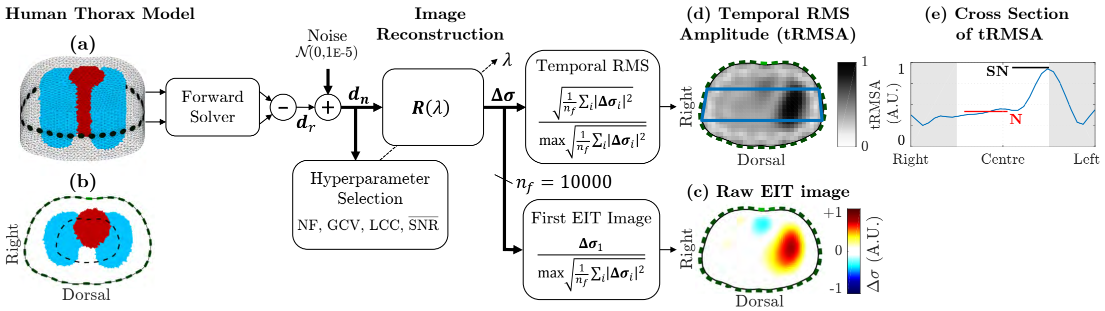
Human Thorax Model
(a)
(b)
Right
Dorsal
Forward Solver
Noise
$\mathcal{N}$(0,1E-5)
d_n
d_r
Image Reconstruction
$R(\lambda)$
λ
Hyperparameter Selection
NF, GCV, LCC, $\overline{\text{SNR}}$
$\Delta\sigma$
$n_f = 10000$
Temporal RMS
$\frac{\sqrt{\frac{1}{n_f}\sum_i|\Delta\sigma_i|^2}}{\max\sqrt{\frac{1}{n_f}\sum_i|\Delta\sigma_i|^2}}$
First EIT Image
$\frac{\Delta\sigma_1}{\max\sqrt{\frac{1}{n_f}\sum_i|\Delta\sigma_i|^2}}$
(d) Temporal RMS Amplitude (tRMSA)
Right
Dorsal
1
0
tRMSA (A.U.)
(c) Raw EIT image
Right
Dorsal
+1
0
-1
$\Delta\sigma$ (A.U.)
(e) Cross Section of tRMSA
1
0
SN
N
Right
Centre
Left

Figure 11.3 – Overview of the simulation experiments: (a) 3D model of human thorax with lungs (blue) and heart (red) and (b) its corresponding 2D model in medical orientation (with ROI for $\overline{\text{SNR}}$ calculation as dashed black line). The difference voltages $\boldsymbol{d}_r$ obtained after forward solving are affected by n_f realizations of additive white Gaussian noise $\mathcal{N}(0, 1\text{E-}5)$ and then reconstructed to n_f noisy EIT images $\boldsymbol{\Delta\sigma}$. The noise level in the reconstructed images is illustrated by one single noisy EIT image and further analyzed by the temporal root mean square of all noisy EIT images as described in the following. (c) Example EIT image with positive/negative conductivity change in left lung and heart, respectively. The green rectangles depict the EIT electrodes. (d) Pixel-wise, temporal root mean squared amplitude (tRMSA) of the n_f noisy EIT image. This image shows the square root of the signal and noise power. The region delineated in blue is used to generate (e) the tRMSA cross section showing a transversal cut through the tRMSA image with the region outside the ROI shaded grey. It shows the ratio of noise-affected signal level SN (left lung) vs. noise level N (right lung) and allows to estimate an approximative SNR $\approx \frac{\text{SN}-\text{N}}{\text{N}}$. In the above example with SN = 0.94 and N = 0.42 we estimate SNR ≈ 1.24. Note that (c), (d), and (e) are normalized to maximal tRMSA.

the skip of the bipolar stimulation pattern (number of inactive electrodes in between the two ones actively measuring voltage/injecting current), (d) the image resolution (i.e. number of pixels) or (e) the reconstruction algorithm (GREIT or GN). Unless otherwise noted, per default, data from 16 equidistantly spaced electrodes and bipolar stimulation with skip 0 (*adjacent* stimulation pattern) were reconstructed using GN onto an image of 32 × 32 pixels.

For each of the scenarios simulated the NP is analysed visually, either on the so-called temporal RMS amplitude (tRMSA) image or its resulting cross section plot described in the following. The tRMSA image (see Figure 11.3d) is calculated as the pixel-wise RMS amplitude (in the temporal domain) from the n_f reconstructed noisy EIT images $\boldsymbol{\Delta\sigma}$. The tRMSA image and the corresponding cross section plot Figure 11.3e show the ratio of noise-affected signal (left lung) vs. noise (right lung) and thus allow a visual analysis of the NP and its spatial distribution as further detailed in Figure 11.3.

Practical Experiments

In a laboratory experiment a resistor phantom (Swisstom Mesh Phantom 32-HG) was connected to the 32-electrode EIT belt of the Swisstom PioneerSet (Swisstom, Landquart, Switzerland). The mesh phantom contains 160 resistors in a star-like arrangement of which four can be short-circuited by a pushbutton resulting in local conductivity perturbations [144]. The four pushbuttons A, B, C and D are located close to electrode 1, 9, 17 and 25 and lead to a local increase in conductivity at the top, right, bottom or left of the reconstructed image, respectively. Five measurements were performed, each with a different skip pattern: 0, 3, 4, 7 and 8. Data were recorded using the Swisstom STEMLab software (Version 2.3.2 rev 749). At the beginning of each measurement four local changes in conductivity were generated by consecutively pressing each of the pushbuttons (A, B, C, D) of the resistor phantom during 5 seconds. Then the phantom was left untouched while the recording continued for 2.5 minutes, enabling the estimation of the device-specific noise characteristics.

Open Geometry Example

The previous experiments concentrate on the application of thoracic EIT where electrodes are placed on a closed geometry. However, there are other uses of EIT, such as geophysics, where the electrodes can be placed on an open geometry. In order to evaluate the potential applicability of the $\overline{\mathrm{SNR}}$ approach for such cases, simulations with 27 electrodes placed inside a circular hole of a 2D model were performed. Two conductivity contrasts shown in Figure 11.9i were reconstructed for three different skips using the GN algorithm with identical $\overline{\mathrm{SNR}}$. The computation of $\overline{\mathrm{SNR}}$ was based on 40 targets placed in the close vicinity around the electrodes as shown by red dots in Figure 11.9i.

11.3 Results

11.3.1 Simulation Experiments

Figure 11.4 to Figure 11.6c show the noise performance of different scenarios and hyperparameter selection approaches resulting from the simulation experiments illustrated in Figure 11.3.

Figure 11.4 shows the noise performance of GN reconstructions for four examples of skip patterns and for different hyperparameter selection approaches: (a) a fixed noise figure (NF = 0.5), (b) GCV, (c) LCC, (d) a fixed $\overline{\mathrm{SNR}}$ of $\overline{\mathrm{SNR}}_1$ = 2.20E-5, and (e) a two-fold higher $\overline{\mathrm{SNR}}_2$ = 4.41E-5.

Similar figures are shown for an identical $\overline{\mathrm{SNR}}_1$ to depict how the noise performance as influenced by: (a) the use of the GREIT – instead of GN – reconstruction algorithm (Figure 11.5), (b) different image resolutions (Figure 11.6a), (c) varying electrode position and number (Figure 11.6b), and finally, (d) different skips combined with varying electrode position and number (Figure 11.6c).

All images in Figure 11.4 to Figure 11.6c are normalized to the maximal tRMSA (as illustrated in Figure 11.3). The reason behind this normalization is that – independent of differences in amplitude response of reconstruction – we would like to display and analyze differences in

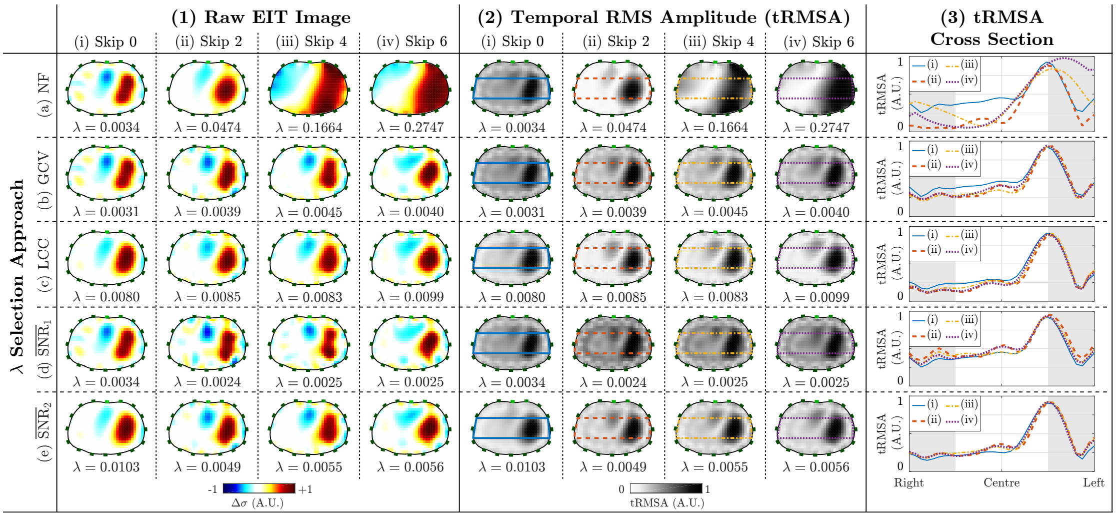

Figure 11.4 – Noise performance of GN reconstructions for four examples of skip pattern (i)-(iv), and five approaches for hyperparameter selection, each shown in one row: (a) fixed noise figure (NF = 0.5), (b) generalized cross-validation (GCV), (c) L-curve criterion (LCC), (d) fixed $\overline{\mathrm{SNR}}$ of $\overline{\mathrm{SNR}}_1 = 2.20\mathrm{E}\text{-}5$ (corresponds to NF = 0.5 at skip 0), and (e) fixed $\overline{\mathrm{SNR}}$ of $\overline{\mathrm{SNR}}_2 = 2 \cdot \overline{\mathrm{SNR}}_1 = 4.41\mathrm{E}\text{-}5$. For each approach and skip we show (1) one single EIT image (all with identical noise), (2) the temporal RMS amplitude (tRMSA) images, and (3) their cross sections along the transverse axis of the zone delineated in the corresponding tRMSA image. All images are normalized to their maximal tRMS amplitude as described in Figure 11.3.

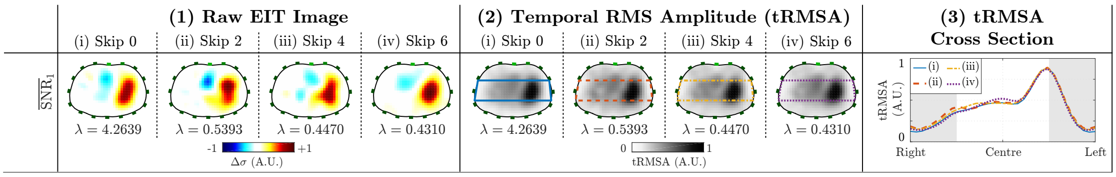

Figure 11.5 – Noise performance of GREIT reconstructions (with fixed $\overline{\mathrm{SNR}} = 2.20\mathrm{E}\text{-}5$) for four examples of skip pattern (i)-(iv). For each skip we show (1) one single EIT image (all with identical noise), (2) the temporal RMS amplitude (tRMSA) images, and (3) their cross sections along the transverse axis of the zone delineated in the corresponding tRMSA image. All images are normalized to their maximal tRMS amplitude as described in Figure 11.3.

NP and thus the ratio of signal level at each pixel relative to the maximal noise-affected signal level.

11.3.2 Practical Experiments

Figure 11.7 depicts EIT images of an identical conductivity change measured on a resistor phantom for five different skip patterns and reconstructed using an algorithm with a fixed NF.

Similar images reconstructed with a fixed $\overline{\mathrm{SNR}}$ are shown in Figure 11.8a. As per default, the calculation of $\overline{\mathrm{SNR}}$ for these images is based on Equation (11.10) with $\sigma_n = 1$. In contrast,

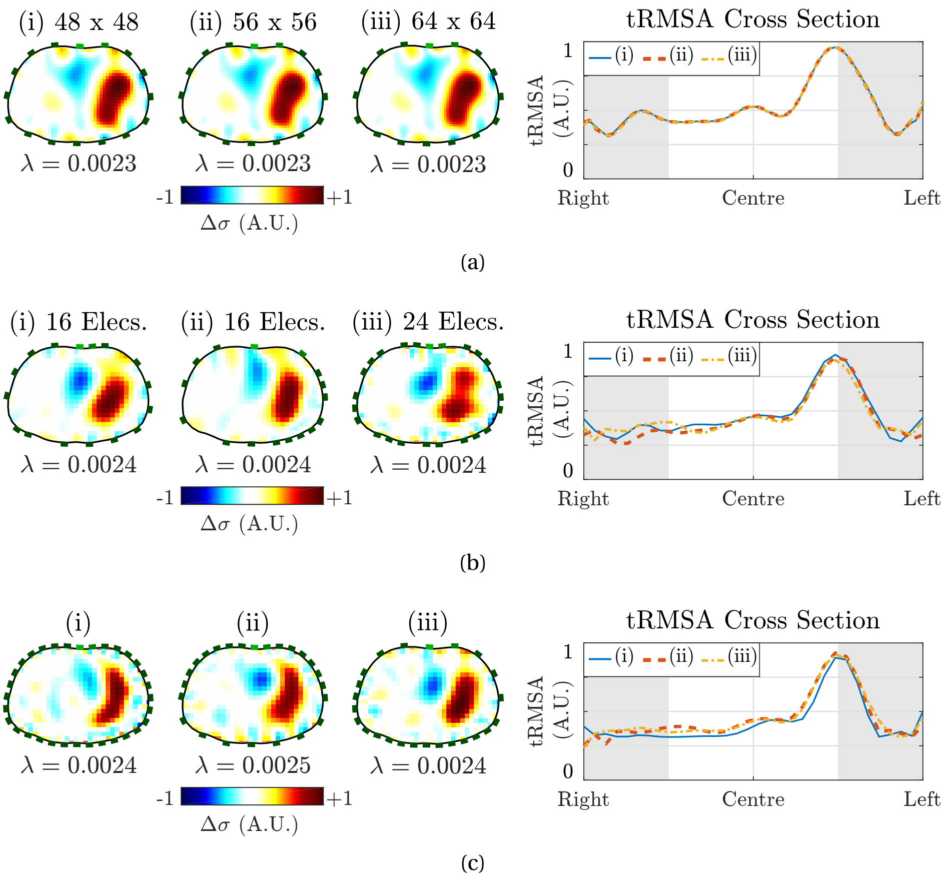

Figure 11.6 – Noise performance of GN reconstructions (with fixed $\overline{\mathrm{SNR}} = 2.20\mathrm{E}\text{-}5$) for:
(a) three examples with a skip 3 and an image resolution of: (i) 48 × 48, (ii) 56 × 56, (iii) 64 × 64.
(b) three examples with a skip 5 and varying electrode position and number, where (i) and (ii) have 16 and (iii) 24 non-equidistantly spaced electrodes.
(c) three examples of varying electrode position and number, and skip pattern: (i) 32 electrodes with skip 3, (ii) 24 electrodes distributed more ventrally with skip 5 and (iii) 24 electrodes distributed more dorsal with skip 7.
For each scenario we show one single EIT image (all with identical noise), and the corresponding cross sections of the tRMSA images on the right. All images are normalized as described in Figure 11.3.

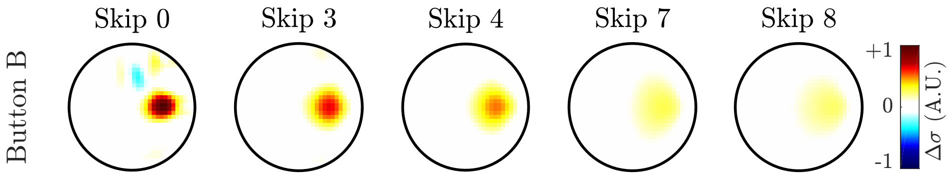
Skip 0
Skip 3
Skip 4
Skip 7
Skip 8
Button B
+1
0
-1
$\Delta\sigma$ (A.U.)

Figure 11.7 – Conductivity changes $\Delta\sigma$ measured on a resistor phantom for five different skip patterns and reconstructed using GREIT with a fixed noise figure (NF = 0.5). Pressing button B on the phantom leads to a local conductivity perturbation close to electrode 9 (right of image). This perturbation is identical for all skip patterns, such that differences in the resulting images can be attributed to differences in image reconstruction. All images are normalized identically to the maximal absolute amplitude of all five images.

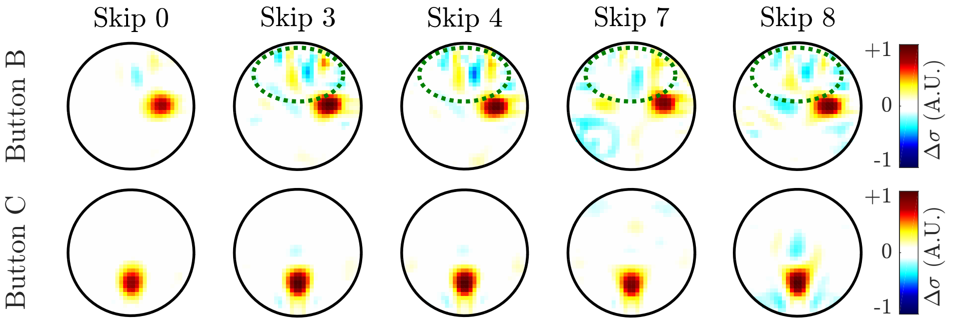
Skip 0
Skip 3
Skip 4
Skip 7
Skip 8
Button B
Button C
+1
0
-1
$\Delta\sigma$ (A.U.)

(a) fixed $\overline{\text{SNR}}$: uniform and uncorrelated noise ($\boldsymbol{\Sigma}_n = \boldsymbol{I}$)

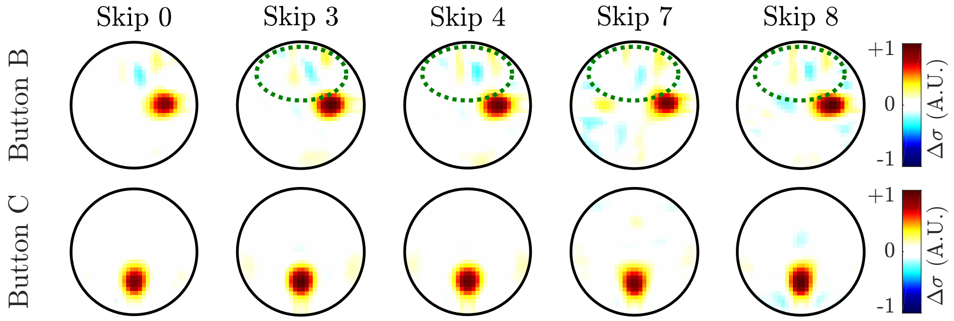
Skip 0
Skip 3
Skip 4
Skip 7
Skip 8
Button B
Button C
+1
0
-1
$\Delta\sigma$ (A.U.)

(b) fixed $\overline{\text{SNR}}$: non-uniform noise ($\boldsymbol{\Sigma}_n = \boldsymbol{\Sigma}_{\text{Est}}$)

Figure 11.8 – Conductivity changes $\Delta\sigma$ measured on a resistor phantom for five different skip patterns. Pressing button B and C on the phantom leads to a local conductivity perturbation close to electrode 9 (right of image) and electrode 17 (bottom of image), respectively. The images were reconstructed using GREIT with a fixed $\overline{\text{SNR}}$ of (a) $\overline{\text{SNR}}_1 = 3.22\text{E-}6$ or (b) $\overline{\text{SNR}}_2 = 5.16\text{E-}3$, both corresponding to a NF = 0.5 at skip 0. The difference in $\overline{\text{SNR}}$ between (a) and (b) is due to the different noise covariances used: (a) $\boldsymbol{\Sigma}_n = \boldsymbol{I}$ or (b) $\boldsymbol{\Sigma}_n = \boldsymbol{\Sigma}_{\text{Est}}$. The green dotted ellipses highlight the zone where differences in image artefacts are observed. All images in one row are normalized identically to the maximal absolute amplitude of all five images.

images in Figure 11.8b show the effect of taking into account the device-inherent noise characteristics ($\overline{\text{SNR}}$ calculation is based on Equation (11.9), with $\mathbf{\Sigma}_n$ equal to the estimated noise covariance $\mathbf{\Sigma}_{\text{Est}}$).

11.3.3 Open Geometry Example

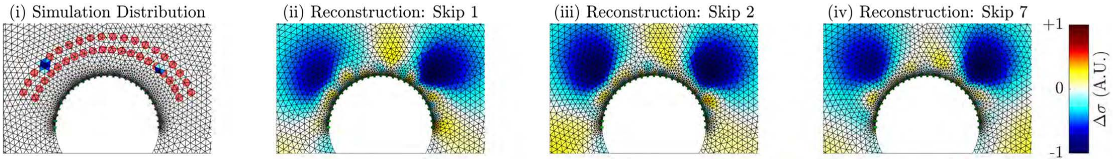
(i) Simulation Distribution
(ii) Reconstruction: Skip 1
(iii) Reconstruction: Skip 2
(iv) Reconstruction: Skip 7
+1
0
-1
$\Delta\sigma$ (A.U.)

Figure 11.9 – Example of 27 electrodes placed inside an open geometry. (i) Shows the $n_t = 40$ targets used to calculate the $\overline{\text{SNR}}$ (red dots) and the two conductivity changes simulated (bluish elements) which were reconstructed with GN algorithms having an identical $\overline{\text{SNR}}$ for three different skips: (ii) 1, (iii) 2 and (iv) 7. The images of the reconstructed conductivity changes $\Delta\sigma$ in (ii) - (iv) are normalized to the maximal absolute amplitude of all three images.

Figure 11.9 ii-iv shows images of the open geometry conductivity change reconstructed for three different skip patterns with identical $\overline{\text{SNR}}$ and noise.

11.4 Discussion

In this chapter we suggest a novel noise performance (NP) metric which allows for a fair comparison of EIT reconstruction algorithms with different measurement configurations (i.e. skip pattern, number and position of electrodes, etc.). We validated its applicability based on three experiments: 1) simulations on a human thorax model, 2) practical measurements on a resistor phantom, and 3) simulation of an open geometry example. The results obtained are discussed in detail hereafter.

11.4.1 Simulation Experiments

Figure 11.4a reveals that the NF approach leads to a very inhomogeneous NP, as the noise level decreases with increasing skip. It thus cannot be used to achieve a similar NP between algorithms with unequal measurement configurations (e.g. different skips). The higher the skip, the more regularized and thus smoothed the result is, when aiming for the same NF. On the other hand, for the GCV (Figure 11.4b) a similar NP can be observed among all four skips, with the exception of skip 0 (i) where the noise level is increased by roughly 50%. This is improved with the LCC (Figure 11.4c) which shows a more homogeneous NP between all skips. Furthermore one can observe that GCV tends to regularize less (smaller λ, higher noise level), which is a known characteristic [146]. However, the latter two approaches (1) require actual data including noise and (2) can only be applied to reconstruction algorithms using Tikhonov-type regularization, i.e. GN but not GREIT. This is why both do not fulfil our requirements of a versatile NP metric.

In contrast, the selection of λ with the $\overline{\text{SNR}}$ approach results in a comparable NP for both $\overline{\text{SNR}}_1 = 2.20\text{E-}5$ (Figure 11.4d) or a two-fold higher $\overline{\text{SNR}}_2 = 4.41\text{E-}5$ (Figure 11.4e). This shows that for the same scenario, the $\overline{\text{SNR}}$ is a robust way to obtain comparable NP between the varying skips. Besides, the NP in the image domain can be flexibly adapted as demonstrated by the two-fold increase in $\overline{\text{SNR}}$ from (d) $\overline{\text{SNR}}_1$ to (e) $\overline{\text{SNR}}_2$ which results in an approximate two-fold increase in NP.

The use of GREIT instead of GN for reconstructing with a fixed $\overline{\text{SNR}}_1$ is shown in Figure 11.5 and reveals a spatial distribution of noise different to that of GN (Figure 11.4d). An attenuation of noise close to the model border can be observed for images reconstructed using GREIT, which is known as an inherent property of this algorithm [6]. Nonetheless, the noise level in the ROI - the region in which we evaluate our NP - is closely comparable. This demonstrates the versatility of our approach by its independence on those two commonly used reconstruction algorithms.

Furthermore, the use of different image sizes as shown in Figure 11.6a confirms the immunity of the $\overline{\text{SNR}}$ approach to changes in image resolution. In addition, it seems to be robust to differences in electrode placement and number. This is shown in Figure 11.6b which depicts the use of non-equidistantly spaced electrodes and a variation in their number for a constant skip of 5. This is extended in Figure 11.6c where not only the electrode placement and number, but also the skip is varied. The slightly lower noise level especially for case (i) is a desired behaviour and can be explained by a higher spatial resolution achieved with 32 electrodes, i.e. the same portion of conductivity change is concentrated into a smaller area. As the resulting sum of the normalized impedance change in the TEZ (the signal level S) is lower for 32 electrodes, we also have a lower noise level to achieve the same SNR.

The tRMSA cross section plots confirm that the NP of the different scenarios shown in Figure 11.4d and Figure 11.5 to Figure 11.6c closely resemble each other. These simulation results highlight the flexibility of the $\overline{\text{SNR}}$ approach in the example of thoracic EIT and corroborate the use of $\overline{\text{SNR}}$ as valuable NP metric by fulfilling the requirements of being insensitive to the 1) measurement configuration (skip, electrode number and position), 2) image resolution and 3) reconstruction algorithm.

11.4.2 Practical Experiments

The aforementioned problems with a fixed NF, are confirmed in experimental measurements as shown in Figure 11.7. These images show an increase in spatial blurring and a corresponding decrease in noise level with increasing skip. Besides, one can observe a decrease in conductivity change which is due to an increase in regularization with increasing skip. A possible solution is given by the $\overline{\text{SNR}}$ approach as depicted in Figure 11.8a, where, independent of the skip, a similar NP is achieved. However, for a conductivity change at the right of the image (button B), artefacts can be observed (green dotted zone). These are present for a skip other than 0 and primarily located at the top of the images, which corresponds to the vicinity of electrode 1. We presume that these specific artefacts are an inherent property of the device used, as it was already reported previously in [54]. When considering the device-specific noise characteristics $\mathbf{\Sigma}_{\text{Est}}$ by using Equation (11.9) for the $\overline{\text{SNR}}$ calculation, these artefacts are reduced and the images in Figure 11.8b still show a comparable NP. This points out that real EIT data are very likely to not have purely uniform noise among all channels [67]. At the same time these results underline the versatility of the $\overline{\text{SNR}}$ approach to incorporate the device-specific noise characteristics in order to calculate more realistic NPs.

In practice, for thoracic EIT measurements, we may predetermine the noise characteristics of our device in the lab (e.g. on a resistor phantom) and later include this information to tune the algorithm before applying it to image living beings.

11.4.3 Open Geometry Example

The images of the open geometry example (see Figure 11.9 ii-iv) show a visually comparable NP. This simple example lets us assume that our approach has the potential to be used for such applications of EIT. However, further investigations in this particular field are required, e.g. regarding the selection of application-specific algorithm parameters (ROI, target size and position, etc.).

11.4.4 Algorithm Parameter Selection

The $\overline{\text{SNR}}$ calculation depends on several parameters (ROI, n_t, r_t, $\mathbf{\Sigma}_n$) which are discussed and justified in the following.

ROI

In thoracic EIT we are primarily interested in respiration- or cardiovascular-induced conductivity changes. It thus makes sense to have an ROI in the centre which covers big parts of the lungs and heart as also shown in Figure 11.3(b). Depending on the application, this ROI should be moved to the region(s) where conductivity changes of interest are most likely to be observed and analysed.

Targets

The number of targets n_t uniformly distributed inside the ROI is chosen high enough to achieve a homogeneous estimate of NP over the entire region. However, a higher n_t leads to increased computation time which explains the suggested value of $n_t = 200$ as compromise. The relative target radius r_t with 5% of the model diameter is justified with being inferior to the inherent spatial resolution of EIT with 32 electrodes [160, 132].

The Ideal $\overline{\text{SNR}}$ Value

Even tough the $\overline{\text{SNR}}$ value allows a fair comparison between different measurement configurations, its absolute value still is related to the noise characteristic ($\mathbf{\Sigma}_n$) and thus depends on factors influencing the voltage amplitude such as drive current, amplification gain, etc. Therefore we cannot recommend a specific range of $\overline{\text{SNR}}$ values as ideal for clinical EIT applications. Nevertheless, we suggest to set $\overline{\text{SNR}}$ such that it corresponds to a NF in the range of 0.5–2 (necessarily calculated for 16 equidistantly spaced electrodes with *adjacent* stimulation, i.e. skip 0) as suggested in [62].

11.4.5 Limitations and Future Work

In the present study we only consider the use of one-step linearised reconstruction algorithms. Nevertheless, the approach could be extended for other reconstructions – by estimating the noise response of the algorithm by means of Monte Carlo simulations – with the drawback of significantly increased computation time.

Furthermore, we restrict the induced disturbances to additive noise, even though there is evidence that this is not always appropriate for real EIT data [67, 49]. This choice is mainly justified to facilitate statistical computations and allow for an analytic and thus computationally efficient solution. Moreover, this does not represent a drawback from the current state of the art, as the NF relies on the same assumption. However, more sophisticated noise models could be taken into account when using Monte Carlo simulations.

Despite the three dimensional nature of the EIT problem and the consequent need for 3D reconstruction [31], almost all clinical chest EIT is measured and reconstructed in 2D [9]. For this reason the analysis in this chapter was also restricted to 2D EIT imaging. However, the $\overline{\text{SNR}}$ approach can be used for 3D EIT without significant modifications. In this case, the TEZ is automatically adapted – via the one-fourth amplitude threshold – to a spherically-shaped region containing the voxels of interest. Nonetheless, when comparing 2D vs 3D reconstructions, the size of the TEZ (V_{TEZ}) required for the correction factor ($k = V_{\text{TEZ}}/V_t$) must be adapted accordingly. The 2D case is only comparable to the 3D case, when its V_{TEZ} includes the area of the TEZ scaled with the slice thickness, which in turn needs to be set empirically or estimated e.g. via an average sensitivity distribution.

Moreover, the current implementation estimates the $\overline{\text{SNR}}$ from spherical targets with uniform conductivity change. However, the lung, the heart or other (parts of) anatomical structures representing more realistic conductivity changes might be better suited targets and therefore explored in the future. The introduction of targets with different shapes and conductivity changes should not be an issue. The only modification necessary would be to normalize each signal estimate S by a correction factor incorporating the relative change in conductivity $\Delta\sigma/\sigma_r$ of each target [6].

11.5 Conclusion

In summary, in this chapter we developed a new measure of noise performance ($\overline{\text{SNR}}$), which permits comparison of EIT reconstruction performance across different measurement configurations. Results are validated by simulations and phantom measurements. This measure offers advantages over current approaches (NF, LCC, GCV), as it is independent of 1) measurement configuration (skip, electrode number and position), 2) image resolution and 3) reconstruction algorithm.

12 Experimental Evaluation of an Improved Measurement Setup

Adapted from the pre-print version of [26]:

Accuracy and Reliability of Noninvasive Stroke Volume Monitoring via ECG-Gated 3D Electrical Impedance Tomography in Healthy Volunteers

Fabian Braun[1,2], Martin Proença[1,2], Andy Adler[3], Thomas Riedel[4,5], Jean-Philippe Thiran[2,6], and Josep Solà[1]

[1]Systems Division, Centre Suisse d'Electronique et de Microtechnique (CSEM), Neuchâtel, Switzerland

[2]Signal Processing Laboratory (LTS5), Ecole Polytechnique Fédérale de Lausanne (EPFL), Lausanne, Switzerland

[3]Systems and Computer Engineering, Carleton University, Ottawa, Canada

[4]Cantonal Hospital Graubuenden, Chur, Switzerland

[5]University Children's Hospital and University of Bern, Bern, Switzerland

[6]Department of Radiology, University Hospital Center (CHUV) and University of Lausanne (UNIL), Lausanne, Switzerland

Submitted to **PLOS ONE**

12.1 Introduction

In this chapter we investigate the feasibility of assessing SV in healthy volunteers.

While the two clinical trials presented in Chapters 8 and 9 use an invasive SV reference, they have the major drawback that the individual – per-patient – variations in SV are low. In contrast, much larger SV variations can be achieved in healthy subjects undergoing an experimental protocol including strenuous physical exercise. In return, these measurements are limited to the use of noninvasive SV reference devices. For the present study, ten healthy volunteers underwent an experimental protocol including postural changes and cycling exercises. EIT-based SV estimations were then compared to reference SV measured noninvasively via the oxygen uptake $\dot{V}_{O_2}$.

In addition, we make use of a 3D EIT setup in combination with an individual – subject-specific – reconstruction model generated by means of a commodity 3D camera. This is because simulations and practical measurements have revealed certain limitations of current EIT devices available for clinical monitoring, i.e. electrode belt displacement, heart displacement or mismatch of the reconstruction model are known to negatively affect SV estimation.

12.2 Methods

12.2.1 Study Protocol and Study Population

Ten healthy adult volunteers (9 male / 1 female, weight: 68.9 ± 10.8 kg, height: 179.3 ± 8.2 cm, BMI: 21.3 ± 2.0 kg/m^2, age: 35.4 ± 4.1 years) were enrolled in the study, of which all provided written informed consent. The study was approved by the local ethics committee of the canton of Vaud, Switzerland (CER-VD, 2017-00709).

This study was performed in the physiology laboratory facilities at the Swiss Center of Electronics and Microtechnique (CSEM, Neuchâtel, Switzerland). There, the subjects underwent an experimental protocol during approximately one hour including postural changes (lying flat,

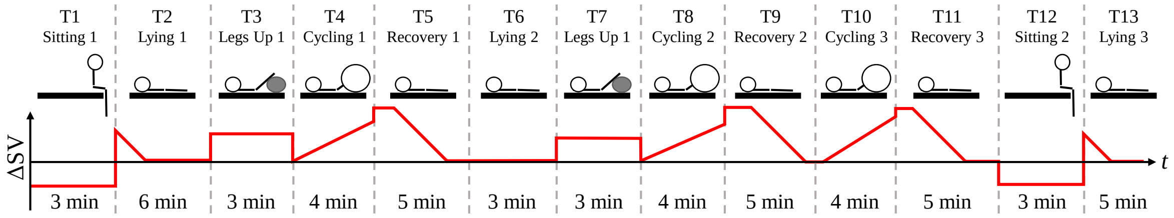

Figure 12.1 – Temporal evolution of the experimental protocol consisting of the thirteen tasks (T1 to T13) illustrated on top and the expected changes in SV shown below. The protocol comprises different postures such as sitting (T1 and T12), lying in supine position (T2, T6 and T13), lying with legs up (T3 and T7), cycling in supine position (T4, T8 and T10) and the subsequent recovery periods (T5, T9 and T11)

lying with legs up, and sitting) and bicycle exercises (cycling in supine position). The thirteen tasks (T1 to T13) performed, were expected to lead to SV variations as illustrated in Figure 12.1 and described hereafter. These SV variations are considered with respect to the baseline SV level at the end of the three lying positions (T2, T6 and T13). While sitting (T1 and T12) a lower SV is expected due to a decrease in cardiac preload. Similarly, while lying with legs up (T3 and T7), a higher SV is expected. Moreover, after the transition from sitting to lying (T1 to T2 and T12 to T13) a sharp increase of SV and subsequent decay to baseline is expected due to the augmentation in cardiac preload caused by the sudden increase in central venous return [145]. Finally, the cycling exercises in supine position (T4, T8 and T10) are expected to increase the SV, with a further – but temporary – augmentation during recovery (T5, T9 and T11) followed by a steady decrease (as reported by Cumming [39] and also known for upright exercise [60]).

12.2.2 Data Acquisition

First, the volunteers were equipped with 32 self-adhesive gel electrodes (BlueSensor T-00-S, AMBU, Ballerup, Denmark), placed on two planes with 16 electrodes each: one above and one below the nipple line, as shown in Figure 12.3a. Second, to obtain a subject-specific anatomical model and the correct electrode positions, the 3D surface of the subject's thorax was acquired using a dedicated software (ReconstructMe, version 2.5.1034, PROFACTOR GmbH, Steyr-Gleink, Austria) in combination with a 3D camera (Kinect XBOX 360, Microsoft, Redmond, USA). An example of such a 3D image is shown in Figure 12.3b. Then, the 32 electrodes were connected to a slightly modified version of the EIT SensorBelt (Swisstom AG, Landquart, Switzerland) [157] in combination with the BB^2 EIT device (Swisstom AG, Landquart, Switzerland). To achieve this connection, the conductive textile was disconnected from the active electrodes and instead, commercially available ECG cables were attached and connected to the self-adhesive gel electrodes. The electrodes were arranged as shown in Figure 12.3a, which results in the use of the "square pattern with skip 4" as suggested by Grychtol et al. [66] for 3D EIT.

An ECG was recorded using the ECG100C module (Biopac Systems, Inc., Goleta, USA). Furthermore, CO reference measurements were performed via the oxygen uptake $\dot{V}_{O_2}$ and the

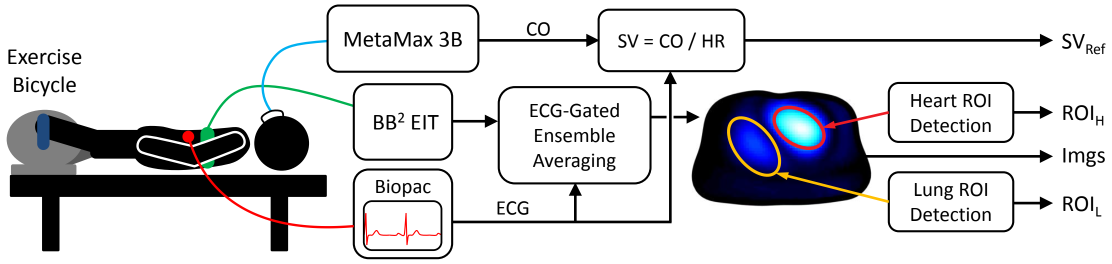

Figure 12.2 – Block diagram of the measurement setup and the first processing steps resulting in ECG-gated EIT images (Imgs) and the regions of heart (ROI$_\mathrm{H}$) and lung (ROI$_\mathrm{L}$).

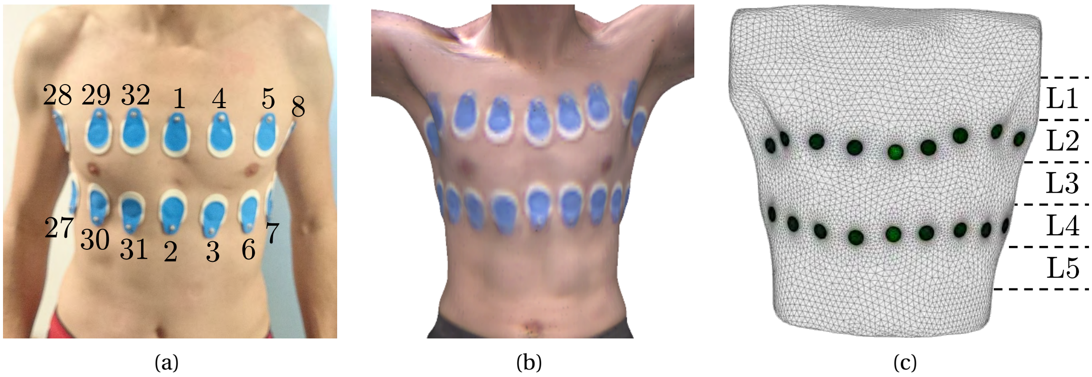

(a) (b) (c)

Figure 12.3 – (a) Placement of the 32 gel electrodes used for EIT: two planes of 16 electrodes each are placed above and below the nipple line. (b) Example image of the 3D camera and (c) the resulting 3D subject-specific model of the thorax including the electrodes (green circles). L1 to L5 illustrate the five planes on which EIT data was reconstructed (see text in Section 12.2.4).

method described by Stringer et al. [143] using MetaMax 3B (CORTEX Biophysik GmbH, Leipzig, Germany). To this end, a mask was placed on the subject's face to measure air flow and gas exchange. This measurement setup is also illustrated in Figure 12.2.

12.2.3 Data Preprocessing

First, EIT and hemodynamic data were manually aligned in the time domain with the help of deliberate spikes induced via synchronous tapping on EIT and ECG electrodes at the beginning and at the end of each recording. Then EIT samples were interpolated in the time domain to correct for the sporadic loss of certain EIT frames. Furthermore, a clock drift between EIT and ECG signals of around 0.1 s/h was observed and corrected for.

As also illustrated in Figure 12.2, EIT data was averaged via ECG-gated ensemble averaging (see Section 3.1.3) to one representative cardiac cycle per measurement. To do so, all data were first low-pass filtered (4th-order Butterworth with $f_c = 6.5\,\mathrm{Hz}$), then high-pass filtered (4th-order Butterworth with $f_c = 0.75 \cdot \mathrm{HR}/60$, with HR as the current heart rate), and finally aligned to the ECG's R-peaks. To this end, the measurements of each of the thirteen tasks (T1 to T13 in Figure 12.1) were split into one-minute sequences and each sequence was averaged to one cardiac cycle as mentioned above. Due to strong movement artefacts, data from the cycling exercises (T4, T8 and T10) were excluded from analysis.

Besides, the continuous CO measurements were divided by the instantaneous HR and averaged in the same one-minute intervals to obtain SV reference values $\mathrm{SV_{Ref}}$. It has to be noted that the CO reference device (MetaMax 3B) does only provide absolute CO values (in L/min) if the maximal oxygen uptake ($\dot{V}_{\mathrm{O_2\text{-}max}}$) is known for each subject, i.e. $\mathrm{CO} = \dot{V}_{\mathrm{O_2}} \Big/ \left(57.21 + 104.7 \frac{\dot{V}_{\mathrm{O_2}}}{\dot{V}_{\mathrm{O_2\text{-}max}}}\right)$ [143]. Since $\dot{V}_{\mathrm{O_2\text{-}max}}$ was not evaluated in the present experimental protocol, it was estimated using the model suggested by Jackson et al. [85]:

$$\dot{V}_{\mathrm{O_2\text{-}max}} = (56.363 + 1.921 \cdot \mathrm{PAS} - 0.381 \cdot \mathrm{A} - 0.754 \cdot \mathrm{BMI} + 10.987 \cdot \mathrm{S}) \, \frac{\mathrm{W}}{1000} \quad [\mathrm{L/min}] \quad (12.1)$$

Where PAS denotes the physical activity on the NASA/JSC scale [85], A the age in years, BMI the body mass index in kg/m^2, S the sex (0 female, 1 male), and W the weight in kg.

12.2.4 Subject-Specific EIT Image Reconstruction

For each volunteer, a subject-specific model for EIT image reconstruction was created. To do so, the 3D surface of the thorax scan (acquired as described in Section 12.2.2 and shown in Figure 12.3b) was processed in Blender (version 2.78c, Blender Foundation, Amsterdam, the Netherlands) by cropping parts not located in the EIT planes of interest (e.g. arms and neck) and transformed to a triangulated mesh. The electrode positions were then manually located in the 3D scan. The thorax mesh was further resampled and smoothed using OpenFlipper (version 3.1, Computer Graphics Group, RWTH Aachen, Germany) [104]. Finally, the electrodes were placed on the mesh using the approach proposed by Grychtol and Adler [65] and implemented in EIDORS [5]. An example of such a subject-specific thorax model is shown in Figure 12.3c.

EIT data were reconstructed using the 3D GREIT algorithm [66] onto images with 32 × 32 × 5 voxels. The five image planes L1 to L5 used for reconstruction (see Figure 12.3c) are equally spaced at a distance of half the spacing between the two electrode planes. L2 is placed at the height of the upper, L4 at the height of the lower, and L3 in between the two electrode planes. The algorithm was trained using roughly 10’000 targets located on eleven equidistantly spaced levels: at each voxel location (on the five image planes L1 to L5) plus six more planes (one located above L1, four in between L1 and L5, and one below L5). To focus image reconstruction on the three central image planes (L2 to L4) the seven target planes located in the middle contain twice as much targets than the two uppermost and lowermost target planes. To achieve a comparable noise performance (independent of the geometry of the subject’s thorax) each algorithm was set to have a fixed image SNR ($\overline{\mathrm{SNR}} = 6.5 \times 10^{-3}$) [25], which compares to an average noise figure [3, 62] of NF = 0.53.

For each subject an individual background conductivity σ_{BG} was used for the reconstruction model. σ_{BG} was obtained by finding the closest fit (in terms of absolute error) between simulated voltages on the thorax model with homogeneous σ_{BG} and the temporal average of measured raw EIT voltages during baseline (defined as the last minute of task T2). The difference EIT images were then reconstructed with respect to the baseline and σ_{BG} was added to each voxel. In this way, an approximative but simple absolute EIT reconstruction was performed.

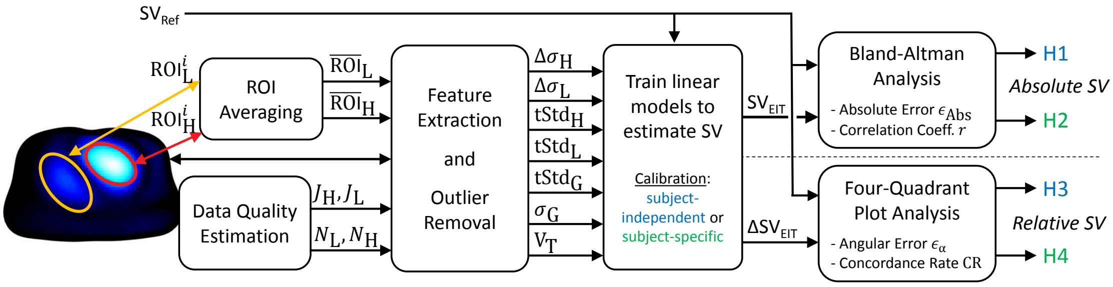
SV_{Ref}
ROI^i_L
ROI^i_H
ROI Averaging
$\overline{ROI}_L$
$\overline{ROI}_H$
Data Quality Estimation
J_H, J_L
N_L, N_H
Feature Extraction and Outlier Removal
$\Delta\sigma_H$
$\Delta\sigma_L$
$tStd_H$
$tStd_L$
$tStd_G$
σ_G
V_T
Train linear models to estimate SV
Calibration:
subject-independent or subject-specific
SV_{EIT}
ΔSV_{EIT}
Bland-Altman Analysis
- Absolute Error ϵ_{Abs}
- Correlation Coeff. r
H1
Absolute SV
H2
Four-Quadrant Plot Analysis
- Angular Error ϵ_α
- Concordance Rate CR
H3
Relative SV
H4

Figure 12.4 – Block diagram of the data analysis. To test the four hypotheses (H1 to H4), different features were extracted from the EIT images and potential outliers with high noise or unstable heart and lung ROIs were removed. Then, the ability to estimate SV with these features via a linear model was evaluated by means of Bland-Altman analysis (absolute SV_{EIT} in H1 and H2) or four-quadrant plot analysis (relative ΔSV_{EIT} in H3 and H4).

12.2.5 Data Analysis

In the present study we tested four hypotheses (H1 to H4), namely whether EIT can be used to either estimate absolute SV (H1 and H2) or to trend relative changes of SV (H3 and H4). For H1 and H3 we used a subject-independent and for H2 and H4 a subject-specific calibration. This analysis is detailed in the current section and illustrated and briefly described in Figure 12.4.

First, from each EIT image sequence of the one-minute averages, the heart and lung regions were determined using the following algorithms: the heart was detected as described in Section 6.2.3 and the lungs via the algorithm proposed by Proença et al. [120, 121]. For each subject an average heart and lung region was calculated and used for the subsequent calculations. To this end, the current ROI (ROI^i_H or ROI^i_L) of the measurement i was averaged to the per-subject average ($\overline{ROI}_H$ or $\overline{ROI}_L$), i.e. $\overline{ROI}_H$ or $\overline{ROI}_L$ contain the biggest connected regions of heart or lung voxels which are present in at least 50 % (determined heuristically) of the individual ROIs.

Second, a variety of features were extracted from the EIT images: 1. $\Delta\sigma_H$, the systolic heart amplitude as the difference of maximum vs minimum in the temporal signal of the heart region; 2. $\Delta\sigma_L$, the systolic lung amplitude, same as $\Delta\sigma_H$ but for the lung region; 3. $tStd_H$, the heart amplitude as the standard deviation (STD) of the temporal signal in the heart region; 4. $tStd_L$, the lung amplitude, same as $tStd_H$ but for the lung region; 5. $tStd_G$, the global amplitude as the STD of the temporal signal of the sum over all voxels; 6. σ_G, the global conductivity as the mean absolute value of all voxels; 7. V_T, the average tidal volume as the peak-to-peak respiratory amplitude from the sum signal over all voxels. The latter two were calculated prior to ensemble averaging and high-pass filtering.

Then, assuming a linear relationship between changes in SV and these features, various linear models were trained and evaluated to test the following four hypotheses:

(H1) **Absolute SV with subject-independent calibration**: For each subject a linear model was trained using all other subjects via leave-one-out cross-validation. The resulting performance was evaluated by means of absolute error ϵ_{Abs} (in mL) between SV_{EIT} and SV_{Ref} resulting from Bland-Altman analysis [12] and correlation coefficient[1] r between SV_{EIT} and SV_{Ref}. Measurements were considered as acceptable if $r \geq 0.7$ (educated guess) and the 95 % limits of agreement of ϵ_{Abs} did not exceed ±24 mL (= ±30 % – the error reported for thermodilution measurements [37] – of the average SV_{Ref}).

(H2) **Absolute SV with subject-specific calibration**: This is identical to the first hypothesis (H1), except that a linear model was trained for each subject individually.

(H3) **Trending of relative SV with subject-independent calibration**: For this and the next hypothesis, the features as well as the reference SV were set relative to an initial baseline[2]. This leads to the measurement of changes $\Delta\text{SV}_{\text{EIT}}$ which are compared to changes in the reference $\Delta\text{SV}_{\text{Ref}}$ by means of angular concordance rate CR and angular error ϵ_α resulting from four-quadrant plot analysis [37, 130], also explained in Section 6.2.4. For each subject a linear model was trained using all other subjects via leave-one-out cross-validation. Measurements with CR ≥ 92 %, a bias of $\epsilon_\alpha \leq \pm 5°$ and its 95 % limits of agreement $\leq \pm 30°$, were considered as acceptable, according to the thresholds suggested by Critchley et al. [38]. The exclusion zone of the four-quadrant plot was set to ±30 % – the error for thermodilution measurements [37].

(H4) **Trending of relative SV with subject-specific calibration**: This is identical to the third hypothesis (H3), except that a linear model was trained for each subject individually.

Finally, to limit the analysis to reliable data, four data quality measures were introduced (identical with the approach in Section 9.2.3): (1) a similarity measure J_H for the heart region of interest (ROI) comparing the current $\text{ROI}_{\text{H}}^{i}$ of the measurement i to the per-subject average $\overline{\text{ROI}_{\text{H}}}$ via the so-called *Jaccard index* ($J_H = |\text{ROI}_{\text{H}}^{i} \cap \overline{\text{ROI}_{\text{H}}}| / |\text{ROI}_{\text{H}}^{i} \cup \overline{\text{ROI}_{\text{H}}}|$) [84]; (2) the same similarity measure as J_H but for the lung ROI denoted as J_L; (3) N_H and (4) N_L as signal quality indicators estimating the average noise level in the heart and lung region from the relative deviation of each pulse used for ensemble averaging (see also Appendix B). Only measurements with $J_H \geq 75\,\%$, $J_L \geq 75\,\%$, $N_H > 2.0$ and $N_L > 2.0$ were considered for analysis. The threshold of N_L and N_H were determined based on visual analysis of ensemble averaged signals.

Moreover, the raw EIT data of subject S07 showed severe issues with electrode contact impedance leading to corrupted EIT images. It was therefore completely removed from analysis.

---

[1] Note that in contrast to the two previous studies (see Chapters 8 and 9), here the correlation coefficient r was used as a valuable measure for the strength of linear relationship between SV_{EIT} and SV_{Ref}. This is because only in the current study sufficient measurements with high variations in SV are available for each patient.

[2] The baseline state was defined as the average of the measurements having the three lowest values of SV_{Ref}.

12.3 Results and Discussion

12.3.1 General Overview of EIT Data

Figure 12.5 exemplifies respiratory activity of each volunteer by means of standard deviation (SD) images. The strongest respiratory activity can be observed at the lower electrode plane (L4) or in between the two planes (L3). Moreover, the two lung lobes appear separated in the lower image planes (L3 to L5) and more unified in the upper planes (L1 to L2), which is comparable to the observations by Karsten et al. [88].

Figure 12.6 shows ECG-gated EIT images by the example of one measurement (last minute of the first recovery sequence – task T5) for the nine subjects analyzed. One can observe that the potential heart regions (blue-white with $\Delta\sigma < 0$) are located in the middle (L3) or lower image plane (L4). On the contrary, the potential lung regions (red-yellow with $\Delta\sigma > 0$) are more present in the upper (L2) or middle image plane (L3). This is in line with the anatomy (i.e. the large pulmonary arteries are located more cranial when compared to the heart, which itself is lower, sitting right on the diaphragm) and observations by Smit et al. [135] who use a high belt placement for cardiovascular EIT of the lungs. Besides, when compared to the other subjects, S08 and S09 show only little activity in the heart with respect to the lung region. It is assumed that for these subjects the lower electrodes were placed too high which decreases the sensitivity in the heart region.

The ECG-gated EIT images shown in Figure 12.7 represent different tasks of the same subject. One can observe a significant difference in spatial conductivity distribution between the following three groups of recordings: (1) sitting in (a) and (j), (2) lying with legs up in (c), and (3) the remaining recordings in supine position. These differences were observed for all

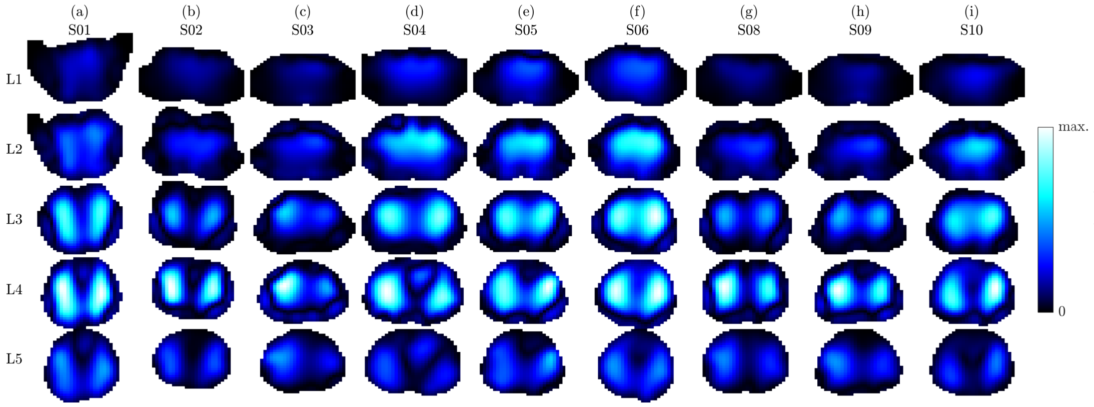

Figure 12.5 – 3D EIT images showing the respiration by means of standard deviation (SD) images on the five planes L1 (highest) to L5 (lowest) for the nine volunteers (a) to (i), in supine position. The images of each subject (each column) were scaled to an individual color scale and show the last minute in the first recovery sequence (task T5). Prior to SD calculation the images were filtered using a 2nd-order Butterworth bandpass with $f_c = \{0.04, 0.5\}$ Hz.

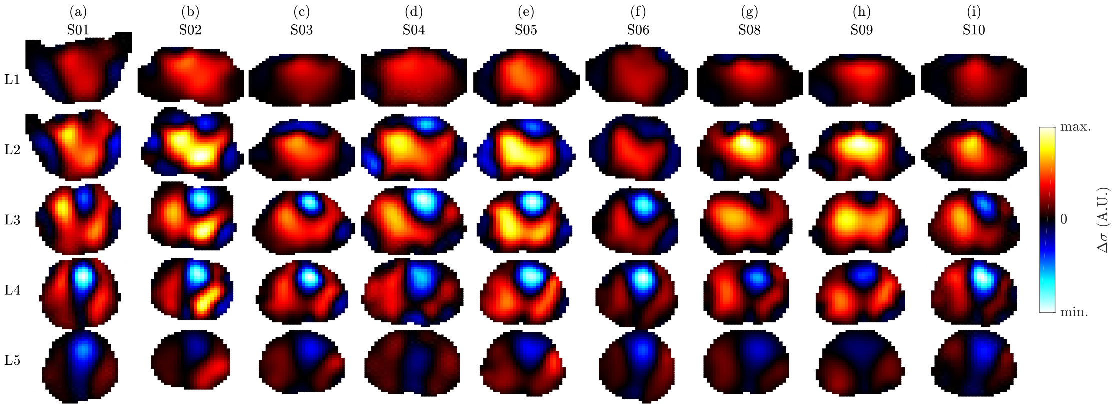
(a)
S01
(b)
S02
(c)
S03
(d)
S04
(e)
S05
(f)
S06
(g)
S08
(h)
S09
(i)
S10
L1
L2
L3
L4
L5
max.
0
min.
Δσ (A.U.)

Figure 12.6 – ECG-gated 3D EIT images showing the conductivity difference (end systole vs end diastole) on the five planes L1 (highest) to L5 (lowest) for the nine volunteers (a) to (i), in supine position. The images of each subject (each column) were scaled to an individual color scale and show the average of the last minute in the first recovery sequence (task T5).

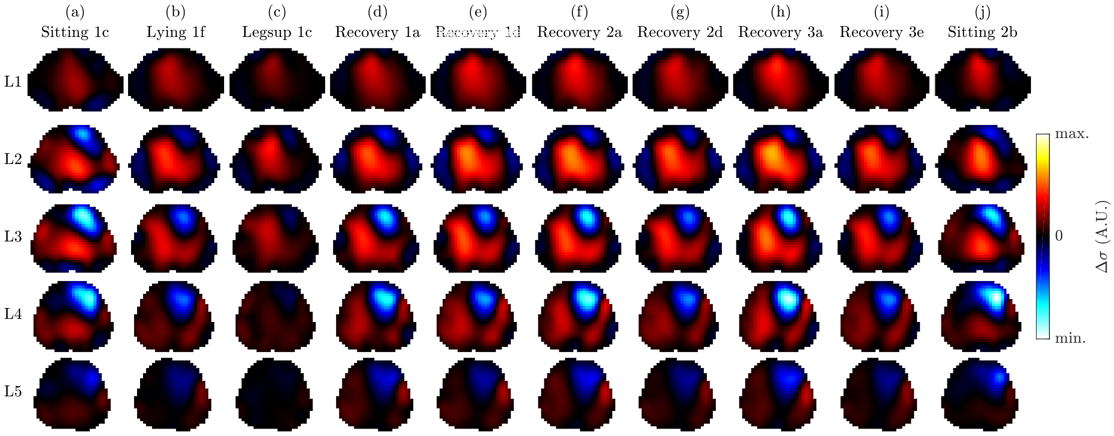
(a)
Sitting 1c
(b)
Lying 1f
(c)
Legsup 1c
(d)
Recovery 1a
(e)
Recovery 1d
(f)
Recovery 2a
(g)
Recovery 2d
(h)
Recovery 3a
(i)
Recovery 3e
(j)
Sitting 2b
L1
L2
L3
L4
L5
max.
0
min.
Δσ (A.U.)

Figure 12.7 – ECG-gated 3D EIT images showing the conductivity difference (end systole vs end diastole) on the five planes L1 (highest) to L5 (lowest) for a selection of ten measurements (a) to (j) of volunteer S05. All images are shown in a common color scale.

subjects and are hypothesized to stem from posture-induced heart and lung displacement as well as gravity-induced liquid redistribution in the lungs. On the other hand, when limiting the analysis to the third group of recordings (i.e. all tasks in supine position, except for lying with legs up), the spatial conductivity distribution remains comparable while mainly the amplitude changes.

The high variability observed between these three groups could lead to changes in the ROIs and also their amplitudes which are not necessarily related to changes in SV. Therefore, to limit our analysis to more controlled scenarios and to make it comparable with previous studies [155, 114, 41] (all measured in supine position), only measurements of the last group were considered, i.e. those recorded in supine position (T2, T5, T6, T9, T11 and T13). From the nine subjects remaining for analysis (S07 was excluded as mentioned before), a total of 242 one-minute sequences were available. From these, 11 (4.5 %) and 4 (1.7 %) were excluded because of a too high noise level in the heart ($N_H > 2.0$) and lungs ($N_L > 2.0$), respectively. Then, 76 (31.4 %) and 0 were excluded due to too high variability of the heart ($J_H < 75\%$) and lung region ($J_L < 75\%$), as specified in Section 12.2.5, as specified in Section 12.2.5. The remaining 151 (62.4 %) one-minute sequences represent controlled measurements (low noise, stable heart and lung regions, all acquired in supine position), which were further used to investigate the feasibility of EIT-based SV monitoring as presented in the next four sections.

12.3.2 Hypothesis 1: Absolute SV with Subject-Independent Calibration

In the current and the following section we report on the feasibility of EIT to determine absolute values of SV (in mL).

Row (H1) in Table 12.1 shows the overall performance (in terms of absolute error ϵ_{Abs} and correlation coefficient r) for a selection of features tested when using a subject-independent (leave-one-out) calibration. One can observe that for none of the eight features an acceptable performance can be achieved. This confirms our previous observations and the findings by other researchers [41, 114] that a subject-specific calibration is required for absolute SV estimation.

Subject-specific performances for hypothesis (H1) are given in the appendix in Table E.1.

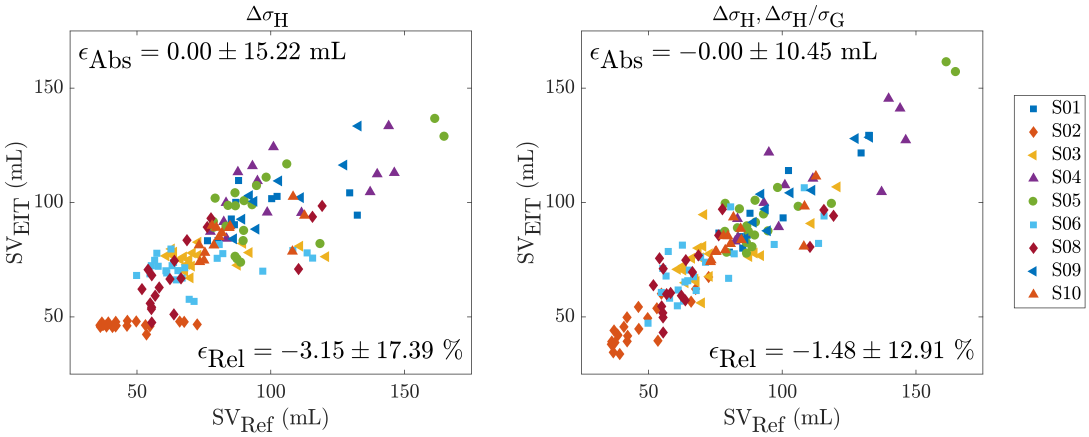

(a) (b)

Figure 12.8 – SV_{EIT} vs SV_{Ref} for a subject-specific calibration in hypothesis (H2) with the features (a) $\Delta\sigma_H$ or (b) $\Delta\sigma_H$ and $\frac{\Delta\sigma_H}{\sigma_G}$.

Table 12.1 – Overall performance for a selection of features and the four hypotheses: (H1) absolute SV via subject-independent calibration, (H2) absolute SV via subject-specific calibration, (H3) relative SV via subject-independent calibration, and (H4) relative SV via subject-specific calibration. (H1) and (H2) are evaluated in terms of absolute error ϵ_{Abs} and correlation coefficient r between $\mathrm{SV}_{\mathrm{EIT}}$ and $\mathrm{SV}_{\mathrm{Ref}}$. (H3) and (H4) are evaluated in terms of angular error ϵ_α and angular concordance rate CR between $\Delta\mathrm{SV}_{\mathrm{EIT}}$ and $\Delta\mathrm{SV}_{\mathrm{Ref}}$. The (†) indicates unrealistic solutions with calibrations coefficients *not* having identical sign for all subjects. Cell shadings indicate whether the acceptance criteria (see Section 12.2.5) are met (green), not met (red), or met but with unrealistic calibration coefficients (yellow). The errors ϵ_{Abs} and ϵ_α are given as Mean ± Std and the 95 % limits of agreement correspond to [Mean − 1.96 · Std, Mean + 1.96 · Std].

	Absolute SV				**Trending of Relative SV**			
	(H1) Hypothesis 1		(H2) Hypothesis 2		(H3) Hypothesis 3		(H4) Hypothesis 4	
	ϵ_{Abs} (mL)	r (1)	ϵ_{Abs} (mL)	r (1)	ϵ_α (°)	CR (%)	ϵ_α (°)	CR (%)
$\Delta\sigma_{\mathrm{H}}$	−0.5 ± 28.2	−0.424	0.0 ± 15.2	0.813	−5.3 ± 25.2	76.9	−1.0 ± 23.0	80.9
$\mathrm{tStd}_{\mathrm{H}}$	−1.0 ± 27.3	0.023	(†) 0.0 ± 14.3	0.836	−4.9 ± 26.5	73.8	(†) −3.9 ± 21.5	83.3
$\Delta\sigma_{\mathrm{L}}$	−0.4 ± 27.3	−0.023	(†) 0.0 ± 15.8	0.796	−12.1 ± 20.3	70.4	(†) −0.2 ± 22.5	84.6
$\mathrm{tStd}_{\mathrm{L}}$	−0.5 ± 28.1	−0.341	(†) 0.0 ± 17.1	0.755	−17.4 ± 16.7	70.2	(†) −5.8 ± 20.4	91.5
$\mathrm{tStd}_{\mathrm{G}}$	(†) −0.5 ± 28.2	−0.710	(†) 0.0 ± 16.8	0.766	(†) −15.6 ± 25.7	73.3	(†) 2.0 ± 24.2	74.4
$\Delta\sigma_{\mathrm{H}}, \frac{\Delta\sigma_{\mathrm{H}}}{\sigma_{\mathrm{G}}}$	−1.7 ± 30.4	−0.365	0.0 ± 10.4	0.917	−1.9 ± 20.4	83.9	1.0 ± 17.5	87.7
$\Delta\sigma_{\mathrm{L}}, \frac{\Delta\sigma_{\mathrm{L}}}{\sigma_{\mathrm{G}}}$	(†) −0.4 ± 28.4	−0.050	0.0 ± 10.3	0.920	−1.7 ± 21.7	84.2	1.3 ± 16.7	93.0
V_{T}	−0.4 ± 24.7	0.371	0.0 ± 9.7	0.929	−1.5 ± 18.5	89.8	−0.4 ± 15.3	94.7

12.3.3 Hypothesis 2: Absolute SV with Subject-Specific Calibration

Row (H2) in Table 12.1 shows the overall performance when using a subject-specific calibration. When concentrating the analysis on the five amplitude features ($\Delta\sigma_{\mathrm{H}}$, $\mathrm{tStd}_{\mathrm{H}}$, $\Delta\sigma_{\mathrm{L}}$, $\mathrm{tStd}_{\mathrm{L}}$, $\mathrm{tStd}_{\mathrm{G}}$), one can observe that all of the overall errors have limits of agreement exceeding the ±24 mL threshold (= ± 30 % of the average $\mathrm{SV}_{\mathrm{Ref}}$ as specified in Section 12.2.5). Moreover, except for $\Delta\sigma_{\mathrm{H}}$, no uniform calibration could be found with either all positive or negative calibration coefficients (marked with a (†)). The relationship between $\mathrm{SV}_{\mathrm{EIT}}$ and $\mathrm{SV}_{\mathrm{Ref}}$ of the feature $\Delta\sigma_{\mathrm{H}}$ is shown in Figure 12.8a. One can observe that at least for subject S03, $\mathrm{SV}_{\mathrm{EIT}}$ does not at all follow the changes in $\mathrm{SV}_{\mathrm{Ref}}$. This particular case of S03 is illustrated in more detail in Figure 12.9 (Middle) by means of the temporal evolution of $\mathrm{SV}_{\mathrm{Ref}}$ in comparison to the two features related to the heart amplitude ($\mathrm{tStd}_{\mathrm{H}}$ and $\Delta\sigma_{\mathrm{H}}$). The same figures for the remaining subjects are available in Appendix E in Figures E.1 to E.8. It is obvious from these findings that – for the present data – changes in the heart-related amplitude ($\mathrm{tStd}_{\mathrm{H}}$ or $\Delta\sigma_{\mathrm{H}}$) are not solely related to changes in SV. This is in line with the findings from simulations (presented in Chapter 6), that the EIT heart signal is influenced by other factors and – among others – scaled with the heart-lung-conductivity contrast (difference of heart vs lung conductivity).

When taking into account the global conductivity σ_{G} to normalize the systolic heart amplitude $\Delta\sigma_{\mathrm{H}}$ (i.e. $\mathrm{SV}_{\mathrm{EIT}} = \kappa_0 + \kappa_1 \cdot \Delta\sigma_{\mathrm{H}} + \kappa_2 \cdot \Delta\sigma_{\mathrm{H}}/\sigma_{\mathrm{G}}$) the absolute error can be reduced to ±10.45 mL

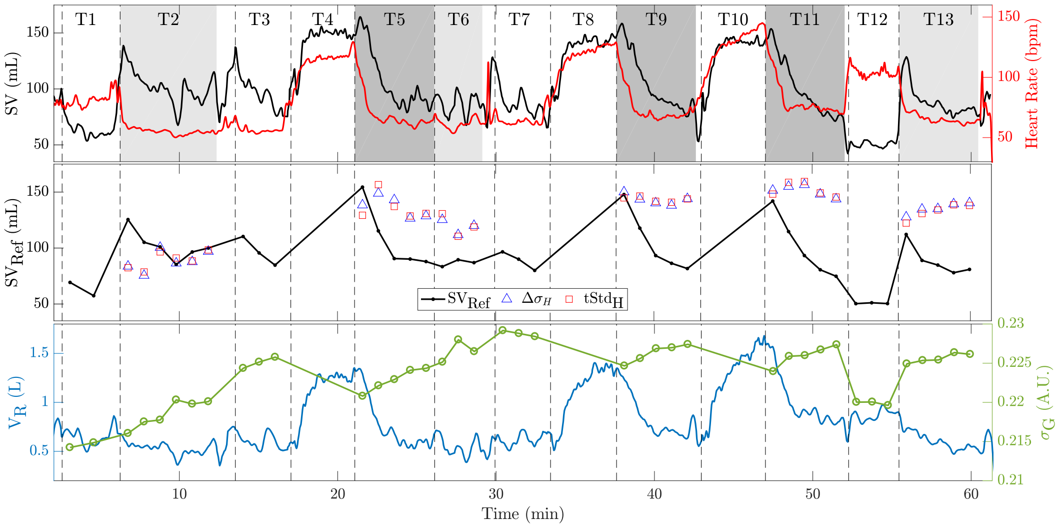

Figure 12.9 – (Top) Example of temporal evolution of reference stroke volume (black) and heart rate (red) for the entire protocol comprised of tasks T1 to T13 (see Figure 12.1) for subject S03. The beginning of each task is marked with a vertical line (- - -) and the particular tasks considered for analysis are shaded in light (lying) or dark gray (recovery). (Middle) One-minute averages used for analysis showing SV_{Ref} and two EIT features: the systolic heart amplitude ($\Delta\sigma_{\text{H}}$) and the temporal standard-deviation of the heart signal during one full cardiac cycle (tStd_{H}). (Bottom) Tidal volume V_{R} (blue) measured by the reference device (MetaMax 3B) and the one-minute averages of the global conductivity feature σ_{G} (green).

as shown in Figure 12.8b and listed in Table 12.1(H2). It is known from simulations (see also Chapter 6) that the EIT heart amplitude is scaled by the aforementioned heart-lung-conductivity contrast (HLC). As σ_{G} contains information about the lung conductivity, it is hypothesized that it serves as a rough estimate of the HLC and thus allows for correction of this scaling. While the exact physiological background is not fully understood, it still shows that normalizing $\Delta\sigma_{\text{H}}$ by σ_{G} can lead to improved results. A similar reduction in error can be achieved when normalizing the lung amplitude by σ_{G}. A possible reason might be that the lung amplitude estimates are similarly affected by changes in global conductivity and thus require normalization.

However, it needs to be mentioned that in the current protocol the EIT-derived tidal volume V_{T} is highly correlated with changes in SV (average corr. coefficient $\overline{r} = 0.85$, range $r \in [0.59, 0.96]$) as also shown by the low absolute error for V_{T} in Table 12.1(H2). At the same time the global conductivity σ_{G} is influenced by the tidal volume V_{T} ($\text{V}_{\text{T}} \uparrow \Rightarrow \sigma_{\text{G}} \downarrow$). Nonetheless, σ_{G} has other influencing factors such as the content of liquid in the lungs (e.g. blood or water), the posture (including the position of the torso and the arms [153]) and the contact impedance of EIT electrodes (i.e. varying external pressure on electrodes can lead to changes in global conductivity [51]). Based on the current protocol, it can neither be excluded nor fully confirmed that using the normalized heart ($\Delta\sigma_{\text{H}}/\sigma_{\text{G}}$) or lung amplitudes ($\Delta\sigma_{\text{L}}/\sigma_{\text{G}}$) leads to an improved estimation of SV (as in this protocol the latter is highly correlated to V_{T} which in turn is related to $1/\sigma_{\text{G}}$).

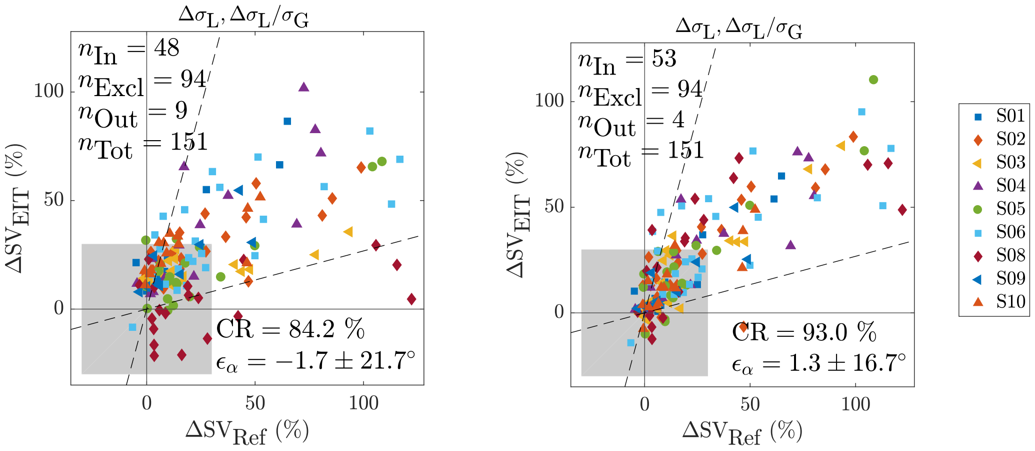

(a) (b)

Figure 12.10 – Trending ability of ΔSV_{EIT} vs ΔSV_{Ref} shown by means of four-quadrant plots for the combination of the two features $\Delta\sigma_L$ and $\frac{\Delta\sigma_L}{\sigma_G}$ and (a) a subject-independent calibration for hypothesis (H3) or (b) a subject-specific calibration for hypothesis (H4). The exclusion zone was set to ±30 %.

Subject-specific performances for hypothesis (H2) are given in the appendix in Table E.2.

12.3.4 Hypothesis 3: Relative SV with Subject-Independent Calibration

In the current and the following section we report on the feasibility of EIT to perform trending of SV, that is following the relative change ΔSV_{EIT} (in %) with respect to an initial baseline value.

The performances obtained for a subject-independent (leave-one-out) calibration are listed in Table 12.1(H3). For none of the features tested, an acceptable trending performance can be obtained. An example is given in Figure 12.10a for the normalized lung amplitude $(\Delta\sigma_L, \Delta\sigma_L/\sigma_G)$ which leads to the best performance in terms of CR (when not considering V_T).

Subject-specific performances for hypothesis (H3) are given in the appendix in Table E.3.

12.3.5 Hypothesis 4: Relative SV with Subject-Specific Calibration

The performances obtained when using a subject-specific calibration are listed in Table 12.1(H4). While the four simple features ($tStd_H$, $\Delta\sigma_L$, $tStd_L$ and $tStd_G$) do not lead to realistic calibration factors with a same sign, $\Delta\sigma_H$ does. However, none of these features fulfill the trending requirements in terms of ϵ_α and CR. This also applies to the normalized versions of $(\Delta\sigma_H, \Delta\sigma_H/\sigma_G)$ and $(\Delta\sigma_L, \Delta\sigma_L/\sigma_G)$. Even though they have a CR very close to or above the acceptable 92 %, they both exceed the acceptance threshold in terms of 95 % limits of agreement with [−33.3, 35.3]° and [−31.4, 34.0]°, respectively. The latter is also shown in Figure 12.10b.

Subject-specific performances for hypothesis (H4) are given in the appendix in Table E.4.

12.3.6 Limitations and Future Work

This study is limited in that it was performed on healthy volunteers which restricts the reference SV to be measured with noninvasive devices. The SV reference measurement device used is not considered as gold standard [37], as simply no noninvasive gold standard exists. Nonetheless, it is possibly among the most accurate when requiring continuous and noninvasive measurements on healthy subjects performing physical exercise. Besides, in the current experimental protocol, the tidal volume $\mathrm{V_T}$ is highly correlated to SV (mainly during post-exercise recovery). In addition, the reference method used to estimate SV relies on the measurement of the oxygen uptake which in turn is related to $\mathrm{V_T}$. Therefore it is unclear whether this does not even exacerbate the high correlation between $\mathrm{V_T}$ and SV. To either confirm or reject our hypothesis that σ_G is useful for normalizing $\Delta\sigma_\mathrm{H}$ and $\Delta\sigma_\mathrm{L}$ – and not simply because it is related to $\mathrm{V_T}$ – a different experiment protocol should be designed, where SV is less correlated to $\mathrm{V_T}$.

The subject-specific EIT reconstruction model used was acquired in sitting position while EIT images were mainly analyzed in supine position. In addition, big differences in the spatial conductivity distribution were observed in EIT images between sitting and supine. To exclude the potential influence of the reconstruction model on these differences, an additional model in supine position (e.g. via MRI scans) should be created. Besides, when aiming for EIT-based SV in different body positions, a deeper understanding of the observed differences is crucial.

One could further criticize the manual synchronization performed between EIT and ECG. However, its accuracy was first tested in the laboratory and the error has shown to be below two EIT frames ($< \pm 40\,\mathrm{ms}$). Moreover, all ensemble averaged sequences were visually verified for physiological meaningful time delays. Even though this approach is sufficient for amplitude-based measures used in the present study, it is not accurate enough for EIT-based timing measures [137, 120] which necessitates an EIT system synchronously measuring ECG [123].

12.4 Conclusion

In this work, we investigated the EIT-based estimation of SV in healthy subjects and compared it to reference measurements derived from the oxygen uptake $\dot{V}_{\mathrm{O_2}}$. Large variations in SV were induced via postural changes and recovery after supine cycling exercise. To minimize known influences of heart and belt displacement on EIT-based SV, 3D EIT with self-adhesive gel electrodes in combination with a subject-specific reconstruction model was applied.

The ECG-gated 3D EIT images show large differences in spatial conductivity distribution between sitting, lying with legs up and supine position. To limit the analysis to very isolated and constant settings, only measurements in supine position were considered and 38.4 %

of the remaining measurements were excluded due to high noise or unstable heart or lung regions. The temporal amplitudes in the heart ($\Delta\sigma_\mathrm{H}$ and tStd_H) [114, 155], the lungs ($\Delta\sigma_\mathrm{L}$ and tStd_L) [41, 113], or in the entire image (tStd_G) were calculated but none of them showed an accurate relation to the reference SV_Ref. Therefore, we cannot confirm the recent observations made in pig experiments [114, 41, 113]. And this despite having used a subject-specific 3D EIT measurement setup to minimize effects of electrode displacement or out-of-EIT-plane movement of the heart.

Based on findings from simulations (see Chapter 6), the heart amplitude $\Delta\sigma_\mathrm{H}$ normalized by the global conductivity σ_G was included as a feature. The resulting linear combination ($\mathrm{SV}_\mathrm{EIT} = \kappa_0 + \kappa_1 \cdot \Delta\sigma_\mathrm{H} + \kappa_2 \cdot \frac{\Delta\sigma_\mathrm{H}}{\sigma_\mathrm{G}}$) leads to more promising results. That is an overall error of 0.0 ± 10.4 mL for absolute SV with a subject-specific calibration. When aiming for the trending of relative changes in SV with the same type of calibration, we achieve a performance of $\epsilon_\alpha = 1.0 \pm 17.5°$ and $\mathrm{CR} = 87.7\,\%$. Similar results were obtained when using the lung amplitude normalized by σ_G, i.e. $\mathrm{SV}_\mathrm{EIT} = \kappa_0 + \kappa_1 \cdot \Delta\sigma_\mathrm{L} + \kappa_2 \cdot \frac{\Delta\sigma_\mathrm{L}}{\sigma_\mathrm{G}}$. In contrast, both absolute and relative SV do not seem to be feasible when using a subject-independent calibration.

However, in the current protocol, SV is highly correlated to the tidal volume V_T, which in turn is related to σ_G. The current findings should therefore be considered with caution since the normalization attempts suggested might primarily lead to a satisfactory outcome because of the relation between V_T and σ_G. To either confirm or reject our hypothesis that $\Delta\sigma_\mathrm{H}$ or $\Delta\sigma_\mathrm{L}$ normalized by σ_G lead to reliable SV estimates, a different experiment protocol is required, where SV is less correlated to V_T.

In conclusion, we could show that even with a subject-specific 3D EIT setup on healthy volunteers, purely amplitude-based features are very unlikely to provide feasible SV estimates in experimental conditions as they are influenced by other factors (such as lung and heart conductivity, posture and electrode contact impedance). While the normalization of the heart or lung amplitudes via the global conductivity shows promise on the current data, this approach requires confirmation in different experimental protocols.

Conclusions Part V

13 Synthesis

The aim of the present thesis was to investigate the feasibility of noninvasively measuring stroke volume (SV) via electrical impedance tomography (EIT), with particular focus on its practical applicability. This was investigated in three different ways. First, the feasibility and limitations of EIT-based SV estimation were studied *in-silico* by means of simulations on a bioimpedance model of the human thorax (Part II). Second, two clinical trials were performed to verify this approach *in-vivo* and under real-life conditions (Part III). Finally, in view of overcoming potential limitations of currently available clinical EIT systems, an improved setup was proposed and tested in an experimental protocol on healthy volunteers (Part IV).

In the following, we first list the major contributions, then summarize the key findings of the present thesis, review its limitations and finally address the aspects requiring further research.

13.1 Thesis Contributions

The major contributions of this thesis can be summarized as follows:

1. The creation of a 4D bioimpedance model used to investigate the origins of EIT signals [21] and the feasibility of estimating hemodynamic parameters via EIT [24, 23, 22].
2. The demonstration via simulations on this model that although the EIT heart amplitude is dominated by ventricular activity [21], it does not represent blood volume changes but rather the alternating spatial replacement of lung vs heart tissue [24].
3. The demonstration via simulations on the same model that measuring absolute SV is extremely challenging but trending of relative SV changes is more promising [24].
4. The demonstration via two clinical studies that measuring absolute SV via EIT is unlikely to be feasible, neither via the heart nor the lung amplitude.
5. The demonstration via the same studies that trending of SV is feasible via the lung amplitude but not via the heart amplitude and only under very controlled conditions.

6. The design of an improved measurement setup (ECG-gated 3D EIT) targeted for SV estimation and intended to overcome potential limitations of available clinical EIT systems.

7. The demonstration via experiments on healthy volunteers that even with this improved setup, EIT-based SV is very challenging since amplitude-based estimates can easily be impaired and that this approach might be limited to very controlled environments only.

8. The creation of a novel noise performance metric ($\overline{\text{SNR}}$) which permits the comparison of EIT reconstruction performance across different measurement setups [25].

13.2 Summary of Achievements

In-Silico EIT Measurements via Simulations on a 4D Bioimpedance Model

The first main achievement of this thesis is the creation of a 4D bioimpedance model of the human thorax allowing for *in silico* measurements of cardiovascular EIT by means of simulations (Chapter 4). The model contains representations of the heart, the aorta and the lungs and reflects the electrical conductivity distribution during one cardiac cycle. It was created in close collaboration with Dr M. Proença whose thesis [118] was focused on the assessment of pulmonary artery pressure and who is the main architect of the lung model.

By means of simulations on this model we gained more insights into the origins of EIT signals in the heart region (Chapter 5). It was found that the heart signal is dominated by ventricular activity (≥77 %) giving hope for EIT-based SV estimation. We further observed that, unlike suggested in the literature [154], the use of an oblique EIT belt placement does not lead to a substantially better separation between ventricular and atrial activity.

In the next step, we studied – still *in silico* – whether the EIT heart amplitude could be used as surrogate measure for SV (Chapter 6). Under isolated conditions the EIT-derived SV (SV_{EIT}) correlated very well ($r > 0.99$) with the reference SV. We further investigated four confounding factors that could potentially deteriorate such measurements. Our analysis showed that changes in hematocrit or detachment of electrode pairs do not substantially impair the estimation of SV. On the other hand, longitudinal or rotational EIT belt displacements and changes in lung air volume can have a severely deteriorating influence on SV_{EIT}. The latter can be explained by the fact that – unlike what is hypothesized in the literature [155, 114] – the EIT heart amplitude does not represent blood volume changes but rather the effects of the alternating spatial replacement of lung vs heart tissue. Therefore, the EIT heart amplitude is scaled by the so-called heart-lung conductivity contrast and affected by variations in heart and lung conductivity such as changes in lung air volume or lung liquid distribution. In addition, these investigations revealed that the absolute measurement of SV is extremely challenging even with a patient-specific calibration. In contrast, trending – that is following changes in SV with respect to a baseline value – is more promising.

Clinical Investigations on EIT-Based SV Monitoring

As the practical applicability was of main interest in this thesis, we investigated to what extent the abovementioned findings could be translated into real-world measurements. To this end, we performed two clinical studies which are summarized in Table 13.1 and explained hereafter.

In the first study, we performed measurements on patients in the operating room (OR) before and after induction of anesthesia (Chapter 8). The EIT-based estimates were then compared to right heart thermodilution, considered as the clinical gold standard measurement for cardiac output (CO). From the eleven patients enrolled in the study, a total of four had to be excluded from analysis due to technical reasons, arrhythmias or too low cardiac EIT signal. In the remaining seven patients we tested different hypotheses addressing the absolute or relative measurement of SV with a patient-independent or patient-specific calibration. To do so, various features including heart and lung amplitudes were extracted from the EIT images and combined to train a linear model for estimating SV_{EIT}. Our findings suggest that the estimation of both absolute and relative SV is – if at all – only feasible via a patient-specific calibration and using information of the heart amplitude. And yet, this could not be fully confirmed as for most patients the variations in SV were too low and fall below the typical error of the reference device. In light of these circumstances the study was prematurely terminated.

The second study presented in Chapter 9 was performed in the ICU. Transpulmonary thermodilution was used as reference and SV was measured before and after fluid challenge, which is the injection of fluid into the circulation used to improve the hemodynamic situation of patients [103]. As solely three measurements were available per patient, only the trending – i.e. following relative changes – of SV with a patient-independent calibration was tested. Our analysis suggests that this is not possible based on the heart amplitude but only via the lung amplitude. For the latter an acceptable trending performance ($\mathrm{CR} = 100\,\%$, $\epsilon_\alpha = -1.6 \pm 11.9°$) is obtained but only after excluding 9 out of 32 measurements considered as outliers with too high noise level. These findings show promise for noninvasive and continuous trending of SV via EIT in the ICU. Whereas they would confirm a recent study on pigs [41], they are in contradiction with previous studies on pigs [113] and humans [155].

Investigations on an Improved Measurement Setup for EIT-Based SV Monitoring

Given the mixed results from the two aforementioned clinical trials and the limitations revealed via simulations, a better suited measurement setup was investigated (Chapter 10). To this end, we identified the limitations of available clinical EIT systems and proposed an improved measurement setup which was realizable with an existing EIT device.

Investigations of different measurement setups revealed a shortcoming regarding EIT image reconstruction; more specifically, the lack of a possibility to configure different reconstruction algorithms so that they can be compared fairly. To overcome this limitation a novel measure of noise performance ($\overline{\mathrm{SNR}}$) was developed. This new approach permits the comparison of

Table 13.1 – Overview of experimental EIT studies performed in this thesis. PAC stands for pulmonary artery catheter and TD for thermodilution.

	Clinical study in the OR	**Clinical study in the ICU**	**Experimental study on healthy adults**
EIT setup	2D, 32 electrodes Swisstom BB^2	2D, 16 electrodes Dräger PulmoVista™ 500	3D, 2x16 electrodes Swisstom BB^2
SV reference	PAC TD	Transpulmonary TD	Oxygen uptake $\dot{V}_{O_2}$
SV variations	Low	Low	High
Environment	Challenging: moving and touching patient is possible	Best possible: not moving nor touching patient	Close to best possible: not touching subject but changes of posture
Main findings	Too low variations in SV and issues with EIT signal quality	Amplitudes in lung but not in heart region can be used to trend SV	Neither lung nor heart amplitudes reliably estimate SV

EIT reconstruction performance across different measurement setups and was successfully validated in simulations and measurements on a resistor phantom (Chapter 11). This measure offers advantages over existing approaches, as it is independent of the measurement setup (skip, electrode number and position), the image resolution and the reconstruction algorithm.

Finally, the aforementioned improved measurement setup was tested in an experimental protocol on ten healthy adult volunteers (Chapter 12). To do so, ECG-gated 3D EIT with 2 planes of 16 electrodes in combination with a subject-specific reconstruction model was applied and reference SV was estimated from the subject's oxygen uptake $\dot{V}_{O_2}$. Large variations in SV were induced by bicycle exercises and changes in posture. The latter revealed significant differences in spatial conductivity distribution between sitting, lying with legs up and lying supine. Therefore, the analysis was restricted to measurements in supine position with low noise and stable heart and lung regions. Despite this very restricted analysis and the use of an improved measurement setup, neither the heart nor the lung amplitude allowed for an accurate estimation of SV. Only when incorporating the global conductivity σ_G for normalizing those amplitudes, SV can be estimated with an acceptable performance. However, this approach is questionable since the tidal volume V_T is highly correlated to SV in the current protocol and σ_G is known to be related to V_T. Therefore, no clear conclusion is possible apart from the one that neither lung nor heart amplitudes are reliable enough to assess SV in healthy volunteers, even when a subject-specific 3D EIT setup was used.

Contradictions, Challenges and Perspectives of EIT-Based SV Monitoring

None of the three experimental studies could confirm our simulations or the previous findings by Vonk Noordegraaf et al. [155] and Pikkemaat et al. [114], i.e. that the heart amplitude can be used to assess SV via EIT. We hypothesize that in practice the heart-based SV estimation is impaired by factors not considered in our simulations, such as the out-of-EIT-plane movement of the heart. Only the study in the ICU raised hope that – under very controlled conditions – SV can be assessed by EIT but via the lung amplitude. Even though this would confirm the recent findings by da Silva Ramos et al. [41], it is partly in contradiction with those of Pikkemaat [113]. Moreover, amplitude-based estimates have shown to be very sensitive to perturbations such as postural changes (see Chapter 12) or even the arm position [153]. Unless a surrogate approach is found which is immune to these perturbations (e.g. via normalized amplitudes), EIT-based SV (purely via amplitude estimates) seems impractical in many – less controlled – scenarios such as the OR or measurements on healthy volunteers.

In contrast, given rather controlled measurement conditions (e.g. in the ICU), where these deteriorating influences might be less present, the two amplitude-based estimates still suffer from limitations which have to be considered. First, the heart amplitude mainly represents heart movement [119, 118] and is further scaled by the heart lung conductivity contrast and thus influenced by changes in heart and lung conductivity (e.g. edema or posture-induced liquid redistribution). Besides, in traditional 2D EIT setups, the amplitude can be influenced by the heart moving out of the electrode plane. Second, the lung amplitude is known to represent not pure perfusion but rather pulsatility [74, 11] and is therefore presumably unable to assess SV in certain pathophysiological conditions.

In summary, EIT-based SV estimation seems unfeasible in most practical scenarios and in particular those where postural changes or patient movement occur (e.g. in OR patients, or in healthy volunteers performing cycling exercises). On the other hand, in very controlled scenarios – such as ventilated ICU patients – EIT might be applied to continuously track changes in SV after having performed an initial calibration (e.g. via transthoracic echocardiography). Yet, constant ventilator settings and posture are required and any change in those will likely imply a recalibration.

13.3 Limitations and Future Work

Simulations and Bioimpedance Model

The current bioimpedance model was successfully used to reveal more about the origins of cardiosynchronous EIT signals and to investigate not only the feasibility but also the limitations of EIT heart amplitude-based SV estimation. Nonetheless, this model is limited in that it is based on one single subject and that it does not incorporate respiration-related changes. Moreover, it does not specifically include skeletal muscles [42] and blood flow-induced changes [57] which are both worth considering in future research.

Our model-based simulations focused on the SV assessment via the heart-related amplitude. Nonetheless, in the ICU study, the lung amplitude revealed to be a better SV estimate. Therefore, the latter approach should be equally scrutinized by means of simulations to better reveal potential limitations and issues. To do so, the extensive lung model (developed by Martin

Proença [118] and already included in the current thorax model) should be used to study this approach under various pathophysiological conditions.

Current and Future Experimental Studies

Each of the three experimental studies performed has its specific strengths and weaknesses as summarized in Table 13.1. While the clinical studies measure reference SV with gold-standard technologies, they suffer from low per-patient variations in SV and the use of single plane (2D) EIT. On the contrary, the experimental study on healthy volunteers uses two-plane (3D) EIT and shows high variations in SV whereas reference measurements were performed noninvasively in a less accurate manner. Moreover, only the study in the ICU was recorded in a sufficiently controlled environment as the other two suffer mostly from postural changes or movement of the subject.

Should it be of interest to further pursue EIT-based SV estimation, we highly recommend restricting the measurements to patients in very controlled environments (such as the ICU) with a minimum of patient movement, no postural changes and fixed ventilator settings. Moreover, higher variations in SV for each patient are needed and only reference devices with a sufficiently high accuracy should be used (e.g. thermodilution). If this proves to be successful, potential limitations should then be explored in more challenging environments. Besides, the use of an EIT system with synchronous ECG measurement [123] is recommended as it facilitates both data acquisition and analysis. Finally, if studies in animals are considered, we suggest the use of an aortic flow probe as a must for SV reference measurements as this is the only reference considered as true gold standard [37].

13.4 Conclusion

In conclusion, the present thesis investigated the noninvasive and continuous monitoring of SV by means of EIT in two different ways.

First, a 4D bioimpedance model of a human thorax was created and used to study the feasibility and limitations of SV estimation via the EIT-derived heart amplitude. Simulations on this model have revealed that an absolute measurement of SV is challenging, but following trends of relative changes is more realistic. Nonetheless, SV estimates obtained via this approach remain impaired by changes in lung conductivity and electrode belt displacement.

Second, the practical applicability of this approach was tested *in vivo* in three experiments: a clinical trial in the OR, another in the ICU and a third study on healthy volunteers. Yet, in none of these studies the EIT-derived heart amplitude could be used to reliably estimate SV. This is in contradiction with the literature and our simulations on the bioimpedance model, which apparently lacks the inclusion of certain effects such as the out-of-EIT-plane movement of the heart. On the other hand, in the ICU, relative changes of SV could successfully be tracked, albeit via the EIT-based lung amplitude. In general, EIT amplitudes have shown to be very sensitive and impaired by various factors so that the approach might be limited to controlled environments like the ICU with the least possible changes in ventilation and posture.

In future, the bioimpedance model should be extended and further simulations should scrutinize the feasibility and limitations of estimating SV via the lung amplitude. In addition, future clinical research should concentrate on testing this approach in controlled environments with higher variations in SV and under various pathophysiological conditions.

Appendix Part VI

A Investigations on Aortic Blood Pressure Measured via EIT

Adapted from the post-print version of [22]:

Aortic Blood Pressure Measured via EIT: Investigation of Different Measurement Settings

Fabian Braun[1,2], Martin Proença[1,2], Michael Rapin[1,3], Mathieu Lemay[1], Andy Adler[4], Bartłomiej Grychtol[5], Josep Solà[1], and Jean-Philippe Thiran[2,6]

[1]Systems Division, Centre Suisse d'Electronique et de Microtechnique (CSEM), Neuchâtel, Switzerland

[2]Signal Processing Laboratory (LTS5), Ecole Polytechnique Fédérale de Lausanne (EPFL), Lausanne, Switzerland

[3]Department of Health Sciences and Technology (D-HEST), Swiss Federal Institute of Technology (ETHZ), Zürich, Switzerland

[4]Systems and Computer Engineering, Carleton University, Ottawa, Canada

[5]Fraunhofer Project Group for Automation in Medicine and Biotechnology, Mannheim, Germany

[6]Department of Radiology, University Hospital Center (CHUV) and University of Lausanne (UNIL), Lausanne, Switzerland

Published in **Physiological Measurement**
Physiol. Meas., vol. 36, no. 6, pp. 1147–1159, 2015

DOI:10.1088/0967-3334/36/6/1147

A.1 Introduction

Hemodynamic parameters are key variables to understand and characterise the health of the human cardiovascular system. Accurate measures of parameters such as heart rate, blood pressure or cardiac output are crucial to help prevent, diagnose and treat circulation-related diseases. As the majority of deaths worldwide are due to a failure of the cardiovascular system [161], it is of great interest to have low-cost and reliable techniques available to assess hemodynamic parameters noninvasively.

Still today, noninvasive blood pressure measurements are routinely performed using an inflatable brachial cuff wrapped around the upper arm. However, this method has a number of limitations such as the discontinuity of the measurements or the use of brachial pressure as poor surrogate for aortic pressure [101]. An alternative approach is based on the pulse wave velocity (PWV) principle: the PWV – the velocity at which the pressure pulse propagates along the arterial tree – allows the continuous estimation of mean arterial pressure. PWV can be measured at different locations and in various ways [14], but all require a reference measurement for initial calibration. One possibility to noninvasively measure aortic PWV is via the aortic pulse arrival time (PAT) by means of electrical impedance tomography (EIT), as shown recently by Solà et al. [137]. Aortic PAT is defined as the arrival time of the blood pressure pulse at a given aortic location. In particular, when measuring time series of aortic pulses, PAT is calculated as the timing of the rising edge of these pulses.

Electrical impedance tomography is a safe, low-cost and noninvasive functional imaging modality [80]. With a belt of electrodes attached around the thorax, thoracic bioimpedance changes are measured. These measurements are then reconstructed into an image sequence which depicts the change of intra-thoracic impedance, revealing lung- and heart-related activity. The exploitation of EIT data for cardiovascular-related activity is still in its infancy [9]. However, the nonionizing and noninvasive nature of EIT makes it an appealing candidate for continuous hemodynamic patient monitoring.

For the EIT-based estimation of mean aortic blood pressure, the temporal impedance changes originating from the descending aorta are analysed. Due to the inherent low spatial resolution of EIT [80], localizing the aorta, which has the size of roughly 5 % of the maximal thorax diameter, represents a challenge. The strong impedance changes originating from the nearby lungs and heart can lead to an elimination of the aortic information, unless EIT images are acquired and processed appropriately. Moreover, the similarity in pulmonary and aortic signal morphology [46] does not facilitate the separation of the two signal sources. The ability of EIT to detect and localize aortic impedance changes can be investigated in simulations using finite element models (FEMs). Such simulations have been applied in the field of impedance cardiography [40, 150]. However, for EIT very few such simulations exist and most of them do not include temporal changes and are thus limited to static models [164, 76]. At present, little is known about the most appropriate measurement setting (electrode position, reconstruction algorithm) which allows a reliable detection of the aortic signal in EIT. This emphasizes the need for further research in this particular field in order to bring cardiovascular EIT a step closer towards clinical practice.

This work is aimed at understanding the effect of various components of an EIT system in the ability to measure systemic blood pressure via the aortic signal, by comparing two commonly used reconstruction algorithms and three traditional transversal EIT belt placements. In this context, an MRI-based 3D hemodynamic model for cardiac EIT simulations of the human thorax is presented. With a simulation-based approach, the influence of the different belt placements and reconstruction algorithms on the capability to measure the aortic PAT is investigated. This is examined by two experiments where 1) the error in EIT-based PAT estimation is quantified and 2) the aortic signal contribution is measured.

This chapter is organized as follows. The methods are presented in Section A.2. The corresponding results are detailed in Section A.3 and interpreted in Section A.4. Finally, in Section A.5, conclusions on the results of this investigation are presented.

A.2 Methods

In Section A.2.1 the creation of the hemodynamic bioimpedance model is presented, starting by describing the MRI recordings, followed by the description of each individual entity (static thorax, dynamic aorta, heart and lungs). This is followed by the introduction of the simulation framework (Section A.2.2) and the subsequent image reconstruction (Section A.2.3), which combine the aforementioned model entities to simulate EIT impedance measures and images (see also Figure A.3). Finally, in Section A.2.4 the two experiments investigating the possibility to measure aortic PAT are presented.

A.2.1 Hemodynamic 3D Thorax Model

MRI Experiments

In order to create the dynamic 3D thorax model, three types of magnetic resonance imaging (MRI) recordings were performed on a human volunteer (62 kg, 178 cm, 28 years old) during expiratory breath-hold: (*M1*) A batch of 2D transverse plane scans covering the thorax outline from the diaphragm up to the apices of the lungs; (*M2*) Two 2D batches of dynamic cardiac cine scans showing the whole heart in short axis or in four chamber long axis view, covering 25 frames of the cardiac cycle; (*M3*) Dynamic 2D scans located at four different placements along the aorta revealing the distension of the aortic cross section with at least 60 frames / heart cycle.

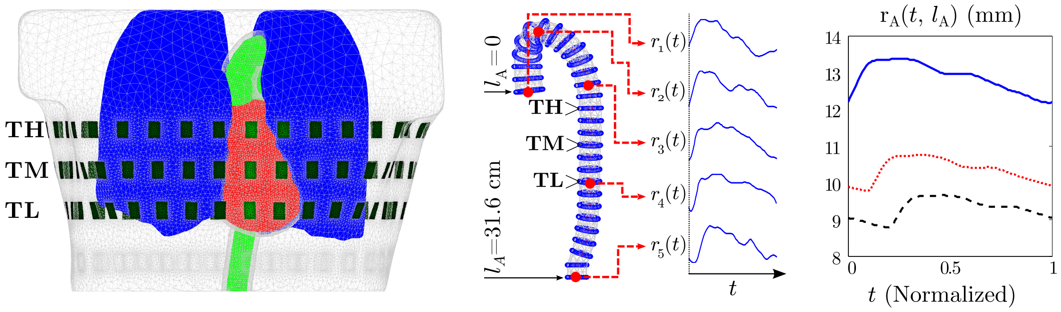

(a) (b) (c)

Figure A.1 – (a) 3D FEM of the human thorax with the lungs (blue), heart (red), aorta (green) and the three different EIT belts (see text in Section A.2.1) TH, TM and TL (green rectangles). (b) Circular model of the aorta (> indicate the belt levels) with the distension dynamics $r_1(t)$ to $r_5(t)$ at five locations (red arrows) which were combined to obtain (c) the time- and position-dependent aortic radius modulation curve $r_A(t, l_A)$, shown at three different positions (——blue, ······red, - - -black: $l_A = 0$, 15.8 or 31.6 cm) along the aorta.

Static Thorax

The thorax outline was segmented from the MRI scan *M1* by a region-growing algorithm using OsiriX [125] and then meshed to a smoothed 3D volume with Netgen [131]. Using the open-source EIT software toolbox EIDORS [5], the application of three EIT belts – each comprised of 32 electrodes – was simulated at different levels along the craniocaudal axis as follows (see also Figure A.1a): (1) the TM (*transversal middle*) belt was placed at the average level of the heart model described later on, which is in between the 9-th and 10-th thoracic vertebra, the belts (2) TH (*transversal high*) and (3) TL (*transversal low*) were placed 3.5 cm higher and lower than TM, respectively. This corresponds to the level of the 8-th (for TH) or in between the 10-th and 11-th (for TL) thoracic vertebras. To ensure accurate calculations, the FEM was refined in the vicinity of the electrodes as described by Grychtol and Adler [65].

Based on observations from the MRI scans, the intra-thoracic background conductivity is composed of 48 % muscle, 47 % fat and 5 % bone (Table A.1).

Dynamic Aorta

The volume of the aorta was extracted from MRI scan *M1* by applying a volumetric snake segmentation [169]. Then, the centreline of the aorta was obtained by skeletonization of this volume. Finally, the aortic model was constructed by interconnecting 29 circles equidistantly spaced on this centreline (Figure A.1b), which all allow individual modulation of their radii.

To determine the temporal development of the aortic radius, an aorta-specific 2D + t snake segmentation [77] was applied to the MRI scans *M3*, leading to a measure of aortic radius at five different locations along the aorta ($r_1(t)$ to $r_5(t)$ in Figure A.1b). These were averaged

Table A.1 – Tissue composition of the different structures in the bioimpedance model.

			Conductivity Range	
Structure	Tissue Composition	σ_{Tissue} (S/m)	σ_{ED} (S/m)	σ_{ES} (S/m)
Background	Muscle, Fat, Bone	0.384, 0.0435, 0.0211	0.206	0.206
Aorta	Blood	0.710	0.710	0.710
Lungs	Lung	0.113	0.113	0.124
Ventricles (Heart)	Blood, Myocardium	0.710, 0.238	0.573	0.494
Atria (Heart)	Blood, Myocardium	0.710, 0.238	0.507	0.599

Note: σ_{Tissue} denotes the conductivity of each tissue individually. σ_{ED} (end diastole) and σ_{ES} (end systole) denote the resulting conductivity range when these tissues are combined in the final structures. All values are at 200 kHz and based on [73].

to one single normalized aortic waveform $P_{\text{A}}(t)$, and combined with the radius of the aorta in relaxed state $R_{\text{A}}(l_{\text{A}})$ (at a position l_{A} from the aortic valve), resulting in the aortic radius modulation function $r_{\text{A}}(t, l_{\text{A}})$ depicted in Figure A.1c and defined as follows:

$$r_{\text{A}}(t, l_{\text{A}}) = R_{\text{A}}(l_{\text{A}}) \left[1 + \text{DIST}_{\text{A}} \cdot P_{\text{A}} \left(t - \frac{l_{\text{A}}}{\text{PWV}_{\text{A}}} \right) \right], \tag{A.1}$$

where PWV_{A} denotes the aortic pulse wave velocity at which the pressure wave travels along the aorta, and DIST_{A} the maximal relative radial distension of every single aorta circle. DIST_{A} was simplified as constant value of 10 %, which is more conservative than the 12 % observed in the MRIs and in the range of normotensive subjects [83]. The individual modulation of the 29 aortic radii based on Equation (A.1), in combination with different PWV_{A} settings, thus allows the simulation of different systemic blood pressure values.

The aorta model is assigned uniformly with the conductivity of blood (Table A.1).

Dynamic Heart

As an MRI-based full heart segmentation is a challenging task [172], the heart was simplified by a geometric model mainly consisting of two cropped ellipsoids representing the atria and ventricles as illustrated in Figure A.2a. To best mimic real heart behaviour, the model has only a slight variation in total heart volume, no longitudinal shortening but radial compression as observed at rest [32] and moderate exercise [141]. The six parameters configuring the model (position of base, apex, AVP_{ES}, AVP_{ED} and both short axis dimensions of the AVP) are shown in Figure A.2 and were determined by fitting the model to the outer heart contours in end diastole and end systole and from manual measurements obtained from MRI scans *M2*. The model is changed over time using one single variable – the ventricular volume $V_{\text{Ventricles}}$ – whereas the resulting atrial and total heart volumes are changed indirectly in a physiologically meaningful range, as shown in Figure A.2b.

The atria and ventricles are assigned a time-varying conductivity which is a combination of blood and myocardium (Table A.1). By considering the myocardium as quasi-incompressible [156, 167], this time-dependence is given by changes in the ratio of varying blood volume and constant myocardial volume.

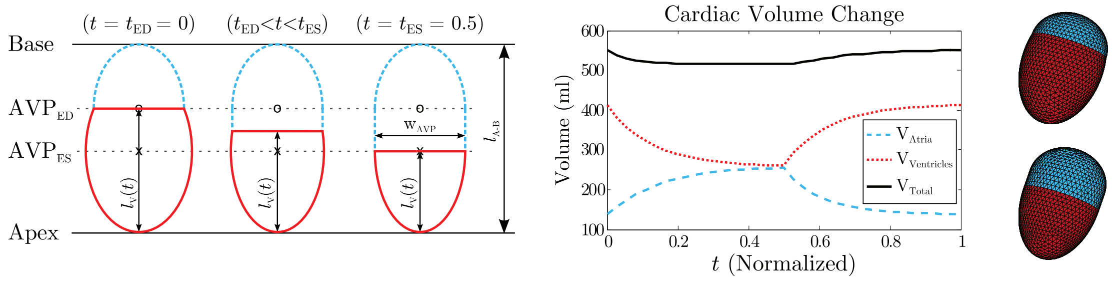

(a) (b) (c)

Figure A.2 – (a) A simplified two-dimensional illustration of the heart model with the atria (- - -blue) and ventricles (——red) at three instants t in time, where t_{ED} and t_{ES} correspond to end diastole and end systole. The horizontal red line shows the atrio-ventricular valve plane (AVP). The heart length l_{A-B}, the ellipsoid centres (o: atrial, x: ventricular) and the AVP size w_{AVP} do not change over time. Modulation of the ventricular volume changes the ventricular dimensions $l_V(t)$ and leads to a displacement of the AVP. (b) Simulated changes of atrial (- - -blue), ventricular (······red) and total heart volume (——black) over the cardiac cycle. (c) Resulting FEM of the heart with the atria (blue) and ventricles (red) at end diastole (top) and end systole (bottom).

Dynamic Lungs

The two lungs were segmented identically to the thorax and then meshed to a 3D volume representation.

Dynamic changes in the lung regions during breath-hold were modelled using a pulmonary artery distension reading $P_L(t)$ obtained from the MRI scans *M3*. The changes in lung conductivity were simulated by propagating this distension pulse along the pulmonary circulation with constant [107] velocity (PWV_L):

$$\sigma_i(t) = \sigma_L \left[1 + \Delta\sigma_{L_{Max}} \cdot P_L \left(t - \frac{d_{PV_i}}{PWV_L} \right) \right], \tag{A.2}$$

where $\sigma_i(t)$ is the time-dependent conductivity of the i-th element in the FEM, located at the distance d_{PV_i} from the pulmonary valve. The baseline lung conductivity σ_L (Table A.1) is increased during the cardiac cycle by a maximum of $\Delta\sigma_{L_{Max}}$, which was set to 10 %, the worst case value reported in the literature [108, 171, 28].

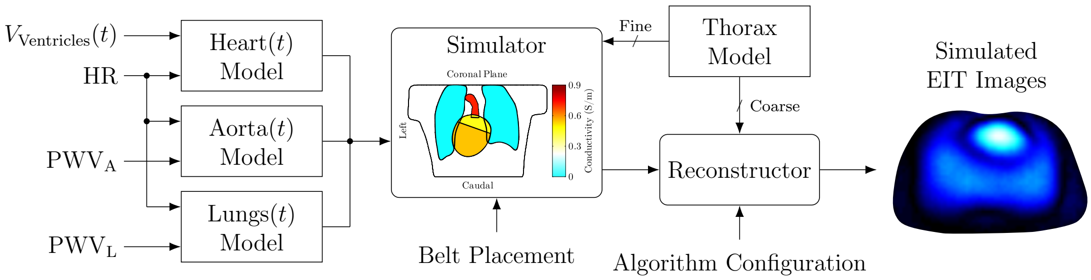
$V_{\text{Ventricles}}(t)$
HR
PWV_A
PWV_L
Heart(t) Model
Aorta(t) Model
Lungs(t) Model
Simulator
Coronal Plane
Left
Caudal
Conductivity (S/m)
0.9
0.6
0.3
0
Fine
Thorax Model
Coarse
Reconstructor
Belt Placement
Algorithm Configuration
Simulated EIT Images

Figure A.3 – Block diagram of the simulation framework. The dynamic models (heart, aorta and lungs) are merged with the thorax model, simulated and reconstructed to images, while parametrizing different hemodynamic parameters (ventricular volume $V_{\text{Ventricles}}(t)$, heart rate HR, aortic PWV_A and pulmonary pulse wave velocity PWV_L).

A.2.2 Bioimpedance Simulations

Simulation Framework

To make use of the dynamic bioimpedance model introduced in the previous section, a flexible simulation framework was developed. It allows the calculation of impedance measures and the subsequent reconstruction of EIT images while parametrizing various hemodynamic and EIT device-related parameters, using different reconstruction algorithms (Figure A.3). The software is written in Matlab and based on EIDORS [5].

The electrical conductivities of the biological tissues were specified based on the IT'IS database [73] at a frequency of 200 kHz and are shown in Table A.1.

Simulating Model Dynamics

For conductivity simulations, the thorax was meshed and locally refined in the regions where moving structures are present (aorta and heart). Besides this refinement, the thorax mesh (comprised of 1.13 million finite elements) contains no specific information about the underlying organ structures. To then merge the dynamics of all individual meshes (aorta, heart, lungs) into a single thorax mesh, at each moment in the cardiac cycle, the individual meshes were mapped to the thorax mesh and the corresponding conductivity values were updated (Figure A.3). Those elements left untouched by this mapping remained assigned with the thoracic background conductivity mentioned in Section A.2.1 and shown in Table A.1.

All impedance measures were simulated for all three electrode belts (TH, TM and TL) – each composed of 32 electrodes – using a quasi-adjacent stimulation pattern with 4 inactive electrodes in between the two ones actively measuring voltage/injecting current [53].

A.2.3 Image Reconstruction

The simulated impedance measurements were reconstructed to EIT images with the following two difference reconstruction algorithms. These algorithms are based on inverse models generated at the height of each belt from a coarse version ($407 \cdot 10^3$ finite elements) of the static thorax model.

- The GREIT algorithm [6] was trained with 4000 uniformly distributed stimulation targets. These targets had a relative diameter of 0.015, which is approximately the size of a pixel ($1/64 \approx 0.015$) and half the minimal aorta radius (0.030). To investigate the performance of the algorithm in detail, the noise figure (NF) and the weighting radius R_W were varied. The NF, which quantifies the extend to which measurement noise is amplified in the resulting images, was set between 0.25 and 2.0 – a practically meaningful range [62]. R_W, which determines the point spread function and thus the resolution, was varied between 0.03 and 0.18. For the final analysis, in a first step, the influence of R_W was investigated with an NF fixed at 1.0. Second, the influence of NF was studied in more detail by setting R_W to the two values which showed best results in the first step.
- A one-step Gauss-Newton (GN) algorithm was used with a Laplace prior and a regularization hyperparameter λ chosen automatically to achieve the given NF as described by Graham and Adler [62]. The NF was varied identically to GREIT.

Both algorithms reconstruct images of 64×64 pixels and an isotropic resolution of 4.6, 4.9 or 5.2 mm/pixel for the TL, TM and TH belt, respectively.

A.2.4 Hemodynamic Simulation Experiments

With the simulation framework introduced in the previous sections two different experiments were performed. These are illustrated in Figure A.4 and described in more detail in the following two sections. It has to be noted that the analysis of both experiments were reduced to the pixels in the aortic region of interest $\text{ROI}_{\text{Aorta}}$, whose determination is explained in the second experiment (SNR experiment, Section A.2.4).

All of the simulations were performed on a Unix machine running Matlab (version 8.0.0.783, 2012b), the EIDORS developer version (version 3.7.1+, SVN revision 4641) and Netgen (version 5.0.0).

PAT Experiment

The first experiment aimed at investigating the possibility to measure aortic pulse arrival time (PAT), related to changes in systemic blood pressure. By modifying both the aortic and pulmonary PWV over a wide and physiologically realistic range, different states of systemic and pulmonary blood pressure were simulated. With this, the capability to determine aortic

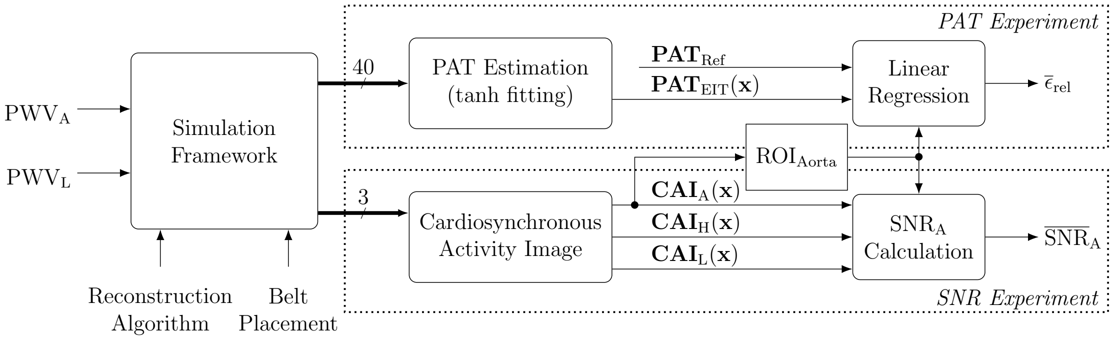
PAT Experiment
PWV$_A$
PWV$_L$
Simulation Framework
40
3
PAT Estimation (tanh fitting)
$\mathbf{PAT}_{\text{Ref}}$
$\mathbf{PAT}_{\text{EIT}}(\mathbf{x})$
Linear Regression
$\overline{\epsilon}_{\text{rel}}$
ROI$_{\text{Aorta}}$
$\mathbf{CAI}_A(\mathbf{x})$
$\mathbf{CAI}_H(\mathbf{x})$
$\mathbf{CAI}_L(\mathbf{x})$
Cardiosynchronous Activity Image
SNR$_A$ Calculation
$\overline{\text{SNR}}_A$
Reconstruction Algorithm
Belt Placement
SNR Experiment

Figure A.4 – Block diagram of the two experiments performed. For a detailed description see PAT experiment and SNR experiment both in Section A.2.4.

PAT variations from EIT images – while being least affected by changes in pulmonary PAT – was investigated for different measurement settings (belt placement and reconstruction algorithm configuration).

For this purpose, 36 instants in the cardiac cycle for 10 aortic and 4 pulmonary pulse wave velocities were simulated in a range of $\text{PWV}_A = \{2,\dots,10\}$ m/s and $\text{PWV}_L = \{1.5,\dots,2.5\}$ m/s, respectively. For each of the forty states simulated (all possible combinations of PWV$_A$ and PWV$_L$), the pixel-wise pulse arrival time (PAT) was calculated by fitting a tanh-model [136] onto the rising slope of the temporal conductivity change. For each pixel at location $\mathbf{x} = (x, y)$, these EIT-based estimates ($\mathbf{PAT}_{\text{EIT}}(\mathbf{x}) \in \mathbb{R}^{40}$) were then compared to their references ($\mathbf{PAT}_{\text{Ref}} \in \mathbb{R}^{40}$), which are given by the known PWV$_A$ and the length of the aorta at the level of each belt. For this purpose, a linear fit of $\mathbf{PAT}_{\text{EIT}}(\mathbf{x})$ onto $\mathbf{PAT}_{\text{Ref}}$ was performed:

$$(\hat{a}(\mathbf{x}), \hat{b}(\mathbf{x})) = \underset{a,b}{\arg\min} ||\mathbf{PAT}_{\text{EIT}}(\mathbf{x}) - (a \cdot \mathbf{PAT}_{\text{Ref}} + b)||_2^2. \tag{A.3}$$

The closeness of fit was evaluated using the metrics described below and illustrated in Figure A.5. The root-mean-square error $\sigma_{\text{EIT}}(\mathbf{x})$, was computed as the deviation of the estimate from the fit:

$$\sigma_{\text{EIT}}(\mathbf{x}) = \sqrt{\frac{\sum_{i=1}^{40} \left[\mathbf{PAT}_{\text{EIT}}^{(i)}(\mathbf{x}) - \left(\hat{a}(\mathbf{x}) \cdot \mathbf{PAT}_{\text{Ref}}^{(i)} + \hat{b}(\mathbf{x})\right)\right]^2}{40-2}}. \tag{A.4}$$

The resulting absolute and relative timing error, $\epsilon_{\text{abs}}(\mathbf{x})$ and $\epsilon_{\text{rel}}(\mathbf{x})$, respectively, are given as in Equation (A.5), where $\Delta\text{PAT}_{\text{Ref}}$ denotes the maximal range of $\mathbf{PAT}_{\text{Ref}}$, as illustrated in Figure A.5.

$$\epsilon_{\text{abs}}(\mathbf{x}) = \frac{2\sigma_{\text{EIT}}(\mathbf{x})}{\hat{a}(\mathbf{x})} \quad \Longrightarrow \quad \epsilon_{\text{rel}}(\mathbf{x}) = \frac{\epsilon_{\text{abs}}(\mathbf{x})}{\Delta\text{PAT}_{\text{Ref}}} = \frac{2\sigma_{\text{EIT}}(\mathbf{x})}{\hat{a}(\mathbf{x}) \cdot \Delta\text{PAT}_{\text{Ref}}} \tag{A.5}$$

As the measurement of blood pressure with a PWV-based approach requires calibration, one is not interested in a one-to-one relationship between $\mathbf{PAT}_{\text{EIT}}(\mathbf{x})$ and $\mathbf{PAT}_{\text{Ref}}$ ($\hat{a} = 1$), but in a best linear relationship between them, i.e. pixels where the lung-induced variations lead to the smallest relative error ϵ_{rel} in aortic PAT estimate.

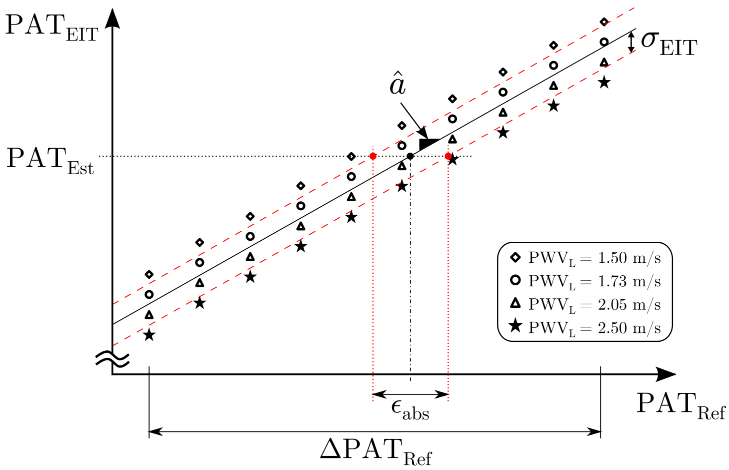
$\mathrm{PAT}_{\mathrm{EIT}}$
σ_{EIT}
$\hat{a}$
$\mathrm{PAT}_{\mathrm{Est}}$
◇ $\mathrm{PWV_L} = 1.50\ \mathrm{m/s}$
○ $\mathrm{PWV_L} = 1.73\ \mathrm{m/s}$
△ $\mathrm{PWV_L} = 2.05\ \mathrm{m/s}$
★ $\mathrm{PWV_L} = 2.50\ \mathrm{m/s}$
ϵ_{abs}
$\mathrm{PAT}_{\mathrm{Ref}}$
$\Delta\mathrm{PAT}_{\mathrm{Ref}}$

Figure A.5 – Illustrative example of the relationship between the estimated $\mathbf{PAT}_{\mathrm{EIT}}$ and simulated aortic PAT values $\mathbf{PAT}_{\mathrm{Ref}}$ for one pixel, showing the fitted linear regression (——black) with the error range (- - -red) and the resulting absolute error ϵ_{abs} for a given estimated PAT ($\mathrm{PAT}_{\mathrm{Est}}$). The variation of $\mathrm{PAT}_{\mathrm{EIT}}$ at identical $\mathrm{PAT}_{\mathrm{Ref}}$ values is caused by undesired pulmonary influences with different $\mathrm{PWV}_{\mathrm{L}}$.

Finally, for comparing the results between the various measurement settings simulated (belt placement and algorithm configuration), $\epsilon_{\mathrm{rel}}(\mathbf{x})$ was reduced to a single figure of merit $\bar{\epsilon}_{\mathrm{rel}}$. This was defined as the average of those four neighbouring pixels (2×2 pixel region $\approx 1/3$ of aorta area) inside the aortic region $\mathrm{ROI}_{\mathrm{Aorta}}$ (described in the next section) having lowest $\epsilon_{\mathrm{rel}}(\mathbf{x})$ values.

SNR Experiment

As mentioned in the introduction the aortic signal is very weak. In order to exploit its information, it is crucial to find pixels where it is present and at the same time least affected by other signals (pulmonary or cardiac). Therefore, the second experiment aimed at quantifying the strength of the aortic signal, relative to the overall signal, at the different aortic candidate pixels for the different measurement settings investigated (belt placements, algorithm configuration).

For this purpose, 36 instants in the cardiac cycle with $\mathrm{PWV_A} = 4.5\ \mathrm{m/s}$, $\mathrm{PWV_L} = 2.0\ \mathrm{m/s}$ were simulated. In this experiment three different artificial scenarios were generated to investigate the individual influence of each of the dynamic models (aorta, lungs and heart) by simulating each source of impedance change separately. Therefore, for each scenario, either the dynamics of (A) the aorta, (H) the heart or (L) the lungs, were simulated, whereas the other structures were frozen to their end diastolic state.

For each of the three scenarios (A), (H) and (L) a so-called *cardiosynchronous activity image*

CAI($\mathbf{x}$) was generated and denoted as CAI_A, CAI_H and CAI_L, respectively. These were calculated by the pixel-wise standard deviation in the time domain. In order to reveal those pixels with highest contribution from the aorta, an aortic signal-to-noise ratio SNR_A was defined as:

$$\text{SNR}_\text{A}(\mathbf{x}) = \frac{\text{CAI}_\text{A}(\mathbf{x})}{\text{CAI}_\text{A}(\mathbf{x}) + \text{CAI}_\text{L}(\mathbf{x}) + \text{CAI}_\text{H}(\mathbf{x})} \in [0,1]. \tag{A.6}$$

Hence, the pixels of interest are those with a high SNR_A and thus with a predominant contribution of aortic signal – compared to pulmonary and cardiac influences. Therefore, the final figure of merit $\overline{\text{SNR}}_\text{A}$ was chosen – similar to the first experiment – as the average of those four neighbouring pixels (2×2 pixel region) having highest SNR_A values inside the aortic region ROI_Aorta. This region of interest, to which the selection of the four best pixels is restricted, was defined as these connected pixels where $\text{CAI}_\text{A}(\mathbf{x})$ is larger than 10 % of its maximal value.

A.3 Results

The dependence of both figures of merit $\bar{\epsilon}_\text{rel}$ (first experiment) and $\overline{\text{SNR}}_\text{A}$ (second experiment) on the noise figure (NF) for three different reconstruction algorithm configurations are shown in Figure A.6. Over the entire range GN shows a lower relative error $\bar{\epsilon}_\text{rel}$ compared to the two GREIT configurations. Starting from a NF of 0.5 (TH and TM) or 0.75 (TL), $\bar{\epsilon}_\text{rel}$ of GN lies below 4.5 % and stabilizes for higher NFs. Regarding the aortic signal contribution, the TH and TM belt placements in combination with GN show highest $\overline{\text{SNR}}_\text{A}$ values, especially for a NF in the range between 0.5 and 1.25.

The two specific GREIT weighting radii R_W used in Figure A.6 ($R_\text{W} = 0.09$ and $R_\text{W} = 0.03$) were selected based on Figure A.7 which shows the dependence of $\bar{\epsilon}_\text{rel}$ and $\overline{\text{SNR}}_\text{A}$ on R_W. For certain belt placements ($\overline{\text{SNR}}_\text{A}$ for TL and TH, or $\bar{\epsilon}_\text{rel}$ for TH) an R_W of 0.09 shows best performance whereas for TM in terms of timing an R_W of 0.03 is favourable.

A.4 Discussion

Two simulation experiments were performed with the aim to 1) quantify the error in EIT-derived PAT estimation and 2) measure the aortic signal contribution at different pixels of the aortic region in EIT image sequences. The goal of these experiments was to investigate the influence of different belt placements and reconstruction algorithms when aiming for an EIT-based monitor of aorta pulsatility.

The first experiment shows the feasibility to estimate the aortic PAT with a minimal error $\bar{\epsilon}_\text{rel}$ of below 3.6 % or 4.3 %, for measurements performed with a TM or TH belt placement and reconstructed with GN, starting from an NF of 0.5 upwards. These errors in terms of EIT-based blood pressure estimation would translate to ±1.4 mmHg or ±1.7 mmHg, when conservatively assuming a relationship of 1 mmHg/ms [138]. The TL belt placement follows from a NF of 0.75 upwards with an error lower than 4.3 %. In comparison, for images reconstructed with

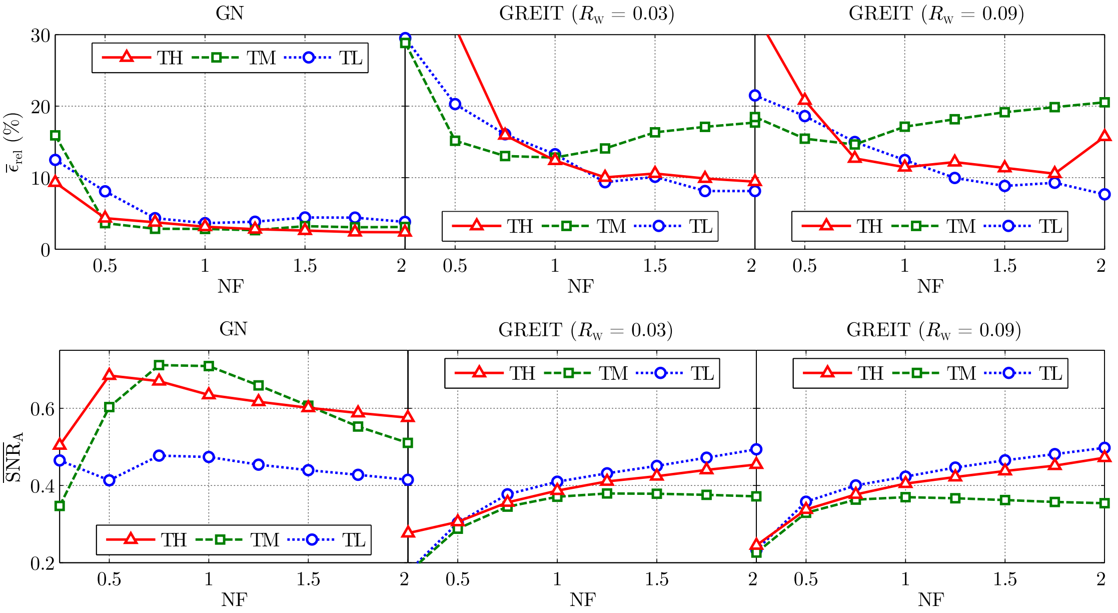

Figure A.6 – (Top row) Relative error $\bar{\epsilon}_{\mathrm{rel}}$ (the lower the better) and (Bottom row) aortic contribution $\overline{\mathrm{SNR}}_{\mathrm{A}}$ (the larger the better) as a function of the noise figure (NF) for the three belt placements (TH, TM, TL) and three different algorithm configurations (Left column) Gauss-Newton, (Middle column) GREIT with $R_{\mathrm{W}} = 0.03$ and (Right column) $R_{\mathrm{W}} = 0.09$.

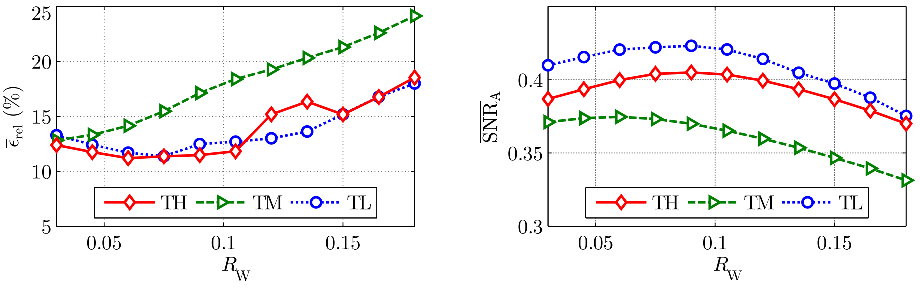

(a) GREIT NF = 1

(b) GREIT NF = 1

Figure A.7 – (a) Relative error $\bar{\epsilon}_{\mathrm{rel}}$ (the lower the better) and (b) aortic contribution $\overline{\mathrm{SNR}}_{\mathrm{A}}$ (the larger the better) as a function of GREIT weighting radius R_{W} for the three belt placements (TH, TM, TL).

GREIT and all three belt placements investigated, the error never falls below 7.6 %, which would correspond to ±3.0 mmHg. However, this is the case for high NFs. At lower NFs, in a range of NF between 0.5 and 1 – which is favourable in order to be more robust to noise – $\overline{\epsilon}_{\mathrm{rel}}$ of GREIT is nearly three-fold higher compared to GN. As these comparisons are made for the two algorithms having identical NFs and image size, the significant differences observed are assumed to be due to a higher spatial smoothing of the GREIT algorithm. As alluded to earlier in Section A.1, even a small influence of the much stronger lung or heart signals can lead to a quasi-elimination of the aortic signal. To summarize, in terms of PAT error $\overline{\epsilon}_{\mathrm{rel}}$, we recommend the use of GN reconstruction and a NF of at least 0.5.

The second experiment reveals that images reconstructed with GN allow best to isolate the aortic signal from the interfering ones (pulmonary and cardiac). This applies in particular to the TM or TH belt placements where aortic signal contributions $\overline{\mathrm{SNR}}_{\mathrm{A}}$ of up to 71 % or 68 % are present (for NFs in the range of 0.5 to 1.0). In contrast, using GREIT, for all three belts analysed, the $\overline{\mathrm{SNR}}_{\mathrm{A}}$ stays below 50 % – or for NFs limited to 1.0 even below 43 %. These findings suggest the use of GN reconstruction with a TM or TH belt placement.

Based on two different simulation experiments showing comparable results, a GN reconstruction (with NF ≥ 0.5) is suggested for measuring aortic PAT. The few discrepancies between $\overline{\mathrm{SNR}}_{\mathrm{A}}$ and $\overline{\epsilon}_{\mathrm{rel}}$ probably stem from the lower specificity of the PAT experiment. Since the cardiac-related activity is not changing between the forty different PAT states of the first experiment, the timing error $\overline{\epsilon}_{\mathrm{rel}}$ can be small in pixels where an accurate aortic PAT estimation is obtained despite a high cardiac contribution. The same applies for pixels having high pulmonary signal influence and located close to the pulmonary valve, where the disturbing $\mathrm{PWV}_{\mathrm{L}}$-dependent variations are negligibly small. This could be improved by simulating different cardiac volume conditions and pulmonary pressure morphologies. However, the current simulations are very time-consuming; the PAT experiment took nearly four days to compute. This is also the reason why the present analysis was limited to a single stimulation pattern. Thus, before performing further investigations, a more efficient implementation of the forward solver is required.

Regarding the performance of GREIT, it needs to be emphasized that an appropriate adjustment of the algorithm parameters (increased image size, modified point spread function) might lead to improved results. This was, however, out of the scope of the present investigations and should be investigated in the future. Moreover, the current analysis did not take into account any noise, which could alter the outcome when comparing the two algorithms. Therefore, we suggest the development of an appropriate noise model and a subsequent noise analysis for future work.

The results for GN suggest that a TM or TH belt placement is preferred over TL. This is somewhat counter-intuitive as one would expect the lowest pulmonary activity for the TL belt (see Figure A.1a). Nevertheless, the larger radial distension of the aorta and increased sensitivity of changes originating from the aortic arch at higher belt levels are arguments in favour of a high belt placement. This might explain our observations from a signal strength perspective as studied in the second experiment. Nevertheless, the rationale for the lower timing errors at higher belt levels (as observed for GN from the first experiment), might be biased by the aforementioned fact that belts placed closer to the pulmonary valve (PV) could show lower timing errors.

As none of the results shows an aortic contribution $\overline{\mathrm{SNR}}_\mathrm{A}$ of more than 71 %, we have to expect pulmonary or cardiac influence in every pixel. A plausible explanation is the low spatial resolution of EIT which leads to an overlap of different signal sources. This in turn might be exaggerated for the pulmonary influence due to the simplistic model used for the lungs which propagates a worst-case conductivity change of 10 % homogeneously throughout the entire lung region. Therefore, improvements towards a more realistic lung model are suggested in order to examine this in more detail.

In conclusion, the confirmation of the current findings by validating against real EIT-based aortic PAT recordings should bring cardiovascular EIT another step closer towards clinical practice.

A.5 Conclusions

Simulations on an MRI-based 3D hemodynamic thorax model were performed to investigate the possibility to measure mean aortic blood pressure via EIT. In terms of both aortic signal strength and EIT-based PAT estimation error, the present study suggests the use of the Gauss-Newton algorithm (GN) (with a noise figure of $\mathrm{NF} \geq 0.5$) for image reconstruction in combination with a transversal electrode belt placement at the level of the heart (TM) or higher (TH). A more realistic lung model, the introduction of noise and the validation against real EIT recordings are suggested for future research. This also implies the practical validation of the method for estimating aortic blood pressure from EIT-derived pulse arrival time in humans.

B Ensemble Averaging and Signal Quality Estimation

Assuming $\boldsymbol{S}_P \in \mathbb{R}^{n_p \times n_f \times n_c}$ as a sequence of EIT images with n_p pixels and n_f frames and n_c cardiac cycles aligned to a cardiosynchronous trigger (e.g. ECG's R-peak or foot of pressure wave). The averaged EIT sequence of one representative cardiac cycle $\boldsymbol{S}_A \in \mathbb{R}^{n_p \times n_f}$ is obtained via *ensemble averaging* (see [122, chap. 3.5.1] or [139, chap. 4.3]) as follows:

$$[\boldsymbol{S}_A]_{pf} = \frac{1}{n_c} \sum_{i=1}^{n_c} [\boldsymbol{S}_P]_{pfi}, \quad \forall p \in [1, n_p] \text{ and } f \in [1, n_f] \tag{B.1}$$

The corresponding deviation $\boldsymbol{S}_D \in \mathbb{R}^{n_p \times n_f}$ of all averaged cardiac cycles is computed via the standard-deviation calculated over all n_c cycles:

$$[\boldsymbol{S}_D]_{pf} = \sqrt{\frac{1}{n_c - 1} \sum_{i=1}^{n_c} \left| [\boldsymbol{S}_P]_{pfi} - [\boldsymbol{S}_A]_{pf} \right|^2}, \quad \forall p \in [1, n_p] \text{ and } f \in [1, n_f] \tag{B.2}$$

The mean deviation image $\boldsymbol{I}_D \in \mathbb{R}^{n_p}$ is obtained by averaging $\boldsymbol{S}_D$ over all n_f frames:

$$[\boldsymbol{I}_D]_p = \frac{1}{n_f} \sum_{i=1}^{n_f} [\boldsymbol{S}_D]_{pi}, \quad \forall p \in [1, n_p] \tag{B.3}$$

The cardiosynchronous activity image (**CAI**) represents the root-mean squared (RMS) amplitude and is computed via the pixel-wise standard-deviation over all n_f frames:

$$[\boldsymbol{I}_A]_p = [\mathbf{CAI}]_p = \sqrt{\frac{1}{n_f - 1} \sum_{i=1}^{n_f} \left| [\boldsymbol{S}_A]_{pi} - \left(\frac{1}{n_f} \sum_{j=1}^{n_f} [\boldsymbol{S}_A]_{pj} \right) \right|^2}, \quad \forall p \in [1, n_p] \tag{B.4}$$

The relative deviation at each pixel represented by $\boldsymbol{I}_R \in \mathbb{R}^{n_p}$ is computed as the ratio of deviation vs activity, i.e. $\boldsymbol{I}_R = \boldsymbol{I}_D \oslash \boldsymbol{I}_A$, where $\oslash$ denotes the Hadamard division (element-wise division).

Finally, the relative noise level N_R in a given region $\boldsymbol{R} \in \{0, 1\}^{n_p}$ is estimated via the relative deviation weighted by the activity at each pixel within $\boldsymbol{R}$:

$$N_R = \sum_{i=1}^{n_p} [\boldsymbol{W}]_i [\boldsymbol{I}_R]_i \text{ , with } \boldsymbol{W} = \frac{\boldsymbol{R} \odot \boldsymbol{I}_A}{\sum_{i=1}^{n_p} [\boldsymbol{R} \odot \boldsymbol{I}_A]_i} \tag{B.5}$$

Where $\odot$ denotes the Hadamard product (element-wise multiplication).

C Measurements in the Operating Room: Additional Figures

H1: Absolute SV with Patient-Independent Calibration

Figure C.1 – SV_{EIT} vs SV_{Ref} for best possible fit for hypothesis 1 (absolute SV with patient-independent calibration) shown for each of the feature sets and number of features investigated. The absolute error ϵ_{Abs} resulting from Bland-Altman analysis is shown in the lower right corner of each graph.

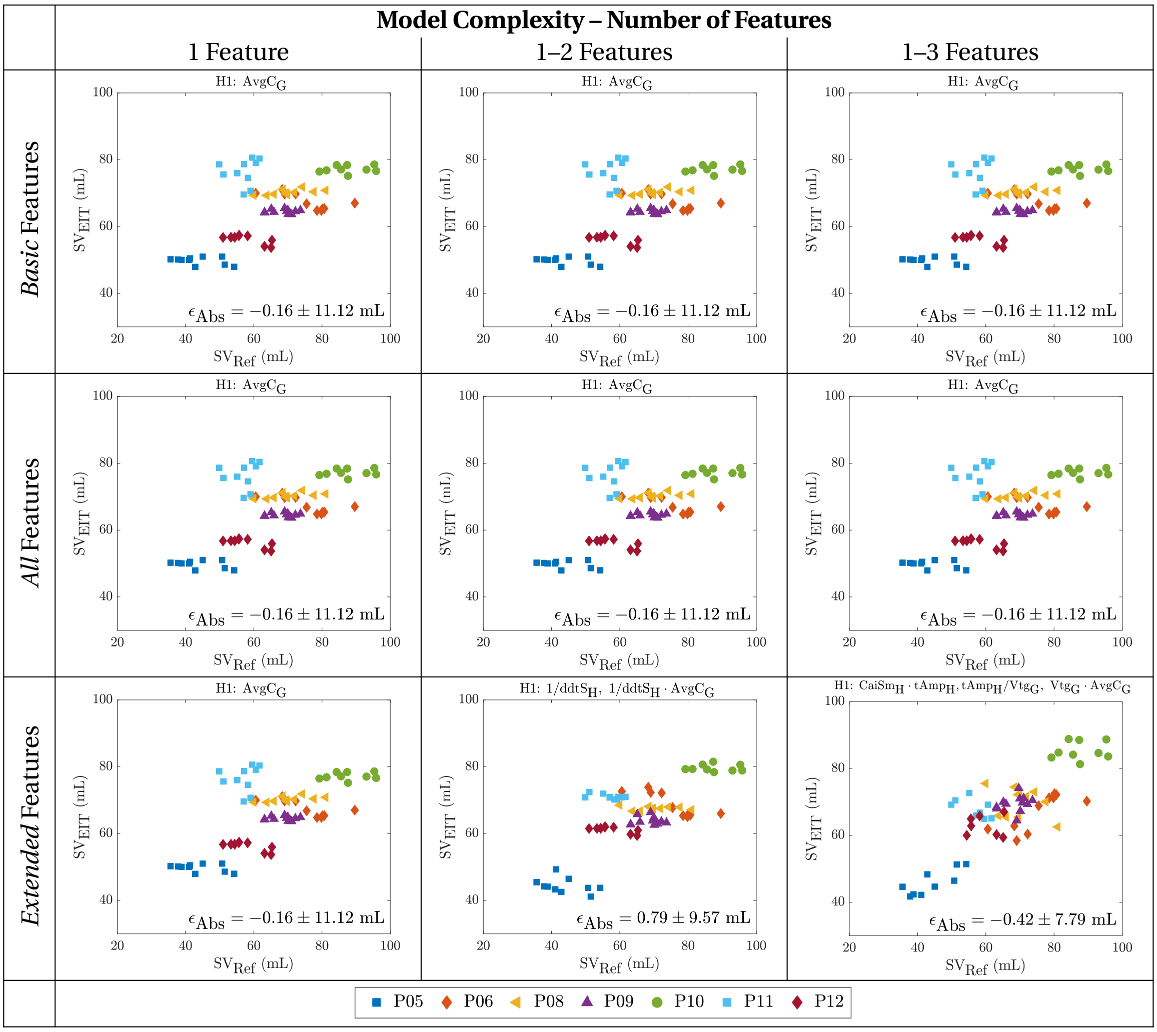

H2: Absolute SV with Patient-Specific Calibration

Figure C.2 – SV_{EIT} vs SV_{Ref} for best possible fit for hypothesis 2 (absolute SV with patient-specific calibration) shown for each of the feature sets and number of features investigated. The absolute error ϵ_{Abs} resulting from Bland-Altman analysis is shown in the lower right corner of each graph.

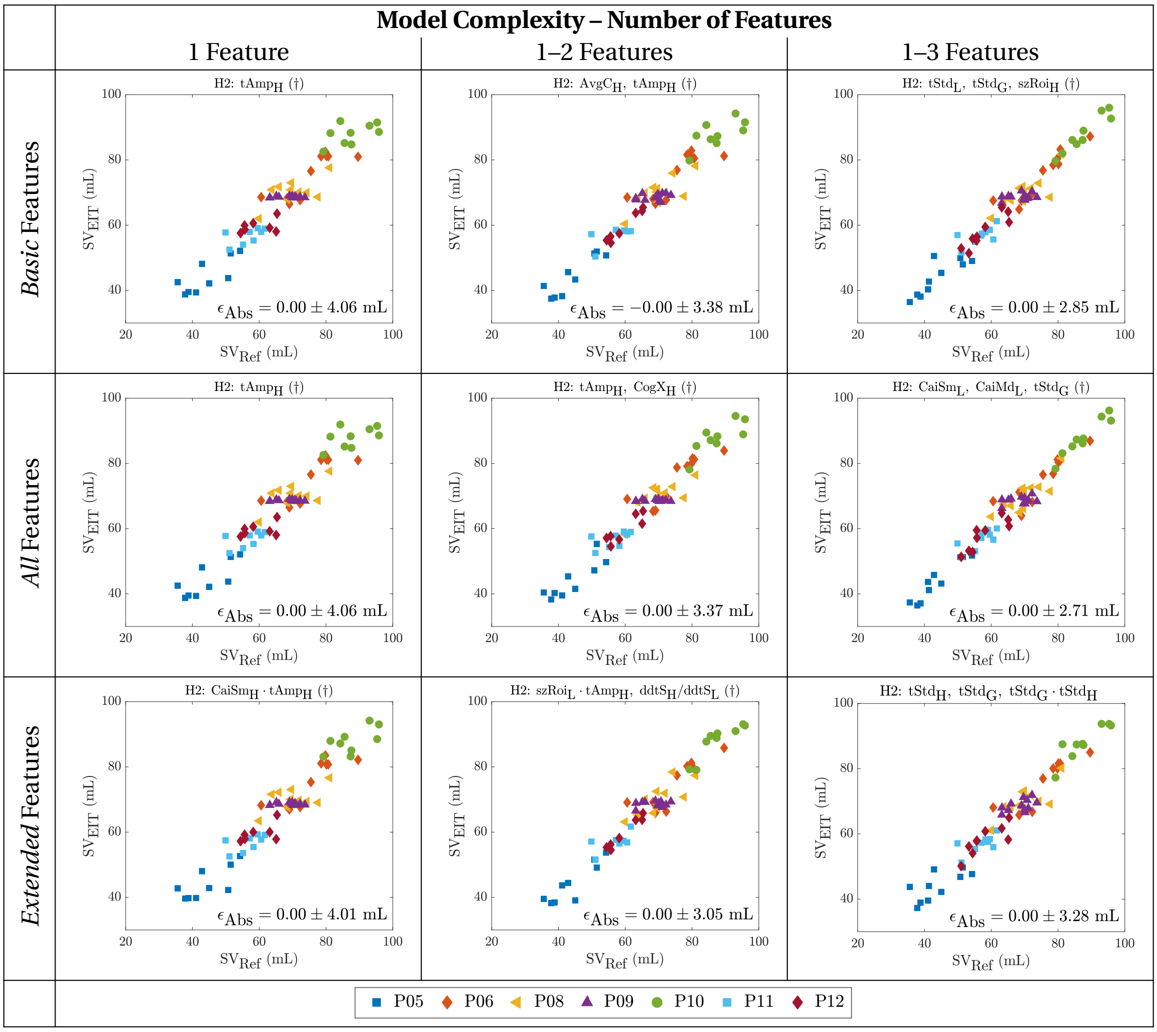

H3: Relative SV with Patient-Independent Calibration

Figure C.3 – Four-quadrant plot analysis between ΔSV_{EIT} vs ΔSV_{Ref} for best possible fits of hypothesis 3 (relative SV with patient-independent calibration) shown for each of the feature sets and number of features investigated. The concordance rate CR and angular error ϵ_α are shown in the lower right corner of each graph.

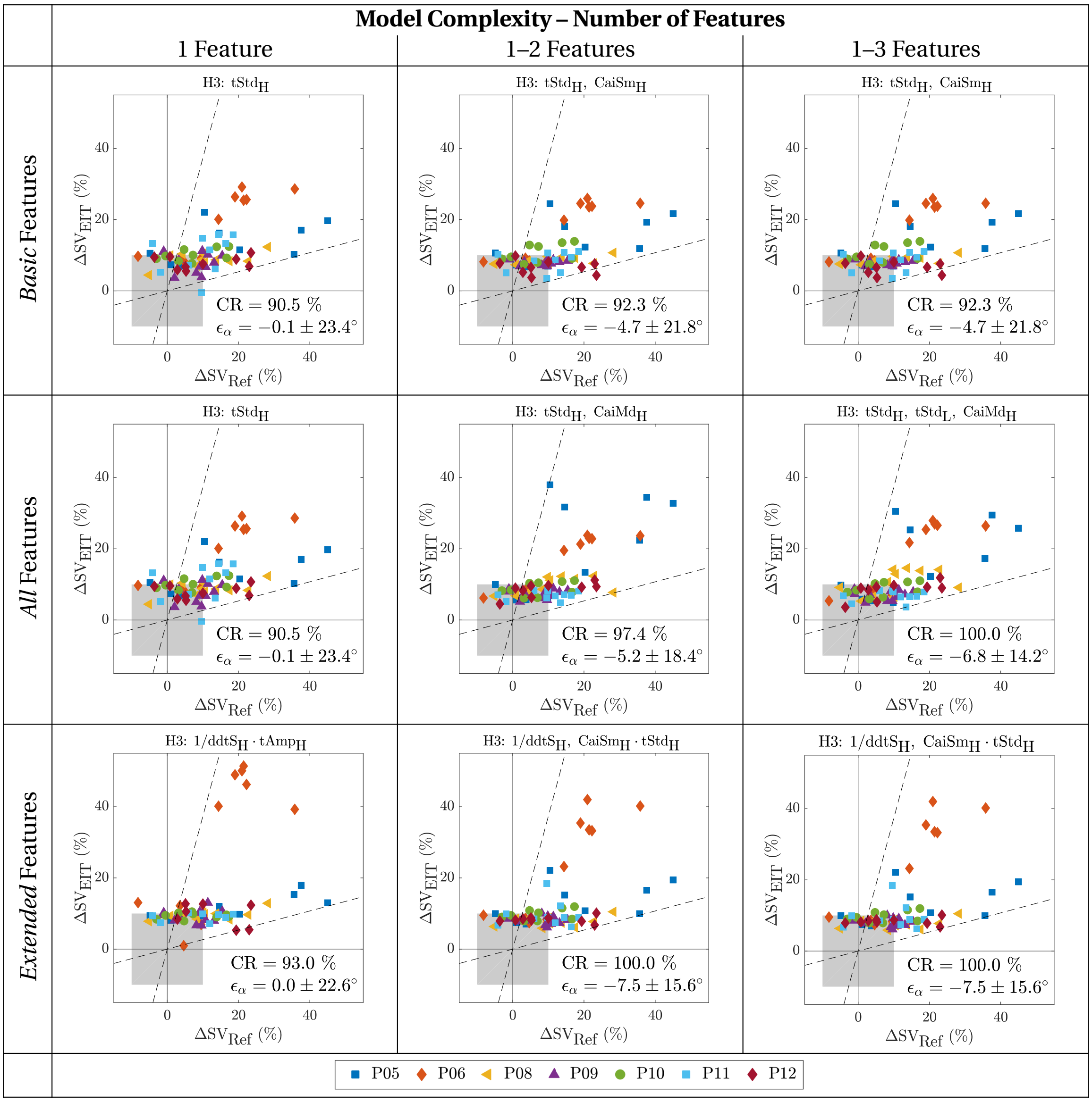

H4: Relative SV with Patient-Specific Calibration

Figure C.4 – Four-quadrant plot analysis between ΔSV_{EIT} vs ΔSV_{Ref} for best possible fits of hypothesis 4 (relative SV with patient-specific calibration) shown for each of the feature sets and number of features investigated. The concordance rate CR and angular error ϵ_α are shown in the lower right corner of each graph.

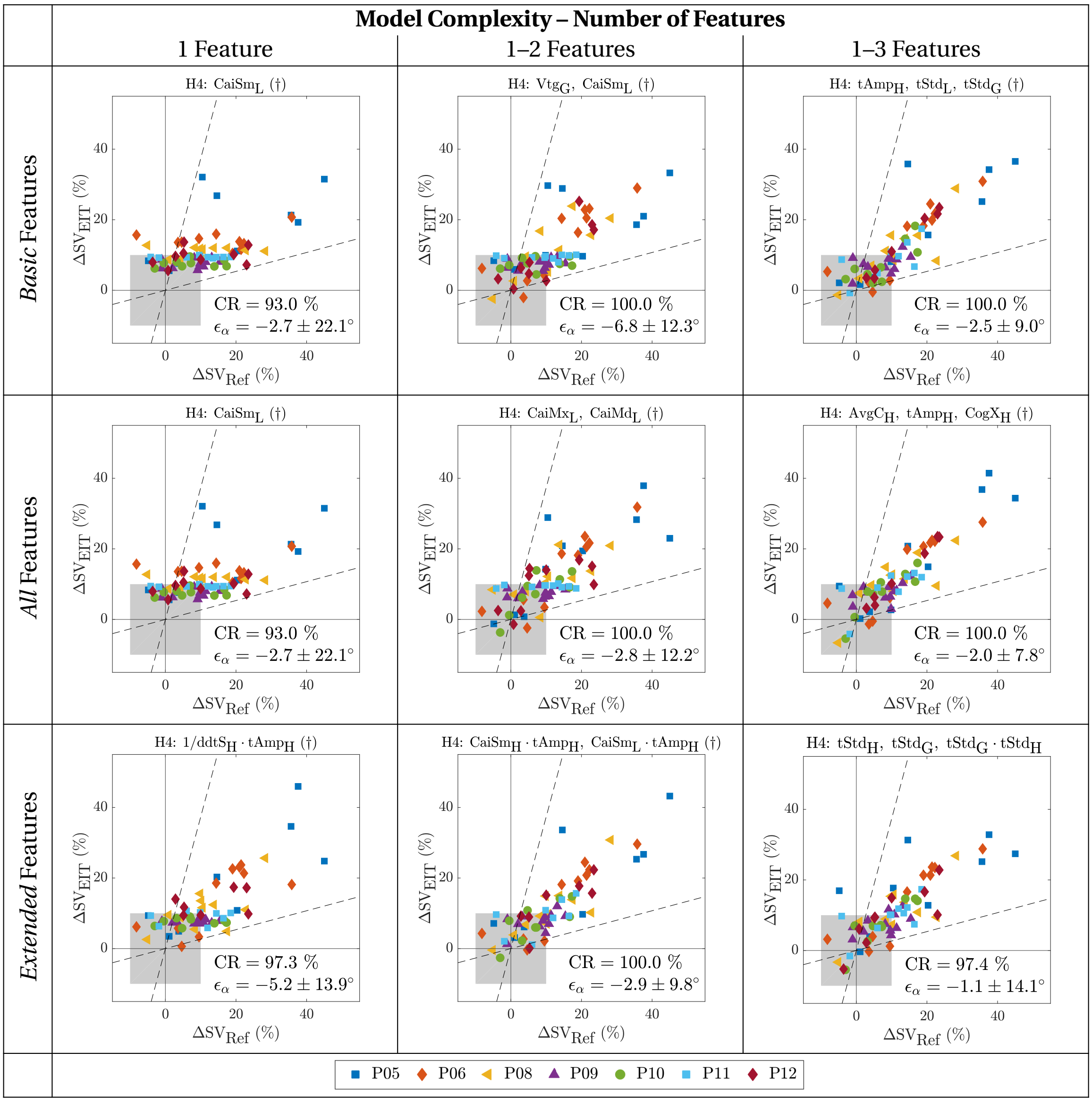

D Measurements in the Intensive Care Unit: Additional Figures

In the following we show the output from ensemble averaged EIT analysis for the three measurements (M1 to M3) of the sixteen subjects (V05 to V20), with the exception of V17 which is already shown in the main text in Figure 9.3.

Figures D.1 to D.15 all show the following: (Top) images of cardiosynchronous activity (CA) for the three measurements M1 to M3 with the averaged (—) and individual (······) ROIs. (Bottom) the corresponding temporal signals of conductivity change in the heart (black) and lung (blue) regions with the minima and maxima used to estimate the amplitudes $\Delta\sigma_{\mathrm{H}}$ and $\Delta\sigma_{\mathrm{L}}$.

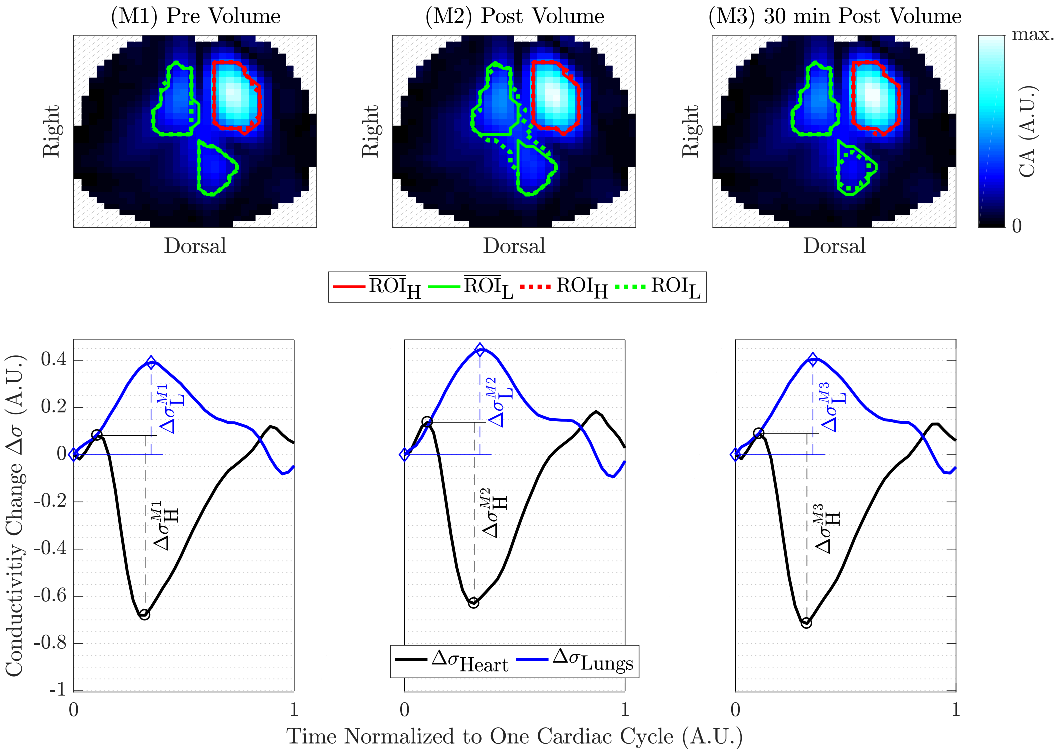

Figure D.1 – EIT analysis example for patient V05. See text in Appendix D for description.

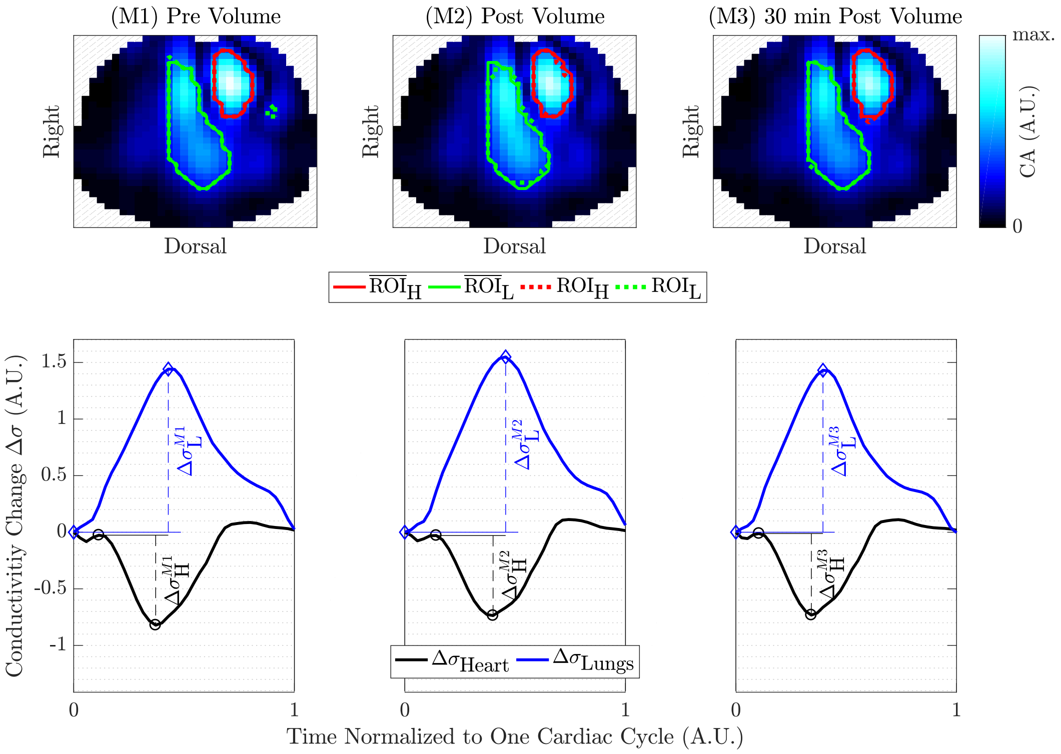
(M1) Pre Volume
(M2) Post Volume
(M3) 30 min Post Volume
Right
Dorsal
max.
CA (A.U.)
0
$\overline{\mathrm{ROI}}_\mathrm{H}$ $\overline{\mathrm{ROI}}_\mathrm{L}$ ROI_H ROI_L
Conductivitiy Change $\Delta\sigma$ (A.U.)
1.5
1
0.5
0
-0.5
-1
$\Delta\sigma_\mathrm{L}^{M1}$
$\Delta\sigma_\mathrm{H}^{M1}$
$\Delta\sigma_\mathrm{L}^{M2}$
$\Delta\sigma_\mathrm{H}^{M2}$
$\Delta\sigma_\mathrm{L}^{M3}$
$\Delta\sigma_\mathrm{H}^{M3}$
$\Delta\sigma_\mathrm{Heart}$ $\Delta\sigma_\mathrm{Lungs}$
0
1
Time Normalized to One Cardiac Cycle (A.U.)

Figure D.2 – EIT analysis example for patient V06. See text in Appendix D for description.

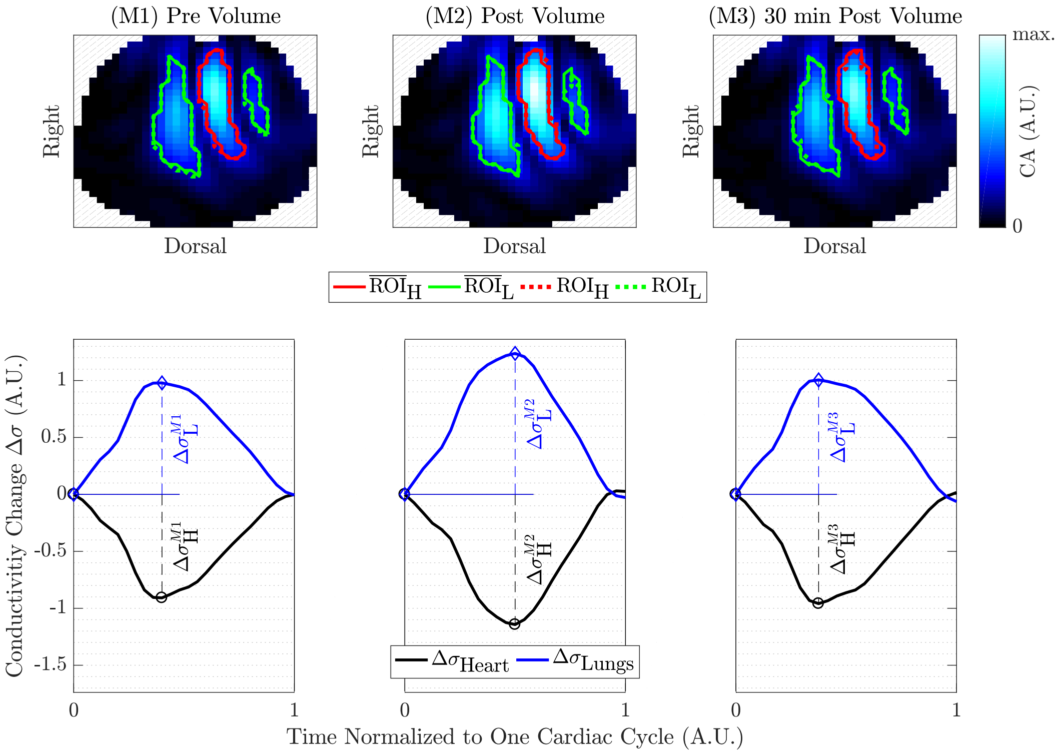
(M1) Pre Volume
(M2) Post Volume
(M3) 30 min Post Volume
Right
Dorsal
max.
CA (A.U.)
0
$\overline{\mathrm{ROI}}_\mathrm{H}$ $\overline{\mathrm{ROI}}_\mathrm{L}$ ROI_H ROI_L
Conductivitiy Change $\Delta\sigma$ (A.U.)
1
0.5
0
-0.5
-1
-1.5
$\Delta\sigma_\mathrm{L}^{M1}$
$\Delta\sigma_\mathrm{H}^{M1}$
$\Delta\sigma_\mathrm{L}^{M2}$
$\Delta\sigma_\mathrm{H}^{M2}$
$\Delta\sigma_\mathrm{L}^{M3}$
$\Delta\sigma_\mathrm{H}^{M3}$
$\Delta\sigma_\mathrm{Heart}$ $\Delta\sigma_\mathrm{Lungs}$
0
1
Time Normalized to One Cardiac Cycle (A.U.)

Figure D.3 – EIT analysis example for patient V07. See text in Appendix D for description.

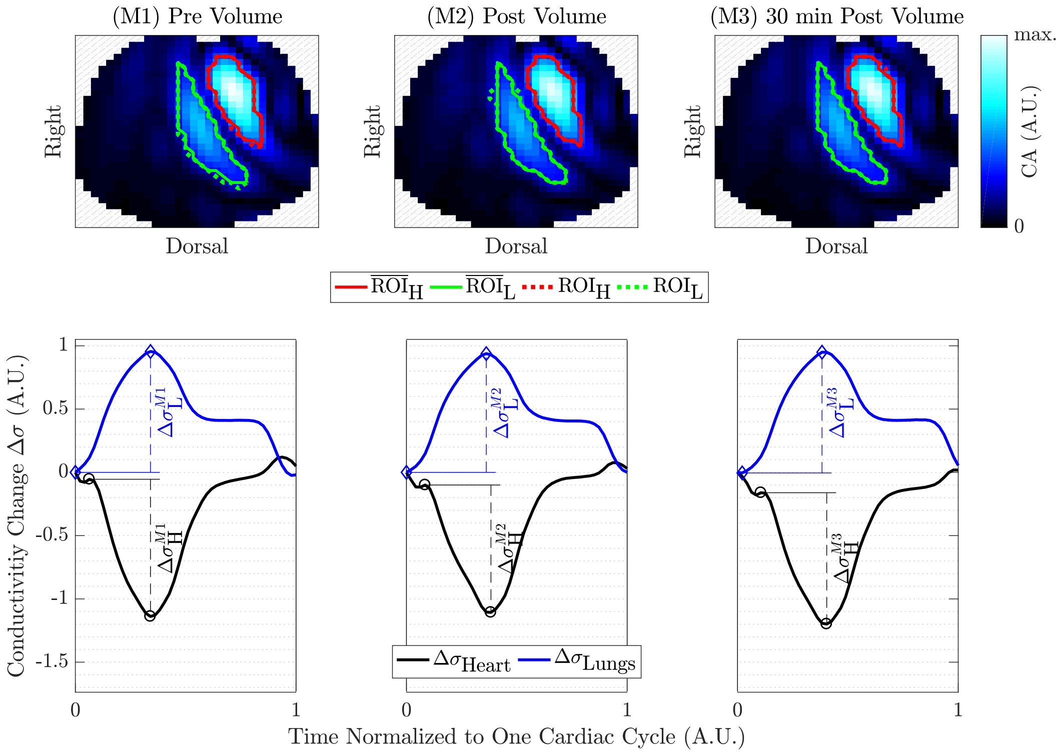
(M1) Pre Volume
(M2) Post Volume
(M3) 30 min Post Volume
Right
Dorsal
max.
CA (A.U.)
0
$\overline{\mathrm{ROI}}_\mathrm{H}$ $\overline{\mathrm{ROI}}_\mathrm{L}$ ROI_H ROI_L
Conductivitiy Change $\Delta\sigma$ (A.U.)
1
0.5
0
-0.5
-1
-1.5
$\Delta\sigma_\mathrm{L}^{M1}$ $\Delta\sigma_\mathrm{H}^{M1}$
$\Delta\sigma_\mathrm{L}^{M2}$ $\Delta\sigma_\mathrm{H}^{M2}$
$\Delta\sigma_\mathrm{L}^{M3}$ $\Delta\sigma_\mathrm{H}^{M3}$
$\Delta\sigma_\mathrm{Heart}$ $\Delta\sigma_\mathrm{Lungs}$
0
1
Time Normalized to One Cardiac Cycle (A.U.)

Figure D.4 – EIT analysis example for patient V08. See text in Appendix D for description.

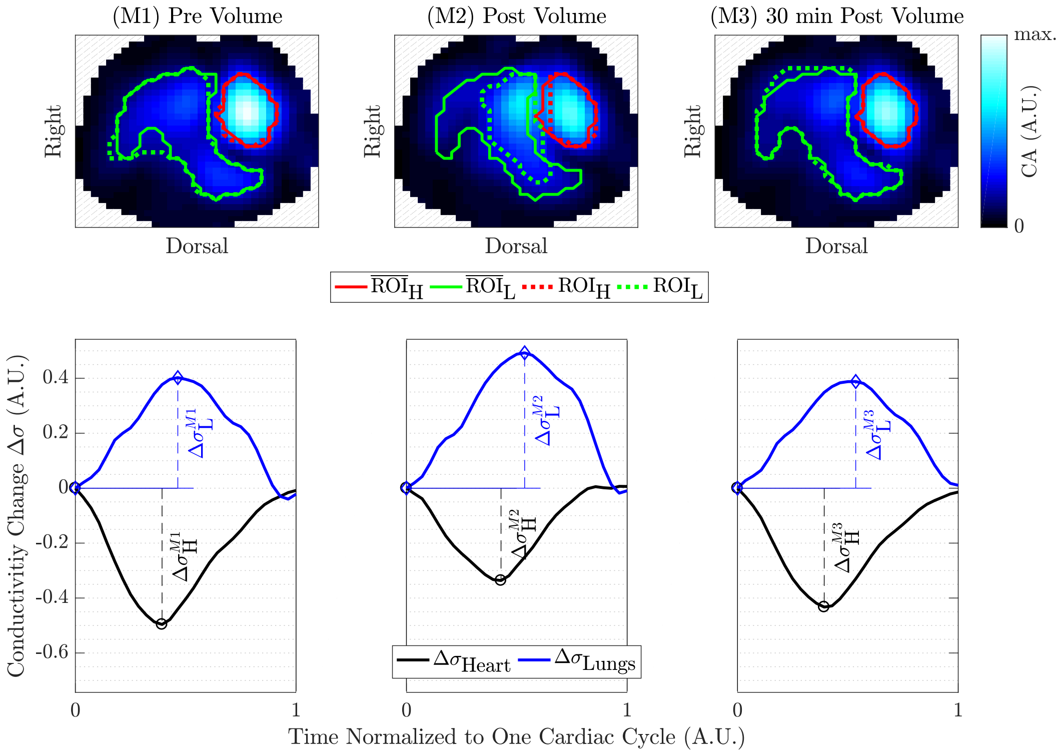
(M1) Pre Volume
(M2) Post Volume
(M3) 30 min Post Volume
Right
Dorsal
max.
CA (A.U.)
0
$\overline{\mathrm{ROI}}_\mathrm{H}$ $\overline{\mathrm{ROI}}_\mathrm{L}$ ROI_H ROI_L
Conductivitiy Change $\Delta\sigma$ (A.U.)
0.4
0.2
0
-0.2
-0.4
-0.6
$\Delta\sigma_\mathrm{L}^{M1}$ $\Delta\sigma_\mathrm{H}^{M1}$
$\Delta\sigma_\mathrm{L}^{M2}$ $\Delta\sigma_\mathrm{H}^{M2}$
$\Delta\sigma_\mathrm{L}^{M3}$ $\Delta\sigma_\mathrm{H}^{M3}$
$\Delta\sigma_\mathrm{Heart}$ $\Delta\sigma_\mathrm{Lungs}$
0
1
Time Normalized to One Cardiac Cycle (A.U.)

Figure D.5 – EIT analysis example for patient V09. See text in Appendix D for description.

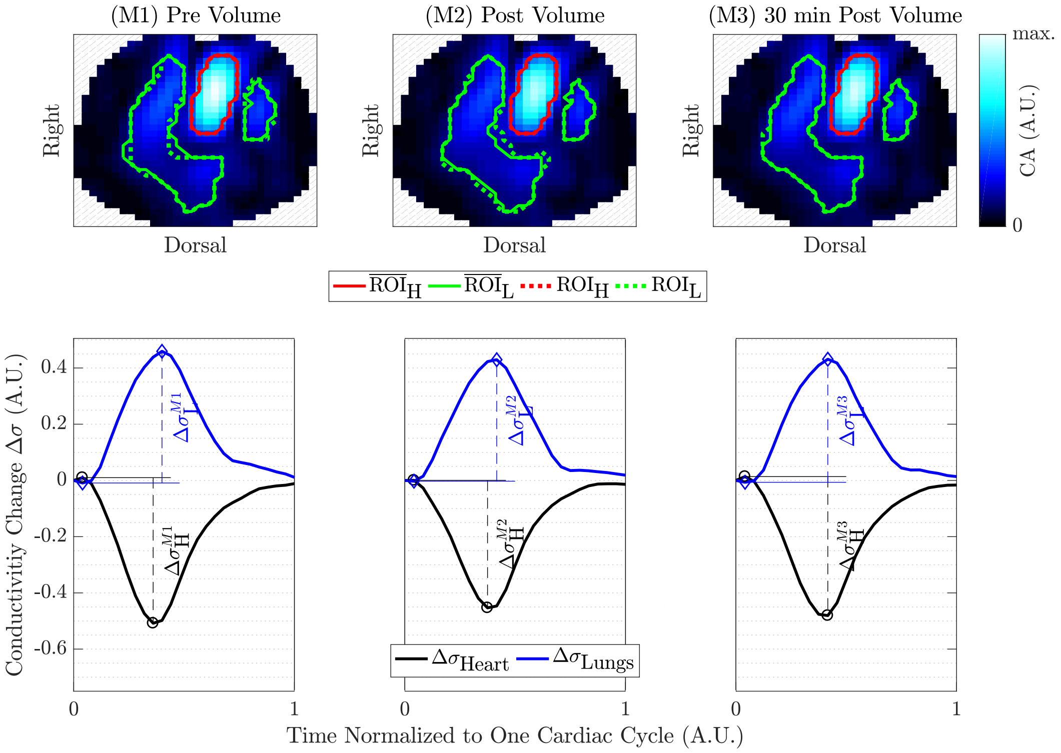

Figure D.6 – EIT analysis example for patient V10. See text in Appendix D for description.

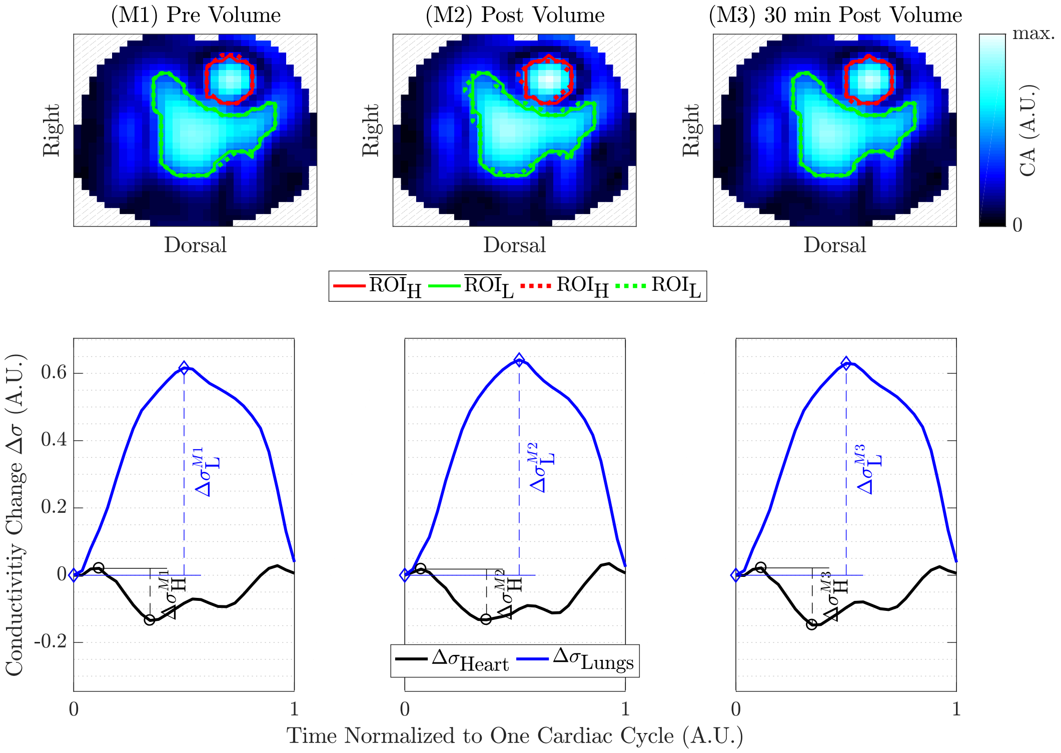

Figure D.7 – EIT analysis example for patient V11. See text in Appendix D for description.

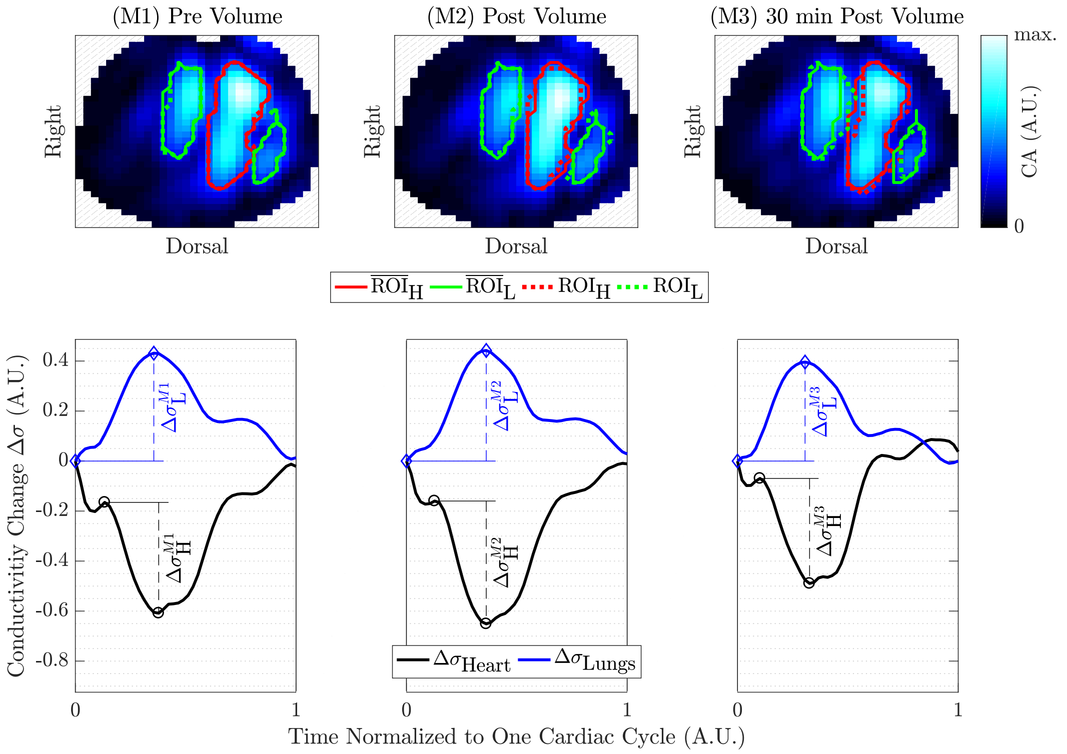

Figure D.8 – EIT analysis example for patient V12. See text in Appendix D for description.

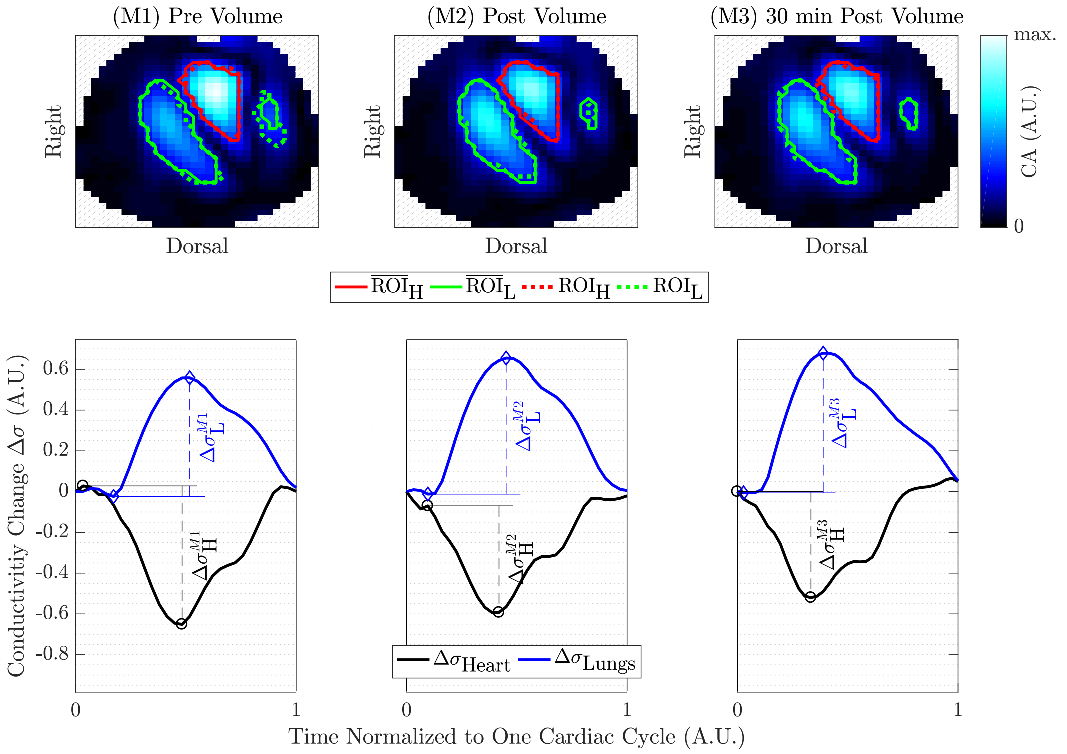

Figure D.9 – EIT analysis example for patient V13. See text in Appendix D for description.

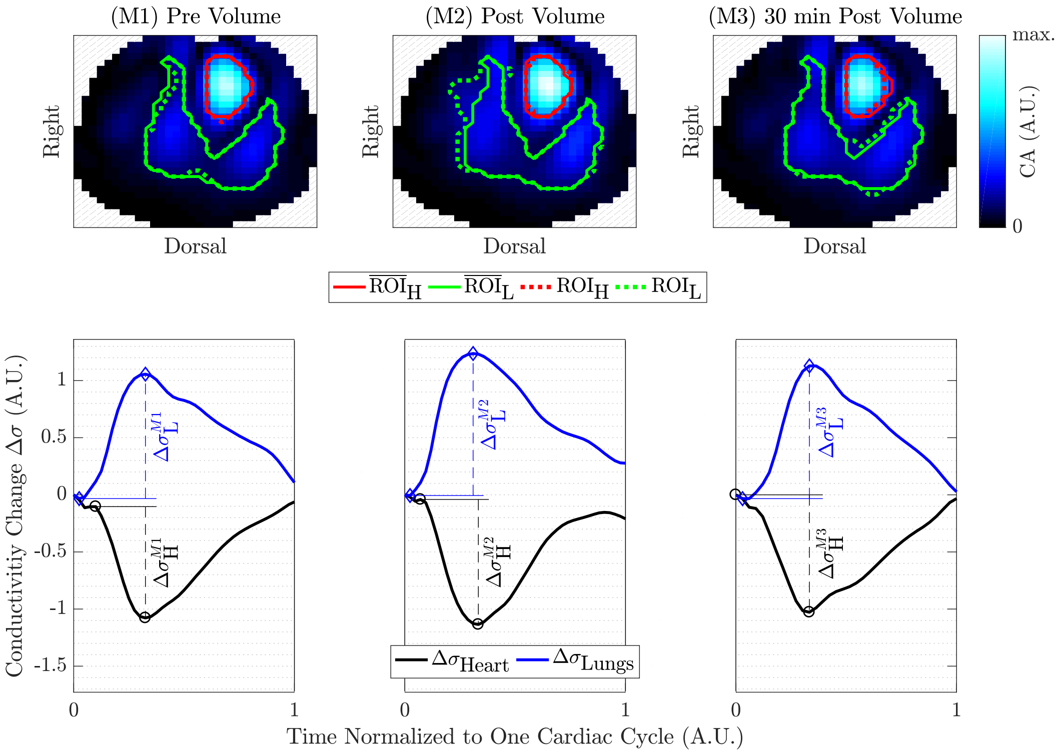
(M1) Pre Volume
(M2) Post Volume
(M3) 30 min Post Volume
Right
Dorsal
max.
CA (A.U.)
0
$\overline{\mathrm{ROI}}_\mathrm{H}$ $\overline{\mathrm{ROI}}_\mathrm{L}$ ROI_H ROI_L
Conductivitiy Change Δσ (A.U.)
1
0.5
0
-0.5
-1
-1.5
$\Delta\sigma_L^{M1}$
$\Delta\sigma_H^{M1}$
$\Delta\sigma_L^{M2}$
$\Delta\sigma_H^{M2}$
$\Delta\sigma_L^{M3}$
$\Delta\sigma_H^{M3}$
$\Delta\sigma_\mathrm{Heart}$ $\Delta\sigma_\mathrm{Lungs}$
0
1
Time Normalized to One Cardiac Cycle (A.U.)

Figure D.10 – EIT analysis example for patient V14. See text in Appendix D for description.

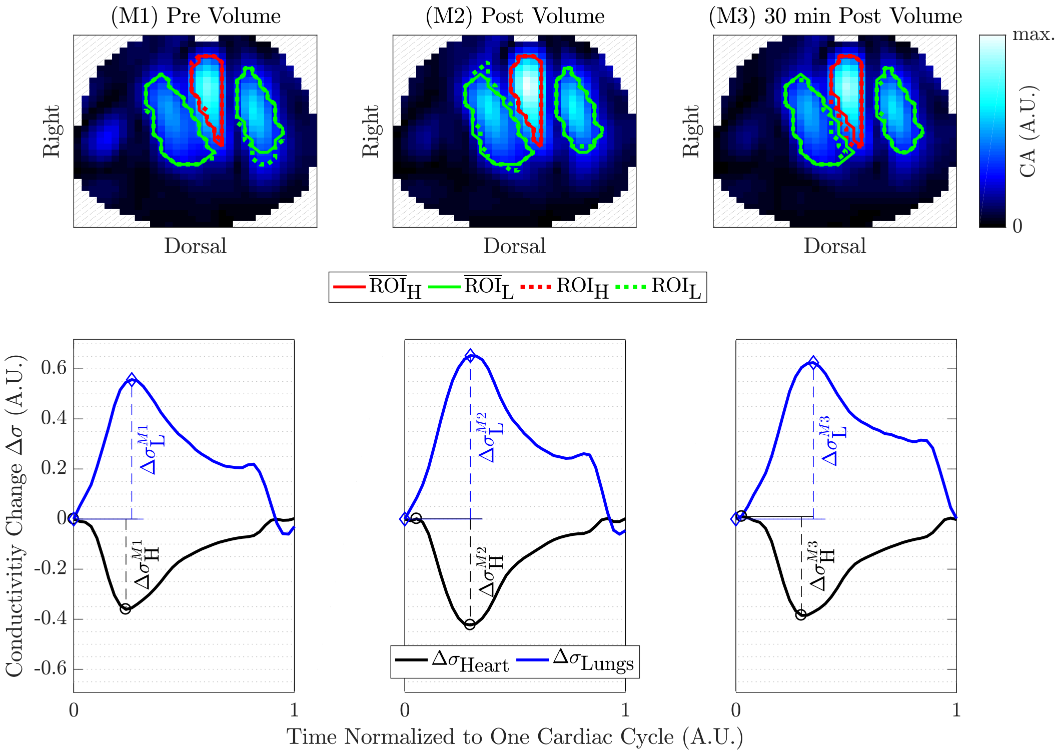
(M1) Pre Volume
(M2) Post Volume
(M3) 30 min Post Volume
Right
Dorsal
max.
CA (A.U.)
0
$\overline{\mathrm{ROI}}_\mathrm{H}$ $\overline{\mathrm{ROI}}_\mathrm{L}$ ROI_H ROI_L
Conductivitiy Change Δσ (A.U.)
0.6
0.4
0.2
0
-0.2
-0.4
-0.6
$\Delta\sigma_L^{M1}$
$\Delta\sigma_H^{M1}$
$\Delta\sigma_L^{M2}$
$\Delta\sigma_H^{M2}$
$\Delta\sigma_L^{M3}$
$\Delta\sigma_H^{M3}$
$\Delta\sigma_\mathrm{Heart}$ $\Delta\sigma_\mathrm{Lungs}$
0
1
Time Normalized to One Cardiac Cycle (A.U.)

Figure D.11 – EIT analysis example for patient V15. See text in Appendix D for description.

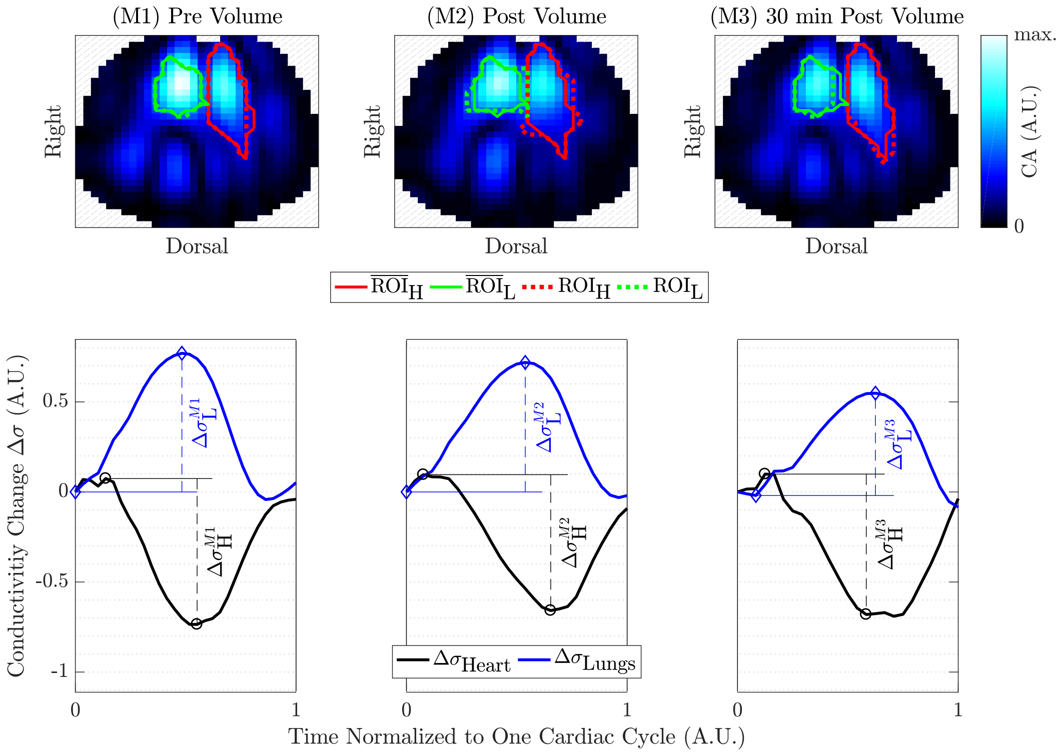
(M1) Pre Volume
(M2) Post Volume
(M3) 30 min Post Volume
Right
Dorsal
max.
CA (A.U.)
0
$\overline{\mathrm{ROI}}_\mathrm{H}$ $\overline{\mathrm{ROI}}_\mathrm{L}$ ROI_H ROI_L
Conductivitiy Change $\Delta\sigma$ (A.U.)
0.5
0
-0.5
-1
$\Delta\sigma^{M1}_\mathrm{L}$ $\Delta\sigma^{M1}_\mathrm{H}$
$\Delta\sigma^{M2}_\mathrm{L}$ $\Delta\sigma^{M2}_\mathrm{H}$
$\Delta\sigma^{M3}_\mathrm{L}$ $\Delta\sigma^{M3}_\mathrm{H}$
$\Delta\sigma_\mathrm{Heart}$ $\Delta\sigma_\mathrm{Lungs}$
0 1
Time Normalized to One Cardiac Cycle (A.U.)

Figure D.12 – EIT analysis example for patient V16. See text in Appendix D for description.

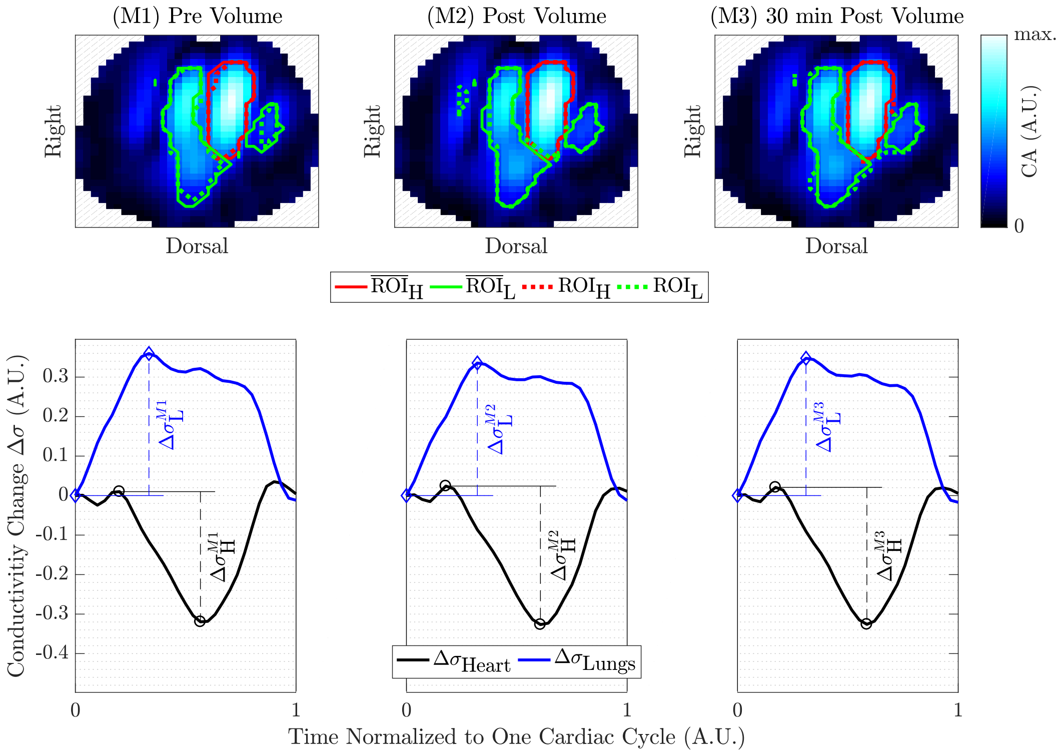
(M1) Pre Volume
(M2) Post Volume
(M3) 30 min Post Volume
Right
Dorsal
max.
CA (A.U.)
0
$\overline{\mathrm{ROI}}_\mathrm{H}$ $\overline{\mathrm{ROI}}_\mathrm{L}$ ROI_H ROI_L
Conductivitiy Change $\Delta\sigma$ (A.U.)
0.3
0.2
0.1
0
-0.1
-0.2
-0.3
-0.4
$\Delta\sigma^{M1}_\mathrm{L}$ $\Delta\sigma^{M1}_\mathrm{H}$
$\Delta\sigma^{M2}_\mathrm{L}$ $\Delta\sigma^{M2}_\mathrm{H}$
$\Delta\sigma^{M3}_\mathrm{L}$ $\Delta\sigma^{M3}_\mathrm{H}$
$\Delta\sigma_\mathrm{Heart}$ $\Delta\sigma_\mathrm{Lungs}$
0 1
Time Normalized to One Cardiac Cycle (A.U.)

Figure D.13 – EIT analysis example for patient V18. See text in Appendix D for description.

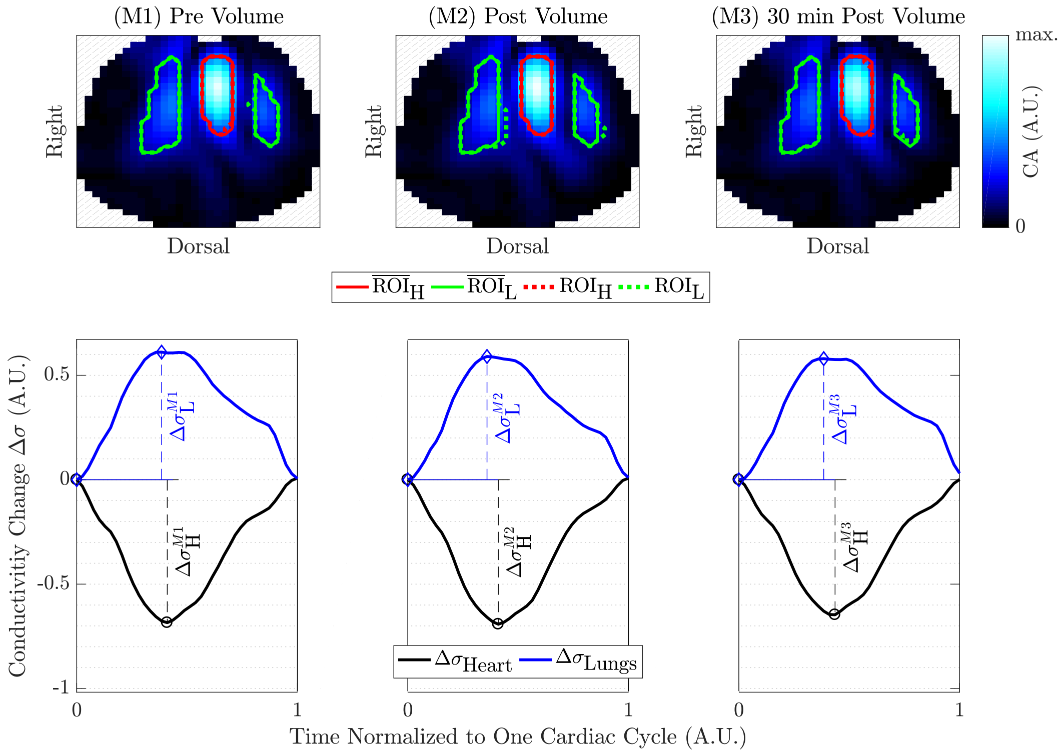
(M1) Pre Volume
(M2) Post Volume
(M3) 30 min Post Volume
Right
Dorsal
max.
CA (A.U.)
0
$\overline{\text{ROI}}_\text{H}$ $\overline{\text{ROI}}_\text{L}$ ROI_H ROI_L
Conductivitiy Change $\Delta\sigma$ (A.U.)
0.5
0
-0.5
-1
$\Delta\sigma_\text{L}^{M1}$
$\Delta\sigma_\text{H}^{M1}$
$\Delta\sigma_\text{L}^{M2}$
$\Delta\sigma_\text{H}^{M2}$
$\Delta\sigma_\text{L}^{M3}$
$\Delta\sigma_\text{H}^{M3}$
$\Delta\sigma_\text{Heart}$ $\Delta\sigma_\text{Lungs}$
0
1
Time Normalized to One Cardiac Cycle (A.U.)

Figure D.14 – EIT analysis example for patient V19. See text in Appendix D for description.

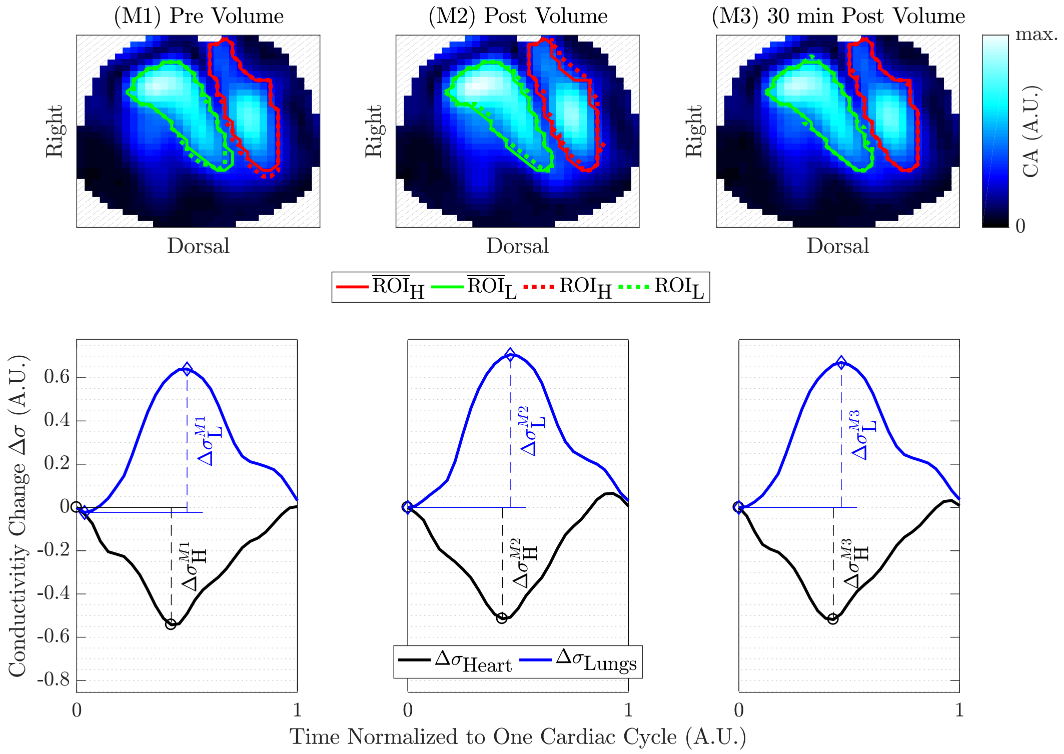
(M1) Pre Volume
(M2) Post Volume
(M3) 30 min Post Volume
Right
Dorsal
max.
CA (A.U.)
0
$\overline{\text{ROI}}_\text{H}$ $\overline{\text{ROI}}_\text{L}$ ROI_H ROI_L
Conductivitiy Change $\Delta\sigma$ (A.U.)
0.6
0.4
0.2
0
-0.2
-0.4
-0.6
-0.8
$\Delta\sigma_\text{L}^{M1}$
$\Delta\sigma_\text{H}^{M1}$
$\Delta\sigma_\text{L}^{M2}$
$\Delta\sigma_\text{H}^{M2}$
$\Delta\sigma_\text{L}^{M3}$
$\Delta\sigma_\text{H}^{M3}$
$\Delta\sigma_\text{Heart}$ $\Delta\sigma_\text{Lungs}$
0
1
Time Normalized to One Cardiac Cycle (A.U.)

Figure D.15 – EIT analysis example for patient V20. See text in Appendix D for description.

E Measurements on Healthy Volunteers: Additional Figures and Tables

In the following we show the temporal evolution of SV_{Ref}, heart rate and EIT-based features for each of the nine subjects considered for analysis, with the exception of S03 which is already shown in the main text in Figure 12.9 and S07 which was excluded from analysis as discussed in Section 12.2.5.

This is followed by Tables E.1 to E.4 showing the overall and subject-specific performance for a selection of features and the hypotheses (H1) to (H4) described in Section 12.2.5.

Figures E.1 to E.8 all show the following: (Top) Temporal evolution of reference stroke volume (black) and heart rate (red) for the entire protocol comprised of tasks T1 to T13 (as described in Figure 12.1). The beginning of each task is marked with a vertical line (- - -) and the particular tasks considered for analysis are shaded in light (lying) or dark gray (recovery). (Middle) One minute averages used for analysis showing SV_{Ref} and two EIT features: the systolic heart amplitude ($\Delta\sigma_H$) and the temporal standard-deviation of the heart signal during one full cardiac cycle ($tStd_H$). (Bottom) Tidal volume V_R (blue) measured by the reference device (MetaMax 3B) and the one minute averages of the global conductivity feature σ_G (green).

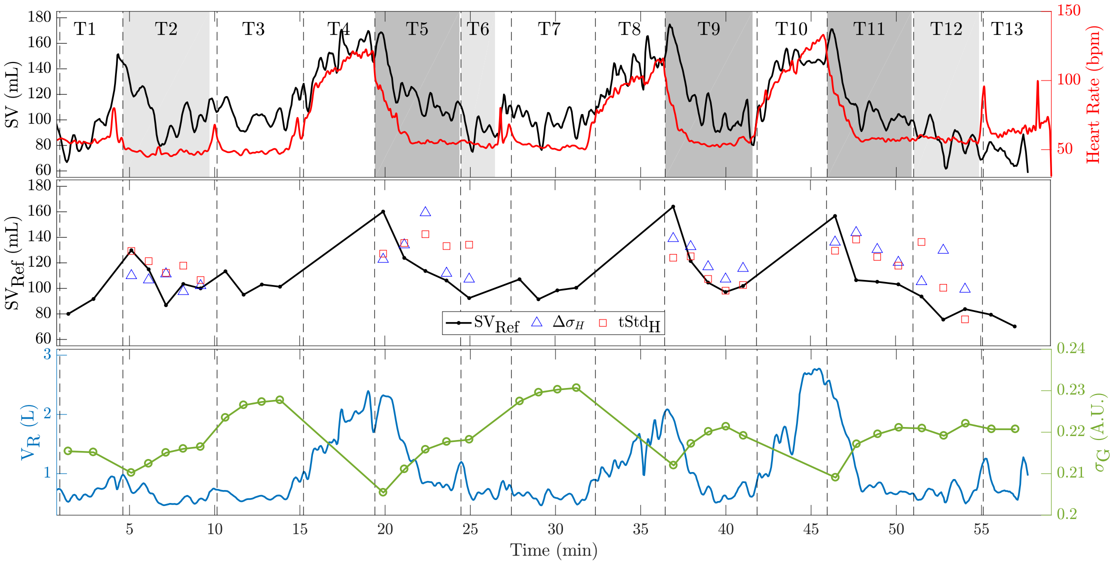

Figure E.1 – Temporal evolution of SV_{Ref}, heart rate and EIT-based features for subject S01. See text in Appendix E for description.

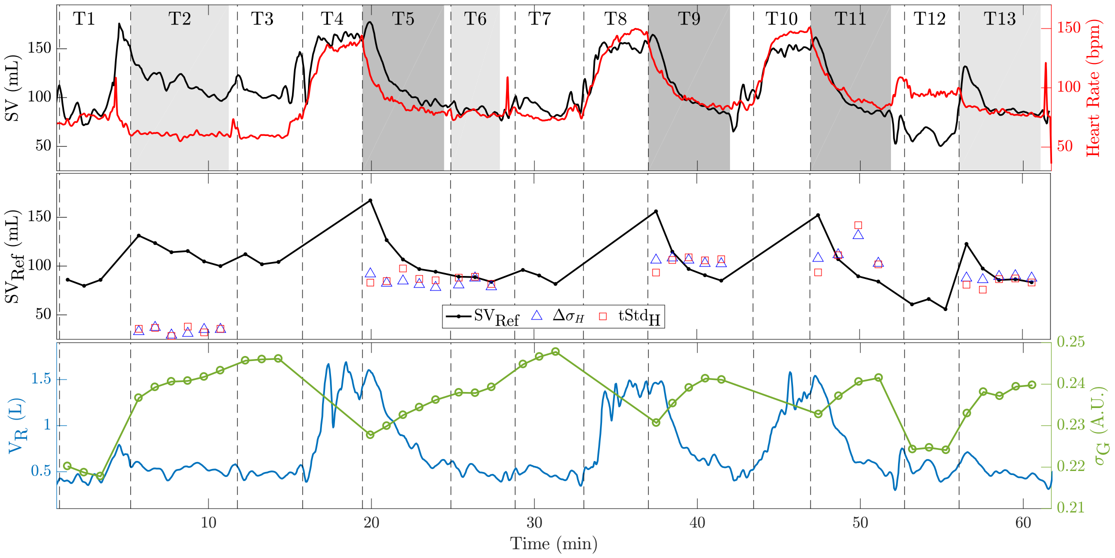

Figure E.2 – Temporal evolution of SV_{Ref}, heart rate and EIT-based features for subject S02. See text in Appendix E for description.

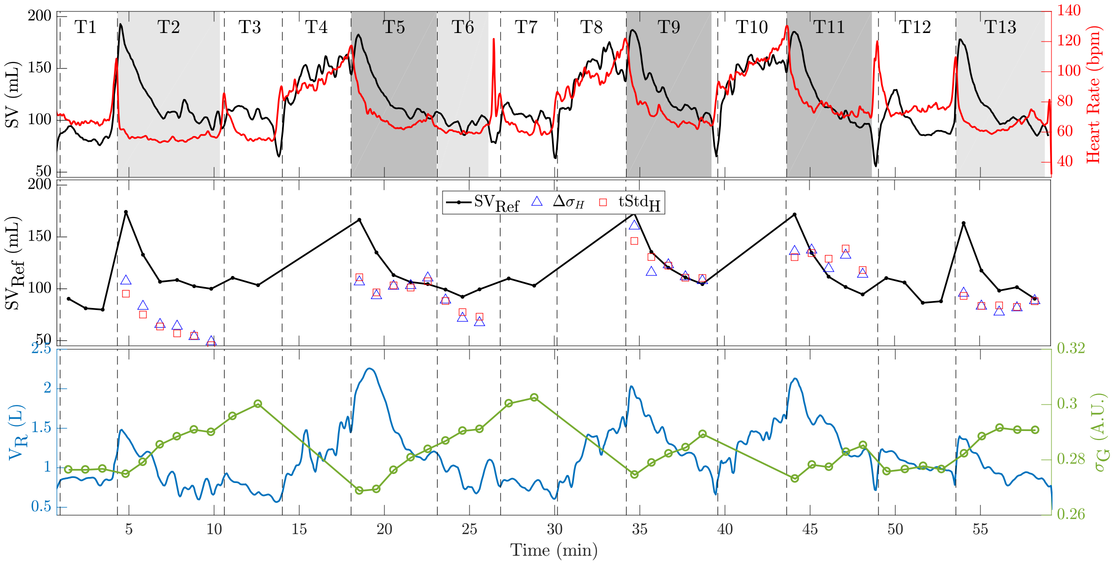

Figure E.3 – Temporal evolution of SV_{Ref}, heart rate and EIT-based features for subject S04. See text in Appendix E for description.

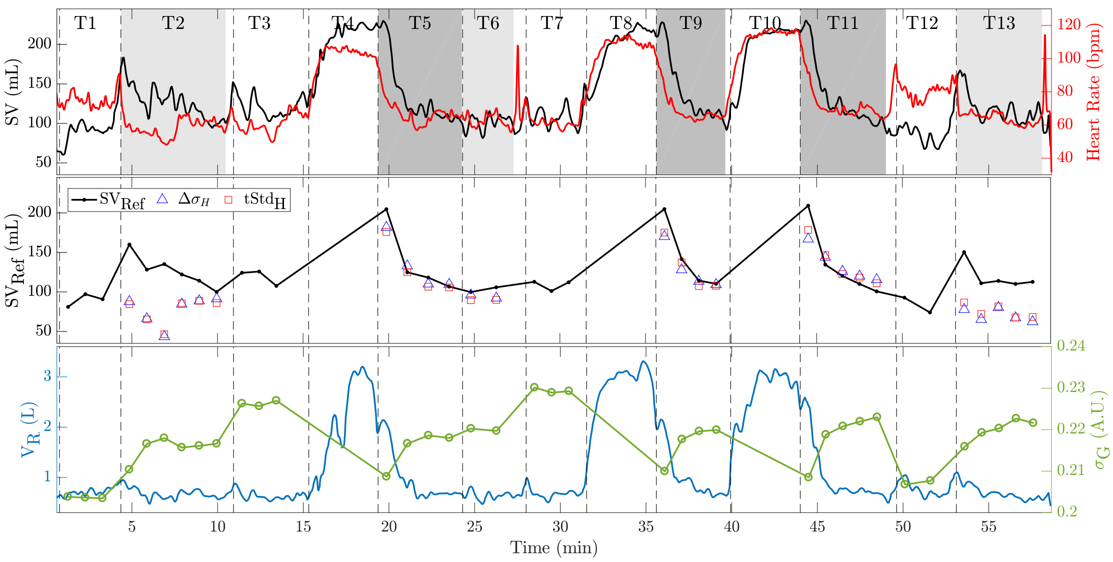

Figure E.4 – Temporal evolution of SV_{Ref}, heart rate and EIT-based features for subject S05. See text in Appendix E for description.

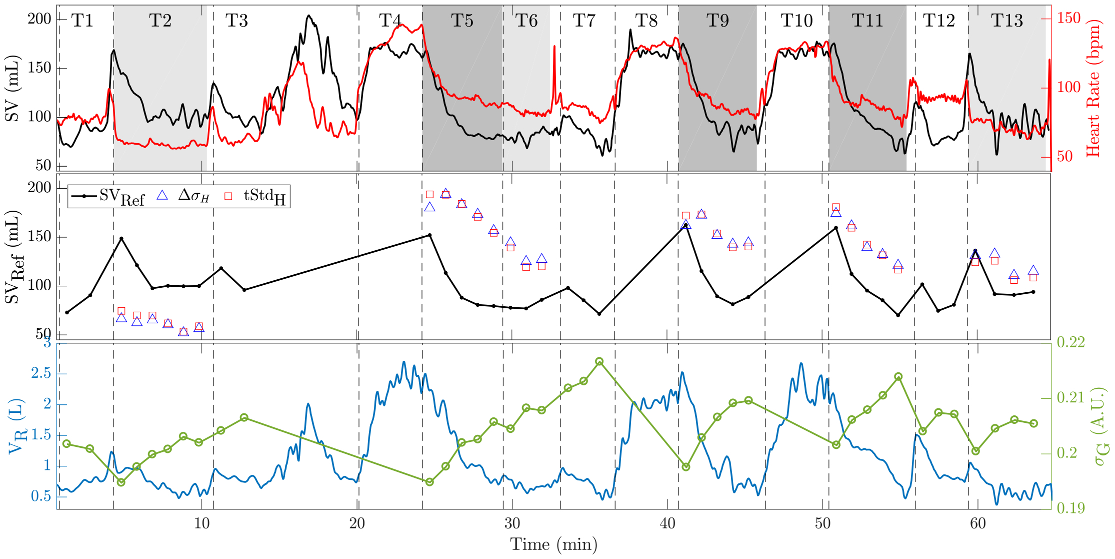

Figure E.5 – Temporal evolution of SV_{Ref}, heart rate and EIT-based features for subject S06. See text in Appendix E for description.

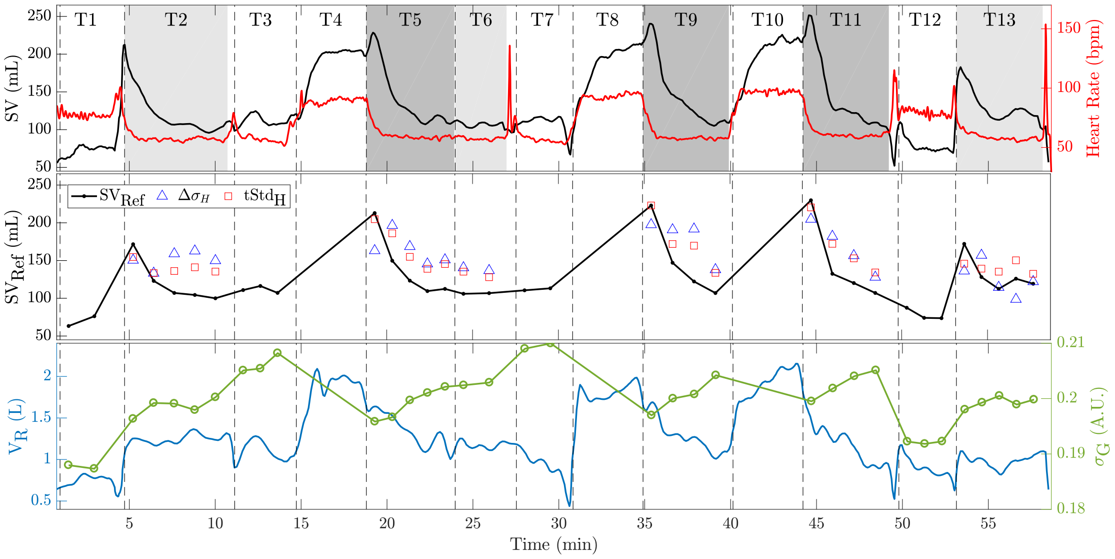

Figure E.6 – Temporal evolution of SV_{Ref}, heart rate and EIT-based features for subject S08. See text in Appendix E for description.

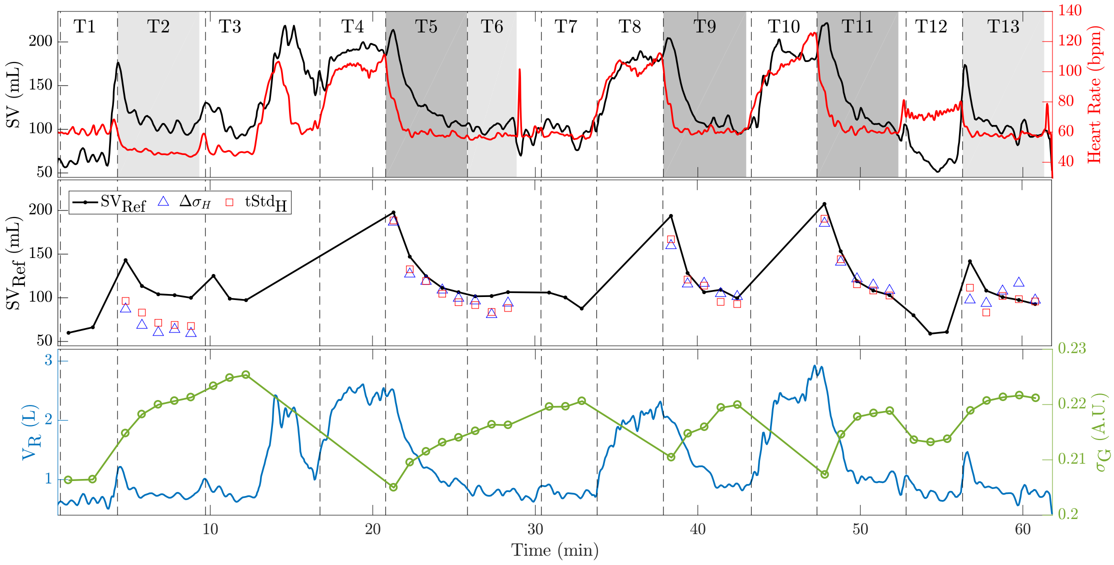

Figure E.7 – Temporal evolution of SV_{Ref}, heart rate and EIT-based features for subject S09. See text in Appendix E for description.

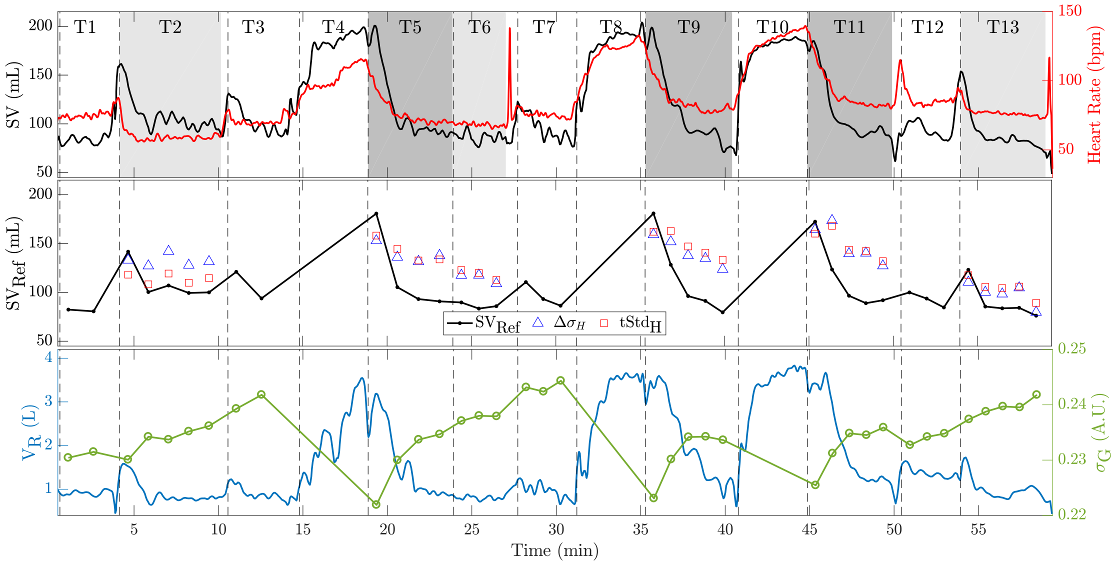

Figure E.8 – Temporal evolution of SV_{Ref}, heart rate and EIT-based features for subject S10. See text in Appendix E for description.

Table E.1 – Subject-specific and overall performance for a selection of eight features (a) to (h) and hypothesis (H1) absolute SV via subject-independent calibration. The performance between SV_EIT and SV_Ref is evaluated in terms of absolute error ϵ_Abs and correlation coefficient r. The (†) indicates unrealistic solutions with calibrations coefficients *not* having identical sign for all subjects. Cell shadings indicate whether the acceptance criteria (see Section 12.2.5) are met (green), not met (red), or met but with unrealistic calibration coefficients (yellow).

	(a) $\Delta\sigma_\mathrm{H}$		(b) tStd_H		(c) $\Delta\sigma_\mathrm{L}$		(d) tStd_L	
	ϵ_Abs (mL)	r (1)	ϵ_Abs (mL)	r (1)	ϵ_Abs (mL)	r (1)	ϵ_Abs (mL)	r (1)
S01	18.7 ± 18.0	0.456	11.7 ± 17.8	0.358	21.6 ± 14.8	0.714	17.9 ± 17.9	0.467
S02	−39.5 ± 11.0	0.118	−38.9 ± 12.6	−0.144	−37.2 ± 13.0	−0.070	−39.4 ± 11.9	−0.035
S03	−7.9 ± 16.2	0.242	−12.8 ± 17.0	0.102	−9.1 ± 24.9	−0.786	−5.6 ± 21.3	−0.753
S04	30.5 ± 23.9	0.563	29.2 ± 23.4	0.426	30.6 ± 20.6	0.784	28.2 ± 24.3	0.358
S05	21.0 ± 23.1	0.696	22.9 ± 19.2	0.778	16.6 ± 24.0	0.172	19.9 ± 25.9	−0.167
S06	−10.5 ± 18.1	0.328	−13.4 ± 17.1	0.417	−3.6 ± 18.9	0.152	−7.5 ± 18.3	0.281
S08	−12.0 ± 20.9	0.720	−6.5 ± 15.2	0.958	−11.1 ± 18.8	0.598	−11.2 ± 20.4	0.482
S09	26.4 ± 15.8	0.893	30.8 ± 12.5	0.935	18.5 ± 16.1	0.356	22.0 ± 16.6	0.235
S10	6.3 ± 12.6	0.577	5.7 ± 10.6	0.639	2.1 ± 12.8	0.366	4.1 ± 13.6	0.161
All	−0.5 ± 28.2	−0.424	−1.0 ± 27.3	0.023	−0.4 ± 27.3	−0.023	−0.5 ± 28.1	−0.341

	(e) tStd_G		(f) $\Delta\sigma_\mathrm{H}$, $\frac{\Delta\sigma_\mathrm{H}}{\sigma_\mathrm{G}}$		(g) $\Delta\sigma_\mathrm{L}$, $\frac{\Delta\sigma_\mathrm{L}}{\sigma_\mathrm{G}}$		(h) V_T	
	ϵ_Abs (mL)	r (1)	ϵ_Abs (mL)	r (1)	ϵ_Abs (mL)	r (1)	ϵ_Abs (mL)	r (1)
S01	18.3 ± 18.6	0.363	17.1 ± 15.4	0.884	21.6 ± 12.3	0.833	15.1 ± 5.5	0.963
S02	−38.8 ± 11.2	−0.186	−52.4 ± 6.3	0.833	−39.4 ± 11.6	0.244	−39.8 ± 9.4	0.898
S03	−5.2 ± 18.3	−0.844	−8.3 ± 15.2	0.546	−15.9 ± 27.9	−0.684	−4.4 ± 13.5	0.590
S04	28.5 ± 25.2	0.069	29.9 ± 22.5	0.815	29.9 ± 20.0	0.803	25.9 ± 17.1	0.791
S05	19.3 ± 25.1	−0.600	25.0 ± 21.8	0.755	23.5 ± 19.5	0.870	24.2 ± 12.9	0.954
S06	−10.0 ± 18.9	−0.100	−8.7 ± 17.2	0.676	−4.9 ± 18.0	0.302	−8.6 ± 11.0	0.814
S08	−11.8 ± 21.5	0.093	−11.7 ± 19.2	0.650	−11.5 ± 17.2	0.698	−18.0 ± 11.8	0.860
S09	26.0 ± 16.7	0.649	28.1 ± 15.8	0.844	22.4 ± 12.8	0.768	25.0 ± 10.0	0.907
S10	5.6 ± 13.9	−0.139	5.1 ± 12.3	0.729	6.1 ± 11.8	0.543	11.9 ± 7.1	0.860
All	(†) −0.5 ± 28.2	−0.710	−1.7 ± 30.4	−0.365	(†) −0.4 ± 28.4	−0.050	−0.4 ± 24.7	0.371

Table E.2 – Subject-specific and overall performance for a selection of eight features (a) to (h) and hypothesis (H2) absolute SV via subject-specific calibration. The performance between SV_{EIT} and SV_{Ref} is evaluated in terms of absolute error ϵ_{Abs} and correlation coefficient r. The (†) indicates unrealistic solutions with calibrations coefficients *not* having identical sign for all subjects. Cell shadings indicate whether the acceptance criteria (see Section 12.2.5) are met (green), not met (red), or met but with unrealistic calibration coefficients (yellow).

	(a) $\Delta\sigma_{\text{H}}$		(b) tStd_{H}		(c) $\Delta\sigma_{\text{L}}$		(d) tStd_{L}	
	ϵ_{Abs} (mL)	r (1)	ϵ_{Abs} (mL)	r (1)	ϵ_{Abs} (mL)	r (1)	ϵ_{Abs} (mL)	r (1)
S01	0.0 ± 16.9	0.456	0.0 ± 17.8	0.358	0.0 ± 13.3	0.714	0.0 ± 16.8	0.467
S02	0.0 ± 10.9	0.118	0.0 ± 10.9	0.144	0.0 ± 11.0	0.070	0.0 ± 11.0	0.035
S03	0.0 ± 16.1	0.242	0.0 ± 16.5	0.102	0.0 ± 10.2	0.786	0.0 ± 10.9	0.753
S04	0.0 ± 20.9	0.563	0.0 ± 22.9	0.426	0.0 ± 15.7	0.784	0.0 ± 23.6	0.358
S05	0.0 ± 17.5	0.696	0.0 ± 15.3	0.778	0.0 ± 24.0	0.172	0.0 ± 24.0	0.167
S06	0.0 ± 17.8	0.328	0.0 ± 17.1	0.417	0.0 ± 18.6	0.152	0.0 ± 18.1	0.281
S08	0.0 ± 14.9	0.720	0.0 ± 6.2	0.958	0.0 ± 17.2	0.598	0.0 ± 18.9	0.482
S09	0.0 ± 7.6	0.893	0.0 ± 6.0	0.935	0.0 ± 15.8	0.356	0.0 ± 16.5	0.235
S10	0.0 ± 11.2	0.577	0.0 ± 10.6	0.639	0.0 ± 12.8	0.366	0.0 ± 13.5	0.161
All	0.0 ± 15.2	0.813	(†) 0.0 ± 14.3	0.836	(†) 0.0 ± 15.8	0.796	(†) 0.0 ± 17.1	0.755

	(e) tStd_{G}		(f) $\Delta\sigma_{\text{H}}$, $\frac{\Delta\sigma_{\text{H}}}{\sigma_{\text{G}}}$		(g) $\Delta\sigma_{\text{L}}$, $\frac{\Delta\sigma_{\text{L}}}{\sigma_{\text{G}}}$		(h) V_{T}	
	ϵ_{Abs} (mL)	r (1)	ϵ_{Abs} (mL)	r (1)	ϵ_{Abs} (mL)	r (1)	ϵ_{Abs} (mL)	r (1)
S01	0.0 ± 17.7	0.363	0.0 ± 6.8	0.934	0.0 ± 6.2	0.946	0.0 ± 5.1	0.963
S02	0.0 ± 10.8	0.186	0.0 ± 5.7	0.855	0.0 ± 6.1	0.831	0.0 ± 4.8	0.898
S03	0.0 ± 8.9	0.844	0.0 ± 11.8	0.701	0.0 ± 7.8	0.883	0.0 ± 13.4	0.590
S04	0.0 ± 25.2	0.069	0.0 ± 13.9	0.835	0.0 ± 13.9	0.834	0.0 ± 15.5	0.791
S05	0.0 ± 19.5	0.600	0.0 ± 9.2	0.925	0.0 ± 9.6	0.919	0.0 ± 7.3	0.954
S06	0.0 ± 18.7	0.100	0.0 ± 12.5	0.747	0.0 ± 12.8	0.731	0.0 ± 10.9	0.814
S08	0.0 ± 21.4	0.093	0.0 ± 14.2	0.751	0.0 ± 15.0	0.719	0.0 ± 11.0	0.860
S09	0.0 ± 12.9	0.649	0.0 ± 5.6	0.943	0.0 ± 9.6	0.825	0.0 ± 7.1	0.907
S10	0.0 ± 13.6	0.139	0.0 ± 9.3	0.738	0.0 ± 7.6	0.835	0.0 ± 7.0	0.860
All	(†) 0.0 ± 16.8	0.766	0.0 ± 10.4	0.917	0.0 ± 10.3	0.920	0.0 ± 9.7	0.929

Table E.3 – Subject-specific and overall performance for a selection of eight features (a) to (h) and hypothesis (H3) relative SV via subject-independent calibration. The performance between $\Delta\mathrm{SV}_\mathrm{EIT}$ and $\Delta\mathrm{SV}_\mathrm{Ref}$ is evaluated in terms of angular error ϵ_α and angular concordance rate CR. The (†) indicates unrealistic solutions with calibrations coefficients *not* having identical sign for all subjects. Cell shadings indicate whether the acceptance criteria (see Section 12.2.5) are met (green), not met (red), or met but with unrealistic calibration coefficients (yellow).

	(a) $\Delta\sigma_\mathrm{H}$		(b) tStd_H		(c) $\Delta\sigma_\mathrm{L}$		(d) tStd_L	
	ϵ_Abs (mL)	r (1)	ϵ_Abs (mL)	r (1)	ϵ_Abs (mL)	r (1)	ϵ_Abs (mL)	r (1)
S01	7.0 ± 22.0	66.7	−3.0 ± 23.8	100.0	−17.5 ± 4.5	100.0	−21.4 ± 3.7	100.0
S02	−19.5 ± 24.5	77.8	−32.9 ± 14.0	28.6	−6.2 ± 25.5	63.6	−14.1 ± 18.7	66.7
S03	−24.7 ± 8.5	80.0	−27.3 ± 10.1	60.0	−35.2 ± 6.4	20.0	−31.7 ± 6.7	60.0
S04	3.4 ± 21.5	88.9	−1.0 ± 23.9	88.9	−10.5 ± 16.0	100.0	−15.3 ± 17.2	100.0
S05	−7.0 ± 18.4	83.3	1.1 ± 19.9	100.0	−11.5 ± 22.5	80.0	−23.1 ± 12.1	50.0
S06	−18.2 ± 28.3	63.6	−10.7 ± 33.4	61.5	−7.6 ± 20.6	75.0	−19.1 ± 13.5	66.7
S08	−22.2 ± 11.5	80.0	−12.2 ± 11.5	100.0	−18.4 ± 14.4	50.0	−23.3 ± 11.5	40.0
S09	14.8 ± 15.8	80.0	18.5 ± 12.7	80.0	−16.4 ± 3.4	100.0	−16.4 ± 4.0	100.0
S10	17.9 ± 18.6	77.8	19.9 ± 17.7	66.7	−2.6 ± 24.8	75.0	2.7 ± 24.0	80.0
All	−5.3 ± 25.2	76.9	−4.9 ± 26.5	73.8	−12.1 ± 20.3	70.4	−17.4 ± 16.7	70.2

	(e) tStd_G		(f) $\Delta\sigma_\mathrm{H}$, $\frac{\Delta\sigma_\mathrm{H}}{\sigma_\mathrm{G}}$		(g) $\Delta\sigma_\mathrm{L}$, $\frac{\Delta\sigma_\mathrm{L}}{\sigma_\mathrm{G}}$		(h) V_T	
	ϵ_Abs (mL)	r (1)	ϵ_Abs (mL)	r (1)	ϵ_Abs (mL)	r (1)	ϵ_Abs (mL)	r (1)
S01	−22.8 ± 0.1	100.0	9.1 ± 8.5	100.0	9.6 ± 8.2	100.0	16.9 ± 8.1	100.0
S02	−21.1 ± 7.7	85.7	−6.4 ± 14.9	88.9	−4.3 ± 15.9	100.0	−9.3 ± 11.7	88.9
S03	−19.9 ± 7.7	100.0	−26.0 ± 2.3	100.0	−23.3 ± 3.3	100.0	−27.4 ± 7.2	40.0
S04	−23.7 ± 5.9	100.0	10.6 ± 14.0	87.5	6.4 ± 14.3	85.7	−2.7 ± 15.8	100.0
S05	−22.1 ± 11.4	50.0	−11.9 ± 4.6	100.0	0.6 ± 26.7	83.3	−15.7 ± 3.1	100.0
S06	0.6 ± 45.7	50.0	2.7 ± 20.6	83.3	5.4 ± 20.2	84.6	2.1 ± 17.7	92.3
S08	−26.0 ± 9.1	40.0	−29.3 ± 9.9	40.0	−35.0 ± 12.1	40.0	−4.0 ± 15.0	100.0
S09	−14.4 ± 2.0	100.0	0.1 ± 12.9	100.0	−3.0 ± 14.0	100.0	−10.4 ± 7.9	100.0
S10	−16.0 ± 2.0	100.0	16.1 ± 19.3	75.0	13.4 ± 20.6	71.4	21.2 ± 13.5	85.7
All	(†)−15.6 ± 25.7	73.3	−1.9 ± 20.4	83.9	−1.7 ± 21.7	84.2	−1.5 ± 18.5	89.8

Table E.4 – Subject-specific and overall performance for a selection of eight features (a) to (h) and hypothesis (H4) relative SV via subject-specific calibration. The performance between ΔSV_{EIT} and ΔSV_{Ref} is evaluated in terms of angular error ϵ_α and angular concordance rate CR. The (†) indicates unrealistic solutions with calibrations coefficients *not* having identical sign for all subjects. Cell shadings indicate whether the acceptance criteria (see Section 12.2.5) are met (green), not met (red), or met but with unrealistic calibration coefficients (yellow).

	(a) $\Delta\sigma_H$		(b) tStd_H		(c) $\Delta\sigma_L$		(d) tStd_L	
	ϵ_{Abs} (mL)	r (1)	ϵ_{Abs} (mL)	r (1)	ϵ_{Abs} (mL)	r (1)	ϵ_{Abs} (mL)	r (1)
S01	−6.2 ± 32.0	66.7	−24.8 ± 1.6	100.0	−8.7 ± 11.0	100.0	−2.6 ± 31.2	33.3
S02	−3.9 ± 24.9	81.8	−13.5 ± 15.7	100.0	−19.3 ± 8.2	100.0	−19.3 ± 8.2	100.0
S03	−14.5 ± 17.4	83.3	−22.3 ± 7.7	80.0	3.5 ± 18.7	85.7	3.7 ± 19.0	85.7
S04	1.7 ± 22.5	88.9	−0.2 ± 23.7	88.9	2.6 ± 17.5	100.0	−1.5 ± 20.8	100.0
S05	0.0 ± 23.4	85.7	1.9 ± 21.3	85.7	−21.0 ± 14.6	75.0	−9.6 ± 24.9	83.3
S06	4.0 ± 24.6	73.7	3.6 ± 26.2	66.7	10.3 ± 24.1	72.7	−2.8 ± 19.1	100.0
S08	7.0 ± 22.6	87.5	3.5 ± 8.0	100.0	6.8 ± 21.8	90.0	1.4 ± 21.4	100.0
S09	−4.5 ± 7.1	100.0	−3.0 ± 3.3	100.0	−21.4 ± 7.7	100.0	−23.9 ± 8.1	100.0
S10	−19.9 ± 16.1	66.7	−18.2 ± 16.2	66.7	−25.0 ± 10.6	66.7	−27.2 ± 4.0	66.7
All	−1.0 ± 23.0	80.9	(†) −3.9 ± 21.5	83.3	(†) −0.2 ± 22.5	84.6	(†) −5.8 ± 20.4	91.5

	(e) tStd_G		(f) $\Delta\sigma_H$, $\frac{\Delta\sigma_H}{\sigma_G}$		(g) $\Delta\sigma_L$, $\frac{\Delta\sigma_L}{\sigma_G}$		(h) V_T	
	ϵ_{Abs} (mL)	r (1)	ϵ_{Abs} (mL)	r (1)	ϵ_{Abs} (mL)	r (1)	ϵ_{Abs} (mL)	r (1)
S01	−22.6 ± 14.2	50.0	1.7 ± 8.9	100.0	1.5 ± 6.2	100.0	1.3 ± 4.8	100.0
S02	−3.4 ± 25.3	81.8	−1.0 ± 16.5	88.9	−6.3 ± 20.0	87.5	−2.5 ± 15.1	88.9
S03	−4.1 ± 7.2	100.0	−7.0 ± 18.7	83.3	−1.0 ± 12.8	100.0	−1.7 ± 25.7	85.7
S04	3.4 ± 24.5	81.8	0.4 ± 15.0	100.0	0.8 ± 15.0	100.0	−1.0 ± 16.0	100.0
S05	10.9 ± 29.2	60.0	−4.2 ± 10.3	100.0	−1.1 ± 6.0	100.0	−2.6 ± 6.4	100.0
S06	10.2 ± 23.3	75.0	5.4 ± 19.4	84.6	5.4 ± 20.8	83.3	1.8 ± 17.0	92.3
S08	−2.2 ± 23.1	60.0	10.7 ± 22.1	77.8	8.3 ± 18.9	90.0	4.6 ± 12.9	100.0
S09	−14.4 ± 9.5	100.0	−1.2 ± 2.4	100.0	−6.6 ± 15.5	100.0	−0.4 ± 9.0	100.0
S10	−26.2 ± 4.5	66.7	−14.7 ± 16.9	66.7	−1.7 ± 17.0	100.0	−8.4 ± 13.3	100.0
All	(†) 2.0 ± 24.2	74.4	1.0 ± 17.5	87.7	1.3 ± 16.7	93.0	−0.4 ± 15.3	94.7

Bibliography

[1] Adler, A. *Measurement of Pulmonary Function with Electrical Impedance Tomography*. PhD thesis, Ecole Polytechnique de Montréal, Montréal, Canada, 1995. http://sce.carleton.ca/faculty/adler/publications/aadler-thesis-1995.pdf.

[2] Adler, A. and Boyle, A. Electrical Impedance Tomography: Tissue Properties to Image Measures. *IEEE Trans. Biomed. Eng.*, in press, 2017. DOI:10.1109/TBME.2017.2728323.

[3] Adler, A. and Guardo, R. Electrical impedance tomography: Regularized imaging and contrast detection. *IEEE Trans. Med. Imaging*, 15(2):170–179, 1996. DOI:10.1109/42.491418.

[4] Adler, A. and Lionheart, W.R.B. Minimizing EIT image artefacts from mesh variability in finite element models. *Physiol. Meas.*, 32(7):823–834, 2011. DOI:10.1088/0967-3334/32/7/S07.

[5] Adler, A. and Lionheart, W.R. Uses and abuses of EIDORS: An extensible software base for EIT. *Physiol. Meas.*, 27(5):S25–S42, 2006. DOI:10.1088/0967-3334/27/5/S03.

[6] Adler, A., Arnold, J.H., Bayford, R., Borsic, A. et al. GREIT: A unified approach to 2D linear EIT reconstruction of lung images. *Physiol. Meas.*, 30(6):S35–S55, 2009. DOI:10.1088/0967-3334/30/6/S03.

[7] Adler, A., Gaburro, R. and Lionheart, W. Electrical Impedance Tomography. In Scherzer, O., ed., *Handbook of Mathematical Methods in Imaging*, pp. 599–654. Springer, New York, USA, 2011. ISBN 978-0-387-92919-4. DOI:10.1007/978-0-387-92920-0_14.

[8] Adler, A., Gaggero, P.O. and Maimaitijiang, Y. Adjacent stimulation and measurement patterns considered harmful. *Physiol. Meas.*, 32(7):731–744, 2011. DOI:10.1088/0967-3334/32/7/S01.

[9] Adler, A., Amato, M.B., Arnold, J.H., Bayford, R. et al. Whither lung EIT: Where are we, where do we want to go and what do we need to get there? *Physiol. Meas.*, 33(5):679–694, 2012. DOI:10.1088/0967-3334/33/5/679.

[10] Adler, A., Boyle, A., Braun, F., Crabb, M.G. et al. *EIDORS v3.9*. Zenodo, 2017. DOI:10.5281/zenodo.583266.

[11] Adler, A., Proença, M., Braun, F., Brunner, J. and Solà, J. Origins of Cardiosynchronous Signals in EIT. In *EIT 2017*, p. 73, Dartmouth, USA, 2017. Zenodo. DOI:10.5281/zenodo.557093.

[12] Altman, D.G. and Bland, J.M. Measurement in Medicine: The Analysis of Method Comparison Studies. *The Statistician*, 32(3):307, 1983. DOI:10.2307/2987937.

[13] Arshad, S.H., Murphy, E.K. and Halter, R.J. Respiratory-gated electrical impedance tomography: A potential technique for quantifying stroke volume. In *SPIE Medical Imaging 2016*, p. 97882D, San Diego, USA, 2016. DOI:10.1117/12.2216595.

[14] Asmar, R. *Arterial Stiffness and Pulse Wave Velocity: Clinical Applications*. Elsevier, Amsterdam, The Netherlands, 1999. ISBN 978-2-84299-148-7.

[15] Bernstein, D.P. Impedance cardiography: Pulsatile blood flow and the biophysical and electrodynamic basis for the stroke volume equations. *J. Electr. Bioimpedance*, 1(1):2–17, 2010. DOI:10.5617/jeb.51.

[16] Betts, J.G., Desaix, P., Johnson, E., Johnson, J.E. et al. *Anatomy & Physiology*. OpenStax, 2017. ISBN 978-1-938168-13-0. http://cnx.org/contents/14fb4ad7-39a1-4eee-ab6e-3ef2482e3e22@8.108.

[17] Bistoquet, A., Oshinski, J. and Skrinjar, O. Myocardial deformation recovery from cine MRI using a nearly incompressible biventricular model. *Med. Image Anal.*, 12(1):69–85, 2008. DOI:10.1016/j.media.2007.10.009.

[18] Borges, J.B., Suarez-Sipmann, F., Bohm, S.H., Tusman, G. et al. Regional lung perfusion estimated by electrical impedance tomography in a piglet model of lung collapse. *J. Appl. Physiol.*, 112(1):225–236, 2012. DOI:10.1152/japplphysiol.01090.2010.

[19] Borsic, A., Attardo, E.A. and Halter, R.J. Multi-GPU Jacobian accelerated computing for soft-field tomography. *Physiol. Meas.*, 33(10):1703–1715, 2012. DOI:10.1088/0967-3334/33/10/1703.

[20] Braun, F. *Systolic Time Intervals Measured by Electrical Impedance Tomography (EIT)*. Master's thesis, Eidgenössische Technische Hochschule Zürich, Zürich, Switzerland, 2013. DOI:10.3929/ethz-a-009947722.

[21] Braun, F., Proença, M., Rapin, M., Alba, X. et al. 4D Heart Model Helps Unveiling Contributors to Cardiac EIT Signal. In *EIT 2015*, p. 107, Neuchâtel, Switzerland, 2015. Zenodo. DOI:10.5281/zenodo.17752.

[22] Braun, F., Proença, M., Rapin, M., Lemay, M. et al. Aortic blood pressure measured via EIT: Investigation of different measurement settings. *Physiol. Meas.*, 36(6):1147–1159, 2015. DOI:10.1088/0967-3334/36/6/1147.

[23] Braun, F., Proença, M., Solà, J., Lemay, M. and Thiran, J.P. EIT-derived stroke volume is impaired by belt displacement. In *ICEBI & EIT 2016*, p. 74, Stockholm, Sweden, 2016. Zenodo. DOI:10.5281/zenodo.55753.

[24] Braun, F., Proença, M., Lemay, M., Bertschi, M. et al. Limitations and Challenges of EIT-Based Monitoring of Stroke Volume and Pulmonary Artery Pressure. *Physiol. Meas.*, in press, 2017. DOI:10.1088/1361-6579/aa9828.

[25] Braun, F., Proenca, M., Sola, J., Thiran, J.P. and Adler, A. A Versatile Noise Performance Metric for Electrical Impedance Tomography Algorithms. *IEEE Trans. Biomed. Eng.*, 64 (10):2321–2330, 2017. DOI:10.1109/TBME.2017.2659540.

[26] Braun, F., Proença, M., Adler, A., Riedel, T. et al. Accuracy and Reliability of Noninvasive Stroke Volume Monitoring via ECG-Gated 3D Electrical Impedance Tomography in Healthy Volunteers. *PLOS ONE*, in review, 2018.

[27] Brown, B.H. and Seagar, A.D. The Sheffield data collection system. *Clin. Phys. Physiol. Meas.*, 8(4A):91–97, 1987. DOI:10.1088/0143-0815/8/4A/012.

[28] Brown, B.H., Leathard, A., Sinton, A., McArdle, F.J. et al. Blood flow imaging using electrical impedance tomography. *Clin. Phys. Physiol. Meas.*, 13(A):175, 1992. DOI:10.1088/0143-0815/13/A/034.

[29] Brown, B. Electrical impedance tomography (EIT): A review. *J. Med. Eng. Technol.*, 27(3): 97–108, 2003. DOI:10.1080/0309190021000059687.

[30] Brown, B., Barber, D., Morice, A. and Leathard, A. Cardiac and respiratory related electrical impedance changes in the human thorax. *IEEE Trans. Biomed. Eng.*, 41(8): 729–734, 1994. DOI:10.1109/10.310088.

[31] Brown, B.H. Medical impedance tomography and process impedance tomography: A brief review. *Meas. Sci. Technol.*, 12(8):991–996, 2001. DOI:10.1088/0957-0233/12/8/301.

[32] Carlsson, M. Total heart volume variation throughout the cardiac cycle in humans. *AJP Heart Circ. Physiol.*, 287(1):H243–H250, 2004. DOI:10.1152/ajpheart.01125.2003.

[33] Cheney, M., Isaacson, D., Newell, J.C., Simske, S. and Goble, J. NOSER: An algorithm for solving the inverse conductivity problem. *Int. J. Imaging Syst. Technol.*, 2(2):66–75, 22/1990. DOI:10.1002/ima.1850020203.

[34] Clement, R.P., Vos, J.J. and Scheeren, T.W. Minimally invasive cardiac output technologies in the ICU: Putting it all together. *Curr. Opin. Crit. Care*, 23(4):302–309, 2017. DOI:10.1097/MCC.0000000000000417.

[35] Connors, A.F. The Effectiveness of Right Heart Catheterization in the Initial Care of Critically Ill Patients. *JAMA J. Am. Med. Assoc.*, 276(11):889–897, 1996. DOI:10.1001/jama.1996.03540110043030.

[36] Correia, T., Gibson, A., Schweiger, M. and Hebden, J. Selection of regularization parameter for optical topography. *J. Biomed. Opt.*, 14(3):034044, 2009. DOI:10.1117/1.3156839.

[37] Critchley, L.A. Minimally Invasive Cardiac Output Monitoring in the Year 2012. In Aronow, W.S., ed., *Artery Bypass*. InTech, Rijeka, Croatia, March 2013. ISBN 978-953-51-1025-5. DOI:10.5772/54413.

[38] Critchley, L.A., Yang, X.X. and Lee, A. Assessment of Trending Ability of Cardiac Output Monitors by Polar Plot Methodology. *J. Cardiothorac. Vasc. Anesth.*, 25(3):536–546, 2011. DOI:10.1053/j.jvca.2011.01.003.

[39] Cumming, G.R. Stroke volume during recovery from supine bicycle exercise. *J. Appl. Physiol.*, 32(5):575–578, 1972.

[40] Cybulski, G. *Ambulatory Impedance Cardiography*, volume 76 of *Lecture Notes in Electrical Engineering*. Springer, Berlin, Germany, 2011. ISBN 978-3-642-11986-6. DOI:10.1007/978-3-642-11987-3.

[41] da Silva Ramos, F.J., Hovnanian, A., Souza, R., Azevedo, L.C.P. et al. Estimation of Stroke Volume and Stroke Volume Changes by Electrical Impedance Tomography. *Anesth. Analg.*, in press, 2017. DOI:10.1213/ANE.0000000000002271.

[42] de Sitter, A., Verdaasdonk, R.M. and Faes, T.J.C. Do mathematical model studies settle the controversy on the origin of cardiac synchronous trans-thoracic electrical impedance variations? A systematic review. *Physiol. Meas.*, 37(9):R88–R108, 2016. DOI:10.1088/0967-3334/37/9/R88.

[43] Deibele, J.M., Luepschen, H. and Leonhardt, S. Dynamic separation of pulmonary and cardiac changes in electrical impedance tomography. *Physiol. Meas.*, 29(6):S1–S14, 2008. DOI:10.1088/0967-3334/29/6/S01.

[44] Dinkelbach, J. and Stender, B. Evaluation of Cardiac Induced Impedance Changes in EIT Images Using 4D Image-based FEM Simulations. In *EIT 2015*, p. 109, Neuchâtel, Switzerland, 2015. Zenodo. DOI:10.5281/zenodo.17752.

[45] Eyuboglu, B.M., Brown, B.H. and Barber, D.C. Problems of cardiac output determination from electrical impedance tomography scans. *Clin. Phys. Physiol. Meas.*, 9(4A):71–77, 1988. DOI:10.1088/0143-0815/9/4A/013.

[46] Eyuboglu, B., Brown, B. and Barber, D. In vivo imaging of cardiac related impedance changes. *IEEE Eng. Med. Biol. Mag.*, 8(1):39–45, 1989. DOI:10.1109/51.32404.

[47] Fagerberg, A., Stenqvist, O. and Åneman, A. Monitoring pulmonary perfusion by electrical impedance tomography: An evaluation in a pig model: EIT and pulmonary perfusion. *Acta Anaesthesiol. Scand.*, 53(2):152–158, 2009. DOI:10.1111/j.1399-6576.2008.01847.x.

[48] Faller, A., Schünke, M., Schünke, G. and Taub, E. *The Human Body: An Introduction to Structure and Function*. Thieme, Stuttgart, Germany, 2004. ISBN 978-3-13-129271-1.

[49] Frangi, A., Riu, P., Rosell, J. and Viergever, M. Propagation of measurement noise through backprojection reconstruction in electrical impedance tomography. *IEEE Trans. Med. Imaging*, 21(6):566–578, 2002. DOI:10.1109/TMI.2002.800612.

[50] Frerichs, I., Hinz, J., Herrmann, P., Weisser, G. et al. Regional lung perfusion as determined by electrical impedance tomography in comparison with electron beam CT imaging. *IEEE Trans. Med. Imaging*, 21(6):646–652, 2002. DOI:10.1109/TMI.2002.800585.

[51] Frerichs, I., Pulletz, S., Elke, G., Gawelczyk, B. et al. Patient examinations using electrical impedance tomography—sources of interference in the intensive care unit. *Physiol. Meas.*, 32(12):L1–L10, 2011. DOI:10.1088/0967-3334/32/12/F01.

[52] Frerichs, I., Amato, M.B.P., van Kaam, A.H., Tingay, D.G. et al. Chest electrical impedance tomography examination, data analysis, terminology, clinical use and recommendations: Consensus statement of the TRanslational EIT developmeNt stuDy group. *Thorax*, 72(1):83–93, 2017. DOI:10.1136/thoraxjnl-2016-208357.

[53] Gaggero, P. *Miniaturization and Distinguishability Limits of Electrical Impedence Tomography for Biomedical Application.* PhD thesis, University of Neuchâtel, Neuchâtel, Switzerland, 2011. http://nbn-resolving.de/urn:nbn:ch:rero-004-110162.

[54] Gaggero, P., Adler, A. and Grychtol, B. Using real data to train GREIT improves image quality. In *EIT 2014*, p. 39, Gananoque, Canada, 2014. Zenodo. DOI:10.5281/zenodo.17749.

[55] Gaggero, P.O., Adler, A., Brunner, J. and Seitz, P. Electrical impedance tomography system based on active electrodes. *Physiol. Meas.*, 33(5):831–847, 2012. DOI:10.1088/0967-3334/33/5/831.

[56] Ganz, W., Donoso, R., Marcus, H.S., Forrester, J.S. and Swan, H.J. A new technique for measurement of cardiac output by thermodilution in man. *Am. J. Cardiol.*, 27(4):392–396, 1971. DOI:10.1016/0002-9149(71)90436-X.

[57] Gaw, R.L. *The Effect of Red Blood Cell Orientation on the Electrical Impedance of Pulsatile Blood with Implications for Impedance Cardiography.* PhD thesis, Queensland University of Technology, Brisbane, Australia, 2010. https://eprints.qut.edu.au/39448/.

[58] Geddes, L.A. and Sadler, C. The specific resistance of blood at body temperature. *Med. Biol. Eng. Comput.*, 11(3):336–339, 1973. DOI:10.1007/BF02475543.

[59] Geuzaine, C. and Remacle, J.F. Gmsh: A 3-D finite element mesh generator with built-in pre-and post-processing facilities. *Int. J. Numer. Methods Eng.*, 79(11):1309–1331, 2009. DOI:10.1002/nme.2579.

[60] Goldberg, D.I. and Shephard, R.J. Stroke volume during recovery from upright bicycle exercise. *J. Appl. Physiol.*, 48(5):833–837, 1980.

[61] Golub, G.H., Heath, M. and Wahba, G. Generalized cross-validation as a method for choosing a good ridge parameter. *Technometrics*, 21(2):215–223, 1979. DOI:10.1080/00401706.1979.10489751.

[62] Graham, B.M. and Adler, A. Objective selection of hyperparameter for EIT. *Physiol. Meas.*, 27(5):S65–S79, 2006. DOI:10.1088/0967-3334/27/5/S06.

[63] Grocott, M.P.W. and Hamilton, M.A. Resuscitation fluids. *Vox Sang.*, 82(1):1–8, 2002. DOI:10.1046/j.1423-0410.2002.00123.x.

[64] Grychtol, B., Lionheart, W.R., Bodenstein, M., Wolf, G.K. and Adler, A. Impact of model shape mismatch on reconstruction quality in electrical impedance tomography. *IEEE Trans. Med. Imaging*, 31(9):1754–1760, 2012. DOI:10.1109/TMI.2012.2200904.

[65] Grychtol, B. and Adler, A. FEM electrode refinement for electrical impedance tomography. In *EMBC 2013*, pp. 6429–6432, Osaka, Japan, 2013. IEEE. DOI:10.1109/EMBC.2013.6611026.

[66] Grychtol, B., Müller, B. and Adler, A. 3D EIT image reconstruction with GREIT. *Physiol. Meas.*, 37(6):785–800, 2016. DOI:10.1088/0967-3334/37/6/785.

[67] Hahn, G., Just, A., Dittmar, J. and Hellige, G. Systematic errors of EIT systems determined by easily-scalable resistive phantoms. *Physiol. Meas.*, 29(6):S163–S172, 2008. DOI:10.1088/0967-3334/29/6/S14.

[68] Hansen, P.C. *Rank-Deficient and Discrete Ill-Posed Problems Numerical Aspects of Linear Inversion*. Society for Industrial and Applied Mathematics, Philadelphia, USA, 1998. ISBN 978-0-89871-403-6. DOI:10.1137/1.9780898719697.

[69] Hansen, P.C. Regularization Tools version 4.0 for Matlab 7.3. *Numer. Algorithms*, 46(2): 189–194, 2007. DOI:10.1007/s11075-007-9136-9.

[70] Hansen, P.C. and O'Leary, D.P. The use of the L-curve in the regularization of discrete ill-posed problems. *SIAM J. Sci. Comput.*, 14(6):1487–1503, 1993. DOI:10.1137/0914086.

[71] Hartinger, A., Guardo, R., Adler, A. and Gagnon, H. Real-Time Management of Faulty Electrodes in Electrical Impedance Tomography. *IEEE Trans. Biomed. Eng.*, 56(2):369–377, 2009. DOI:10.1109/TBME.2008.2003103.

[72] Harvey, S., Harrison, D.A., Singer, M., Ashcroft, J. et al. Assessment of the clinical effectiveness of pulmonary artery catheters in management of patients in intensive care (PAC-Man): A randomised controlled trial. *The Lancet*, 366(9484):472–477, 2005. DOI:10.1016/S0140-6736(05)67061-4.

[73] Hasgall, P.A., Neufeld, E., Gosselin, M.C., Klingenböck, A. and Kuster, N. IT'IS Database for thermal and electromagnetic parameters of biological tissues. August 2014. DOI:10.13099/ViP-Database-V2.5.

[74] Hellige, G. and Hahn, G. Cardiac-related impedance changes obtained by electrical impedance tomography: An acceptable parameter for assessment of pulmonary perfusion? *Crit. Care*, 15(3):430, 2011. DOI:10.1186/cc10231.

[75] Henderson, R.P. and Webster, J.G. An Impedance Camera for Spatially Specific Measurements of the Thorax. *IEEE Trans. Biomed. Eng.*, BME-25(3):250–254, 1978. DOI:10.1109/TBME.1978.326329.

[76] Hermans, F.K., Heethaar, R.M., Cotton, R.T. and Harkara, A. Image-based simulation of electrical impedance techniques applied on the human thorax for cardio-pulmonary applications. In *COMSOL Conf. 2009*, Milan, Italy, 2009.

[77] Herment, A., Kachenoura, N., Lefort, M., Bensalah, M. et al. Automated segmentation of the aorta from phase contrast MR images: Validation against expert tracing in healthy volunteers and in patients with a dilated aorta. *J. Magn. Reson. Imaging*, 31(4):881–888, 2010. DOI:10.1002/jmri.22124.

[78] Hinz, J., Hahn, G., Neumann, P., Sydow, M. et al. End-expiratory lung impedance change enables bedside monitoring of end-expiratory lung volume change. *Intensive Care Med.*, 29(1):37–43, 2003. DOI:10.1007/s00134-002-1555-4.

[79] Hofer, C.K., Ganter, M.T. and Zollinger, A. What technique should I use to measure cardiac output? *Curr. Opin. Crit. Care*, 13(3):308–317, 2007. DOI:10.1097/MCC.0b013e3280c56afb.

[80] Holder, D., ed. *Electrical Impedance Tomography: Methods, History, and Applications*. Series in medical physics and biomedical engineering. Institute of Physics Publishing, Bristol, UK, 2005. ISBN 978-0-7503-0952-3. DOI:10.1201/9781420034462.

[81] Hoogendoorn, C., Duchateau, N., Sanchez-Quintana, D., Whitmarsh, T. et al. A High-Resolution Atlas and Statistical Model of the Human Heart From Multislice CT. *IEEE Trans. Med. Imaging*, 32(1):28–44, 2013. DOI:10.1109/TMI.2012.2230015.

[82] IEC 60601-1:2005. *Medical Electrical Equipment - Part 1: General Requirements for Basic Safety and Essential Performance*. International Electrotechnical Commission (IEC), Geneva, Switzerland, 2015.

[83] Isnard, R.N., Pannier, B.M., Laurent, S., London, G.M. et al. Pulsatile diameter and elastic modulus of the aortic arch in essential hypertension: A noninvasive study. *J. Am. Coll. Cardiol.*, 13(2):399–405, 1989. DOI:10.1016/0735-1097(89)90518-4.

[84] Jaccard, P. The distribution of the flora in the alpine zone. *New Phytol.*, 11(2):37–50, 1912. DOI:10.1111/j.1469-8137.1912.tb05611.x.

[85] Jackson, A.S., Blair, S.N., Mahar, M.T., Wier, L.T. et al. Prediction of functional aerobic capacity without exercise testing. *Med. Sci. Sports Exerc.*, 22(6):863–870, 1990. DOI:10.1249/00005768-199012000-00021.

[86] Jaffe, M.B. Partial CO2 rebreathing cardiac output–operating principles of the NICO™ system. *J. Clin. Monit. Comput.*, 15(6):387–401, 1999. DOI:10.1023/A:1009981313076.

[87] Joosten, A., Desebbe, O., Suehiro, K., Murphy, L.S.L. et al. Accuracy and precision of non-invasive cardiac output monitoring devices in perioperative medicine: A systematic review and meta-analysis. *BJA Br. J. Anaesth.*, 118(3):298–310, 2017. DOI:10.1093/bja/aew461.

[88] Karsten, J., Stueber, T., Voigt, N., Teschner, E. and Heinze, H. Influence of different electrode belt positions on electrical impedance tomography imaging of regional ventilation: A prospective observational study. *Crit. Care*, 20(1):3, 2016. DOI:10.1186/s13054-015-1161-9.

[89] Kern, J.W. and Shoemaker, W.C. Meta-analysis of hemodynamic optimization in high-risk patients. *Crit. Care Med.*, 30(8):1686–1692, 2002. DOI:10.1097/00003246-200208000-00002.

[90] Kubicek, W., Karnegis, J., Patterson, R., Witsoe, D. and Mattson, R. Development and evaluation of an impedance cardiac output system. *Aerosp. Med.*, 37(12):1208–1212, 1966.

[91] Lamia, B., Kim, H.K., Severyn, D.A. and Pinsky, M.R. Cross-comparisons of trending accuracies of continuous cardiac-output measurements: Pulse contour analysis, bioreactance, and pulmonary-artery catheter. *J. Clin. Monit. Comput.*, in press, 2017. DOI:10.1007/s10877-017-9983-4.

[92] Levick, J.R. *An Introduction to Cardiovascular Physiology 5E.* Hodder Arnold, London, UK, 2010. ISBN 978-0-340-94204-8.

[93] Lionheart, W.R.B. EIT reconstruction algorithms: Pitfalls, challenges and recent developments. *Physiol. Meas.*, 25(1):125–142, 2004. DOI:10.1088/0967-3334/25/1/021.

[94] Lionheart, W.R., Kaipio, J. and McLeod, C.N. Generalized optimal current patterns and electrical safety in EIT. *Physiol. Meas.*, 22(1):85–90, 2001. DOI:10.1088/0967-3334/22/1/311.

[95] Liu, J., Chen, Y., Maisog, J.M. and Luta, G. A new point containment test algorithm based on preprocessing and determining triangles. *Comput.-Aided Des.*, 42(12):1143–1150, 2010. DOI:10.1016/j.cad.2010.08.002.

[96] Maisch, S., Bohm, S.H., Solà, J., Goepfert, M.S. et al. Heart-lung interactions measured by electrical impedance tomography. *Crit. Care Med.*, 39(9):2173–2176, 2011. DOI:10.1097/CCM.0b013e3182227e65.

[97] Mamatjan, Y., Gaggero, P., Grychtol, B. and Adler, A. Compensating Electrode Errors due to Electrode Detachment in Electrical Impedance Tomography. In *CMBES Conf.*, Ottawa, Canada, 2013.

[98] Mamatjan, Y., Grychtol, B., Gaggero, P., Justiz, J. et al. Evaluation and Real-Time Monitoring of Data Quality in Electrical Impedance Tomography. *IEEE Trans. Med. Imaging*, 32 (11):1997–2005, 2013. DOI:10.1109/TMI.2013.2269867.

[99] Marik, P.E. Noninvasive Cardiac Output Monitors: A State-of the-Art Review. *J. Cardiothorac. Vasc. Anesth.*, 27(1):121–134, 2013. DOI:10.1053/j.jvca.2012.03.022.

[100] Marik, P.E., Cavallazzi, R., Vasu, T. and Hirani, A. Dynamic changes in arterial waveform derived variables and fluid responsiveness in mechanically ventilated patients: A systematic review of the literature. *Crit. Care Med.*, 37(9):2642–2647, 2009. DOI:10.1097/CCM.0b013e3181a590da.

[101] McEniery, C.M., Cockcroft, J.R., Roman, M.J., Franklin, S.S. and Wilkinson, I.B. Central blood pressure: Current evidence and clinical importance. *Eur. Heart J.*, 35(26):1719–1725, 2014. DOI:10.1093/eurheartj/eht565.

[102] Mhajna, M. and Abboud, S. Assessment of cardiac stroke volume in patients with implanted cardiac pacemaker using parametric electrical impedance tomography: A theoretical 2D study. *Int. J. Numer. Methods Biomed. Eng.*, 29(5):630–640, 2013. DOI:10.1002/cnm.2550.

[103] Michard, F. and Teboul, J.L. Predicting Fluid Responsiveness in ICU Patients. *Chest*, 121 (6):2000–2008, 2002. DOI:10.1378/chest.121.6.2000.

[104] Möbius, J. and Kobbelt, L. OpenFlipper: An Open Source Geometry Processing and Rendering Framework. In *Curves and Surfaces 2010*, volume 6920, pp. 488–500, Avignon, France, 2010. Springer. DOI:10.1007/978-3-642-27413-8_31.

[105] Murphy, E., Halter, R. and Odame, K. Simulation study for the design of an EIT system for cardiac output monitoring. In *NEBEC 2015*, Troy, USA, 2015. IEEE. DOI:10.1109/NEBEC.2015.7117182.

[106] Nguyen, D.T., Jin, C., Thiagalingam, A. and McEwan, A.L. A review on electrical impedance tomography for pulmonary perfusion imaging. *Physiol. Meas.*, 33(5):695–706, 2012. DOI:10.1088/0967-3334/33/5/695.

[107] Nichols, W.W., Nichols, W.W. and McDonald, D.A., eds. *McDonald's Blood Flow in Arteries: Theoretic, Experimental, and Clinical Principles.* Hodder Arnold, London, 6th edition, 2011. ISBN 978-0-340-98501-4. DOI:10.1201/b13568.

[108] Nopp, P., Zhao, T.X., Brown, B.H. and Wang, W. Cardiac-related changes in lung resistivity as a function of frequency and location obtained from EITS images. *Physiol. Meas.*, 17 (4A):A213–A225, 1996. DOI:10.1088/0967-3334/17/4A/026.

[109] Otsu, N. A Threshold Selection Method from Gray-Level Histograms. *IEEE Trans. Syst. Man Cybern.*, 9(1):62–66, 1979. DOI:10.1109/TSMC.1979.4310076.

[110] Patterson, R.P., Zhang, J., Mason, L.I. and Jerosch-Herold, M. Variability in the cardiac EIT image as a function of electrode position, lung volume and body position. *Physiol. Meas.*, 22(1):159–166, 2001. DOI:10.1088/0967-3334/22/1/319.

[111] Patterson, R. Impedance cardiography: What is the source of the signal? In *J. Phys. Conf. Ser.*, volume 224, p. 012118. IOP Publishing, 2010. DOI:10.1088/1742-6596/224/1/012118.

[112] Pikkemaat, R. and Leonhardt, S. Separation of ventilation and perfusion related signals within EIT-data streams. In *J. Phys. Conf. Ser.*, volume 224, p. 012028, 2010. DOI:10.1088/1742-6596/224/1/012028.

[113] Pikkemaat, R. *Kardiopulmonales Monitoring mit Hilfe der elektrischen Impedanztomographie*. Number 30 in Aachener Beiträge zur Medizintechnik. Shaker, Aachen, Germany, 2015. ISBN 978-3-8440-3808-8. http://d-nb.info/107591549X.

[114] Pikkemaat, R., Lundin, S., Stenqvist, O., Hilgers, R.D. and Leonhardt, S. Recent Advances in and Limitations of Cardiac Output Monitoring by Means of Electrical Impedance Tomography. *Anesth. Analg.*, 119(1):76–83, 2014. DOI:10.1213/ANE.0000000000000241.

[115] Pironet, A., Dauby, P.C., Chase, J.G., Morimont, P. et al. A comparison between four techniques to measure cardiac output. In *EMBC 2106*, pp. 2717–2720, Orlando, USA, 2016. IEEE. DOI:10.1109/EMBC.2016.7591291.

[116] Poeze, M., Greve, J.M. and Ramsay, G. Meta-analysis of hemodynamic optimization: Relationship to methodological quality. *Critical Care*, 9(6):R771, 2005. DOI:10.1186/cc3902.

[117] Popuri, K., Cobzas, D., Jagersand, M., Esfandiari, N. and Baracos, V. FEM-based automatic segmentation of muscle and fat tissues from thoracic CT images. In *ISBI 2013*, pp. 149–152, San Francisco, USA, 2013. IEEE. DOI:10.1109/ISBI.2013.6556434.

[118] Proença, M. *Non-Invasive Hemodynamic Monitoring by Electrical Impedance Tomography*. PhD thesis, École Polytechnique Fédérale de Lausanne, Lausanne, Switzerland, 2017. DOI:10.5075/epfl-thesis-7444.

[119] Proença, M., Braun, F., Rapin, M., Solà, J. et al. Influence of heart motion on cardiac output estimation by means of electrical impedance tomography: A case study. *Physiol. Meas.*, 36(6):1075–1091, 2015. DOI:10.1088/0967-3334/36/6/1075.

[120] Proença, M., Braun, F., Solà, J., Adler, A. et al. Non-invasive monitoring of pulmonary artery pressure from timing information by EIT: Experimental evaluation during induced hypoxia. *Physiol. Meas.*, 37(6):713–726, 2016. DOI:10.1088/0967-3334/37/6/713.

[121] Proença, M., Braun, F., Solà, J., Thiran, J.P. and Lemay, M. Noninvasive pulmonary artery pressure monitoring by EIT: A model-based feasibility study. *Med. Biol. Eng. Comput.*, 55(6):949–963, 2017. DOI:10.1007/s11517-016-1570-1.

[122] Rangayyan, R.M. *Biomedical Signal Analysis*. Wiley, New York, USA, 2002. ISBN 978-0-470-54420-4. DOI:10.1109/9780470544204.

[123] Rapin, M., Braun, F., Wacker, J. and Chételat, O. A wearable EIT system based on cooperative sensors. In *EIT 2017*, p. 24, Dartmouth, USA, 2017. Zenodo. DOI:10.5281/zenodo.557093.

[124] Reuter, D.A., Huang, C., Edrich, T., Shernan, S.K. and Eltzschig, H.K. Cardiac Output Monitoring Using Indicator-Dilution Techniques: Basics, Limits, and Perspectives. *Anesth. Analg.*, 110(3):799–811, 2010. DOI:10.1213/ANE.0b013e3181cc885a.

[125] Rosset, A., Spadola, L. and Ratib, O. OsiriX: An Open-Source Software for Navigating in Multidimensional DICOM Images. *J. Digit. Imaging*, 17(3):205–216, 2004. DOI:10.1007/s10278-004-1014-6.

[126] Roth, C.J., Ehrl, A., Becher, T., Frerichs, I. et al. Correlation between alveolar ventilation and electrical properties of lung parenchyma. *Physiol. Meas.*, 36(6):1211–1226, 2015. DOI:10.1088/0967-3334/36/6/1211.

[127] Samouëlian, A., Cousin, I., Tabbagh, A., Bruand, A. and Richard, G. Electrical resistivity survey in soil science: A review. *Soil Tillage Res.*, 83(2):173–193, 2005. DOI:10.1016/j.still.2004.10.004.

[128] Sandham, J.D., Hull, R.D., Brant, R.F., Knox, L. et al. A randomized, controlled trial of the use of pulmonary-artery catheters in high-risk surgical patients. *N. Engl. J. Med.*, 348(1): 5–14, 2003. DOI:10.1056/NEJMoa021108.

[129] Saugel, B., Cecconi, M., Wagner, J.Y. and Reuter, D.A. Noninvasive continuous cardiac output monitoring in perioperative and intensive care medicine. *Br. J. Anaesth.*, 114(4): 562–575, 2015. DOI:10.1093/bja/aeu447.

[130] Saugel, B., Grothe, O. and Wagner, J.Y. Tracking Changes in Cardiac Output: Statistical Considerations on the 4-Quadrant Plot and the Polar Plot Methodology. *Anesth. Analg.*, 121(2):514–524, 2015. DOI:10.1213/ANE.0000000000000725.

[131] Schöberl, J. NETGEN An advancing front 2D/3D-mesh generator based on abstract rules. *Comput. Vis. Sci.*, 1(1):41–52, 1997. DOI:10.1007/s007910050004.

[132] Seagar, A.D., Barber, D.C. and Brown, B.H. Theoretical limits to sensitivity and resolution in impedance imaging. *Clin. Phys. Physiol. Meas.*, 8(4A):13–31, 1987. DOI:10.1088/0143-0815/8/4A/003.

[133] Segars, W.P., Sturgeon, G., Mendonca, S., Grimes, J. and Tsui, B.M.W. 4D XCAT phantom for multimodality imaging research. *Med. Phys.*, 37(9):4902–4915, 2010. DOI:10.1118/1.3480985.

[134] Silva, O.L., Lima, R.G., Martins, T.C., de Moura, F.S. et al. Influence of current injection pattern and electric potential measurement strategies in electrical impedance tomography. *Control Eng. Pract.*, 58(Supplement C):276–286, 2017. DOI:10.1016/j.conengprac.2016.03.003.

[135] Smit, H.J., Vonk-Noordegraaf, A., Boonstra, A., de Vries, P.M. and Postmus, P.E. Assessment of the Pulmonary Volume Pulse in Idiopathic Pulmonary Arterial Hypertension by Means of Electrical Impedance Tomography. *Respiration*, 73(5):597–602, 2006. DOI:10.1159/000088694.

[136] Solà, J., Vetter, R., Renevey, P., Chételat, O. et al. Parametric estimation of pulse arrival time: A robust approach to pulse wave velocity. *Physiol. Meas.*, 30(7):603–615, 2009. DOI:10.1088/0967-3334/30/7/006.

[137] Solà, J., Adler, A., Santos, A., Tusman, G. et al. Non-invasive monitoring of central blood pressure by electrical impedance tomography: First experimental evidence. *Med. Biol. Eng. Comput.*, 49(4):409–415, 2011. DOI:10.1007/s11517-011-0753-z.

[138] Solà, J., Proenca, M., Ferrario, D., Porchet, J.A. et al. Noninvasive and Nonocclusive Blood Pressure Estimation Via a Chest Sensor. *IEEE Trans. Biomed. Eng.*, 60(12):3505–3513, 2013. DOI:10.1109/TBME.2013.2272699.

[139] Sörnmo, L. and Laguna, P. *Bioelectrical Signal Processing in Cardiac and Neurological Applications*. Elsevier Academic Press, Amsterdam, The Netherlands, 2005. ISBN 978-0-12-437552-9. DOI:10.1016/B978-0-12-437552-9.50012-X.

[140] Squara, P. Bioreactance: A new method for non-invasive Cardiac Output monitoring. In *Yearbook of Intensive Care and Emergency Medicine*, pp. 619–630. Springer, Berlin, Germany, 2008. ISBN 978-3-540-77290-3. DOI:10.1007/978-3-540-77290-3_58.

[141] Steding-Ehrenborg, K., Jablonowski, R., Arvidsson, P.M., Carlsson, M. et al. Moderate intensity supine exercise causes decreased cardiac volumes and increased outer volume variations: A cardiovascular magnetic resonance study. *J. Cardiovasc. Magn. Reson.*, 15 (1):96, 2013. DOI:10.1186/1532-429X-15-96.

[142] Stetz, C.W., Miller, R.G., Kelly, G.E. and Raffin, T.A. Reliability of the Thermodilution Method in the Determination of Cardiac Output in Clinical Practice. *Am. Rev. Respir. Dis.*, 126(6):1001–1004, 1982. DOI:10.1164/arrd.1982.126.6.1001.

[143] Stringer, W.W., Hansen, J.E. and Wasserman, K. Cardiac output estimated noninvasively from oxygen uptake during exercise. *J. Appl. Physiol.*, 82(3):908–912, 1997.

[144] Swisstom. *Swisstom Resistor Mesh Phantom User Manual 1ST504-103*. Landquart, Switzerland, 2013.

[145] Takahashi, T., Okada, A., Saitoh, T., Hayano, J. and Miyamoto, Y. Difference in human cardiovascular response between upright and supine recovery from upright cycle exercise. *Eur. J. Appl. Physiol.*, 81(3):233–239, 2000. DOI:10.1007/s004210050036.

[146] Tenorio, L. Statistical regularization of inverse problems. *SIAM Rev.*, 43(2):347–366, 2001. DOI:10.1137/S0036144500358232.

[147] Tizzard, A., Demosthenous, A. and Bayford, R. Alternate algorithm to reconstruct shape in wearable device. In *ICEBI & EIT 2016*, p. 128, Stockholm, Sweden, 2016. Zenodo. DOI:10.5281/zenodo.55753.

[148] Trepte, C.J.C., Phillips, C., Solà, J., Adler, A. et al. Electrical impedance tomography for non-invasive assessment of stroke volume variation in health and experimental lung injury. *Br. J. Anaesth.*, 118(1):68–76, 2017. DOI:10.1093/bja/aew341.

[149] Ulbrich, M., Marleaux, B., Mühlsteff, J., Schoth, F. et al. High spatial and temporal resolution 4D FEM simulation of the thoracic bioimpedance using MRI scans. *J. Phys. Conf. Ser.*, 434:012074, 2013. DOI:10.1088/1742-6596/434/1/012074.

[150] Ulbrich, M., Mühlsteff, J., Leonhardt, S. and Walter, M. Influence of physiological sources on the impedance cardiogram analyzed using 4D FEM simulations. *Physiol. Meas.*, 35(7):1451–1468, 2014. DOI:10.1088/0967-3334/35/7/1451.

[151] Unberath, M., Maier, A., Fleischmann, D., Hornegger, J. and Fahrig, R. Open-source 4D statistical shape model of the heart for X-ray projection imaging. In *ISBI 2015*, pp. 739–742, New York, USA, 2015. IEEE. DOI:10.1109/ISBI.2015.7163978.

[152] Vincent, J.L., Rhodes, A., Perel, A., Martin, G.S. et al. Clinical review: Update on hemodynamic monitoring-a consensus of 16. *Crit. Care*, 15(4):229, 2011. DOI:10.1186/cc10291.

[153] Vogt, B., Mendes, L., Chouvarda, I., Perantoni, E. et al. Influence of torso and arm positions on chest examinations by electrical impedance tomography. *Physiol. Meas.*, 37(6):904–921, 2016. DOI:10.1088/0967-3334/37/6/904.

[154] Vonk Noordegraaf, A., Faes, T.J.C., Janse, A., Marcus, J.T. et al. Improvement of cardiac imaging in electrical impedance tomography by means of a new electrode configuration. *Physiol. Meas.*, 17(3):179–188, 1996. DOI:10.1088/0967-3334/17/3/004.

[155] Vonk Noordegraaf, A., Janse, A., Marcus, J.T., Bronzwaer, J.G. et al. Determination of stroke volume by means of electrical impedance tomography. *Physiol. Meas.*, 21(2):285–293, 2000. DOI:10.1088/0967-3334/21/2/308.

[156] Vossoughi, J., Vaishnav, R.N. and Patel, D.J. Compressibility of the myocardial tissue. *Adv Bioeng*, 1980:45–48, 1980.

[157] Waldmann, A.D., Wodack, K.H., März, A., Ukere, A. et al. Performance of Novel Patient Interface for Electrical Impedance Tomography Applications. *J. Med. Biol. Eng.*, 37(4):561–566, 2017. DOI:10.1007/s40846-017-0264-y.

[158] Weise, T. *Global Optimization Algorithms-Theory and Application*, volume 2. Self-published, 2009. http://www.it-weise.de/projects/book.pdf.

[159] Westerhof, N., Stergiopulos, N. and Noble, M.I. *Snapshots of Hemodynamics*. Springer, Boston, USA, 2010. ISBN 978-1-4419-6362-8. DOI:10.1007/978-1-4419-6363-5.

[160] Wheeler, J.L., Wang, W. and Tang, M. A comparison of methods for measurement of spatial resolution in two-dimensional circular EIT images. *Physiol. Meas.*, 23(1):169–176, 2002. DOI:10.1088/0967-3334/23/1/316.

[161] WHO. *Global Status Report on Noncommunicable Diseases 2014*. World Health Organization, Geneva, 2014. ISBN 978-92-4-156485-4.

[162] World Health Organization. *A Prioritized Research Agenda for Prevention and Control of Noncommunicable Diseases*. World Health Organization, Geneva, 2011. ISBN 978-92-4-156420-5.

[163] World Health Organization. Cardiovascular Diseases (CVDs) - Fact Sheet 317, May 2017. http://www.who.int/mediacentre/factsheets/fs317/en/.

[164] Yang, F., Zhang, J. and Patterson, R. Development of an Anatomically Realistic Forward Solver for Thoracic Electrical Impedance Tomography. *J. Med. Eng.*, 2013:1–7, 2013. DOI:10.1155/2013/983938.

[165] Yerworth, R. and Bayford, R. The effect of serial data collection on the accuracy of electrical impedance tomography images. *Physiol. Meas.*, 34(6):659–669, 2013. DOI:10.1088/0967-3334/34/6/659.

[166] Yerworth, R.J., Frerichs, I. and Bayford, R. Analysis and compensation for errors in electrical impedance tomography images and ventilation-related measures due to serial data collection. *J Clin Monit Comput*, 31(5):1093–1101, 2017. DOI:10.1007/s10877-016-9920-y.

[167] Yin, F.C., Chan, C.C. and Judd, R.M. Compressibility of perfused passive myocardium. *Am. J. Physiol.-Heart Circ. Physiol.*, 271(5):H1864–H1870, 1996.

[168] York, T. Status of electrical tomography in industrial applications. *J. Electron. Imaging*, 10(3):608–619, 2001. DOI:10.1117/1.1377308.

[169] Yushkevich, P.A., Piven, J., Hazlett, H.C., Smith, R.G. et al. User-guided 3D active contour segmentation of anatomical structures: Significantly improved efficiency and reliability. *NeuroImage*, 31(3):1116–1128, 2006. DOI:10.1016/j.neuroimage.2006.01.015.

[170] Zhang, J., Qin, L., Allen, T. and Patterson, R.P. Human CT measurements of structure/electrode position changes during respiration with electrical impedance tomography. *Open Biomed. Eng. J.*, 7:109–115, 2013. DOI:10.2174/1874120701307010109.

[171] Zhao, T.X., Brown, B.H., Nopp, P., Wang, W. et al. Modelling of cardiac-related changes in lung resistivity measured with EITS. *Physiol. Meas.*, 17(4A):A227–A234, 1996. DOI:10.1088/0967-3334/17/4A/027.

[172] Zhuang, X. Challenges and methodologies of fully automatic whole heart segmentation: A review. *J. Healthc. Eng.*, 4(3):371–407, 2013. DOI:10.1260/2040-2295.4.3.371.

[173] Zlochiver, S., Freimark, D., Arad, M., Adunsky, A. and Abboud, S. Parametric EIT for monitoring cardiac stroke volume. *Physiol. Meas.*, 27(5):S139–S146, 2006. DOI:10.1088/0967-3334/27/5/S12.

Curriculum Vitae

Born May 19, 1985 in Altstätten (SG), Switzerland.
Single, citizen of Untereggen (SG), Switzerland.

CSEM SA, Fabian Braun
Rue Jaquet-Droz 1
CH-2002 Neuchâtel
Switzerland

Tel.: +41 32 720 5039
E-Mail: fabian.braun@csem.ch
fabbraun@hispeed.ch

Research Interests

Biomedical signal processing for the noninvasive assessment of physiological parameters.

Education

12/2013–01/2018	PhD Thesis in Electrical Engineering, Swiss Federal Institute of Technology Lausanne (EPFL), Lausanne, Switzerland and Swiss Center for Electronics and Microtechnology (CSEM), Neuchâtel, Switzerland
10/2012–05/2013	Master's Thesis, Swiss Center for Electronics and Microtechnology (CSEM), Neuchâtel, Switzerland
09/2010–05/2013	Master of Science in Biomedical Engineering, Swiss Federal Institute of Technology Zürich (ETHZ), Zürich, Switzerland
09/2009–12/2009	Bachelor's Thesis, University of Stavanger (UiS), Stavanger, Norway
10/2006–01/2010	Bachelor of Science in Electrical Engineering, University of Applied Sciences Rapperswil (HSR), Rapperswil, Switzerland
08/2001–08/2005	Apprenticeship as Electronics Technician, Setila AG, Widnau, Switzerland

Professional Experience

12/2013–01/2018	R&D Engineer, Swiss Center for Electronics and Microtechnology (CSEM), Neuchâtel, Switzerland
06/2013–11/2013	Software Engineer, Swisstom AG, Landquart, Switzerland
06/2011–07/2011	Summer Job, Institute of Biomedical Engineering, Swiss Federal Institute of Technology Zürich (ETHZ), Zürich, Switzerland
03/2010–07/2010	Embedded System Design Engineer, Miromico AG, Zürich, Switzerland
08/2005–09/2009	Hard- and Software Developer, Vectronix AG, Heerbrugg, Switzerland

Languages

German	Native speaker
English	Fluent in written and spoken (CAE 2010)
French	Fluent in spoken, intermediate in written

List of Publications

Journal Papers

1. **Braun, F.**, Proença, M., Adler, A., Riedel, T. et al. Accuracy and Reliability of Noninvasive Stroke Volume Monitoring via ECG-Gated 3D Electrical Impedance Tomography in Healthy Volunteers. *PLOS ONE*, in review, 2018
2. **Braun, F.**, Proença, M., Lemay, M., Bertschi, M. et al. Limitations and Challenges of EIT-Based Monitoring of Stroke Volume and Pulmonary Artery Pressure. *Physiol. Meas.*, in press, 2017. DOI:10.1088/1361-6579/aa9828
3. **Braun, F.**, Proenca, M., Sola, J., Thiran, J.P. and Adler, A. A Versatile Noise Performance Metric for Electrical Impedance Tomography Algorithms. *IEEE Trans. Biomed. Eng.*, 64(10): 2321–2330, 2017. DOI:10.1109/TBME.2017.2659540
4. Proença, M., **Braun, F.**, Solà, J., Thiran, J.P. and Lemay, M. Noninvasive pulmonary artery pressure monitoring by EIT: A model-based feasibility study. *Med. Biol. Eng. Comput.*, 55(6): 949–963, 2017. DOI:10.1007/s11517-016-1570-1
5. Quandt, B.M., **Braun, F.**, Ferrario, D., Rossi, R.M. et al. Body-monitoring with photonic textiles: A reflective heartbeat sensor based on polymer optical fibres. *J. R. Soc. Interface*, 14 (128):20170060, 2017. DOI:10.1098/rsif.2017.0060
6. Quandt, B.M., Hufenus, R., Weisse, B., **Braun, F.** et al. Optimization of novel melt-extruded polymer optical fibers designed for pressure sensor applications. *Eur. Polym. J.*, 88:44–55, 2017. DOI:10.1016/j.eurpolymj.2016.12.032
7. Proença, M., **Braun, F.**, Solà, J., Adler, A. et al. Non-invasive monitoring of pulmonary artery pressure from timing information by EIT: Experimental evaluation during induced hypoxia. *Physiol. Meas.*, 37(6):713–726, 2016. DOI:10.1088/0967-3334/37/6/713
8. **Braun, F.**, Proença, M., Rapin, M., Lemay, M. et al. Aortic blood pressure measured via EIT: Investigation of different measurement settings. *Physiol. Meas.*, 36(6):1147–1159, 2015. DOI:10.1088/0967-3334/36/6/1147
9. Proença, M., **Braun, F.**, Rapin, M., Solà, J. et al. Influence of heart motion on cardiac output estimation by means of electrical impedance tomography: A case study. *Physiol. Meas.*, 36(6): 1075–1091, 2015. DOI:10.1088/0967-3334/36/6/1075
10. Rapin, M., Proença, M., **Braun, F.**, Meier, C. et al. Cooperative dry-electrode sensors for multi-lead biopotential and bioimpedance monitoring. *Physiol. Meas.*, 36(4):767–783, 2015. DOI:10.1088/0967-3334/36/4/767
11. Zimmermann, R., **Braun, F.**, Achtnich, T., Lambercy, O. et al. Silicon photomultipliers for improved detection of low light levels in miniature near-infrared spectroscopy instruments. *Biomed. Opt. Express*, 4(5):659–666, 2013. DOI:10.1364/BOE.4.000659

Conference Papers

1. **Braun, F.**, Lemkaddem, A., Moser, V., Dasen, S. et al. Contactless Respiration Monitoring in Real-Time via a Video Camera. In *EMBEC & NBC 2017*, volume 65, pp. 567–570, Tampere, Finland, 2017. Springer Singapore. DOI:10.1007/978-981-10-5122-7˙142. **Among the ten finalists in the Young Investigators Competition.**

2. Solà, J., Vybornova, A., **Braun, F.**, Proença, M. et al. Performance of Systolic Blood Pressure estimation from radial Pulse Arrival Time (PAT) in anesthetized patients. In *EMBEC & NBC 2017*, volume 65, pp. 864–867, Tampere, Finland, 2017. Springer Singapore. DOI:10.1007/978-981-10-5122-7˙216

3. Rapin, M., **Braun, F.**, Wacker, J. and Chételat, O. A wearable EIT system based on cooperative sensors. In *EIT 2017*, p. 24, Dartmouth, USA, 2017. Zenodo. DOI:10.5281/zenodo.557093

4. Adler, A., Proença, M., **Braun, F.**, Brunner, J. and Solà, J. Origins of Cardiosynchronous Signals in EIT. In *EIT 2017*, p. 73, Dartmouth, USA, 2017. Zenodo. DOI:10.5281/zenodo.557093

5. Adler, A., Boyle, A., **Braun, F.**, Crabb, M.G. et al. EIDORS Version 3.9. In *EIT 2017*, p. 63, Dartmouth, USA, 2017. Zenodo. DOI:10.5281/zenodo.557093

6. Fallet, S., Schoenenberger, Y., Martin, L., **Braun, F.** et al. Imaging Photoplethysmography: A Real-time Signal Quality Index. In *CinC 2017*, volume in press, Rennes, France, 2017. IEEE

7. **Braun, F.**, Proença, M., Solà, J., Lemay, M. and Thiran, J.P. EIT-derived stroke volume is impaired by belt displacement. In *ICEBI & EIT 2016*, p. 74, Stockholm, Sweden, 2016. Zenodo. DOI:10.5281/zenodo.55753

8. Proença, M., **Braun, F.**, Solà, J., Adler, A. et al. Pulmonary artery pressure by EIT: Experimental evaluation. In *ICEBI & EIT 2016*, p. 122, Stockholm, Sweden, 2016. Zenodo. DOI:10.5281/zenodo.55753

9. **Braun, F.**, Lemkaddem, A., Moser, V., Dasen, S. and Grossenbacher, O. Camera-Based Respiration Monitoring. In *BMT 2016*, volume 61, p. S253, Basel, Switzerland, 2016. De Gruyter. DOI:10.1515/bmt-2016-5023

10. Solà, J., Proença, M., **Braun, F.**, Pierrel, N. et al. Continuous non-invasive monitoring of blood pressure in the operating room: A cuffless optical technology at the fingertip. *Curr. Dir. Biomed. Eng.*, 2(1):267–271, 2016. DOI:10.1515/cdbme-2016-0060

11. Proenca, M., **Braun, F.**, Muntane, E., Sola, J. et al. Non-invasive monitoring of pulmonary artery pressure at the bedside. In *EMBC 2016*, pp. 4236–4239, Orlando, USA, 2016. IEEE. DOI:10.1109/EMBC.2016.7591662

12. Solà, J., **Braun, F.**, Muntane, E., Verjus, C. et al. Towards an unsupervised device for the diagnosis of childhood pneumonia in low resource settings: Automatic segmentation of respiratory sounds. In *EMBC 2016*, pp. 283–286, Orlando, USA, 2016. IEEE. DOI:10.1109/EMBC.2016.7590695

13. Fallet, S., Moser, V., **Braun, F.** and Vesin, J.M. Imaging photoplethysmography: What are the best locations on the face to estimate heart rate? In *CinC 2016*, pp. 341–344, Vancouver, Canada, 2016. IEEE. DOI:10.23919/CIC.2016.7868749

14. Fallet, S., Mirmohamadsadeghi, L., Moser, V., **Braun, F.** and Vesin, J.M. Real-time approaches for heart rate monitoring using imaging photoplethysmography. In *CinC 2016*, pp. 345–348, Vancouver, Canada, 2016. IEEE. DOI:10.23919/CIC.2016.7868750

15. Mirmohamadsadeghi, L., Fallet, S., Moser, V., **Braun, F.** and Vesin, J.M. Real-time respiratory rate estimation using imaging photoplethysmography inter-beat intervals. In *CinC 2016*, pp. 861–864, Vancouver, Canada, 2016. IEEE. DOI:10.23919/CIC.2016.7868879

16. **Braun, F.**, Proença, M., Rapin, M., Alba, X. et al. 4D Heart Model Helps Unveiling Contributors to Cardiac EIT Signal. In *EIT 2015*, p. 107, Neuchâtel, Switzerland, 2015. Zenodo. DOI:10.5281/zenodo.17752. **Winner of the Best Student Paper Award.**

17. Proenca, M., **Braun, F.**, Rapin, M., Solà, J. et al. Feasibility of EIT-based pulmonary arterial pressure monitoring. In *EIT 2015*, p. 108, Neuchâtel, Switzerland, 2015. Zenodo. DOI:10.5281/zenodo.17752

18. Adler, A., **Braun, F.** and Solà, J. Distinguishability as a noise performance metric for EIT algorithms. In *EIT 2015*, p. 21, Neuchâtel, Switzerland, 2015. Zenodo. DOI:10.5281/zenodo.17752

19. Rapin, M., Proenca, M., **Braun, F.**, Solà, J. and Chételat, O. Cooperative sensors: A new approach towards wearable EIT systems. In *EIT 2015*, p. 44, Neuchâtel, Switzerland, 2015. Zenodo. DOI:10.5281/zenodo.17752

20. **Braun, F.**, Proença, M., Rapin, M., Alba, X. et al. Stroke volume measured via electrical impedance tomography (EIT): A simulation-based feasibility study. In *SSBE 2015*, Neuchâtel, Switzerland, 2015

21. Proença, M., **Braun, F.**, Rapin, M., Solà, J. et al. Non-invasive pulmonary artery pressure monitoring: A pulse wave velocity approach. In *SSBE 2015*, Neuchâtel, Switzerland, 2015. **Winner of the Best Poster Award.**

22. Rapin, M., **Braun, F.**, Proença, M., Wacker, J. and Chételat, O. Wearable 12-lead ECG monitoring system by means of cooperative sensors. In *SSBE 2015*, Neuchâtel, Switzerland, 2015

23. **Braun, F.**, Proenca, M., Rapin, M., Grychtol, B. et al. Comparing belt positions for monitoring the descending aorta by EIT. In *EIT 2014*, p. 76, Gananoque, Canada, 2014. Zenodo. DOI:10.5281/zenodo.17749

24. Proenca, M., **Braun, F.**, Rapin, M., Solà, J. et al. Influence of heart motion on EIT-based stroke volume estimation. In *EIT 2014*, p. 77, Gananoque, Canada, 2014. Zenodo. DOI:10.5281/zenodo.17749

25. Rapin, M., Proenca, M., **Braun, F.**, Solà, J. et al. Discarding the Direct Component in Electrical Impedance Tomography. In *EIT 2014*, p. 65, Gananoque, Canada, 2014. Zenodo. DOI:10.5281/zenodo.17749

26. Proença, M., Rapin, M., **Braun, F.**, Solà, J. et al. Cardiac output measured by electrical impedance tomography: Applications and limitations. In *BioCAS 2014*, pp. 236–239, Lausanne, Switzerland, 2014. IEEE. DOI:10.1109/BioCAS.2014.6981706

27. Proenca, M., **Braun, F.**, Lemay, M., Grychtol, B. et al. Understanding the Genesis of Cardiac Signals in Electrical Impedance Tomography. In *BIOSIGNALS 2014*, pp. 27–34, Angers, France, 2014. DOI:10.5220/0004793400270034

28. **Braun, F.**, Proença, M., Rapin, M., Grychtol, B. et al. Non-invasive blood pressure estimation via electrical impedance tomography (EIT): Influence of belt position. In *SSBE 2014*, Zürich, Switzerland, 2014

29. Proença, M., **Braun, F.**, Rapin, M., Solà, J. et al. Non-invasive stroke volume estimation via electrical impedance tomography: Influence of heart motion. In *SSBE 2014*, Zürich, Switzerland, 2014

30. **Braun, F.**, Proença, M., Grychtol, B., Adler, A. et al. Investigation on the Origin of Cardiogenic Activity in Electrical Impedance Tomography (EIT). In *Intensive Care Medicine*, volume 39(Suppl 2), pp. S236–S237, Berlin, Germany, 2013. Springer. DOI:10.1007/s00134-013-3095-5

Reports

1. **Braun, F.** *Systolic Time Intervals Measured by Electrical Impedance Tomography (EIT).* Master's thesis, Eidgenössische Technische Hochschule Zürich, Zürich, Switzerland, 2013. DOI:10.3929/ethz-a-009947722
2. Achtnich, T. and **Braun, F.** *Design and Evaluation of a Modular fNIRS Probe for Employment in Neuroimaging Applications.* Semester project report, Eidgenössische Technische Hochschule Zürich, Zürich, Switzerland, 2012. DOI:10.3929/ethz-a-007564212

Software

1. Adler, A., Boyle, A., **Braun, F.**, Crabb, M.G. et al. *EIDORS v3.9.* Zenodo, 2017. DOI:10.5281/zenodo.583266